

# ISI

**bilimi ve tekniđi**  
**dergisi**

**Journal of Thermal Science**  
**and Technology**

**2023 Cilt/Volume 43 Sayı/Number 1**  
**ISSN 1300-3615**

Türk Isı Bilimi ve Tekniđi Derneđi tarafından yılda iki kez  
Nisan ve Ekim aylarında yayınlanır.

*A publication of the Turkish Society for Thermal Sciences and  
Technology, published twice a year, in April and October.*

**TIBTD Adına Yayın Sahibi Sorumlu Yayımcı/Publisher:**  
Prof. Dr. Nuri YÜCEL, Gazi Üniversitesi

**Sorumlu Yazı İşleri Müdürü-Editör/Editor-in-Chief:**  
Prof. Dr. Selin ARADAĞ ÇELEBİOĞLU  
TED Üniversitesi  
submit@tibtd.org.tr

**Yayın Türü:** Yaygın, süreli

**Editörler Kurulu/Editorial Board:**

Prof. Dr. Murat KÖKSAL, Hacettepe Üniversitesi  
Doç. Dr. Özgür EKİCİ, Hacettepe Üniversitesi  
Doç. Dr. Özgür BAYER, Orta Dođu Teknik Üniversitesi

**Dil Editörleri (Language Editors):**

Prof. Dr. Zafer DURSUNKAYA, Orta Dođu Teknik  
Üniversitesi (İngilizce/English)  
Prof. Dr. Haşmet TÜRKÖĞLU, Çankaya Üniversitesi  
(Türkçe/ Turkish)

**Baskı/Printed at:** KALKAN Matbaacılık San. Tic. Ltd.  
Büyük Sanayi 1. Cadde, Alibey İş Hanı No: 99/32 İskitler,  
ANKARA 312 342 16 56

**TIBTD**

**Türk Isı Bilimi ve Tekniđi Derneđi:** Dernek ve bu dergi,  
Türkiye'de ısı bilimi ve tekniđini geliştirmek amacıyla 1976  
yılında Prof. Dr. Yalçın A. GÖĞÜŞ tarafından kurulmuştur.

**Turkish Society of Thermal Sciences and Technology:** The  
association and the journal was founded by Prof. Dr. Yalçın A.  
GÖĞÜŞ in 1976 to improve thermal sciences and technology  
in Turkey.

**Adresi/Adress:** TIBTD, Mühendislik Fakültesi, Zemin Kat  
No.22 Gazi Üniversitesi, 06570 ANKARA  
**http://www.tibtd.org.tr, ibtd@tibtd.org.tr**  
**Üyelik aidatları için:** İş Bankası Maltepe Şubesi Hesap No:  
42120867567, IBAN: TR08 0006 4000 0014 2120 8675 67

**Yönetim Kurulu/Executive Board:**

Prof. Dr. Nuri YÜCEL (Başkan), Prof. Dr. İlhami HORUZ  
(Bşk. Yrd.), Prof. Dr. Selin ARADAĞ ÇELEBİOĞLU  
(Editör), Prof. Dr. Mustafa Zeki YILMAZOĞLU (Genel Sek.),  
Doç. Dr. Duygu UYSAL (Muhasip Üye), Prof. Dr. Oğuz  
TURGUT, Doç. Dr. Ülkü Ece AYLI

## **İÇİNDEKİLER / CONTENTS**

### **Sayfa / Page**

Numerical investigation of plate cooling using multiple impinging jets in different alignments <i>Farklı dizilimlerde çoklu çarpan jetler ile plaka soğutmasının sayısal olarak incelemesi</i> Alperen YILDIZELI and Sertaç ÇADIRCI	1
Investigation of heat transfer improvements of graphene oxide-water and diamond-water nanofluids in cross flow impinging jet flow channels having fin <i>Kanatçıklı çapraz akış çarpan jet akışlı kanallarda grafen oksit-su ve elmas-su nanoakışkanlarının ısı transferi iyileştirmelerinin araştırılması</i> Koray KARABULUT	11
Investigation of heat convection during vehicle braking <i>Taşıt frenlemesi esnasında oluşan ısı taşınımının incelenmesi</i> Cansu AY GÖKÇE and Abdullah DEMİR	31
Difüzyon absorpsiyonlu soğutma sisteminde CuO ve TiO <sub>2</sub> nano partiküllerinin enerji ve ekserji performansına etkisi <i>The effect of CuO and TiO<sub>2</sub> nano particles on energy and exergy performance in diffusion absorption refrigeration system</i> Abdullah YILDIZ ve Sinan SUNAL	41
Analysis of thermal crack formation in water-charged air-cooled heat exchangers for heavy-duty vehicles <i>Ağır hizmet araçları için su şarjlı hava soğutmalı ısı değiştiricilerinde ısıl çatlak oluşumunun analizi</i> İsmail Hakkı SAVCI	59
Damlacık sayısı ve damlacıklar arası yatay mesafenin maksimum yayılma alanı ve ısı transferi performansı üzerine etkilerinin sayısal incelenmesi <i>Numerical investigation of the effects of droplet number and horizontal distance on maximum spreading area and heat transfer performance</i> Ahmet GÜLTEKİN, Nejet ERKAN, Üner ÇOLAK ve Shunichi SUZUKI	69
Effects of roughness elements on V-corrugated absorber plate solar air heaters <i>Pürüzlülük elemanlarının V-kat levhali güneş hava ısıtucularına etkileri</i> Hussain SHAWISH and Murat ÖZDENEFİ	81
Geometric optimization of a nanostructured W-SiO <sub>2</sub> -W selective emitter with temperature dependent emissivity for thermophotovoltaic applications <i>Sıcaklığa bağlı yayılım gösteren nano yapıllı W-SiO<sub>2</sub>-W seçici yayıcının termofotovoltaik uygulamalar için geometrik optimizasyonu</i> Eslem Enis ATAĞ, Elif Begüm ELÇİOĞLU and Tuba OKUTUCU-ÖZYURT	95
Mikroalg ve mikroalg-etanol karışımları kullanımının motor performansı ve emisyonları üzerine bir inceleme <i>An investigation on engine performance and emissions of using microalgae and microalgae-ethanol blends</i> Gönenç DURAN, Muhammed DÖNMEZ ve Cumali İLKİLİÇ	107
The performance of water jet pumps and their application in slurry transportation <i>Su jet pompalarının performansı ve katı-sıvı karışım taşımacılığında uygulanması</i> Mehmet Ali KÖKPİNAR and Mustafa GÖĞÜŞ	119

### **Amaç/Objective**

Isı bilimi ve tekniđinin geliştirilmesini teşvik etmek, ısı bilimi ve tekniđi alanında özgün, teorik, sayısal ve deneysel çalışmaların yayınlanmasına olanak sağlamaktır.

*To contribute to the improvement of thermal sciences and technology and publication of original, theoretical, numerical and experimental studies in thermal sciences and technology.*

### **İçerik/Content**

Isı bilimi ve tekniđi alanındaki özgün ve derleme makaleler.  
*Original and review articles in thermal sciences and technology.*

### **Değerlendirme/Evaluation**

Dergi hakemli bir dergi olup, her bir makale konusunda uzman en az iki hakem tarafından değerlendirilir.  
*Each article published in this journal is evaluated by at least two referees.*

Science Citation Index Expanded (SCIE), Engineering Index (EI), EBSCO ve Mühendislik ve Temel Bilimler Veri Tabanı (TÜBİTAK-ULAKBİM) tarafından taranmaktadır.  
*Indexed by Science Citation Index Expanded (SCIE), Engineering Index (EI), EBSCO and Engineering and Natural Sciences Data Base (TÜBİTAK-ULAKBİM).*



## NUMERICAL INVESTIGATION OF PLATE COOLING USING MULTIPLE IMPINGING JETS IN DIFFERENT ALIGNMENTS

Alperen YILDIZELI\* and Sertac CADIRCI\*\*

Department of Mechanical Engineering, Istanbul Technical University  
34437 Gumussuyu, Istanbul, Turkey

\*yildizeli@itu.edu.tr, ORCID: 0000-0002-1097-1359

\*\*cadircis@itu.edu.tr, ORCID: 0000-0002-2281-721X

(Geliş Tarihi: 24.02.2022, Kabul Tarihi: 06.01.2023)

**Abstract:** In this study, convective heat transfer by multiple impinging jet arrays in different arrangements is numerically investigated using Computational Fluid Dynamics (CFD). Computational domain consists of multiple jet array either in inline or staggered alignment and a target plate to be cooled by impinging jets. Distance between the jet array and the target plate is kept constant at  $H=28$  mm. Diameter of circular jet nozzles is fixed at  $D=5$  mm for all configurations. Effects of jet Reynolds number ( $Re_j$ ), spacing between circular jets and the alignment of the jet nozzles on aerothermal performance are parametrically investigated in the scope of this study. For staggered and inline alignments of the jet nozzles,  $Re_j$  ranges from 5000 to 20000 and the ratio of the spacing to the jet diameter ( $s/D$ ) changes between 2 and 6. CFD calculations are performed using finite volume based ANSYS-Fluent flow solver. Simulations are conducted for incompressible, steady and turbulent flow using  $k-\omega$  SST turbulence model with ideal gas assumption for density and Sutherland law for viscosity. After intensive mesh convergence and validation tests, appropriate mesh resolution is determined and parametric investigations are performed. The study reveals that most dominant parameter for plate cooling is  $Re_j$  followed by spacing between jets and finally jet alignment. For all  $Re_j$ , inline jet nozzle alignment provides 15% higher average heat transfer rate than staggered alignment when  $s/D$  is close to the lower limit. However, it is shown that jet alignment does not affect thermal performance when  $s/D$  is higher.

**Keywords:** Computational Fluid Dynamics (CFD), Multiple impinging jets, Heat transfer enhancement.

## FARKLI DİZİMLERDE ÇOKLU ÇARPAN JETLER İLE PLAKA SOĞUTMASININ SAYISAL OLARAK İNCELEMESİ

**Özet:** Bu çalışmada, iki farklı dizilim ile konumlandırılmış çoklu çarpan jetler ile gerçekleştirilen taşınım ısı transferi Hesaplamalı Akışkanlar Dinamiği (HAD) yöntemleri ile sayısal olarak incelenmiştir. Çözüm hacmi, hizalı veya şaşırtmalı olarak dizilmiş jetler, jet plakası, soğutulması hedeflenen plaka ve arada bulunan akış hacmini kapsamaktadır. Jet dizisi ile hedef plakası arasındaki mesafe  $H=28$  mm olup, sabittir. Tüm dizilimlerde dairesel jet orifislerinin çapı sabit olup,  $D=5$  mm'dir. Çalışma kapsamında jet Reynolds sayısının ( $Re_j$ ), ardışık jetler arasındaki mesafenin ve jet orifisleri dizilim tipinin aerothermal performans üzerindeki etkileri parametrik olarak incelenmiştir. Jet orifislerinin şaşırtmalı ve hizalı dizildiği durumlar için,  $Re_j$ 'nin 5000 ila 20000 arasında değiştiği ve ardışık orifisler arasındaki mesafenin orifis çapına oranının ( $s/D$ ) 2 ila 6 arasında olduğu durumlar incelenmiştir. HAD hesaplamaları sonlu hacim yöntemi temelli ANSYS-Fluent akış çözücüsü kullanılarak yapılmıştır. Simülasyonlar sırasında, hal denklemleri için ideal gaz varsayımı ve viskozitenin sıcaklıkla değişimini ifade etmek için Sutherland yasası kullanılmıştır. HAD analizleri  $k-\omega$  SST türbülans modeli kullanılarak sıkıştırılmaz, daimi ve türbülanslı akışlar için yapılmıştır. Çözüm açısından bağımsızlık ve doğrulama analizlerinin ardından uygun çözüm ağı belirlenmiş ve parametrik çalışmalar gerçekleştirilmiştir. Çalışma, hedef plakanın soğutulmasında en baskın parametrenin  $Re_j$  olduğunu, ardından jetler arasındaki mesafe ve son olarak jet dizilimi olduğunu ortaya koymaktadır. Jetlerin birbirine yakın olduğu durumlarda hizalı dizilimin, şaşırtmalı dizilime göre %15 civarında daha yüksek ısı transferi sağladığı görülmüştür. Buna karşılık ardışık jetlerin birbirinden uzak olduğu durumlarda hizalama tipinin ısı performansına etkisinin görülmediği HAD analizleri ile ortaya konmuştur.

**Anahtar Kelimeler:** Hesaplamalı Akışkanlar Dinamiği (HAD), Çoklu çarpan jet, Isı transferi iyileştirmesi.

## NOMENCLATURE

D	Nozzle diameter [m]
E	Total energy [ $\text{m}^2/\text{s}^2$ ]
HTU	Heat Transfer Uniformity [ $=q''_{\text{ave}}/(q''_{\text{max}} - q''_{\text{min}})$ ]
k	Turbulence kinetic energy [ $\text{m}^2/\text{s}^2$ ]
$k_{\text{eff}}$	Effective thermal conductivity [W/mK]
Nu	Nusselt number [ $=hD/k_{\text{eff}}$ ]
PP	Pumping Power [W]
p	Pressure [Pa]
$Re_j$	Jet Reynolds number [ $=\rho DV_{\text{jet}}/\mu$ ]
T	Temperature [K]
u	Velocity [m/s]

### Greek symbols

$\eta$	Performance evaluation indicator [ $=Nu^a HTU^b / PP^c$ ]
$\rho$	Density [ $\text{kg}/\text{m}^3$ ]
$\omega$	Turbulence specific dissipation rate [1/s]
$\mu$	Dynamic viscosity [kg/ms]

## INTRODUCTION

In most industrial applications cooling by forced convection with the consideration of cost-effective designs has become an urgent need over the last 30 years. In such applications, cooling by air is preferred since air can be widely found and cooling by air doesn't require precooling and exhaust air can be sent back to the atmosphere after filtering. Based on these advantages, air induced impinging jet cooling systems have become popular in many industrial applications and drawn the attention of researchers. Examples of cooling by multiple impinging jets in various industrial areas include blades' cooling in turbomachinery, electronics' cooling, quenching processes in glass and steel industries and air floatation dryers.

Chougule et al. (2011), investigated the effects of jet Reynolds number and distance between jets and plate on average Nusselt number in cooling by multiple impinging jets. They used a multiple impinging jet system consisting of nine jets in an inline arrangement and found that the k- $\omega$ -SST turbulence model predicted flow field and heat transfer rates more accurately than the other turbulence models. They revealed that the average Nusselt number increased with decreasing distance between jets and plate and increasing  $Re_j$ . Wu et al. (2019), have investigated immersed impinging jet cooling system design for high-power electronics. For different air flow rates and temperatures, they conducted experiments to thermally characterize the cooling system in terms of Nusselt number. Additionally, they have conducted simulations and found compatible findings with their experimental results. Chen et al. (2020), have studied impinging jet cooling system in staggered configuration of jet nozzles. Roughness effects of the target plate were simulated with micro pin fins in the study. In addition to experiments, numerical simulations have been carried

out. For different crossflow schemes, ribs were found to be effective on average Nusselt number while they were not effective as much on pressure losses. Finally, they found that the inline arrangement of jet nozzles results in higher thermal performance compared to the staggered alignment. Tepe (2021), has numerically investigated the effects of plate to target distance, nozzle spacing and Reynolds number on heat transfer performance of an impinging jet cooling system on a concave surface. After comprehensive verification studies, the k- $\omega$  SST turbulence model was chosen to be used for further simulations. Tepe (2021) found that with increasing plate to target distance and spacings, the average Nusselt number tends to decrease. In addition, spacing between sequential jets plays an important role in heat transfer uniformity. Zuckerman and Lior (2005) compared the performances of various turbulence models in the numerical modelling of multiple impinging jet flows. They compared the computational costs, and accuracies in heat transfer calculation and observed secondary Nusselt peaks in detail. In this study, the deviations of the turbulence models such as k- $\epsilon$ , k- $\omega$ , RSM (Reynolds Stress Model) and ASM (Algebraic Stress Model) from the experimental data are shown and the superiority of v2-f and k- $\omega$  SST turbulence models in predicting the flow field with high accuracy close to experiments have been highlighted. Obot and Trabold (1987) compared the effects of dominant parameters of the multiple impinging jet cooling system. They experimentally investigated the effects of three various jet to plate spacing ratios,  $Re_j$  varying between 1000 and 21000, three crossflow schemes and jet to plate spacing ratios of 2 to 16. Based on the evaluation of measurements, low crossflow velocities and low jet to plate spacing ratios achieved enhanced heat transfer rates. Wen et al. (2018) investigated the effects of jet nozzle arrangement on heat transfer uniformity. In their study, they concluded that increasing the number of jets provided a uniform heat transfer distribution on the impinging plate and showed that varying the jet diameter in radial position increased the overall heat transfer. Chang and Shen (2019) investigated the effects of grooves on the impinging plate using two different web patterns along with the jet Reynolds, jet to plate distance and the jet diameter. They showed that heat transfer could be enhanced by using grooves and satisfying the conditions such as lower jet to plate distance than the jet diameter and moderate  $Re_j$  ranging from 5000 to 20000. Vinze et al. (2019) experimentally investigated the effects of dimples on impinging plate on heat transfer in a multiple impinging jet cooling system at various jet Reynolds numbers, jet to plate distances, jet to jet spacing, dimple depths and eccentricities of dimples. They found that heat transfer enhancement could be achieved if the spacing between the jets was four times higher than the jet's diameter and dimples were used on the impinging plate. Xing and Weigand (2013) investigated the effect of the distance between the impinging plate and the jet array on heat transfer experimentally. At different impingement system

configurations, they examined an array consisting of 81 jets. They obtained Nu distribution on the surface by using the Thermochromic Liquid Cristal measurement technique and also solved one-dimensional time dependent heat transfer equation. In their study, they showed that for all impingement system configurations, higher thermal performance was achieved when the distance between the jet and the impinging plate was three times higher than the jet diameter. The thermal performance improvement provided by impinging jet systems has led researchers to utilize impinging jets for different perspectives in various application areas. Fu et. al (2021), investigated a novel application of impinging jet cooling for batteries of hybrid cars. They measured heat and momentum transfer of impinging jet cooling under cross-flow conditions created in a wind tunnel. They conducted CFD simulations based on  $k-\omega$  SST turbulence model, compared numerical results with experiments and concluded that the vortex generation due to crossflow improves heat transfer. In their study, it was mentioned that the inlet jet pressure and jet height are also important parameters. Bijarchi et. al (2019), examined Swinging Sloth Impinging Jet (SSIJ) numerically. Parametric investigations were carried out with a 2D laminar model involving jet to plate distance, jet Reynolds number and the swinging frequency. The results showed that oscillation frequencies up to 10 Hz increase heat transfer by preventing boundary layer development. They also showed that, dimensionless jet to plate distances of 0.35 to 0.5 resulted in higher local Nusselt numbers. Sabato et. al (2019), numerically investigated the effect of different nozzle diameters and nozzle orientations on power electronic cooling utilizing impinging jet systems. Parametric simulations revealed that smaller nozzle diameters and inline arrangement showed better thermal performance. It has also been mentioned that required pumping power for impinging jet system is lower than for conventional power electronic cooling systems. Chauhan and Tankur (2014), developed a mathematical model for impinging jet solar air heaters and investigated the effects of Reynolds number, spanwise and streamwise distance between sequential jets and the diameter of jets on thermal efficiency. They concluded that, under certain operating conditions involving Reynolds number, impinging jet solar air heater shows higher thermal efficiency than the conventional design. The main challenge of industrial cooling applications is to maintain uniform and performant cooling with acceptable power requirements. Thus, the problem becomes a multi-objective industrial design problem. Consequently, the definition of those related parameters and a global performance evaluation become important to compare different configurations. In the current study, the cooling effect of multiple jets on an impinging plate with higher constant surface temperature is investigated numerically. To do this, the effects of the physical parameters such as jet Reynolds number and design parameters such as the spacing between the jets and jet's alignments on the heat transfer performance are examined. On a simplified cooling

system, numerical simulations carried out with ANSYS Fluent provided a deep insight into the performance of various configurations based on heat transfer capabilities, heat transfer uniformity and finally energy consumption. As recent studies in the literature have shown, researchers have found different results from their studies due to the lack of overall evaluation parameters that include the necessary objective functions to indicate aero-thermal performance. The originality of the current study is based on the opportunity to select the appropriate design that meets the specific demands of industrial application. For this need, a performance evaluation indicator involving average Nu, heat transfer uniformity (HTU) and pumping power (PP) is defined which enables overall performance comparison between various designs.

## METHODOLOGY

In this section, the problem of interest is introduced together with its computational domain and boundary conditions. The CFD approach and necessary mesh convergence tests and validation by experiments are explained in detail.

### Computational Domain, Mesh and Boundary Conditions

Figures 1a and 1b show the computational domains for inline and staggered alignments, respectively. The model consists of a confinement wall with jet nozzles and a target plate placed opposite to it. The jet diameter, spacing between jet nozzles and the constant jet to plate distance are denoted by  $D$ ,  $s$  and  $H$ , respectively. Several grid configurations consisting of tetrahedral and hexahedral elements are generated by ANSYS-Meshing and converted to polyhedral meshes in ANSYS-Fluent.

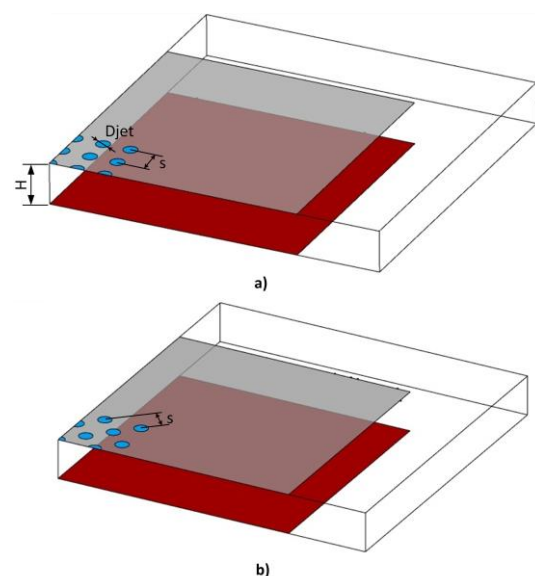


**Figure 1.** Computational Domains of: a) inline, b) staggered alignments.

The implemented boundary conditions are as follows: the plates are walls with no-slip boundary condition, the jet nozzles are prescribed with velocity inlet according to the jet Reynolds number and all lateral surfaces have pressure outlet. Thermal boundary conditions are as follows: constant temperature of 300.15 K is applied to each jet and the confinement wall, and the target plate is subjected to a constant temperature of 330.15 K. It should be pointed out that the geometric specifications of the impinging jet configurations such as the jet nozzle diameter  $D=5\text{mm}$ , jet to plate distance  $H=28\text{mm}$ , spacing ratios to the jet diameter  $2 < s/D < 6$  and the boundary conditions including the jet Reynolds number  $5000 < Re_j < 20000$  are consistent with other studies.

### Numerical Approach and Governing Equations

The CFD calculations have been carried out by finite-volume based flow solver ANSYS-Fluent. The continuity equation in Eq.(1), RANS equations in Eq.(2) and the energy equation in Eq.(3) together with transport equations for the  $k-\omega$  SST turbulence model in Eq.(4) and Eq.(5) are solved numerically until their convergence criteria have been achieved. Readers may refer to (Menter, 1994) for details of the  $k-\omega$  SST turbulence model. The Reynolds-averaged Navier-Stokes (RANS) equations in Eq.(1) and Eq.(2) show the same form as the instantaneous Navier-Stokes equations, but all the variables are ensemble-averaged, thus additional terms will appear that represent the effect of turbulence. These additional terms are the so-called Reynolds-stresses or turbulent-stresses associated with momentum fluctuations. In Eq.(2) they are represented by  $(-\rho u_i' u_j')$  and they have to be modeled in order to close Eq.(2). In the modeled energy equation in Eq.(3),  $E$  represents the total energy,  $k_{eff}$  is the effective thermal conductivity and  $(\tau_{ij})_{eff}$  is the deviatoric stress tensor. The SIMPLE algorithm was used with upwind schemes for all variables. The residuals to satisfy numerical convergence for continuity, momentum, turbulence and energy equations are determined as  $10^{-3}$ ,  $10^{-4}$ ,  $10^{-4}$  and  $10^{-6}$ , respectively.

$$\frac{\partial \rho}{\partial t} + \frac{\partial}{\partial x_i} (\rho u_i) = 0 \quad (1)$$

$$\begin{aligned} \frac{\partial}{\partial t} (\rho u_i) + \frac{\partial}{\partial x_j} (\rho u_i u_j) = - \frac{\partial p}{\partial x_i} + \\ \frac{\partial}{\partial x_j} \left[ \mu \left( \frac{\partial u_i}{\partial x_j} + \frac{\partial u_j}{\partial x_i} - \frac{2}{3} \delta_{ij} \frac{\partial u_l}{\partial x_l} \right) \right] + \frac{\partial}{\partial x_j} \left( -\rho u_i' u_j' \right) \end{aligned} \quad (2)$$

$$\begin{aligned} \frac{\partial}{\partial t} (\rho E) + \frac{\partial}{\partial x_i} (u_i (\rho E + p)) = \\ \frac{\partial}{\partial x_j} \left( k_{eff} \frac{\partial T}{\partial x_j} + u_i (\tau_{ij})_{eff} \right) + S_h \end{aligned} \quad (3)$$

$$\frac{D\rho k}{Dt} = \tau_{ij} \frac{\partial u_i}{\partial x_j} - \beta^* \rho \omega k + \frac{\partial}{\partial x_j} \left[ (\mu + \sigma_k \mu_t) \frac{\partial k}{\partial x_j} \right] \quad (4)$$

$$\begin{aligned} \frac{D\rho \omega}{Dt} = \frac{\gamma}{v_t} \tau_{ij} \frac{\partial u_i}{\partial x_j} - \beta \rho \omega^2 + \\ \frac{\partial}{\partial x_j} \left[ (\mu + \sigma_\omega \mu_t) \frac{\partial \omega}{\partial x_j} \right] + 2(1 - F_1) \frac{\rho \sigma_\omega \omega}{\omega} \frac{\partial k}{\partial x_j} \frac{\partial \omega}{\partial x_j} \end{aligned} \quad (5)$$

Air flow is assumed to be steady and incompressible with ideal gas and Sutherland law approaches in order to consider the changes of density and viscosity with respect to temperature for realistic predictions. Jet Reynolds number, local Nusselt number and area weighted average Nusselt number are given in Equations (6), (7) and (8), respectively.

$$Re_j = \frac{\rho V_{jet} D}{\mu} \quad (6)$$

$$Nu(x, y) = \frac{hD}{k_{eff}} = \frac{q''(x, y)D}{k_{eff}(T_{plate} - T_{jet})} \quad (7)$$

$$\overline{Nu} = \frac{1}{A_{target, plate}} \int Nu(x, y) dA_{target, plate} \quad (8)$$

Thermal conductivity of air is taken as 0.02749 W/mK for Nusselt calculations which is in accordance with the temperature ranges of the case.

### Turbulence Model

Different turbulence models that resolve wall vicinity have been compared in order to determine the appropriate turbulence model. Wall  $y^+$  constraints have been considered to compare each turbulence model with proper mesh. Comparison of the numerical and experimental results is presented in Figure 2.

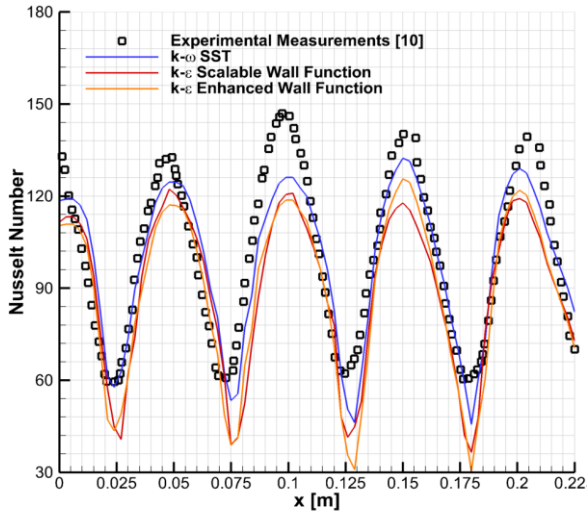


**Figure 2.** Turbulence model verification.

As can be seen from Figure 2, in accordance with other studies, the  $k-\omega$  SST turbulence model was found to be in better agreement with the experimental data in the literature. Thus, the following studies were conducted with the  $k-\omega$  SST turbulence model.

### Mesh Convergence Tests and Validation Results

Before starting a comprehensive parametric investigation of the impinging jet configurations, intensive mesh convergence tests have been carried out to determine the adequate number of elements. The calculations were conducted according to the before-mentioned numerical approach and procedure with the same boundary conditions. Figure 3a indicates the local Nusselt number variation on the target plate for different number of elements and the comparison of the numerical results with the experimental data available in literature (Xing Y. and Weigand B., 2013). This validation study reveals that a mesh consisting of 4.6 million elements is found to be sufficient for further calculations. The deviations in the peaks of the Nu distribution along the plate are associated with the complexity of the impinging jet flow such as wash-up vortices and wall jet collision-separation that can be captured more accurately by numerical simulations rather than measurements. However, the average Nu does not change considerably in the mesh tests. Figure 3b supports this finding by showing that relative error in the average Nu converges as the number of elements increases.

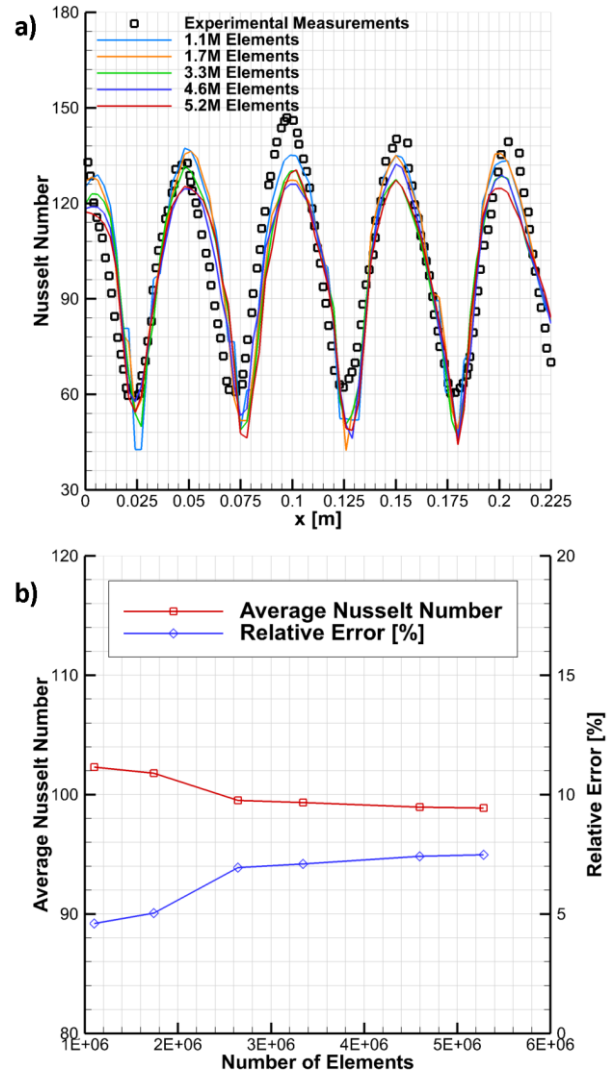


**Figure 3.** Results of mesh convergence tests a) Nu variation validated by experiments (Xing Y. and Weigand B., 2013) b) Mesh convergence summary

## RESULTS

In this study, average Nu is considered as the objective function to examine the overall thermal performance of the impingement designs. Fig.4 shows the average Nu maps as a function of jet Reynolds number  $Re_j$  and  $s/D$  for inline and staggered alignments where there are 160 investigated cases in total.

In Figures 4a and 4b, it is obvious that  $Re_j$  is more dominant than the spacing between jets in enhancing forced convection. Increasing the Reynolds number affects both momentum and energy transfer positively which causes controversial results like increased demand for pumping power versus enhanced heat transfer. In the inline alignment, increasing  $s/D$  from 2 to 6 causes a relative 68% enhancement at all  $Re_j$  in cooling performance i.e. in average Nu. Distributing the jets to an extent up to six times of the jet diameter shows a %90 increase in average Nu values for staggered alignment. The effect of  $s/D$  can be associated with the peaks in the local Nu distribution as

demonstrated in Fig.3a, since uniformly distributed jets produce more cooling effect than jets close together.

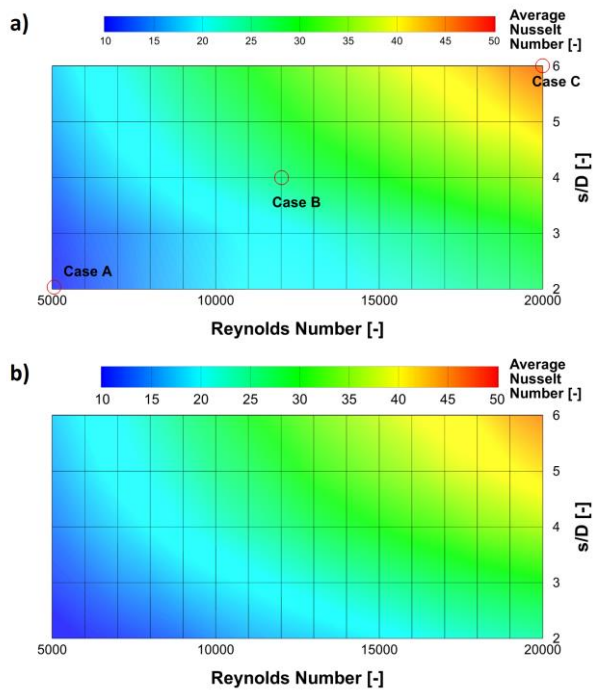


**Figure 4.** Average Nusselt maps for a) inline and b) staggered alignments, colours denote average Nu.

For inline and staggered alignments, increasing  $Re_j$  from 5000 to 20000 results in a relative 170% enhancement in cooling performance at all  $s/D$  ratios. When the performance of inline alignment is compared with the staggered one, overall averaged Nu values increased by 15% at  $s/D=2$  for all  $Re_j$ . However, at higher  $s/D$  ratios, both configurations showed a 3% difference in overall averaged Nu for all  $Re_j$ . The influence of both alignments on the cooling performance is found to be remarkable at low  $s/D$  ratios rather than higher  $s/D$  ratios. Nevertheless, the alignment is always less significant than other parameters in terms of cooling performance. In accordance with the literature and Figure 4, it can be concluded that, jet Re as the flow attribute and  $s/D$  ratio as the main geometric design parameter affect overall Nu values on the target plate; indicating that, these two parameters have to be taken into consideration for forced convection applications utilizing impinging jets. Non-uniform cooling of materials causes large temperature gradients and thermal stresses which reduces the lifetime. Thus, cooling a material subjected to high temperatures uniformly is a major demand in most industrial applications involving thermal processes. In the current study, heat transfer uniformity has been taken into account and investigated as a target function depending on the parameters governing the cooling process. Heat transfer uniformity (HTU) is defined as the ratio of the average heat transfer rate to the difference between the maximum and minimum heat transfer rates as given in Eq.(9).

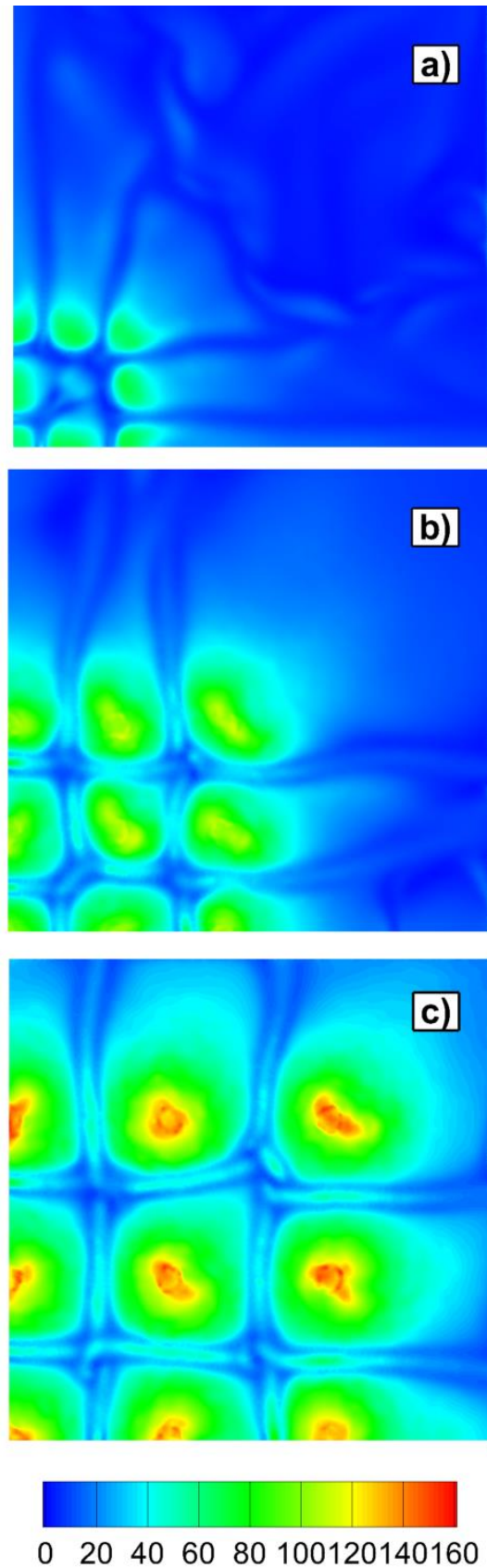


**Figure 5.** Surface Nusselt contours on target plate for three cases: a) Case A, b) Case B, c) Case C.

$$HTU = \frac{q''_{average}}{q''_{max} - q''_{min}} \quad (9)$$

Figure 5 demonstrates three representative individual cases selected from the design space for inline alignment. They are denoted by Case A, B and C and their local Nu contours on the target plate are shown in Fig. 5a, 5b and 5c, respectively. The corresponding cases have the specifications  $(Re_j; s/D) = (5000; 2)$ ,  $(12000; 4)$  and  $(20000; 6)$ , respectively. As it can be seen obviously, Case C has the highest Nusselt values at stagnation points and the lowest HTU value, in other words, the most uniformly distributed heat transfer is obtained in Case C among selected designs. Case A and Case B display that with decreasing  $Re_j$  and  $s/D$ , Nusselt peaks at stagnation points decrease as well as the average Nu and as a result, higher HTU values are observed which represents non-uniform cooling.

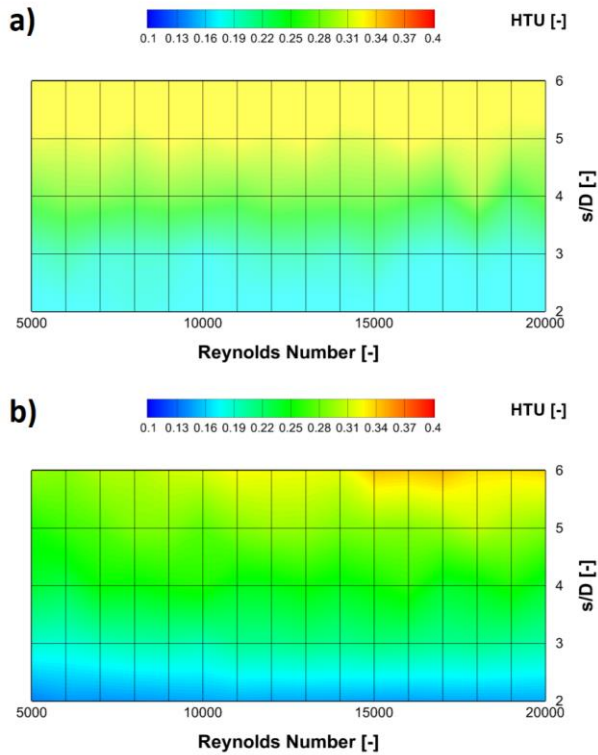


**Figure 6.** Heat transfer uniformity maps for a) inline and b) staggered alignments, colors denote HTU.

Figures 6a and 6b show heat transfer uniformity (HTU) maps on the design space for inline and staggered configurations, respectively. If HTU is investigated in order to evaluate uniform cooling, it should be pointed out that the alignment is a crucial factor acting on the capability of the impingement configuration. As it is shown in Figure 6, cooling the target plate is more uniformly achieved by inline alignment of the jet nozzles than by the staggered alignment. For the  $s/D$  value of two, inline alignment provides 30% to 40% higher HTU values. As  $s/D$  increases, the effect of alignment on heat transfer uniformity vanishes. For constant spacing, the effect of alignment on heat

transfer uniformity is more dominant at lower  $Re$  values. In this respect, the  $s/D$  ratio maintains HTU more radically than the jet Reynolds number for the two alignments. In summary, increasing  $s/D$  to its upper limit supports uniform cooling performance at a lower HTU for both alignments. The power required to deliver jets to the impinging plate is calculated and plotted on the design space as shown in Fig.7. Eq.(10) shows the calculation of pumping power as the multiplication of pressure difference by the total volumetric flow rate of the jets  $Q$ .  $P_{inlet}$  and  $P_{outlet}$  denote the total pressures at the jet nozzle and pressure outlet, respectively.

$$PP = (P_{inlet} - P_{outlet})Q \quad (10)$$

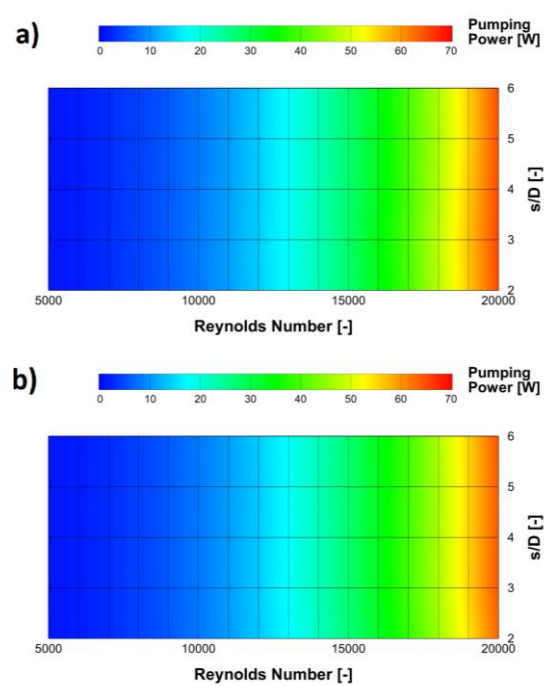


**Figure 7.** Pumping power results for a) inline and b) staggered alignments, colors denote pumping power

Since the power necessary for delivering air flow is directly related to the jet velocity, the pumping power strictly depends on the jet Reynolds number, hence it almost does not change with  $s/D$ . For two jet alignments, increasing  $Re_j$  from 5000 to 20000 considerably increases the pumping power which is necessary for corresponding cooling. As indicated in Fig.7, it was found out that the pumping power benefits from  $Re_j$  more than the average Nu in both configurations.



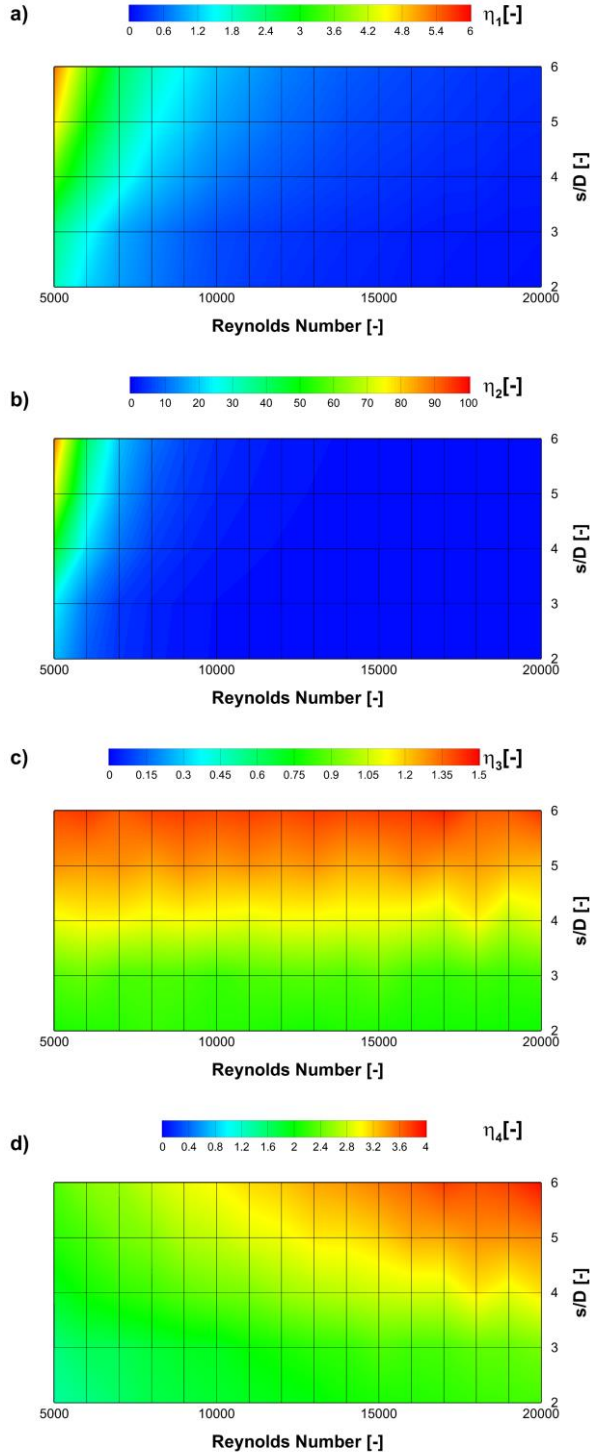


**Figure 8.** Performance evaluation indicator ( $\eta$ ) maps for four different set of exponents a)  $a=b=c=1$ , b)  $a=2$   $b=1$   $c=2$ , c)  $a=0.4$   $b=0.7$   $c=0.1$ , d)  $a=0.5$ ,  $b=0.5$ ,  $c=0$ ; colors denote  $\eta$ .

To evaluate the effects of each parameter for an overall comparison, performance evaluation indicator  $\eta$  in Eq.(11) was defined which depends on Nu, HTU and the pumping power. Suggested performance evaluation indicator reduces the multi objective decision making process consisting of three criteria into a single scalar by using weighted product method approach (Triantaphyllou, 2000). Performance evaluation indicator consist of constant a, b and c exponents for

Nu, HTU and pumping power, respectively. Values of three exponents can be set in accordance with the importance of Nu, HTU and the pumping power for different applications. On the other hand, weighting of those constants has to be conducted by respecting the rule of the weighted product scalarization method where the condition ( $a+b+c=1$ ) has to be satisfied. It should be pointed out that in Fig. 8 the graphics for  $\eta$  were obtained for four different configurations of arbitrary a,b and c exponents. Figures 8a and 8b show that the highest  $\eta$  values are obtained for the designs consisting of the highest  $s/D$  and lowest  $Re_j$  when overall heat transfer and energy consumption are prioritized as much as HTU. On the other hand, Figure 8c shows designs consisting of the highest  $s/D$  values become more preferable regardless of  $Re_j$  when HTU is more favourable than overall heat transfer and energy consumption. In Figure 8d, it can be seen that, designs with highest  $s/D$  together with highest  $Re_j$  become preferable when energy consumption is not regarded.

$$\eta = \frac{Nu^{-a} \times HTU^b}{PP^c} \quad (11)$$

## CONCLUSION

In this study, forced convective heat transfer by impinging jets is investigated numerically for two different arrangements which are widely used in literature. The CFD calculations have been carried out by the flow solver ANSYS-Fluent with k- $\omega$  SST turbulence model for steady, incompressible air flow with ideal gas assumption and Sutherland law. In the current study, the problem has been investigated on the basis of the individual effects of the parameters on the objective functions rather than optimized solution and the results are evaluated for the whole design space. The CFD results reveal that jet Reynolds number is the most significant parameter in enhancing average Nu on the target plate followed by the spacing ratio to the jet diameter and finally alignment of the jet nozzles. The alignment of the jets nozzles is found to be insignificant in enhancing the cooling performance but can affect the uniformity of heat transfer. It is also shown that the pumping power remains almost the same for two alignments at all jet Reynolds numbers. In order to observe overall performance of different designs with a single indicator, overall heat transfer rate, required pumping power and heat transfer uniformity are combined into a single performance evaluation indicator by using weighted product method. It is shown that the suggested performance evaluation indicator provides a robust approach to determine optimum designs. By using suggested  $\eta$  indicators, one can suggest useful design points by selecting the a, b and c exponents based on the demands for different particular applications. In such applications, multi-objective optimizations should be integrated into the solution

procedure so that a balance is established for the aerothermal demands.

## REFERENCES

Bijarchi, M. A., Eghtesad, A., Afshin, H., and Shafii, M. B., 2019, Obtaining uniform cooling on a hot surface by a novel swinging slot impinging jet. *Applied Thermal Engineering*, 150, 781-790.  
<https://doi.org/10.1016/j.applthermaleng.2019.01.037>

Chang S.W. and Shen H.D, 2019, Heat transfer of impinging jet array with web-patterned grooves on nozzle plate, *International Journal of Heat and Mass Transfer*, 141, 129–144.  
<https://doi.org/10.1016/j.ijheatmasstransfer.2019.06.048>

Chauhan, R. and Thakur, N. S., 2014, Investigation of the thermohydraulic performance of impinging jet solar air heater, *Energy*, 68, 255-261.  
[doi.org/10.1016/j.energy.2014.02.059](https://doi.org/10.1016/j.energy.2014.02.059)

Chen, L. and Brakmann, R. G., 2020, Detailed investigation of staggered jet impingement array cooling performance with cubic micro pin fin roughened target plate, *Applied Thermal Engineering*, 171, 115095.  
[doi.org/10.1016/j.applthermaleng.2020.115095](https://doi.org/10.1016/j.applthermaleng.2020.115095)

Chougule, N. K., Parishwad, G. V., Gore, P. R., Pagnis, S., and Sapali, S. N., 2011, CFD analysis of multi-jet air impingement on flat plate, *Proceedings of the World Congress on Engineering 2011*, London, United Kingdom.

Fu, J., Li, Y., Cao, Z., Sundén, B., Bao, J. and Xie, G., 2022, Effect of an impinging jet on the flow characteristics and thermal performance of mainstream in battery cooling of hybrid electric vehicles. *International Journal of Heat and Mass Transfer*, 183, 122206.  
[doi.org/10.1016/j.ijheatmasstransfer.2021.122206](https://doi.org/10.1016/j.ijheatmasstransfer.2021.122206)

Menter F.R., 1994, Two-Equation Eddy-Viscosity Turbulence Models for Engineering Applications, *AIAA Journal*, 32, 8.  
[doi.org/10.2514/3.12149](https://doi.org/10.2514/3.12149)

Obot N. T. and Trabold T. A., 1987, Impingement heat transfer within arrays of circular jets: Part 1—effects of minimum, intermediate, and complete crossflow for small and large spacings., *Journal of Heat Transfer*, 109, 872–879.  
[doi.org/10.1115/1.3248197](https://doi.org/10.1115/1.3248197)

Sabato, M., Fregni, A., Stalio, E., Brusiani, F., Tranchero, M. and Baritaud, T., 2019, Numerical study of submerged impinging jets for power electronics cooling. *International Journal of Heat and Mass Transfer*, 141, 707-718.  
[doi.org/10.1016/j.ijheatmasstransfer.2019.06.081](https://doi.org/10.1016/j.ijheatmasstransfer.2019.06.081)

Tepe, A.Ü., 2021, Numerical investigation of a novel jet hole design for staggered array jet impingement cooling on a semicircular concave surface, *International Journal of Thermal Sciences*, 162, 106792.  
[doi.org/10.1016/j.ijthermalsci.2020.106792](https://doi.org/10.1016/j.ijthermalsci.2020.106792)

Triantaphyllou, E., 2000, *Multi-criteria decision making methods: A comparative study*. Springer, Boston, MA, 320-325.

Vinze, R., Khade, A., Kuntikana, P., Ravitej, M., Suresh, B., Kesavan, V., and Prabhu, S. V., 2019, Effect of dimple pitch and depth on jet impingement heat transfer over dimpled surface impinged by multiple jets, *International Journal of Thermal Sciences*, 145, 105974.  
[doi.org/10.1016/j.ijthermalsci.2019.105974](https://doi.org/10.1016/j.ijthermalsci.2019.105974)

Wen, Z. X., He, Y. L., and Ma, Z., 2018, Effects of nozzle arrangement on uniformity of multiple impinging jets heat transfer in a fast cooling simulation device, *Computers and Fluids*, 164, 83-93.  
[doi.org/10.1016/j.compfluid.2017.05.012](https://doi.org/10.1016/j.compfluid.2017.05.012)

Wu, R., Fan, Y., Hong, T., Zou, H., Hu, R., and Luo, X., 2019, An immersed jet array impingement cooling device with distributed returns for direct body liquid cooling of high power electronics, *Applied Thermal Engineering*, 162, 114259.  
[doi.org/10.1016/j.applthermaleng.2019.114259](https://doi.org/10.1016/j.applthermaleng.2019.114259)

Xing Y. and Weigand B., 2013, Optimum jet-to-plate spacing of inline impingement heat transfer for different crossflow schemes, *Journal of Heat Transfer*, 135, 7.  
[doi.org/10.1016/j.ijheatmasstransfer.2015.10.022](https://doi.org/10.1016/j.ijheatmasstransfer.2015.10.022)

Zuckerman N. and Lior N., 2005, Impingement heat transfer: Correlations and numerical modeling, *Journal of Heat Transfer*, 127, 544–552.  
[doi.org/10.1115/1.186192](https://doi.org/10.1115/1.186192)



## INVESTIGATION OF HEAT TRANSFER IMPROVEMENTS OF GRAPHENE OXIDE-WATER AND DIAMOND-WATER NANOFLUIDS IN CROSS-FLOW-IMPINGING JET FLOW CHANNELS HAVING FIN

**Koray KARABULUT**

Sivas Cumhuriyet University, Sivas Technical Sciences Vocational School, Department of Electric and Energy  
Sivas, Turkey

kkarabulut@cumhuriyet.edu.tr, ORCID: 0000-0001-5680-0988

(Geliş Tarihi: 18.09.2022, Kabul Tarihi: 27.02.2023)

**Abstract:** In this study, the heat transfer from two different model surfaces (roof and crown) and flow structure in the channels with the cross flow-impinging jet flow were numerically analyzed by using water, 0.02% GO (Graphene Oxide)-Water and 2% Diamond-Water nanofluids. The numerical study was carried out steady and three dimensional using the Ansys-Fluent program with k-ε turbulence model. A fin with 90° angle was added on the upper channel surface from the impinging jet inlet at distinct distances. A constant heat flux of 1000 W/m<sup>2</sup> was applied to the model surfaces. The channel heights are fixed and the Re range of the fluids is 5000-15000. The numerical results obtained from the study were compared with the results of the experimental studies in the literature and it was seen that the results were compatible and acceptable. The results of the study were comparatively examined for water and nanofluids as the mean Nu and surface temperature variations for each model in the channels without fins and at different fin distances. Also, velocity and temperature contour distributions of the combined jet Diamond-Water nanofluid flow were visualized. However, performance coefficient (C) and mean Nu (Nu<sub>m</sub>) and, surface temperature values (T<sub>m</sub>) were evaluated for all three patterned surfaces in the channels. Nu<sub>m</sub> increases for GO-Water nanofluid at Re=15000 and fin distance of 2D are 47.53% and 57.42% compared to the case of using finless and water fluid for the roof and crown model surfaces, respectively.

**Keywords:** Cross flow-impinging jet flow, Carbon-based nanofluid, Fin, Heat transfer.

## KANATÇIKLI ÇAPRAZ-AKIŞ-ÇARPAN JET AKIŞLI KANALLARDA GRAFEN OKSİT-SU VE ELMAS-SU NANOAKIŞKANLARININ ISI TRANSFERİ İYİLEŞTİRMELERİNİN ARAŞTIRILMASI

**Özet:** Bu çalışmada, çapraz akış-çarpın jet akışlı kanallarda iki farklı model yüzeyinden (çatı ve taç) olan ısı transferi ve akış yapısı su, %0,02 GO (Grafen Oksit)-Su ve %2 Elmas-Su nanoakışkanları kullanılarak sayısal olarak analiz edilmiştir. Sayısal çalışma, k-ε türbülans modelli Ansys-Fluent programı kullanılarak sürekli ve üç boyutlu olarak gerçekleştirilmiştir. Kanal üst yüzeyine çarpın jet girişinden itibaren farklı mesafelerde 90° açılı bir kanatçık eklenmiştir. Model yüzeylerine 1000 W/m<sup>2</sup> lik bir sabit ısı akısı uygulanmıştır. Kanal yükseklikleri sabittir ve akışkanların Re sayısı aralığı 5000-15000' dir. Çalışmadan elde edilen sayısal sonuçlar, literatürdeki çalışmanın deneysel sonuçlarıyla karşılaştırılmış ve sonuçların makul ve kabul edilebilir olduğu görülmüştür. Sonuçlar, kanatçiksız ve farklı kanatçık uzaklıklarında kanallardaki her bir model için ortalama Nu sayısı ve yüzey sıcaklık değişimleri şeklinde su ve nanoakışkanlar için karşılaştırmalı olarak incelenmiştir. Ayrıca, birleşik jet Elmas-Su nanoakışkan akışının hız ve sıcaklık konturu dağılımları görselleştirilmiştir. Bununla birlikte, performans katsayısı (C) ve ortalama Nu (Nu<sub>m</sub>) ve yüzey sıcaklık değerleri (T<sub>m</sub>) kanallarda bulunan her üç desenli yüzey için değerlendirilmiştir. Re=15000 ve 2D kanatçık uzaklığında GO-Su nanoakışkan için Nu<sub>m</sub> artışları, kanatçiksız ve su akışkanını kullanılan durumla kıyaslandığında çatı ve taç model yüzeyleri için sırasıyla %47,53 ve %57,42' dir.

**Anahtar Kelimeler:** Çapraz akış-çarpın jet akışı, Karbon tabanlı nanoakışkan, Kanatçık, Isı transferi.

### NOMENCLATURE

A <sub>c</sub>	Cross-sectional area of the channel [m <sup>2</sup> ]	W	Width of the channel [mm]
C	Performance Coefficient [=Nu/ΔP]	H	Height of the channel [mm]
D	Jet inlet diameter [mm]	m	One side length of the model [mm]
L	Length of the channel [mm]	P <sub>c</sub>	Wet area of the channel [m <sup>2</sup> ]
		θ	Fin angle [°]
		f	Friction factor [=2ΔPD/ρLV <sup>2</sup> ]

$h$	Heat convection coefficient [W/m <sup>2</sup> K]
$k_f$	Thermal conductivity of the fluid [W/mK]
$V$	The velocity of the fluid at the inlet of the channel [m/s]
$c_p$	Specific heat of the fluid [J/kgK]
$p$	Pressure [Pa]
$q''$	Heat flux on model surfaces [W/m <sup>2</sup> ]
$N$	Distance of fin from jet inlet [mm]
$T$	Temperature [K]
$u_i$	Velocity components in x, y and z coordinates [m/s]
$Re$	Reynolds number [ $=\rho VD/\mu$ ]
$Nu$	Nusselt number [ $=hL/k$ ]
$\mu$	Dynamic viscosity [kg/sm]
$\mu_t$	Turbulent viscosity [kg/sm]
$\nu$	Kinematic viscosity [m <sup>2</sup> /s]
$\rho$	Density of the fluid [kg/m <sup>3</sup> ]
$k$	Kinetic energy of turbulent flow [m <sup>2</sup> /s <sup>2</sup> ]
$\epsilon$	Turbulent dissipation rate [m <sup>2</sup> /s <sup>3</sup> ]

### Subscripts

atm	Atmosphere
bf	Base fluid (Water)
c	Channel
f	Fluid
h	Hydraulic
j	Jet
m	Mean
nf	Nanofluid
o	Outlet
p	Nanoparticle
s	Surface

## INTRODUCTION

Conservation of energy and the development of alternative energy sources are the biggest problems nowadays. Although traditional energy resources are expected to be exhausted in the next twenty to thirty years, energy wars are also on the agenda of the world's countries. Therefore, energy should be used economically and efficiently in all areas.

With traditional and inefficient heat transfer methods, more energy is consumed and sufficient and desired heat transfer performance cannot be achieved (Naga Ramesh et al., 2021). The cross-flow cooling method, which is used to increase heat transfer from electronic elements, is one of the most widely used methods. This method is based on the principle of sending the cold fluid over all the components with a fan, thereby cooling the entire electronic components. However, since this method is based on cooling all circuit elements, it may fail to transfer heat from components at very high temperatures. Another method of heat transfer is impinging jet cooling. In this method, cold fluid is locally sprayed onto an element with a high temperature by a nozzle. While a high-temperature circuit

component can be cooled with the impinging jet, it may be insufficient in cooling the entire circuit. However, there are multiple elements in an electronic circuit whose temperatures are quite different from each other. For this reason, it is difficult to reach the conditions that can keep the whole circuit safely with a single type of cooling method. Implementing the impinging jet and cross-flow cooling method together and applying it as a combined jet flow (cross flow and impinging jet) can create a beneficial situation with high cooling capacity. While the circuit elements as a whole can be cooled to a certain temperature level with cross-flow, only the very high-temperature elements in the circuit can be cooled pointwise by the impinging jet flow (Kılıç, 2018; Teamah et al., 2015).

In the literature, there are many studies evaluating only cross flow or only jet flow. Since the model examined in this study is more like jet flow, the literature review focused more on jet flow. However, many numerical and experimental studies on impinging jets exist in the literature. In these studies, the effects of variables such as the type of fluid used for the impinging jets, the geometry of the flow area, the turbulence model, the Re value, the jet distance and the heat flux on the heat transfer from the circuit components were investigated. In addition, studies on cooling methods in which cross flow and impinging jet flow are used together are limited, regarding the directing of the fluid to the heated surfaces in the channel, as researched in this study, a study in which detailed channel and heated surface designs are used and carbon-based GO-Water and Diamond-Water nanofluids, the importance and use of which have been increasing in recent years, have not been found in the literature.

The flow and heat transfer properties of an impinging circular jet flow on a concave surface with constant heat flux were investigated numerically and experimentally by Hadipour and Zargarabadi (2018) at different jet-to-plate ratios. The effects of different H/D (channel height/jet inlet diameter) ratios, Re values and jet diameter values were investigated and it was seen that the heat transfer increased with the increase in jet diameter at a constant Re. Karabulut and Alnak (2021) numerically investigated the cooling of copper plate surfaces in rectangular ducts with two different patterns in the form of roof and trapezoidal with a single air jet flow at different jet inlet widths. While the jet inlet widths were  $0.5 D_h$  and  $D_h$ , the distances between the jet and the plate ( $H/D_h$ ) were 3 and 6. As a result, they determined that at  $0.5 D_h$  jet width,  $H/D_h=6$ , and  $Re=5000$ , the mean Nu value was 25.92% higher on the roof patterned surface than on the trapezoidal surface. In another study carried out by Karabulut and Alnak (2020), heat transfer from copper plate surfaces with different patterns as rampart and rectangular was investigated using a single air jet stream in rectangular cross-section channels whose three sides are closed and one side is open, the distance between the jet and the

plate ( $H/D_h$ ) is between 4-10. As a result of their research, they found a 31.45% higher mean Nu value on rectangular patterned surfaces compared to rampart patterned surfaces for the value where the Re is 4000 and the distance between the jet and the plate is 4. Nagesha et al. (2020) carried out experimental research on heat transfer from a single circular jet impinging on a flat plate with a protrusion of depths 1, 2 and 3 mm. Besides, they performed numerical simulations using ANSYS Fluent program to compare the results with those from experiments. Their results showed that the increase of jet Re and relative depth of protrusion enhances the heat transfer on the impinging surfaces up to 16.69% compared to a flat surface. In another work, round jet impingement on a heated flat plate at constant heat flux was analyzed experimentally and numerically by Issac et al. (2020). Experiments were done at various Re values ( $Re_d=10000$  to 25000) and at four different nozzles to plate spacing ( $h/d=4, 6, 8$  and, 10). However,  $k-\omega$  SST, Realizable  $k-\epsilon$ , RNG  $k-\epsilon$  and  $v^2f$  turbulence models were used to validate the numerical results with experimental results. They observed that the inlet turbulent intensity and eddy viscosity ratio are significant for the accurate prediction of realistic results. Huang et al. (2021) experimentally and numerically examined the heat transfer coefficients of a synthetic jet flow impingement onto the tip region of a longitudinal fin used in an electronics cooling system. The effects of different parameters, such as amplitude and frequency of diaphragm movement and jet-to-cooled-surface spacing were taken into consideration. Heat transfer coefficient values as high as  $650 \text{ W/m}^2\text{K}$  were obtained with high-frequency diaphragm movement. Rathore and Verma (2022) performed numerical work about the effects of variation in Re and offset ratio (OR) on turbulent flow and thermal characteristics of oblique offset jet. Re and OR were considered in the range of  $Re=10000-25000$  and  $OR=3-11$ . The obliquity angle of the offset jet range was taken as  $90^\circ-45^\circ$  at an interval of  $15^\circ$ . They obtained that process of heat transfer from heated impingement wall to fluid is more intense for a higher value of jet obliquity angle and Re. Zou et al. (2022) used high-speed compressed air impinging to research the interfacial heat transfer and gas flow in the process of air-cooling in their experiment and numerical simulation. The effect of sample diameter and jet distance (distance from jet to cooling surface) on the flow pattern and temperature fields was studied. The results showed that smaller jet distances had a bigger interfacial heat transfer coefficient. Demircan (2019) numerically investigated the heat transfer from the electronic circuit element by cross-flow-impinging jet. Investigations were made at different values of Re and jet-channel velocity ratios. It was concluded that the heat transfer increased significantly with the improvement of Re and velocity ratios. Mergen (2014) investigated heat transfer by impinging jet-cross flow from an electronic element with a constant heat flux of  $3500 \text{ W/m}^2$ . As a result, it was determined that the heat transfer decreased with the decrease of the jet

Re/channel Re ( $Re_j/Re_c$ ) ratio. Heat transfer with impinging air jet-cross flow coexistence on a constant heat flux element was investigated numerically by Öztürk and Demircan (2022). In their study, the researchers investigated the heat transfer from a single element in the channel for different jet inlet velocity/channel inlet velocity ratios (0, 1, 2, and 3) and for different angles of the fins ( $0^\circ, 22.5^\circ, 45^\circ, 67.5^\circ$  and  $90^\circ$ ) placed in the duct, While the ratio of channel height to jet diameter was taken as constant and 3, the air was used as a fluid in the channel. It was determined that the highest heat transfer from the element was reached when the ratio of the inlet velocity to the channel inlet velocity was 3 and the fin angle was  $90^\circ$ . Maghrabie et al. (2017) numerically evaluated the heat transfer with the impinging jet-cross flow combination of a system consisting of seven circuit elements along the channel and determined the effect of the jet position change on the heat transfer.

When the jet impingement studies using nanofluids are examined, Chang and Yang (2014) studied the heat transfer performance of jet impingement flow boiling using  $\text{Al}_2\text{O}_3$ -Water nanofluid. The heat transfer performance of the jet impingement flow of the  $\text{Al}_2\text{O}_3$ -water nanofluid was found to be worse than the water used as the working fluid. It was determined that the decrease in heat transfer performance was due to the formation of a nano-absorption layer on the heated surface, which resulted in an increase in thermal resistance. However, while the formation of the nano-absorption layer is prevented by applying acoustic vibration to the heated surface, the heat transfer performance obtained using  $\text{Al}_2\text{O}_3$ -Water nanofluid is better than that obtained using water. Datta et al. (2018) carried out a numerical simulation to investigate the heat transfer performance using  $\text{Al}_2\text{O}_3$ -Water nanofluid in a confined slot jet impinging on a convex surface. In order to investigate the flow behaviour and convective heat transfer performance of the system, different parameters such as various Re values, and the distance between the jet and the plate were considered. They determined that the mean Nu and heat transfer coefficient increased significantly with the increase in the jet inlet Re. Kumar et al. (2021) used a heat sink combined with airfoil columns in the jet impingement condition to increase the heat transfer rate. While doing this, they used water and  $\text{CuO}$ -Water nanofluid with 1% concentration in their research. In their results, they found a 10% reduction in heat sink temperature when they used water fluid as a jet fluid, while the temperature drop was 14% when they used nanofluid. The flow of 0-6%  $\text{Al}_2\text{O}_3$ -Water nanofluid in a microchannel with a serrated injection jet on the upper wall of the microchannel and using a magnetic field of 0-40 Hartman intensity was investigated by Jalali et al. (2022). The lower microchannel wall with the jet impingement chamber had a constant temperature, while the upper microchannel wall was insulated between the impinging jets. In order to increase heat transfer, the recessed mode

was applied for impinging jets. The results showed that when the notch height was high, the heat transfer was higher. Selimefendigil and Chamka (2020) aimed to numerically analyze the convection heat transfer properties in cooling an isothermal surface with a cavity-like part using a CuO-Water nano jet. They carried out their work by changing the volumetric concentration (0-4%) of the nanoparticle at different values of Re (100-400), different cavity lengths (5w-40w) and heights (w-5w). They found that when the cavity length is low, the contribution of the curved wall of the cavity to the mean Nu is significant and the mean heat transfer increases by 35-46% when nanofluid is used instead of water at the highest volumetric concentration. Abdullah et al. (2019) investigated the effect of TiO<sub>2</sub> nanofluid concentration on the heat transfer of double jet impinging on an aluminium plate surface by experimental analysis. Apart from this, the nozzle distance of the double jet and the nozzle-plate distance were considered as variables. Based on these data, they found that the flow structure of the double jet is an important condition affecting the heat transfer increase. In addition, they determined that the distances and nanoparticle concentration, which affect the flow structure, also affect the Nu together with the Re. Shi et al. (2021) experimentally investigated the effects of nano-aluminium additives on the instability of round water jets. Flow visualization in and near the exit of two transparent nozzles was obtained by high-speed shadow imaging technique and it was determined that the effects of nanoparticle additives on jet instability were mainly caused by viscosity increase and cavitation promotion.

As can be seen from the literature investigations, there are many studies with impinging jets. Although the number of combined jet flow studies in which the impinging jet and cross-flow are applied together using nanofluids is quite low, the study using GO-Water and Diamond-Water nanofluids, which exhibit high heat transfer performance at low concentrations, has not been found in the literature. In this study, heat transfer from two different model surfaces of roof and crown and flow structure in combined jet flow channels with H=3D height were numerically analyzed using water, 0.02% GO-Water and 2% Diamond-Water nanofluids without fin and with a fin at 90° angle at N=1.5D and 2D fin distances from the impinging jet inlet. The reason why the elements in the channel were chosen as different model surfaces is to increase the contact of the combined jet flow on the patterned surfaces to be cooled and it is to increase the heat transfer effect by ensuring that the jet flow is directed towards the other pattern in the channel after hitting a patterned surface. Considering the study conducted by Öztürk and Demircan (2022) in literature; the fin was positioned in such a way that it does not hinder the flow so that the cross-flow coming from the channel can be better directed on the models in the first row and the velocity of the fluid in the space between the models can be increased. Numerical research was carried out by solving steady and three-

dimensional energy and Navier-Stokes equations using the Ansys-Fluent program with the k-ε turbulence model. While the lower and upper surfaces of the fin and channel are adiabatic, the model surfaces have a constant heat flux of 1000 W/m<sup>2</sup>, which is also applied in the literature (Shi et al., 2021; Kilic et al., 2017; Karabulut, 2019; Alnak et al., 2021). As it is known, overheating occurs under the intense working load of electronic elements. With this heat load, the temperatures of the elements can reach temperatures ranging from 308 to 353 K. In this study, the range of surface temperatures obtained for the roof and crown models is 303.4-307.2 K and 303.2-306.6 K, respectively. Therefore, it is seen that the constant heat flux approach of 1000 W/m<sup>2</sup> applied to the surfaces is correct. The Re range studied for fluids is 5000-15000. These selected Re values have been chosen based on the studies in the literature and represent both the jet Re (Re<sub>j</sub>) and the channel Re (Re<sub>c</sub>). Accordingly, in the study H=3D channel height, for GO-Water nanofluid flow in the jet and channel, the flow rates are V<sub>j</sub>=0.355 m/s and V<sub>c</sub>=0.103 m/s at values where the Re is 5000, respectively. For Re=15000, these values are V<sub>j</sub>=1.064 m/s and V<sub>c</sub>=0.310 m/s, respectively. Therefore, considering the studies reached in the literature, the Re range (Re=5000-15000) studied for both jet and channel flow is accepted as turbulent. The thermal conductivity, density and viscosity of the 0.02% volumetric concentration GO-Water nanofluid used in the study were obtained experimentally and only the specific heat was found with the help of the analytical model in the literature proposed by Pak and Cho (1998) by using the mixture rule of the base fluid and nanoparticle. However, the thermophysical properties of Diamond-Water nanofluid with 2% volumetric concentration were found with the help of the equations found in the literature. In addition to this, analyzes were carried out with the assumption that the nanofluid is a single-phase fluid. The results of the study were compared with the results of the equation obtained as a result of the experimental study in the literature and they were found to be compatible. The results were analyzed as the mean Nu and surface temperature variations for each roof and crown model surface in the channels. However, velocity and temperature contour distributions of the Diamond-Water nanofluid in finless and differentially spaced (N) finned channels for combined jet flow were presented for Re=11000. The mean Nu (Nu<sub>m</sub>) and mean surface temperature (T<sub>m</sub>) values were evaluated for all models found in the channels with Re=5000 and 15000 values in the finless and differentially spaced (N=1.5D and 2D) finned cases. In addition, the pressure drops of the fins and nanofluids compared to the Nu value increase in the combined jet flow channels according to the finless and water use cases were interpreted by considering the performance coefficient (C).

## Preparation of GO-Water Nanofluid

The Graphene Oxide (GO) nanoparticle used in this study was synthesized from graphite. While synthesizing the GO nanoparticle, graphite was treated with various chemicals such as nitric and sulfuric acid as well as sodium nitrate, hydrogen peroxide and potassium permanganate. After these processes, graphite was passed through distilled water to separate it from acids and chemicals, and then oven-dried to obtain GO nanoparticles (Hajjar et al., 2014; Hummers and Offeman, 1958). GO-Water nanofluid was obtained with a two-stage nanofluid preparation method using the synthesized GO nanoparticle. The two-step procedure consists of mixing water with nanoparticles directly and passing it through an ultrasonicator device that generates ultrasonic sound waves to prevent the aggregation of nanoparticles in the resulting nanofluid. In addition, ultrasonic sound waves were used to mix the nanoparticles with the base fluid. GO nanoparticles were prepared by measuring with a precision balance with a precision of 0.1 mg, depending on the desired volumetric concentration. To obtain GO-Water nanofluid with 0.02% volumetric concentration, 0.8 g of GO nanoparticles were used. The obtained nanofluid was exposed to sound waves with an ultrasonicator device with a 50 Hz frequency and 230 W maximum power for 5 hours to ensure its stability. It was seen that the prepared nanofluid could preserve its stability without sedimentation for two months after being used in the experiments. Besides, it was decided that the stability of nanofluid was enabled in the result of the observation and Zeta potential measurements. While suspensions with high Zeta potential are in balance as electrical, suspensions with low Zeta potential tend to coagulate or aggregate. It is known that nanofluids with a Zeta potential between 40-60 mV have perfect stability. The Zeta potential value of the GO nanofluid used in the experiments is in the range of 45-65 mV, which is fairly higher than 25 mV which is the stability criteria value. In addition, an scanning electron microscope (SEM) image was exhibited to present the morphology of the experimentally obtained GO nanoparticle used in this study in Fig. 1 (Eravcu, 2016).

The volumetric nanoparticle concentration in the nanofluid is calculated by Eq. (1) (Karabulut et al., 2020).

$$\frac{v_p}{v_{nf}} = \frac{v_p}{v_{bf} + v_p} = \frac{\frac{m_p}{\rho_p}}{\frac{m_p}{\rho_p} + \frac{m_{bf}}{\rho_{bf}}} = \frac{m_p \rho_{bf}}{m_p \rho_{bf} + m_{bf} \rho_p} \quad (1)$$

In Equation (1),  $m_p$  and  $m_{bf}$  show the masses of nanoparticles and water, respectively, and  $\rho_{bf}$  and  $\rho_p$

show the densities of water and nanoparticles, respectively.

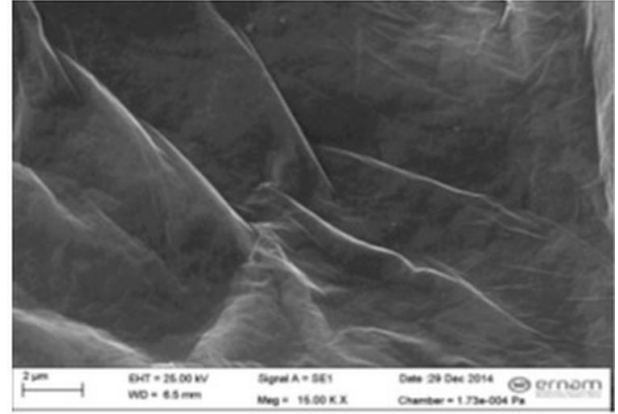


Figure 1. Image of GO obtained from the SEM (Eravcu, 2016)

## Thermophysical Properties of GO-Water Nanofluid

While the viscosity value of the prepared nanofluid was measured with the Malvern Kinexus Pro cone and plate tension-controlled rheometer, the measurement of the thermal conductivity coefficient was carried out using the hot wire method, which is widely used in the literature, using the KD2 Pro thermal conductivity meter. Density measurements of the nanofluid were made experimentally with the Anton-Paar DMA 4200 Density Meter. Before the experimental thermophysical measurements of the GO-Water nanofluid used in the devices were carried out, measurements were made with water and the devices were calibrated. Then, the measurement values of the thermophysical properties of the nanofluid were taken after making more than one measurement and convincing the accuracy of it. However, the specific heat value of the nanofluid was obtained as a result of the analytical model proposed by Pak and Cho (1998) in Eq. (2).

$$c_{pnf} = (1 - \phi)c_{pbf} + \phi c_{pp} \quad (2)$$

In Equation (2),  $p$ ,  $nf$  and  $bf$  denote particle, nanofluid and water fluid, respectively. In addition, due to the low concentration (0.02%), the specific heat value obtained as a result of the calculation of the nanofluid was taken as equal to water, since it is close to water.

Apart from the specific heat of GO-Water nanofluid and water, other thermophysical properties were obtained experimentally and are shown in Tab. 1 (Karabulut et al., 2020).

Uncertainty analyses of the measured values were obtained using Taylor (1997)'s uncertainty analysis method and were given in Tab. 2. The values shown are the maximum values for the given parameters, taking into account all experimental situations.

**Table 1.** Thermophysical properties of GO-Water and Water at 303 K

Fluid	k (W/mK)	$\rho$ (kg/m <sup>3</sup> )	$c_p$ (J/kgK)	$\mu$ (Ns/m <sup>2</sup> )
Water	0.6172	995.8	4178.4	803.4x10 <sup>-6</sup>
GO-Water	0.678	996.1	4178.4	1060x10 <sup>-6</sup>

**Table 2.** Results of uncertainty analysis for experimental values

Variable	Absolute uncertainty range	Unit
k	±0.006	W/mK
$\rho$	±9.9	kg/m <sup>3</sup>
$\mu$	±1.2x10 <sup>-6</sup>	Ns/m <sup>2</sup>
$c_p$	±41.78	J/kgK

### Thermophysical Properties of Diamond-Water Nanofluid

Thermophysical properties of Diamond-Water nanofluid with 2% volumetric concentration, which is one of the working fluids used in this study, were obtained with the help of equations (Maxwell, 1873) found in the literature and widely used and shown in Tab. 3. In addition, the thermophysical properties of the solid diamond nanoparticle are also taken from the relevant study in the literature (Mohammed et al., 2011). The specific heat of the Diamond-Water nanofluid was calculated by Eq. (2).

The Eqs. (3, 4 and, 5) indicating density ( $\rho$ ), thermal conductivity ( $k$ ) and viscosity ( $\mu$ ) of the Diamond-Water Nanofluid are as follows (Maxwell, 1873; Mohammed et al., 2011).

The density of Diamond-Water Nanofluid

$$\rho_{nf} = (1 - \phi)\rho_{nf} + \phi\rho_p \quad (3)$$

Thermal Conductivity of Diamond-Water Nanofluid

$$k_{nf} = \frac{k_p + 2k_{bf} + 2(k_p - k_{bf})\phi}{k_p + 2k_{bf} - 2(k_p - k_{bf})\phi} k_{bf} \quad (4)$$

The viscosity of Diamond-Water Nanofluid

$$\mu_{nf} = \mu_{bf} (1 + 2.5\phi) \quad (5)$$

**Table 3.** Thermophysical properties of Water, Diamond-Water and, Diamond at 303 K

Properties	Water	Diamond-Water Nanofluid	Diamond
k (W/mK)	0.6172	0.6685	1000
$\rho$ (kg/m <sup>3</sup> )	995.8	1046.08	3510
$c_p$ (J/kgK)	4178.4	4104.77	497.26
$\mu$ (Ns/m <sup>2</sup> )	803.4x10 <sup>-6</sup>	843.57x10 <sup>-6</sup>	-

### NUMERICAL METHOD

The Ansys-Fluent program was used to solve the forced convection heat transfer of the combined jet flow on the model surfaces.

Accurate modelling of turbulence is essential in heat transfer processes. However, direct numerical simulations of turbulent fluids are very difficult and also a time-consuming process. Although there are various turbulence models (Genç et al., 2009; Genç, 2010; Genç et al., 2011) used in numerical modelling, among these models in terms of being economical and yielding results with acceptable accuracy in many flow events; the k- $\epsilon$  turbulence model, which is a semi-empirical model, is widely used (Wang and Mujumdar, 2005). In one of the studies on impinging jets, Wang and Mujumdar (2005) tested several k- $\epsilon$  turbulence models with low Re values for turbulent jets. They found that the models were able to determine the general shape of the Nu distribution and that the models were better applied at the stagnation point for large jet-plate distances. In their study, they determined that the k- $\epsilon$  turbulence model performs well in determining the heat transfer properties of impinging jets when compared to the standard high Re models. In addition, they saw that the k- $\epsilon$  turbulence model is suitable as it approaches reducing the kinetic energy production and the result that should be in the stagnation region compared to other turbulence models in the study. Accordingly, considering the results obtained from the studies in the literature, the standard k- $\epsilon$  turbulence model was used for the channels in numerical calculations in this study.

Flow and heat transfer were done by solutions of differential equations derived from the equations of conservation of mass (continuity) (Eq. 6), momentum (Eq. 7) and energy (Eq. 8) for continuous, in which there is no body force, as follows (Wang and Mujumdar, 2005; Karabulut, 2019; Alnak et al., 2021).

Continuity equation

$$\frac{\partial \bar{u}_i}{\partial x_j} = 0 \quad (6)$$



Momentum equation

$$\rho \frac{\partial}{\partial x_j} (\bar{u}_i \bar{u}_j) = \frac{\partial \bar{P}}{\partial x_i} + \frac{\partial}{\partial x_j} \left[ \mu \left( \frac{\partial \bar{u}_i}{\partial x_j} + \frac{\partial \bar{u}_j}{\partial x_i} \right) - \rho \overline{u'_i u'_j} \right] \quad (7)$$

Energy equation

$$\rho c_p \frac{\partial}{\partial x_i} (\bar{u}_i \bar{T}) = \frac{\partial}{\partial x_i} \left[ k \frac{\partial \bar{T}}{\partial x_i} - \rho c_p \overline{T' u'_i} \right] \quad (8)$$

Equations of turbulence kinetic energy and turbulence kinetic energy disappearance of turbulent flow due to combined jet flow in the channel are given in Eqs. 9 and 10, respectively.

Turbulence kinetic energy equation

$$\frac{\partial}{\partial x_i} (\rho k u_i) + \frac{\partial}{\partial y} (\rho k) = \frac{\partial}{\partial x_j} \left[ \mu + \frac{\mu_t}{\sigma_k} \frac{\partial k}{\partial x_j} \right] + G_k - \rho \varepsilon \quad (9)$$

Turbulence kinetic energy disappearance equation

$$\frac{\partial}{\partial x_i} (\rho \varepsilon u_i) + \frac{\partial}{\partial y} (\rho \varepsilon) = \frac{\partial}{\partial x_j} \left[ \left( \mu + \frac{\mu_t}{\sigma_\varepsilon} \right) \frac{\partial \varepsilon}{\partial x_j} \right] + C_{1\varepsilon} \frac{\varepsilon}{k} G_k - C_{2\varepsilon} \rho \frac{\varepsilon^2}{k} \quad (10)$$

In these equations,  $\rho$  is the density of the fluid,  $k$  is the kinetic energy of the turbulent flow,  $u_i$  is the velocity components in the  $x$ ,  $y$  and  $z$  directions,  $\mu$  is the viscosity of the fluid,  $\sigma_k$  ( $\sigma_k=1$ ) is the turbulent kinetic energy Pr. The equations showing turbulence kinetic energy production ( $G_k$ ) and turbulent viscosity ( $\mu_t$ ) are as follows (Alnak et al., 2021; Genç et al., 2009).

$$G_k = -\rho \overline{u'_i u'_j} \frac{\partial u_j}{\partial x_i} \quad (11)$$

$$\mu_t = C_\mu \rho \frac{k^2}{\varepsilon} \quad (12)$$

The turbulence disappearance Pr is denoted by  $\sigma_\varepsilon$ , while  $C_{1\varepsilon}=1.44$ ,  $C_{2\varepsilon}=1.92$ ,  $C_\mu=0.09$ , and  $\sigma_\varepsilon=1.3$  are coefficients in the equations (Saleha et al., 2015).

Heat transfer coefficient  $h$  and  $Nu$  are calculated with Eqs. 13 and 14, respectively (Incropera et al., 2007).

$$h = \frac{q''}{T_s - T_a} \quad (13)$$

Nu value

$$-k_f \left( \frac{\partial T}{\partial n} \right)_s = h(T_a - T_s) \text{ and } Nu = \frac{h(3m)}{k_a} \quad (14)$$

In these equations,  $T_a$  and  $T_s$  are the mean surface temperatures of the fluid and the model (K), respectively,  $k_f$  is the thermal conductivity of the fluid (W/m.K),  $3m$  is the total surface length of the model with which the fluid is in contact (m), and  $h$  and  $h_m$  are the point and mean convective heat transfer coefficient (W/m<sup>2</sup>.K) along the model surface, respectively, where  $n$  is the direction perpendicular to the surface. The model surface mean heat transfer coefficient and  $Nu$  value ( $Nu_m$ ) are found in Eqs. 15 and 16 as given below, respectively.

Model surface mean heat transfer coefficient

$$h_m = \frac{1}{3m} \int_0^{3m} h dx \quad (15)$$

Model surface mean Nu value

$$Nu_m = \frac{h_m(3m)}{k_f} \quad (16)$$

Eq. 17 showing the hydraulic diameter of the channel is as follows.

$$D_{ch} = \frac{4A_c}{P_c} = \frac{4(H.W)}{2(H+W)} \quad (17)$$

In this equation,  $A_c$  and  $P_c$  represent the cross-sectional area and perimeter of the channel, respectively, while the height and width of the channel are represented by  $H$  and  $W$ . Jet inlet diameter  $D$  is equal to circular inlet jet hydraulic diameter  $D_{chjet}$ .

The Re values of the channel and the jet are determined using Eqs. (18) and (19).

$$Re_c = \frac{\rho V_c D_{ch}}{\mu} \quad (18)$$

$$Re_j = \frac{\rho V_j D_j}{\mu} \quad (19)$$

In these equations, the channel and jet flow velocities of the fluid are denoted by  $V_c$  and  $V_j$  (m/s), respectively.

The pressure drop ( $\Delta P$ ) is calculated by the following Eq. (20)

$$\Delta P = \frac{f \rho L}{2D_{ch}} V_c^2 \quad (20)$$

In this equation,  $\Delta P$  represents the pressure drop (Pa) between the inlets and outlets of finless and finned ducts,  $f$  represents the friction factor, and  $L$  represents the length of the duct (m).

The coefficient of performance ( $C$ ) is found in the following Eq. (21) (Alnak, 2020).

$$C = \frac{(Nu_{m-finned} / Nu_{m-finless})}{(\Delta P_{finned} / \Delta P_{finless})} \quad (21)$$

## MODEL GEOMETRIES

While the dimensions of the impinging jet-cross flow combined jet flow finned channels and the models with roof and crown surfaces and fin geometry in the channels are given in Figs. 2 (a), (b), and (c), the dimensions of the channels are given in Tab. 4 (Öztürk and Demircan, 2022). During all tests, there are three models in each channel. The “Without fin” case refers to channels with models but no fin. The fin with  $90^\circ$  angle was placed in the channel as one at  $N=1.5D$  and  $N=2D$  distances from the impinging jet inlet towards the cross-flow channel entrance. In addition, the regular tetrahedral mesh structure used in the numerical

calculations of the combined jet flow channels is shown in Fig. 3.

In addition, the assumptions and boundary conditions made in this study are as follows. (a) Steady, three-dimensional and turbulent flow volumes were used, (b) Water, 0.02% GO-Water and 2% Diamond-Water nanofluids used as incompressible fluids were both jet and cross-flow fluids, (c) The thermal properties of the fluids are constant and independent of temperature, (d) The surfaces of the channel and the fin are adiabatic, (e) There is no heat source on water, nanofluid and patterned surfaces, (f) The outlet pressure of the duct was taken as equal to the atmospheric pressure ( $P_o=P_{atm}$ ), (g) It was determined as  $\partial T/\partial x=0$  assuming that the temperature difference at the exit of the channel was negligible, (h) It is assumed that there is a non-slip boundary condition on the channel, fin and pattern surfaces, and therefore, all velocity component values on the mentioned surfaces are zero.

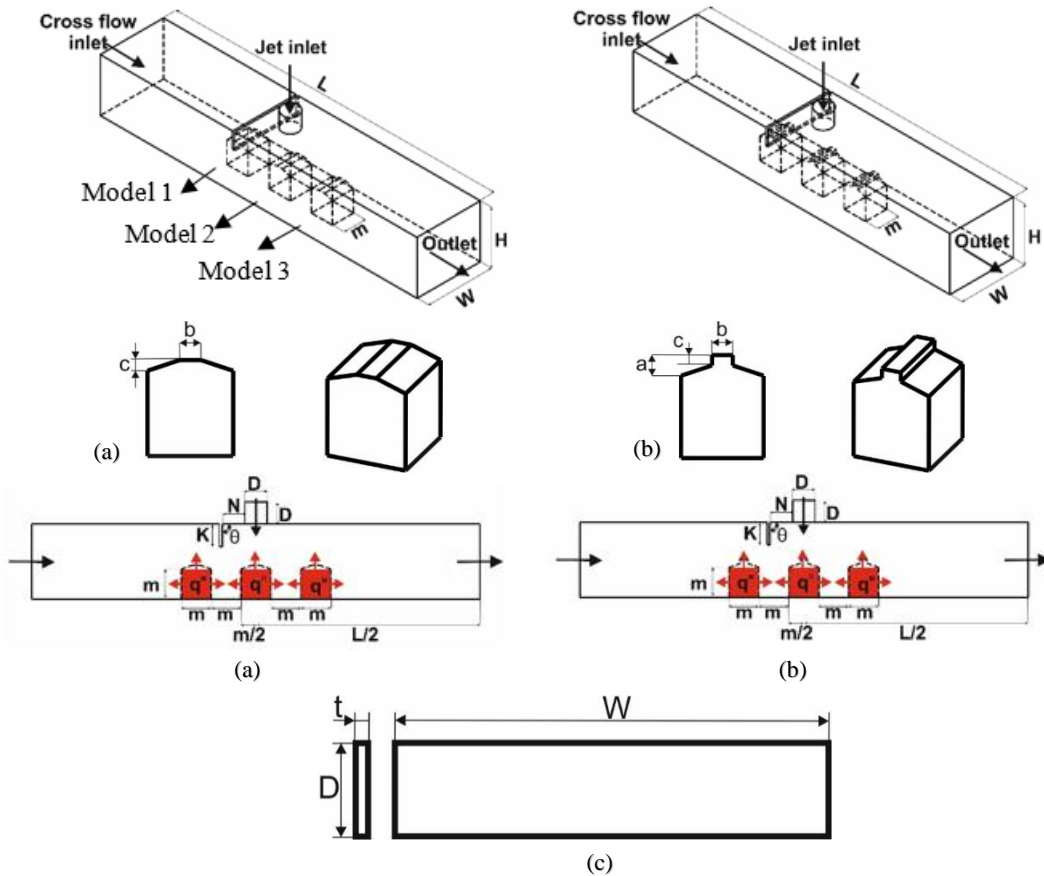
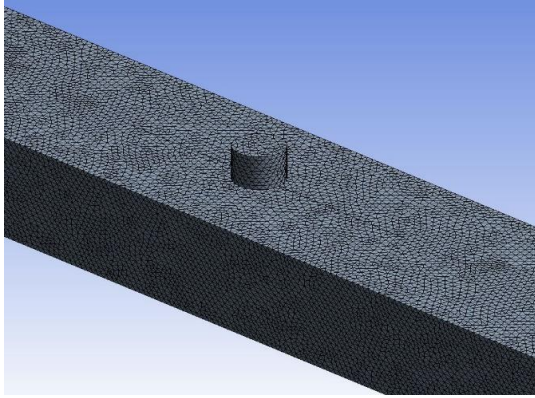


Figure 2. Views of channels with (a) Roof (b) Crown model surfaces (c) fin geometry

**Table 4.** Dimensions of the channels

Variable	Measurement
D	15 mm
L	66D
W	4D
H	3D
M	20 mm
$\theta$	90°
N	1.5D, 2D
a	5 mm
b	5 mm
c	2.5 mm
t	0.1 mm



**Figure 3.** Representation of the regular tetrahedral mesh structure used in the channel

## FINDINGS AND DISCUSSION

In the study, shown in Fig. 4, the results obtained by examining different Re values in the case of only jet flow and by using the equation ( $\overline{Nu} = 1.29 Re^{0.5} Pr^{0.4}$ ) as a result of the experimental investigations of Ma and Bergles (1983) were compared among themselves, and it was determined that the experimental results of Ma and Bergles (1983) and the numerical results of the presented study were compatible and consistent.

In addition, the numerical results of this study were compared with the experimental study of the turbulent flow around a cube exposed to cross flow and impinging jet combined flow by Masip et al. (2012) and it was pointed out in Fig. 5. Masip et al. (2012) placed a cube-shaped model in a 2000x300x30mm channel in their study. Assuming that all surfaces of the channel were taken adiabatically, by taking the ratio of the jet Re ( $Re_j$ ) to the channel Re ( $Re_c$ ) equal ( $Re_j/Re_c=1$ ), the flow structures around the electronic model were investigated at different positions ( $x/h$ ). As can be seen in Fig. 5, it was determined that the velocity profiles obtained as a result of the experimental study conducted by Masip et al. (2012) were quite compatible with each other.

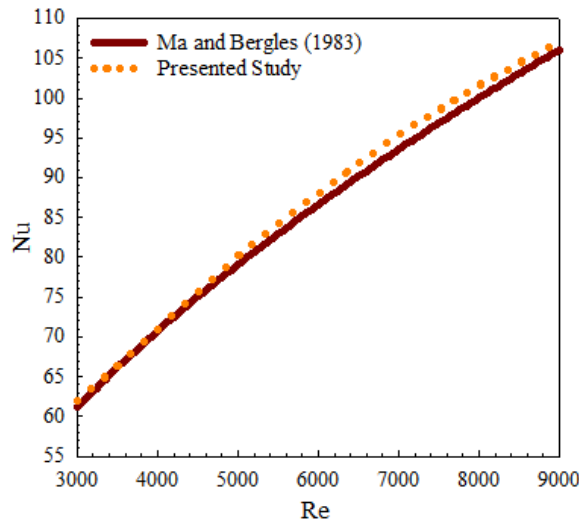


**Figure 4.** Comparison of the presented study and the results of Ma and Bergles (1983)

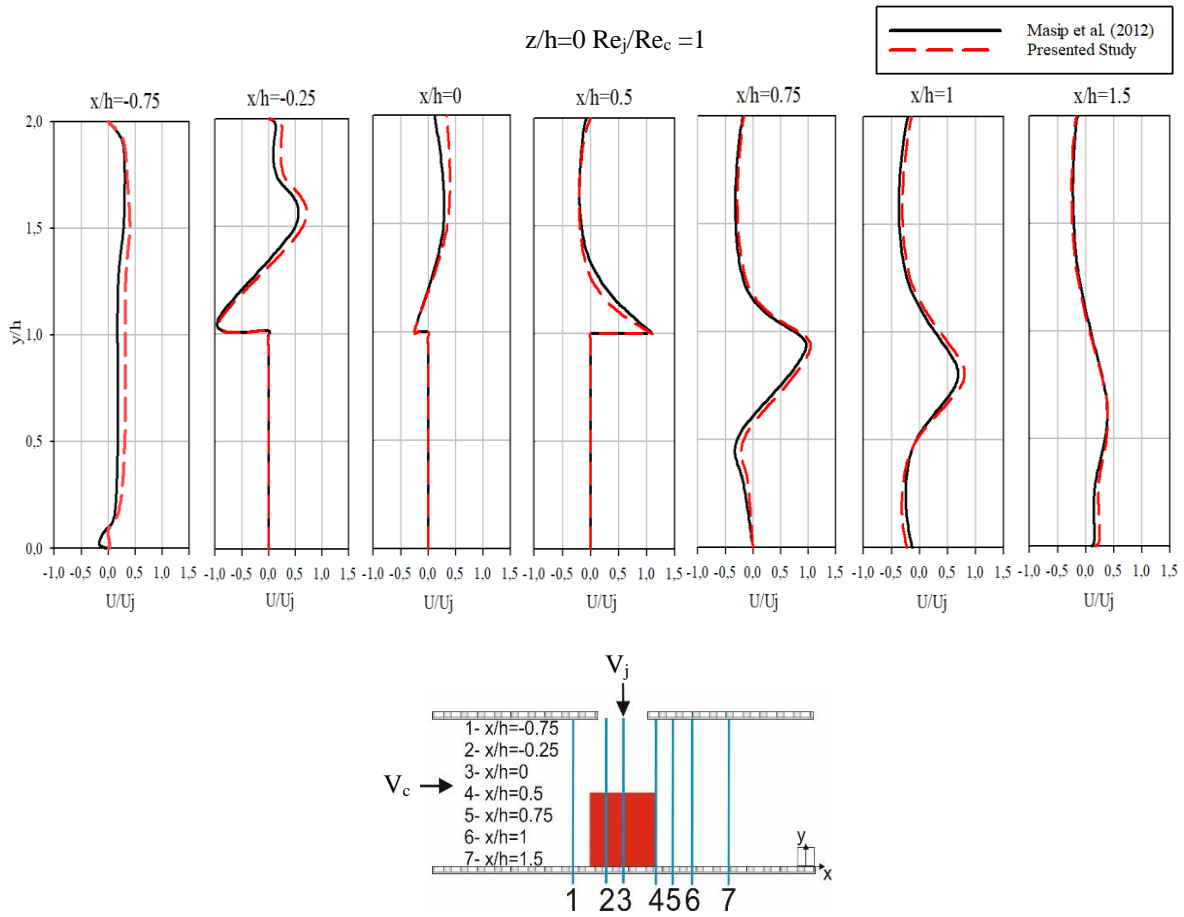


**Figure 5.** Comparison of the presented study and the results of Masip et al. (2012)

Provided that the variation of  $Nu$  depending on the mesh number was determined; by determining the most suitable number of mesh elements in the channel, the effect of mesh number on the mean  $Nu$  value ( $Nu_m$ ) in

the finless combined jet flow channel was presented in Tab. 5 at different  $Re$  values. Accordingly, it was found that 2022840 mesh elements will give reliable and accurate results for the finless channel.

**Table 5.** Variation of  $Nu_m$  with  $Re$  depending on the number of mesh elements

Mesh number	$Re=5000$ $Nu_m$	$Re=7000$ $Nu_m$	$Re=9000$ $Nu_m$
1758412	86.48	108.84	127.40
2022840	86.52	108.88	127.43
2245786	86.52	108.87	127.42

The mean  $Nu$  value variations of roof and crown model surfaces according to model rows in channels having combined jet flow without fin and with  $90^\circ$  angled fin at  $1.5D$  and  $2D$  distance ( $N$ ) by using Water,  $0.02\%$  GO-Water and,  $2\%$  Diamond-Water nanofluids are shown in Figs. 6 and 7, respectively. As the nanofluids in the combined jet flow channels contain GO and Diamond nanoparticles with a higher thermal conductivity coefficient in nano size ( $10^{-9}$  m) for both patterned model surfaces, the  $Nu$  value is higher than the channels in which only water is used, which means an increase in heat transfer from the surfaces to the nanofluid. While the  $Nu$  values are higher in the channel in which GO-Water nanofluid is used for both roof and crown model surfaces and fin distances ( $N=1.5D$  and  $2D$ ) in the first row (Model 1), compared to the channels in which

Diamond-Water nanofluid is used, the  $Nu$  values depending on  $Re$  are higher in finned channels compared to roof patterned surfaces for the crown patterned surfaces. In addition,  $Nu$  values are higher for all pattern rows, water and for both nanofluids as a result of better mobility for the roof model surfaces in the case of the finless channels compared to the crown model surfaces. While the mean  $Nu$  value for the Model 1 surface with roof at  $Re=11000$  is  $10.24\%$  higher for the GO-Water nanofluid in the case with  $N=2D$  fin distance than  $N=1.5D$ , this increment value is  $26.82\%$  for the crown model surface. As can be seen, when the fin is moved away from the jet inlet, the cooling of the surfaces improves as the cross flow is better directed on the surfaces and contributes additionally to the impinging jet flow. When the Model 2 surfaces, which are in the second row in the channels, are examined, it is

seen that the highest Nu values are reached in the channels with  $N=2D$  fin distance in both models for this model row, which is under the influence of the directly impinging jet. In addition, Nu values in this model row, where the combined jet effect is the most intense, are higher than both Model 1 and Model 3. In the case where the Re is 15000 for the  $N=2D$  fin position in the channels in which the Diamond-Water nanofluid is used, the value of mean Nu of the second-row surface with the crown model (Model 2) is 17.9% higher than the surface with the roof model in the same row. Model 3, located at the end of the channel, has the least combined jet effect for both model surfaces. Therefore, Nu values show a decrease for this model row (Model 3) especially compared to Model 2. When GO-Water nanofluid is used in channels with  $N=1.5D$  fin distance at  $Re=7000$ , compared to channels without fins and water fluid is used, the mean Nu increase values in Model 3 compared to Model 2 on crown and roof model surfaces are found to be 53.76% and 36.34% less, respectively.

According to the placement rows of the roof and crown model surfaces in the channel without a fin and, with  $N=1.5D$  and  $N=2D$  fin distance by using Water, 0.02% GO-Water and 2% Diamond-Water nanofluids, the mean temperature variations on the model surfaces are given depending on the Re in Figs. 8 and 9, respectively. With the increase of Re in all model rows for both model surfaces, the heat transfer from the surfaces increases with the mobility of the fluid in the combined jet flow channels. Accordingly, the temperature of the model surfaces decreases. However, when the fin is added to the channel and especially in the  $N=2D$  fin distance with GO-Water nanofluid, while the cooling of the surfaces is at the best level compared to the finless condition for all model rows and both model shapes; lower surface temperature values can be obtained on the crown model surfaces than that of the roof model. Since Model 2 is under the direct impact of the impinging jet, the combined jet effect increases on the model surface, and the surface temperature values decrease on both model-shaped surfaces compared to Model 1. Besides, while the cooling effect is better in finned channels, for the  $N=2D$  distance where nanofluids are used, more reduction in surface temperatures is provided due to the increase in heat transfer on both model surfaces. When Model 3, which is in the third row in the channels, is examined, the decrease in the combined jet flow intensity in the models in this row for both model surfaces causes the surface temperatures to increase compared to Model 2 and depending on the model shape. Better orientation of the combined jet flow towards Model 3 after hitting Model 2 ensures that the surface temperature is lower for the crown model surface than that of the roof model.

C (Performance Coefficient) in the combined jet flow channels using Water, 0.02% GO-Water and, 2% Diamond-Water nanofluids belonging to the roof and crown model surfaces are shown according to different

fin placement distances ( $N=1.5D$  and  $2D$ ) in Figs. 10 and 11, respectively. For both model surfaces, higher C coefficient values are obtained in channels with  $N=1.5D$  fin distance and Diamond-Water nanofluid than in channels with  $N=2D$  fin distance using GO-Water nanofluid and Water. This situation is caused by the less pressure drop of the Diamond-Water nanofluid compared to the GO-Water nanofluid, while the fact that the fin makes difficult of the flow passage in the  $N=2D$  position is another factor that increases the pressure drop compared to the  $N=1.5D$  position. Therefore, although the Nu values are higher for the  $2D$  distance, the C values obtained for the  $1.5D$  fin distance are higher than the  $2D$  distance due to the low-pressure losses. For  $N=1.5D$  at  $Re=11000$ , the C value obtained for the Diamond-Water nanofluid on the crown model surface is 6.05% higher than the roof model surface. However, as the pressure drop increases with the increase in the Re, the C values also decrease. Besides, the fact that the C is more than 1 indicates that the use of a fin has an increasing effect on heat transfer despite the pressure drop.

Mean Nu ( $Nu_m$ ) and surface temperature ( $T_m$ ) values for all three roof and crown model surfaces in the combined jet flow channels at Re values of 5000 and 15000 are given in Tab. 6 for without fin and with fin and,  $N=1.5D$  and  $N=2D$  fin distance, respectively. In the case of using fins in both model surface channels,  $Nu_m$  values increase while  $T_m$  values decrease. However, when nanofluid is used, higher  $Nu_m$  values are obtained due to the increase in heat transfer from the model surfaces compared to the water fluid, while the mean surface temperature values ( $T_m$ ) decrease with the cooling effect. In addition, the highest  $Nu_m$  values are reached on the crown patterned surfaces with fins at  $N=2D$  distance and using GO-Water nanofluid compared to the  $N=1.5D$  fin distance and the use of Diamond-Water nanofluid.  $Nu_m$  increases for GO-Water nanofluid at  $Re=15000$  and  $N=2D$  fin distance according to  $N=1.5D$  are 7.24% and 16.38% compared to the case of using finless and water fluid for roof and crown models, respectively. Accordingly, lower  $T_m$  values are obtained in the channels with crown model surfaces compared to channels with roof surfaces. Besides,  $Nu_m$  increases for GO-Water and Diamond-Water nanofluids at  $Re=15000$  and  $N=2D$  are 47.53%-46.21% and 57.42%-56.18% compared to the case of using finless and water fluid for roof and crown models, respectively.

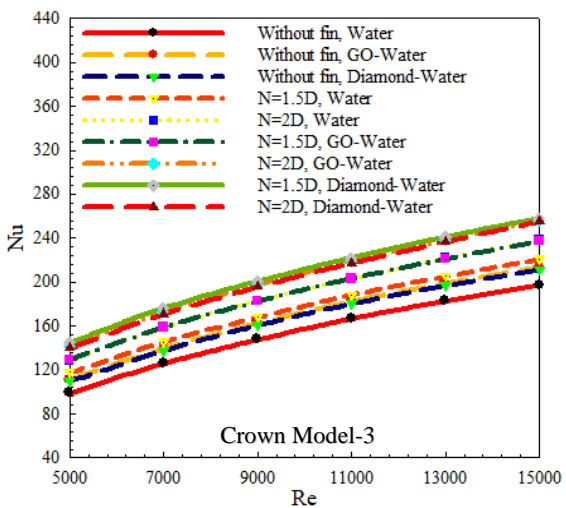
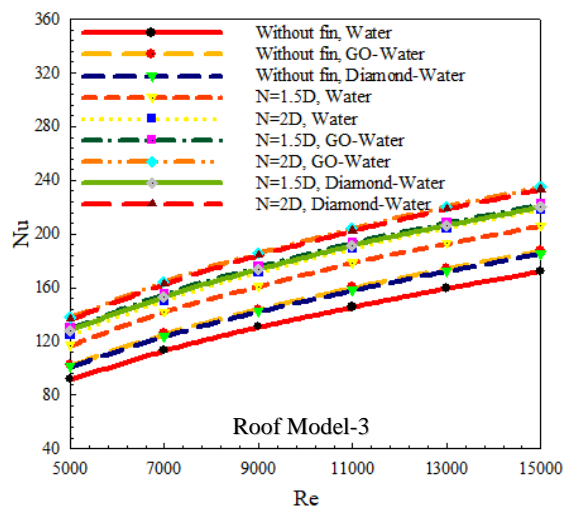
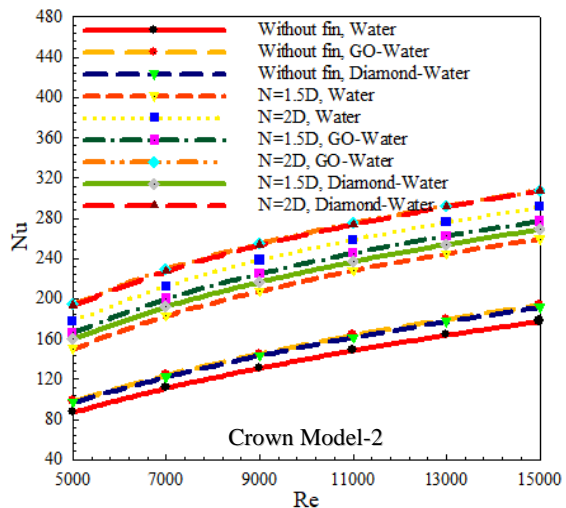
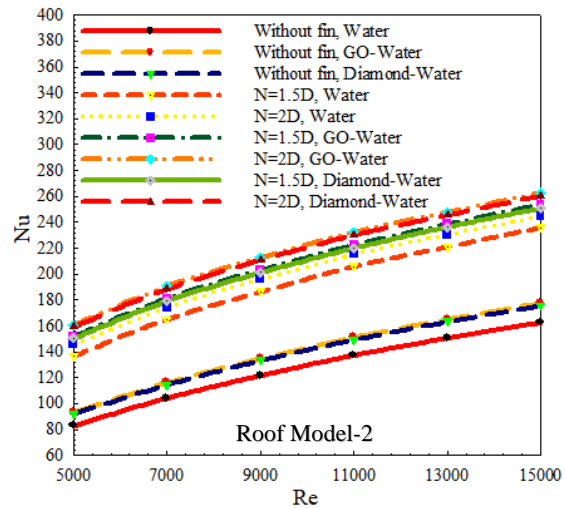
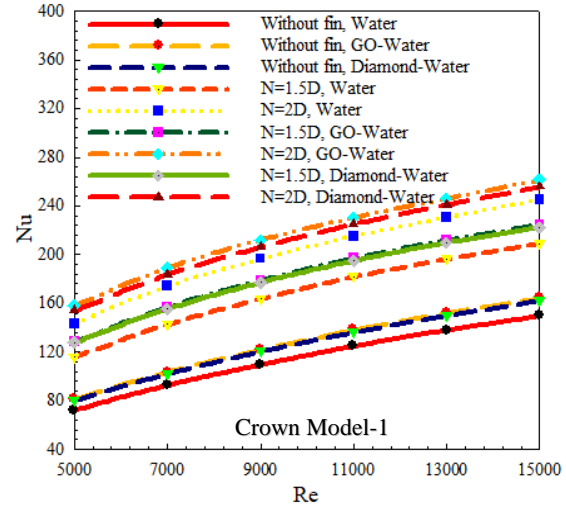
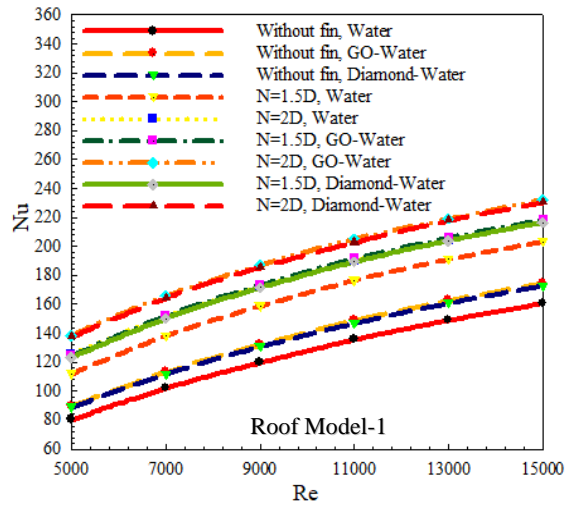


**Figure 6.** Variation of mean Nu value with Re according to model rows in cross flow-impinging jet flow channels with roof model

**Figure 7.** Variation of mean Nu value with Re according to model rows in cross flow-impinging jet flow channels with crown model

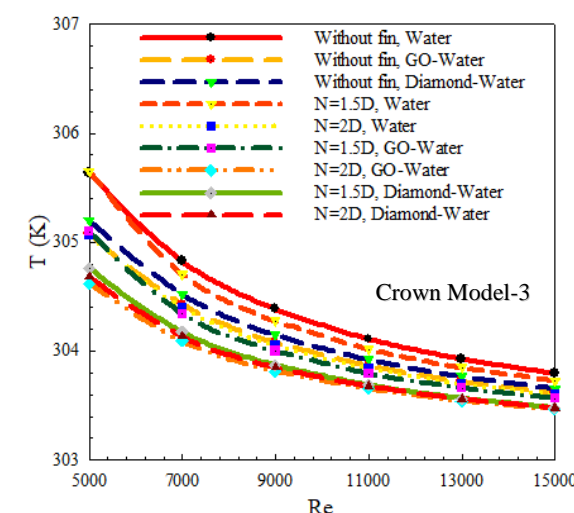
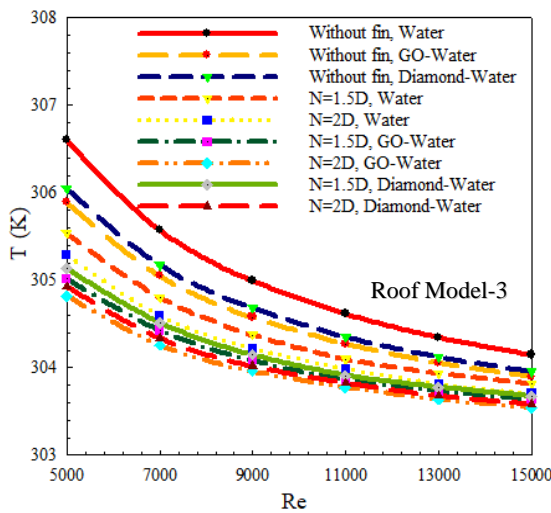
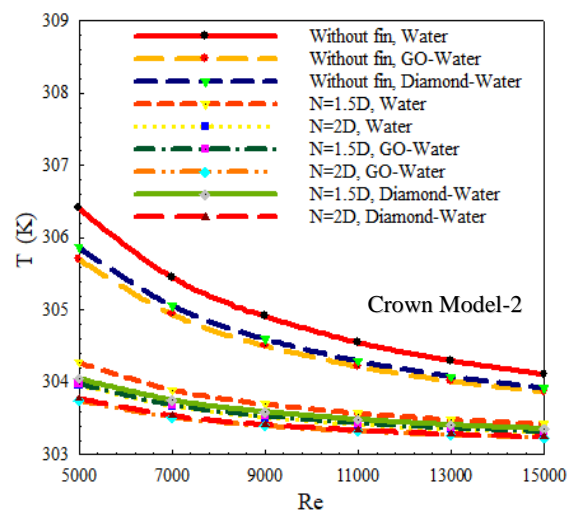
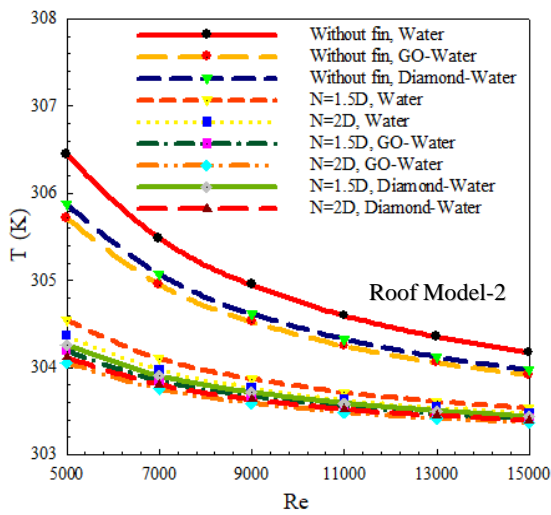
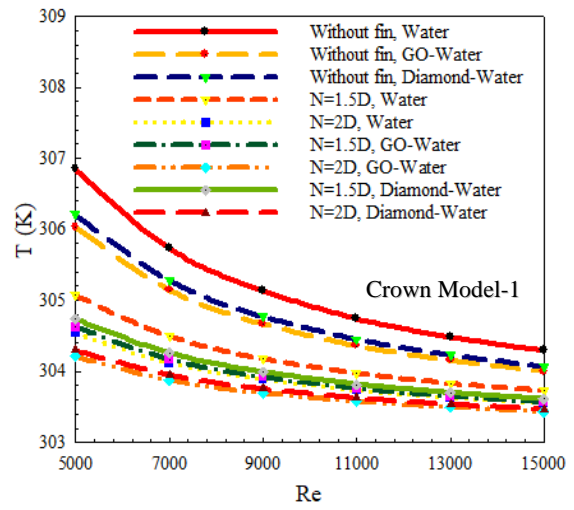
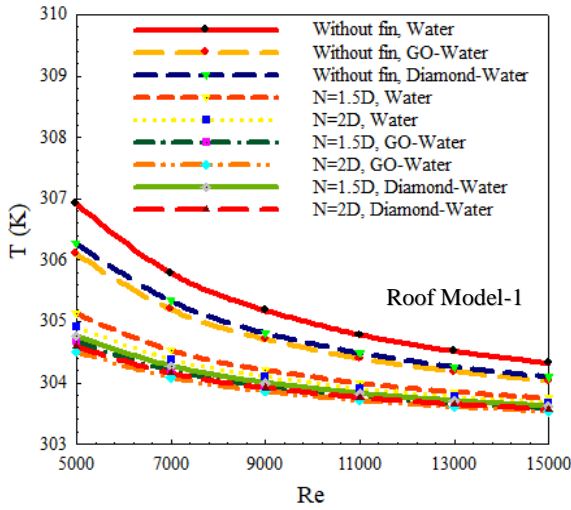


**Figure 8.** Variation of mean surface temperature ( $T$ ) with  $Re$  according to model rows in cross flow-impinging jet flow channels with roof model

**Figure 9.** Variation of mean surface temperature ( $T$ ) with  $Re$  according to model rows in cross flow-impinging jet flow channels with crown model

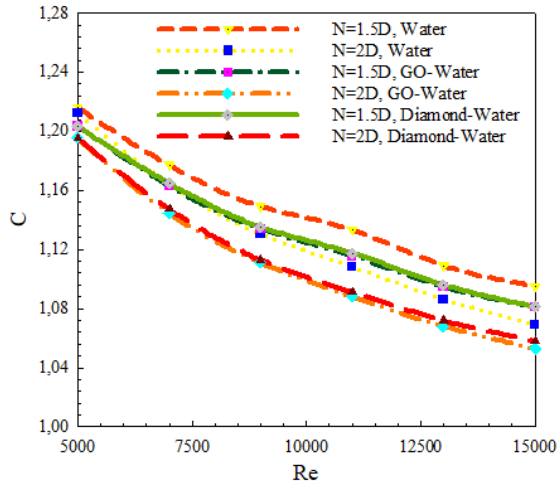


**Figure 10.** Variation of  $C$  with  $Re$  for  $N=1.5D$  and  $N=2D$  in cross-flow-impinging jet-flow channels with roof model

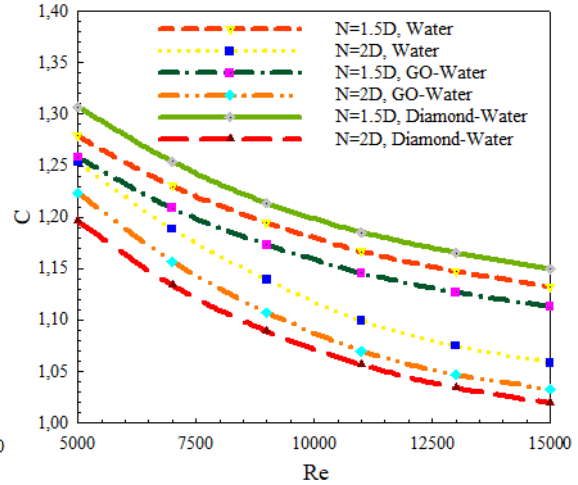


**Figure 11.** Variation of  $C$  with  $Re$  for  $N=1.5D$  and  $N=2D$  in cross-flow-impinging jet-flow channels with crown model

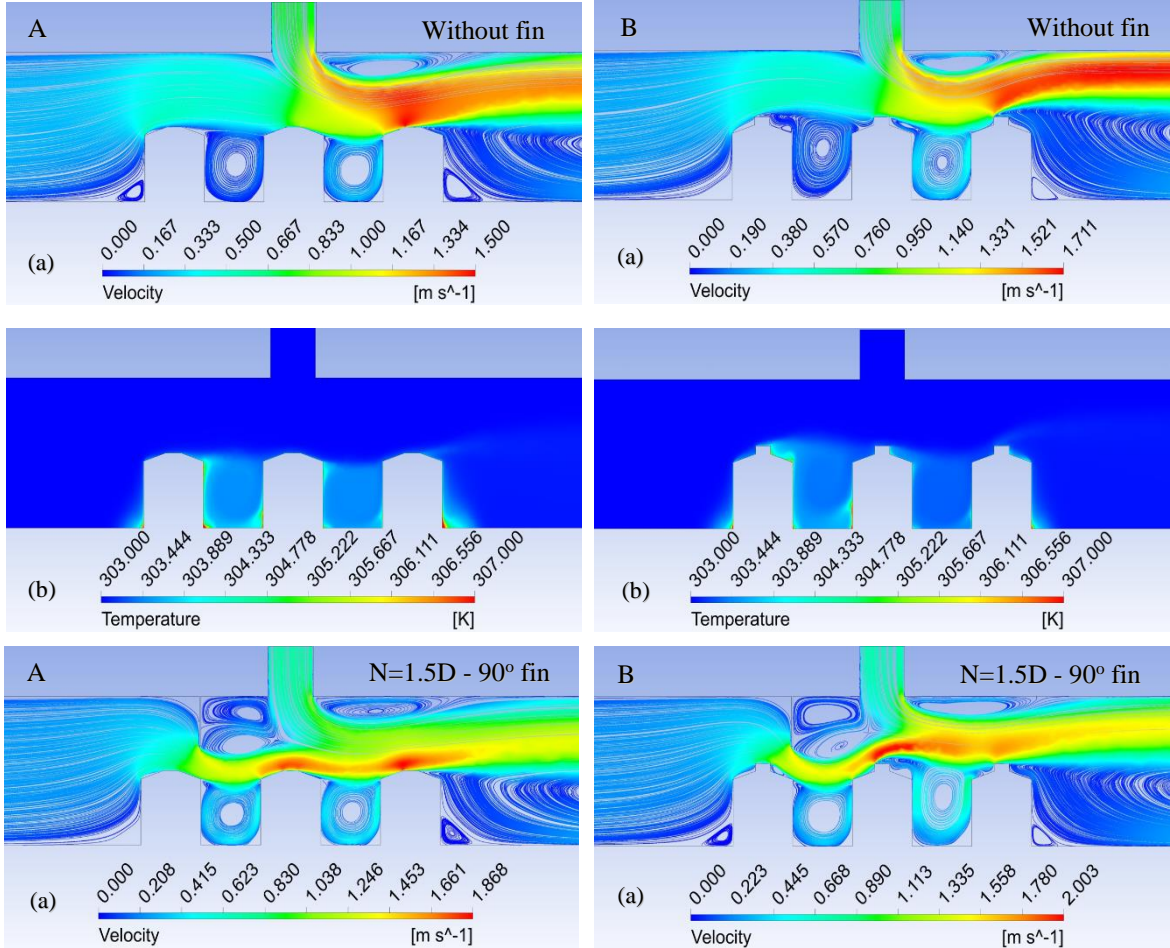
In Fig. 12 A-Roof Model and B-Crown Model, (a) velocity and (b) temperature contour distributions are presented in the combined jet flow channels without fin and, with  $90^\circ$  angled fin having  $N=1.5D$  and  $2D$  distance by using Diamond-Water nanofluid at  $Re=11000$ , respectively. As can be seen from the velocity contour distributions, the velocity values on Model 1 are lower since Model 1 is mostly under the influence of the cross-flow coming from the channel inlet in the finless condition in both model-surfaced channels. Although there is an impinging jet flow on Model 2, the cross-flow drags this flow towards Model 3, increasing the combined jet flow velocity on this model without fin. For this reason, although Model 3 is at the end of the channel, the cooling performance is close to Model 2 under the impact of the impinging jet, as can be seen from the temperature distributions for both model shapes, in the finless condition. This is also contributed by the recirculation zones on the upper right side of the

impinging jet flows in the channels to direct the combined jet flow towards Model 3. When fins are added to the channels ( $\theta=90^\circ$ ), since the cross-flow from the channel can be directed on the model surfaces, the contact of the fluid with the surface increases, at the same time, a jet flow effect occurs on the surfaces due to the decrease in the flow passage cross-sectional area. When the fin is placed at a distance of  $N=1.5D$  from the channel, the combined jet flow effect of the fluid shows itself with velocity increases on all models and for both model shapes; in  $N=2D$  fin position, the velocity of the fluid on Model 3 decreases as the fluid hits the upper part of Model 2 and is directed to the upper part of the channel for Model 3 with the crown pattern. Besides, with the use of fins, the heat transfer from the model surfaces is increased by providing the movement of the fluid located between the models and circulating in itself, which contributes negatively to the cooling of the models.



**Table 6.** Analysis results of  $Nu_m$  and  $T_m$  values for all three roof and crown model surfaces in cross-flow-impinging jet channels with Water, GO-Water and, Diamond-Water nanofluid

			Re=5000		Re=15000	
			Roof Model	Crown Model	Roof Model	Crown Model
<b>Without fin</b>	Water	$Nu_m$	84.891	86.197	164.991	174.560
<b>Without fin</b>	GO-Water	$Nu_m$	95.098	96.865	179.896	190.352
<b>Without fin</b>	Diamond-Water	$Nu_m$	94.042	95.74	177.944	188.281
<b>N=1.5D</b>	Water	$Nu_m$	122.028	127.987	215.094	229.679
<b>N=2D</b>	Water	$Nu_m$	131.943	150.110	226.793	258.162
<b>N=1.5D</b>	GO-Water	$Nu_m$	135.338	141.486	231.474	246.209
<b>N=2D</b>	GO-Water	$Nu_m$	145.735	164.749	243.420	274.793
<b>N=1.5D</b>	Diamond-Water	$Nu_m$	134.024	144.407	229.090	249.710
<b>N=2D</b>	Diamond-Water	$Nu_m$	144.409	162.347	241.246	272.638
<b>Without fin</b>	Water	$T_m$ (K)	306.652	306.297	304.208	304.062
<b>Without fin</b>	GO-Water	$T_m$ (K)	305.900	305.606	303.943	303.827
<b>Without fin</b>	Diamond-Water	$T_m$ (K)	306.061	305.755	304.003	303.880
<b>N=1.5D</b>	Water	$T_m$ (K)	305.067	304.998	303.695	303.624
<b>N=2D</b>	Water	$T_m$ (K)	304.857	304.523	303.618	303.487
<b>N=1.5D</b>	GO-Water	$T_m$ (K)	304.627	304.570	303.541	303.485
<b>N=2D</b>	GO-Water	$T_m$ (K)	304.460	304.192	303.481	303.378
<b>N=1.5D</b>	Diamond-Water	$T_m$ (K)	304.719	304.516	303.576	303.483
<b>N=2D</b>	Diamond-Water	$T_m$ (K)	304.542	304.250	303.512	303.395



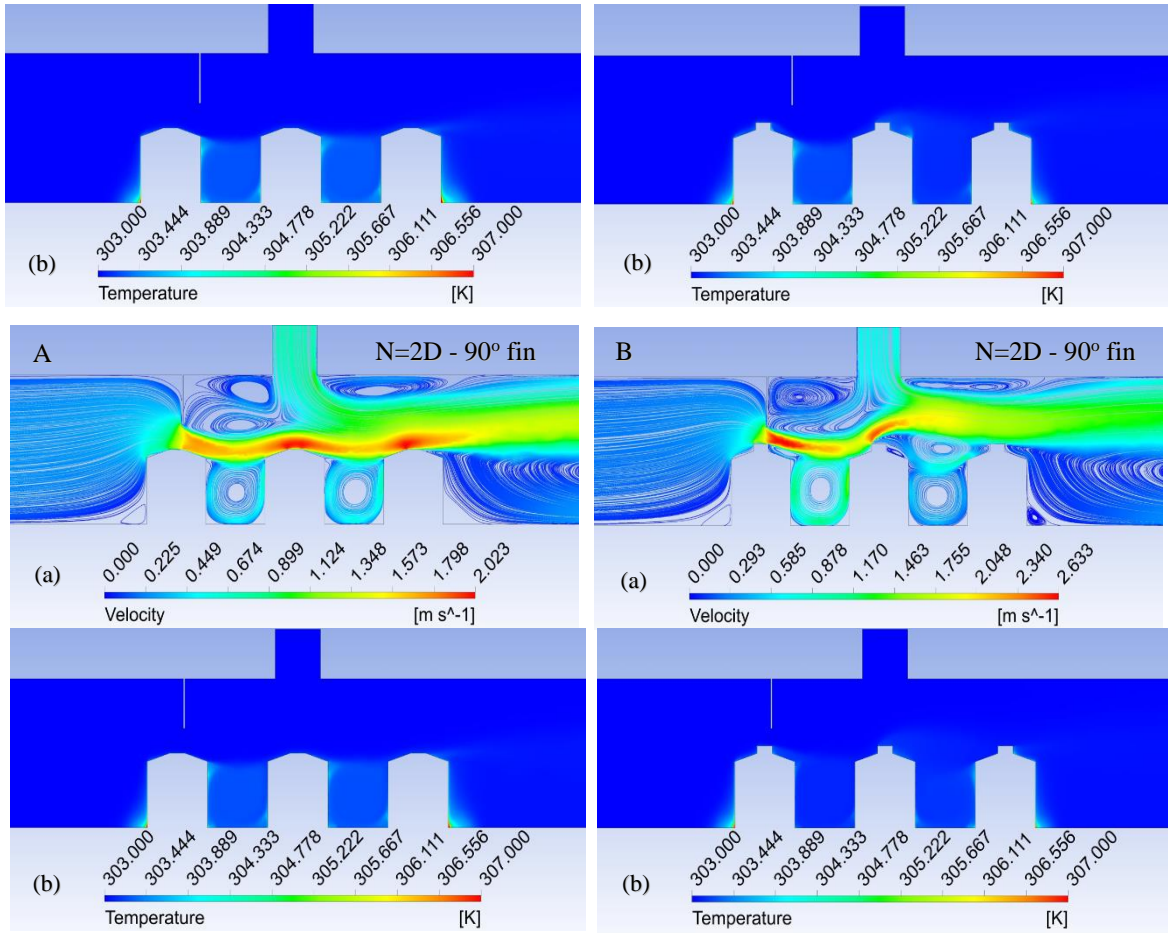


**Figure 12.** (a) Velocity (b) Temperature contour distributions in cross flow-impinging jet flow channels with A-Roof B-Crown model for Diamond-Water nanofluid

## CONCLUSIONS

In this study, the heat transfer and flow structure from the roof and crown model surfaces in the combined jet flow channels with  $H=3D$  height by using cross flow-impinging jet flow were numerically analyzed without fin and with fin angle of  $90^\circ$  and, fin arranged from the impinging jet inlet as  $N=1.5D$  and  $N=2D$  distances. While a constant heat flux of  $1000 \text{ W/m}^2$  was applied to the model surfaces, Water, GO-Water and Diamond-Water nanofluids with a volumetric concentration of 0.02% and 2%, respectively, were used as fluids in the channels. As a result of this numerical study, in which a detailed examination of the cross-flow-impinging jet flow using different nanofluids was made, the following results can be reached.

- Nu values are higher for all pattern rows, water and for both nanofluids for the roof model surfaces in the case of the finless channels compared to the crown model surfaces.

- While the Nu values are higher in the channel in which GO-Water nanofluid is used for the roof and crown model surfaces and fin distances ( $N=1.5D$  and  $2D$ ) in the first row (Model 1), compared to the channels in

which Diamond-Water nanofluid is used, the Nu values depending on Re are higher in finned channels compared to roof model surfaces for the crown model.

- While the mean Nu value for the Model 1 surface with roof at  $Re=11000$  is 10.24% higher for the GO-Water nanofluid in the case with  $N=2D$  fin distance than  $N=1.5D$ , this increment value is 26.82% for the crown model surface.

- At  $Re=15000$  for the  $N=2D$  fin position in the channels in which the Diamond-Water nanofluid is used, the mean Nu value of the crown model (Model 2) is 17.9% higher than the surface with the roof Model 2.

- When the GO-Water nanofluid is used in channels with  $N=1.5D$  fin distance at  $Re=7000$ , compared to channels without fins and water fluid is used, the mean Nu increase values in Model 3 compared to Model 2 on crown and roof model surfaces are found to be 53.76% and 36.34% less, respectively.

- The highest  $Nu_m$  values are reached on the crown patterned surfaces with a fin at  $N=2D$  distance and using

GO-Water nanofluid compared to the  $N=1.5D$  fin distance and the use of Diamond-Water nanofluid.

-  $Nu_m$  increases for GO-Water nanofluid at  $Re=15000$  and  $N=2D$  fin distance according to  $N=1.5D$  are 7.24% and 16.38% compared to the case of using finless and water fluid for roof and crown models, respectively. Accordingly, lower  $T_m$  values are obtained in the channels with crown model surfaces compared to channels with roof surfaces.

- Although the  $Nu$  values are higher for the  $2D$  distance, the  $C$  values obtained for the  $1.5D$  fin distance are higher than the  $2D$  distance due to low-pressure losses.

- For  $N=1.5D$  at  $Re=11000$ , the  $C$  value obtained for the Diamond-Water nanofluid on the crown model surface is 6.05% higher than the roof model surface. However, as the pressure drop increases with the increase in the  $Re$ , the  $C$  values also decrease.

As a result, increasing the heat transfer from the model surfaces in the combined jet flow channels is of great importance in terms of the operation of the circuit within safe temperature limits. In this case, apart from the model shape of the surfaces, the fin setup and fin placement used to direct the fluid in the channel to the model surfaces, the channel and jet  $Re$  values and the thermophysical properties of the fluid are the main factors.

## ACKNOWLEDGMENTS

This study was supported by Sivas Cumhuriyet University Scientific Research Projects (CUBAP) unit with project number TEKNO-2021-031.

## REFERENCES

Abdullah M. F., Zulkifli R., Harun Z., Abdullah S., Wan Ghopa W. A., Najm A. S., Sulaiman N. H., 2019, Impact of the  $TiO_2$  Nano Solution Concentration on Heat Transfer Enhancement of the Twin Impingement Jet of A Heated Aluminium Plate, *Micromachines*, 10, 176.

Alnak D. E., Koca F., Alnak Y. A., 2021, Numerical Investigation of Heat Transfer from Heated Surfaces of Different Shapes, *J. Eng. Therm.*, 30, 494-507.

Alnak D. E., 2020, Thermohydraulic Performance Study of Different Square Baffle Angles in Cross-Corrugated Channel, *J. Energy Storage*, 28, 101295.

Chang T. B., Yang Y. K., 2014, Heat Transfer Performance of Jet Impingement Flow Boiling Using

$Al_2O_3$ -Water Nanofluid, *J. Mech. Sci. Technol.*, 28, 1559-1566.

Datta A., Jaiswal A., Halder P., 2018, Heat Transfer Analysis of Slot Jet Impingement Using Nano-Fluid on Convex Surface, *IOP Conf Series-Mat. Sci. Eng.*, 402, 012098.

Demircan T., 2019, Numerical Analysis of Cooling An Electronic Circuit Component with Cross Flow and Jet Combination, *J. Mech.*, 35, 395-404.

Eravcu F., 2016, *Synthesis, Characterization, Rheology, Thermal Conductivity and Stability of Carbon-Based Nanomaterials*, MSc. Thesis, Sivas Cumhuriyet University, Sivas, Turkey.

Genç M. S., Kaynak Ü., Yapıcı H., 2011, Performance of Transition Model for Predicting Low  $Re$  Aerofoil Flows without/with Single and Simultaneous Blowing and Suction, *Eur. J. Mech. B/Fluids*, 30, 218-235.

Genç M. S., 2010, Numerical Simulation of Flow Over A Thin Aerofoil at A High Reynolds Number Using A Transition Model, *Proc. Inst. Mech. Eng. Part C: J. Mech. Eng. Sci.*, 24, 2155-2164.

Genç M. S., Kaynak U., Lock G. D., 2009, Flow Over An Aerofoil without and with A Leading- Edge Slat at A Transitional Reynolds Number, *Proc. Inst. Mech. Eng. Part G: J. Aeros. Eng.*, 223, 217-231.

Hadipour A, Zargarabadi M. R., 2018, Heat Transfer and Flow Characteristics of Impinging Jet on A Concave Surface at Small Nozzle to Surface Distances, *Appl. Therm. Eng.*, 138, 534-541.

Hajjar Z., Rashidi A., Ghozatloo A., 2014, Enhanced Thermal Conductivities of Graphene Oxide Nanofluids, *Int. Commun. Heat Mass Transf.*, 57, 128-131.

Huang L., Yeom T., Simon T., Cui T., 2021, An Experimental and Numerical Study on Heat Transfer Enhancement of A Heat Sink Fin by Synthetic Jet Impingement, *Heat Mass Transf.*, 57, 583-593.

Hummers W. S., Offeman R. E., 1958, Preparation of Graphitic Oxide, *J. American Chem. Soc.*, 80, 1339.

Incropera F. P., Dewit D. P., Bergman T. L., Lavine A. S., 2007, *Fundamentals of Heat and Mass Transfer*, 6<sup>th</sup> Ed. In: John Wiley&Sons, United States of America.

Issac J., Singh D., Kango S., 2020, Experimental and Numerical Investigation Of Heat Transfer

- Characteristics of Jet Impingement on A Flat Plate, *Heat Mass Transf*, 56, 531-546.
- Jalali E., Sajadi S. M., Ghaemi F., Baleanu D., 2022, Numerical Analysis of the Effect of Hot Dent Infusion Jet on the Fluid Flow and Heat Transfer Rate Through the Microchannel in the Presence of External Magnetic Field, *J. Therm. Anal. Calorim.*, 147, 8397-8409.
- Karabulut K., Alnak D. E., 2021, Investigation of the Effects of Different Patterned Surface Geometries on Heat Transfer in A Rectangular Channel, *Tesisat Mühendisliği Dergisi*, 183, 37-49.
- Karabulut K., Alnak D. E., 2020, Study of Cooling of the Varied Designed Warmed Surfaces with An Air Jet Impingement, *Pamukkale Univ. J. Eng. Sci*, 26, 88-98.
- Karabulut K., Buyruk E., Kilinc F., 2020, Experimental and Numerical Investigation of Convection Heat Transfer in A Circular Copper Tube Using Graphene Oxide Nanofluid, *J. Braz. Soc. Mech. Sci. Eng.*, 42, 230.
- Karabulut K., 2019, Heat Transfer Improvement Study of Electronic Component Surfaces Using Air Jet Impingement, *J. Comp. Electronics*, 18, 1259-1271.
- Kılıç M., 2018, Investigation of Combined Effect of Nanofluids and Impinging Jets on Cooling of Electronic Systems, *Çukurova Univ J Fac Eng Arch*, 18, 121-132.
- Kilic M., Calisir T., Baskaya S., 2017, Experimental and Numerical Investigation of Vortex Promoter Effects on Heat Transfer from Heated Electronic Components in A Rectangular Channel with An Impinging Jet, *Heat Transf. Res.*, 48, 435-463.
- Kilic M., Calisir T., Baskaya S., 2016, Experimental and Numerical Study of Heat Transfer from A Heated Flat Plate in A Rectangular Channel with An Impinging Air Jet, *J. Braz. Soc. Mech. Sci. Eng.*, 39, 329-344.
- Kumar D., Zunaid M., Gautam S., 2021, Heat Sink Analysis in Jet Impingement with Air Foil Pillars and Nanoparticles, *Mater. Today: Proc.*, 46, 10752-10756.
- Ma C. F., Bergles A. E., 1983, Boiling Jet Impingement Cooling of Simulated Microelectronic Chips, *Heat Transf. Elect. Equ. HTD*, 28, 5-12.
- Maghrabie H. M., Attalla M., Fawaz H. E., Khalil M., 2017, Numerical Investigation of Heat Transfer and Pressure Drop of In-Line Array of Heated Obstacles Cooled by Jet Impingement in Cross-Flow, *Alexandria Eng. J.*, 56, 285-296.
- Masip Y., Rivas A., Larraona G. S., Anton R., Ramos J. C., Moshfegh B., 2012, Experimental Study of the Turbulent Flow Around A Single Wall-Mounted Cube Exposed to A Cross-Flow and An Impinging Jet, *Int. J. Heat Fluid Flow*, 38, 50-71.
- Maxwell J. C., 1873, *A Treatise on Electricity and Magnetism*, Clarendon Press, Oxford, United Kingdom.
- Mergen S., 2014, *Numerical Investigation of the Cooling of An Electronic Component with the Combination of Cross Flow and Impinging Jet*. MSc Thesis, University of Gazi, Ankara, Türkiye.
- Mohammed H. A., Gunnasegaran P., Shuaib N. H., 2011, The Impact of Various Nanofluid Types on Triangular Microchannels Heat Sink Cooling Performance, *Int. Commun. Heat Mass Transf.*, 3, 767-773.
- Naga Ramesh K., Karthikeya Sharma T., Amba Prasad Rao G., 2021, Latest Advancements in Heat Transfer Enhancement in the Micro-Channel Heat Sinks: A Review, *Arch. Comput. Methods Eng*, 28 (3), 135-3165.
- Nagesha K., Srinivasan K., Sundararajan T., 2020, Heat Transfer Characteristics of Single Circular Jet Impinging on A Flat Surface with A Protrusion, *Heat Mass Transf*, 56, 1901-1920.
- Öztürk S. M., Demircan T., 2022, Numerical Analysis of the Effects of Fin Angle on Flow and Heat Transfer Characteristics for Cooling An Electronic Component with Impinging Jet and Cross-Flow Combination, *J. Fac. Eng. Arch. Gazi Univ.*, 37, 57-74.
- Pak B. C., Cho Y. I., 1998, Hydrodynamic and Heat Transfer Study of Dispersed Fluids with Submicron Metallic Oxide Particles, *Exp. Heat Transf.*, 11, 151-170.
- Rathore S. S., Verma S. K., 2022, Numerical Investigation on the Efficacy of Jet Obliquity for Fluid Flow and Thermal Characteristics of Turbulent Offset Jet, *Heat Mass Transf*, 58, 1223-1246.
- Saleha N., Fadela N., Abbes A., 2015, Improving Cooling Effectiveness by Use Chamfers on the Top of Electronic Components, *Microelect. Reliab.*, 55, 1067-1076.
- Selimefendigil F., Chamkha A. J., 2020, Cooling of An Isothermal Surface Having A Cavity Component by Using CuO-Water Nano-Jet, *Int. J. Num. Methods Heat & Fluid Flow*, 30, 2169-2191.

Shi W., Li F., Lin Q., Fang G., 2021, Experimental Study on Instability of Round Nanofluid Jets at Low Velocity, *Exp. Therm. Fluid. Sci.*, 120, 110253.

Taylor J. R., 1997, *An Introduction to Error Analysis: The Study of Uncertainties in Physical Measurements*, University Science Books, Sausalito, United States of America.

Teamah M. A., Dawood M. M., Shehata A., 2015, Numerical and Experimental Investigation of Flow Structure and Behavior of Nanofluids Flow Impingement on Horizontal Flat Plate, *Exp. Therm. Fluid Sci.*, 74, 235-246.

Wang S. J., Mujumdar A. S., 2005, A Comparative Study of Five Low Reynolds Number  $k-\epsilon$  Models for Impingement Heat Transfer, *App. Therm. Eng.*, 25, 31-44.

Zou L., Ning L., Wang X., Li Z., He L., Li H., 2022, Evaluation of Interfacial Heat Transfer Coefficient Based on the Experiment and Numerical Simulation in the Air-Cooling Process, *Heat Mass Transf.*, 58, 337-354.



## INVESTIGATION OF HEAT CONVECTION DURING VEHICLE BRAKING

Cansu AY GÖKÇE\* and Abdullah DEMİR\*\*

\* Karadeniz Technical University, Department of Mechanical Engineering, Trabzon, Turkey

cansuay@ktu.edu.tr, ORCID: 0000-0001-6504-5830

\*\* Marmara University, Department of Mechanical Engineering, İstanbul, Turkey

ademir@marmara.edu.tr, ORCID: 0000-0003-4042-7626

(Geliş Tarihi: 25.06.2021, Kabul Tarihi: 14.03.2023)

**Abstract:** The brake system is the most significant active safety system that converts the vehicle's mechanical energy into heat energy based on the braking pair's friction. The transfer of heat in the brake pair during braking occurs by conduction, convection, and radiation. In disc brakes, which are widely used today, the effect of the heat transfer coefficient, which continually changes with the disc's angular velocity on the cooling of the braking pairs is important. The change in heat convection coefficient can be calculated with a numerical approach. In this study, on disc temperature effect of heat convection coefficient and angular velocity has been examined with the finite element method using the experimental data in the SAE J2522 Comprehensive Brake Efficiency Test Standard, fading test procedure. Disc brake design has been designed in the SOLIDWORKS program, and analysis has been carried out using ANSYS 2020 R2 in steady-state thermal analysis. It has been determined that the cooling amounts at the initial of braking are higher than the cooling amounts at the end of braking, and the effect of cooling by convection in the reduction of the temperature difference at the end of braking compared to the initial state is between 91.22% and 91.74%.

**Keywords:** Disc brake, heat transfer, convection, fading

## TAŞIT FRENLEMESİ ESNASINDA OLUŞAN ISI TAŞINIMININ İNCELENMESİ

**Özet:** Fren sistemi, frenleme çiftleri arasındaki sürtünme esasına göre taşıtın mekanik enerjisini ısı enerjisine dönüştüren, en önemli aktif emniyet sistemidir. Frenleme esnasında fren çiftindeki ısının transfer edilmesi iletim, taşınım ve ışınım yoluyla gerçekleşmektedir. Günümüzde yaygın olarak kullanılan disk frenlerde, diskin açısal hızının etkisiyle sürekli olarak değişen ısı taşınım katsayısının frenleme çiftlerindeki soğutma üzerine etkisi önemlidir. Isı taşınım katsayısındaki değişim ise sayısal yaklaşımla hesaplanabilmektedir. Bu çalışmada SAE J2522 Kapsamlı Fren Etkinlik Test Standardı sıcaklıkla fren zayıflaması test prosedüründeki deneysel veriler kullanılarak, açısal hız ile ısı taşınım katsayısının disk sıcaklıkları üzerine etkisi, sonlu elemanlar metoduyla incelenmiştir. Disk fren tasarımı SOLIDWORKS programında, analiz ise ANSYS 2020 R2'de kararlı durum termik analizde gerçekleştirilmiştir. Frenleme başlangıcındaki soğutma miktarlarının frenleme sonundaki soğutma miktarlarından daha yüksek olduğu ve frenleme sonundaki sıcaklık farkının ilk duruma göre azalmasında taşınım ile soğutma etkisinin %91,22 ile %91,74 arasında olduğu tespit edilmiştir.

**Anahtar kelimeler:** Disk fren, ısı transferi, taşınım, sıcaklıkla fren zayıflaması

### NOMENCLATURE

**D** : Characteristic length (mm)  
**d<sub>o</sub>** : Disc's outer diameter (mm)  
**h** : Heat transfer coefficient (Wm<sup>2</sup>/K)  
**k<sub>a</sub>** : Thermal conductivity (W/mK)  
**Re** : Reynolds number  
**R** : Tire diameter (mm)  
**T** : Temperature (K)  
**t** : Time (s)  
**w** : Angular velocity rad/s

### Greek symbols

**ρ** : Density of the air (kg/m<sup>3</sup>)

**μ** : Dynamic viscosity (kg/ms)  
**T<sub>ri</sub>** : Initial temperature of disc  
**T<sub>rf</sub>** : Final temperature of disc

### INTRODUCTION

In the disc-pad couple of a vehicle, most of the kinetic energy is converted into thermal energy due to the friction effect, and generated heat is dissipated in the surrounding environment. Therefore, one of the fundamental problems of a braking system is how to handle the thermal energy generated throughout its movement. A large of the produced heat flows out to the air, even if the heat dissipation mechanisms are different

(conduction, convection, and radiation). As a result, heat is dissipated by convection (Saiz *et al*, 2015).

A large amount of heat produced in the disc-pad couple contact area during braking creates unequal temperature distributions on the disc, and the disc-pad pair temperature rises as a result of the heating of the brake pair during mutual slip. (Belhocine and Bouchetara, 2012). A vehicle's braking performance is importantly influenced by the temperature increase in the disc-pad couple. Increased temperatures during braking may reason brake fade, premature wear, brake fluid vaporization, bearing failure, thermal cracks, and thermally-excited vibration. That is why it is significant to predict a given brake system's temperature rise and assess its thermal performance in the early design stage (Lee, 1999).

Belhocine and Bouchetara (2012) have stated that the study aims to analyze the thermal behaviour of full and ventilated brake discs by utilizing parameters such as brake type, disc geometric design, and disc material. They have noticed for a ventilated disc out of cast iron FG15, the temperature rises to 345.44 °C in 1.85 s, behind it drops quickly. They have found out that the variation in temperature between a full and ventilated disc having the same material is about 60 °C at the moment  $t = 1.8839$  s. They have concluded that the disc's geometric design is an essential factor in the improvement of the cooling process of the discs. Kishore and Vineesh (2021) have used the axle-mounted disc brake system used in the coaches of Indian railways for braking of the train in their study. In their work, temperature evolution during the braking process has been analyzed with the finite element method. The maximum peak temperature increase of 215 °C is observed on the disc at 290 mm in the radial direction at about 60% of braking time while stop braking from 160 kmph. They indicated that peak temperature at different stop braking speeds states to be linearly rises with stop braking speeds. Abhishek *et al* (2020) carried out the static structural and thermal analysis with various disc materials (Gray Cast Iron, Titanium Ti-6Al-4V and Chromium-Vanadium Steel) using ANSYS. They indicated that the newly designed ventilated brake disc shows a more appropriate temperature gradient than the drilled contour disc regardless of the three metals utilized in this analysis. Chromium-Vanadium steel of these three materials has established a smaller maximum temperature in the ventilated disc, about 216.22 °C. The drilled contour disc with gray cast iron has showed the best temperature gradient, producing a maximum temperature of 320.01 °C compared to the others.

Jihan *et al* (2020) have embedded heat pipes on the surfaces of the ventilated brake disc. The brake bench test

and numerical simulation analysis of heat pipe ventilated brake disc and general ventilated brake disc under the condition of repeated fifteen braking and continuous downhill braking have carried out, respectively. They indicated that the highest temperature has decreased by 7 °C during continuous downhill braking, and better heat transfer effects have achieved through inserting heat pipes on the surfaces of ventilated brake disc under the two braking conditions.

In the literature, the heat transfer coefficient value has been taken constant in most of the thermal studies for the brake disc (Mugilan, 2022; Dubale, 2021; Dhir, 2018; Nathi, 2012). In the thermal analysis carried out in this study, the temperature and total heat flux values have been examined, taking into account the variable heat transfer coefficient depending on the angular velocity values obtained from the tests performed according to the SAE J2522 brake standard (Demir, 2009). The disc design has been designed in SOLIDWORKS, and the steady-state thermal analysis has been carried out in ANSYS 2020 R2.

## MATERIAL AND METHOD

### Analyzed brake disc-pad pair

There are many different types of friction materials in use today. Whatever kind of friction material is chosen, the functional requirements of friction material for road vehicles include properties such as providing a consistent and reliable friction force, being resistant to wear, being robust against mechanically and thermally applied loads during use (Day, 2014). In this study, gray cast iron disc is chosen that meets the friction material properties.

In this study, the front brake disc parameters of a automobile are used, and the design of the disc is made in the SOLIDWORKS program (see Fig. 1). Geometric dimensions and material properties of the disc-pad couple are given in Table 1 (Demir, 2009).

**Table 1.** Geometric dimensions and material properties

Properties	Value
Disc's weight (kg)	5
Disc thickness (mm)	22.05
Pad thickness (mm)	12
Disc diameter (mm)	255
Wheel diameter (mm)	298
Disc's density (kg/m <sup>3</sup> )	7228
Specific heat of the disc (J/kg.K)	419
Conduction coefficient (W/m.K)	48
Pad surface area (mm <sup>2</sup> )	4213

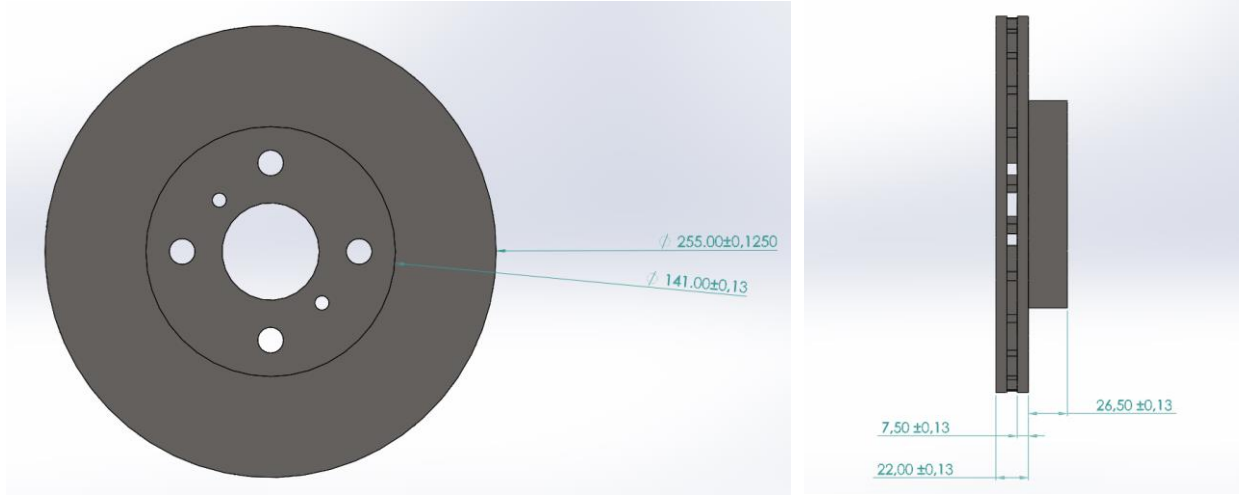


**Figure 1.** Geometric dimensions of the disc

### Braking procedure

SAE Recommended Practice describes an inertia-dynamometer test procedure to evaluate the behavior of friction material related to temperature, pressure, and speed for vehicles appointed with hydraulic brake system. SAE J2522 is a universal effectiveness test handy only when target friction levels for specific sections or a baseline material are available for comparison. Engineers use the SAE J2522 that contains green effectiveness, burnish (or bedding), characteristic check, speed/pressure sensitivity, cold braking check, motorway braking check, fade, recovery, pressure sensitivity, increasing temperature sensitivity, and pressure sensitivity primarily for passenger cars, SUV's, light and medium duty trucks evaluation (Carlos and Ferro, 2005). In this study, the fading procedure of the SAE J2522 brake test standard has been selected for the passenger car front brake disc analysis. The initial condition values received from the experiment made according to the SAE J2522 brake standard are given in Table 2.

**Table 2.** Braking conditions

Conditions	Value
Braking velocity (km/h)	100
Release velocity (km/h)	5
Friction coefficient	0.412
Brake application control	0.4g
Initial brake temperature (°C)	100-550
Braking time (s)	7.439
Number of decelerations	15

### Finite Element Method

The heat transfer radiation is neglected and material properties are assumed to be isotropic and independent of temperature while performing thermal analysis with FEM.

In this article, it requires understanding the equations utilized inside the ANSYS where steady-state thermal analysis is done for the braking. The differential equation in a cylindrical coordinate system (r, z) for steady state is (Lewis *et al*, 2004);

$$k_r \frac{\partial^2 T}{\partial r^2} + \frac{k_r}{r} \frac{\partial T}{\partial r} + k_z \frac{\partial^2 T}{\partial z^2} + G = 0 \quad (1)$$

The boundary conditions are;

$$T = T_b \quad \text{on } T_1$$

$$k_r \frac{\partial T}{\partial r} + k_z \frac{\partial T}{\partial z} n + h(T - T_a) + q = 0 \quad \text{on } T_2 \quad (2)$$

The temperature distribution is described as follows:

$$T = \frac{1}{2A} (a_i + b_i r + c_i z) T_i + \frac{1}{2A} (a_j + b_j r + c_j z) T_j + \frac{1}{2A} (a_k + b_k r + c_k z) T_k \quad (3)$$

Matrix form of heat transfer problem for steady state;

$$[K][T] = \{f\} \quad (4)$$

$$[K] = \int_{\Omega} [B]^T [D] [B] d\Omega + \int h [N]^T [N] dT \quad (5)$$

$$[B] = \left\{ \frac{\partial T}{\partial y} \right\} = \begin{bmatrix} \frac{\partial N_i}{\partial r} & \frac{\partial N_j}{\partial r} & \frac{\partial N_k}{\partial r} \\ \frac{\partial N_i}{\partial z} & \frac{\partial N_j}{\partial z} & \frac{\partial N_k}{\partial z} \end{bmatrix} \quad (6)$$

$$[D] = \begin{bmatrix} k_r & 0 \\ 0 & k_z \end{bmatrix} \quad (7)$$

Thermal stiffness matrix is;



$$[K] = \frac{2\pi\bar{r}k_r}{4A} \begin{bmatrix} b_i^2 & b_i b_j & b_i b_k \\ b_i b_j & b_j^2 & b_j b_k \\ b_i b_k & b_j b_k & b_k^2 \end{bmatrix} + \frac{2\pi\bar{r}k_z}{4A} \begin{bmatrix} c_i^2 & c_i c_j & c_i c_k \\ c_i c_j & c_j^2 & c_j c_k \\ c_i c_k & c_j c_k & c_k^2 \end{bmatrix} + \frac{2\pi h l_{ij}}{12} \begin{bmatrix} 3r_i + r_j & r_i + r_j & 0 \\ r_i + r_j & r_i + 3r_j & 0 \\ 0 & 0 & 0 \end{bmatrix} \quad (8)$$

Load vector is;

$$\{f\} = \int_{\Omega} G[N]^T d\Omega - \int_T q[N]^T dT + \int_T h T_a [N]^T dT$$

$$= \frac{2\pi GA}{12} \cdot \begin{bmatrix} 2 & 1 & 1 \\ 1 & 2 & 1 \\ 1 & 1 & 2 \end{bmatrix} \cdot \begin{bmatrix} r_i \\ r_j \\ r_k \end{bmatrix} - \frac{2\pi q l_{jk}}{6} \begin{bmatrix} 0 \\ 2r_j + r_k \\ r_j + 2r_k \end{bmatrix} + \frac{2\pi h T_a l_{ij}}{6} \begin{bmatrix} 2r_i + r_j \\ r_i + 2r_j \\ 0 \end{bmatrix} \quad (9)$$

To see the temperature values of brake disc has made steady-state thermal analysis utilizing the finite element method. Here, the temperature and convection surfaces are chosen as in Fig. 2. The disc-pad couple is meshed consisting of 27704 nodes and 13952 elements. In the model, skewness is 0.46371, and orthogonal quality is 0.53403. These values approve the high mesh quality in this study (ANSYS, 2015).

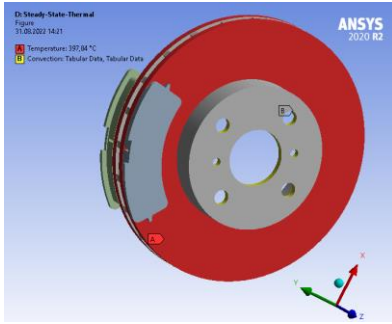


Fig. 2 Boundary conditions of steady-state thermal analysis

### Heat transfer coefficient

All properties of air such as temperature, density, viscosity, and thermal conductivity play a significant role in calculating the heat transfer coefficient. Considering that all these properties of air can be determined, it can be thought that the heat transfer coefficient for the brake disc will take a fixed value. However, due to the rotation of the disc around its axis at different speeds during braking, the ambient air and the angular velocity value of the brake disc affect each other. This situation makes it possible to determine the heat transfer coefficient values in return to varying angular velocity values during

braking. First of all, the values corresponding to the temperature of air (295.15 K) in the ambient condition should be determined by the interpolation method (Çengel and Ghajar, 2015). With the values ( $\rho_{air} = 1.2002 \text{ kg/m}^3$ ,  $\mu_{air} = 1.82 \cdot 10^{-5} \text{ kg/m.s}$ ) obtained for 295.15 K, the disc's outer diameter ( $d_o = 0.256 \text{ m}$ ) and the tire diameter ( $R = 0.596 \text{ m}$ ) is positioned in the formula, and the Re number depending on the angular velocity is obtained as  $10061.63 \cdot w$  by using Equation (10).

$$Re = \frac{wR\rho_a d_o}{\mu_a} = 10061.63 \cdot w \quad (10)$$

The heat transfer coefficient formula changing as dependent on airflow characteristic has been given in Equation (11) (Limpert, 2001). (Laminar flow if  $Re \leq 2.4 \cdot 10^5$ , turbulent flow if  $Re > 2.4 \cdot 10^5$ )

$$h = \begin{cases} 0.7 \left(\frac{k_a}{D}\right) \cdot Re^{0.55}, & Re \leq 2.4 \cdot 10^5 \\ 0.4 \left(\frac{k_a}{D}\right) \cdot Re^{0.8}, & Re > 2.4 \cdot 10^5 \end{cases} \quad (11)$$

The Re number ( $10061.63 \cdot w$ ), the thermal conductivity ( $k_{air} = 0.02585 \text{ W/m.K}$ ), and the disc's outer diameter ( $D = 0.256 \text{ m}$ ) is written in Equation (11). Equation (12) has been obtained by leaving the angular velocity alone in the section on the right side of the equation. If the value of angular velocity is less than or equal to 23.85, the upper part of Equation (12) is used; if it is large, the lower part is used. In this way, different heat transfer coefficient values are obtained different time of the braking procedure alternating angular velocities.

$$h = \begin{cases} 11.24 \cdot w^{0.55}, & w \leq 23.85 \\ 6.43 \cdot w^{0.8}, & w > 23.85 \end{cases} \quad (12)$$

### Braking Analysis

One of the most important parameters affecting the rising temperatures during braking is the convection in the regions where the disc comes into contact with air. Because very high temperatures are undesirable for the disc and pad couple, the transfer of heat to air via convection, in other words, the cooling of the disc, is an issue that needs to be examined. In this study, while the heat convection coefficient values were defined in the ANSYS program, a function was created with the angular velocity values obtained from the tests performed according to the SAE J2522 standard. In this function, heat convection coefficient data was obtained for each angular velocity value, and 1000 data sets were created by defining the steps in the program. Graphs consisting of 1000 data of temperature and heat transfer coefficient for braking in the temperature ranges of 284-417 °C, 397-507 °C, 421-526 °C, and 496-584 °C are shown in Fig. 3, respectively.

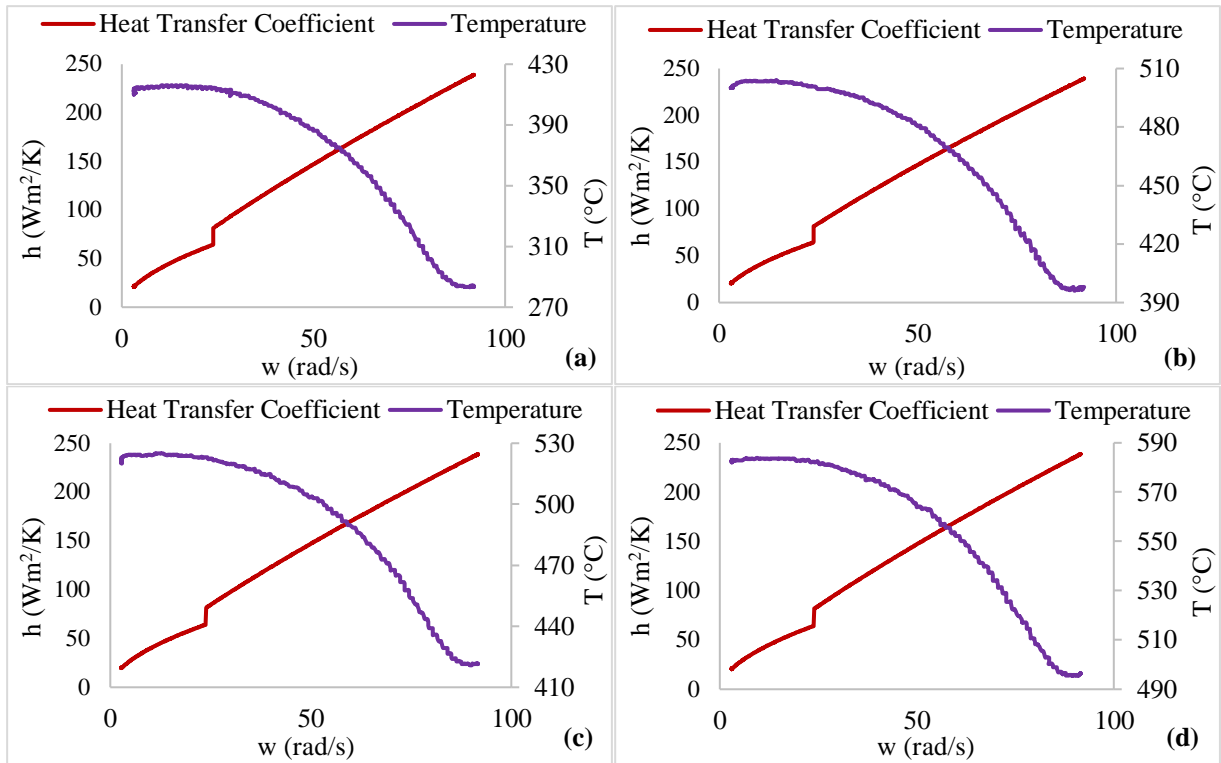


**Figure 3.** Change of temperature and heat transfer coefficient, 284-417 °C (a), 397-507 °C (b), 421-526 °C (c), and 496-584 °C (d)

During the braking analysis, while the temperature increased over time, the heat transfer coefficient values decreased due to the decrease in the angular velocity of the disc. There was a sudden decrease in the heat transfer coefficient when the angular velocity was 23.85 rad/s for braking in different temperature ranges. The breakage seen in Fig. 3 shows the transition of the flow from turbulent to laminar, after a particular value of the change in Re number (Laminar flow if  $Re \leq 2.4 \cdot 10^5$ , turbulent flow if  $Re > 2.4 \cdot 10^5$ ) with together decrease in the flow velocity. This study, it has been aimed to see the effect of heat transfer coefficient on temperatures depending on the angular velocity with the data used during thermal analysis.

## RESULTS AND DISCUSSIONS

### Experimental analysis of repeated braking

The graph of the initial and final temperatures of the disc measured as a result of repeated braking in the experimental study made according to the SAE J2522 brake standard is presented in Fig. 4. The test is done at Link Engineering Company. The temperature measurements are carried out with a thermocouple. In the experimental study, the results of repetitive braking have revealed that the temperatures increased at the finish of each braking repetition and 15 braking repetitions.

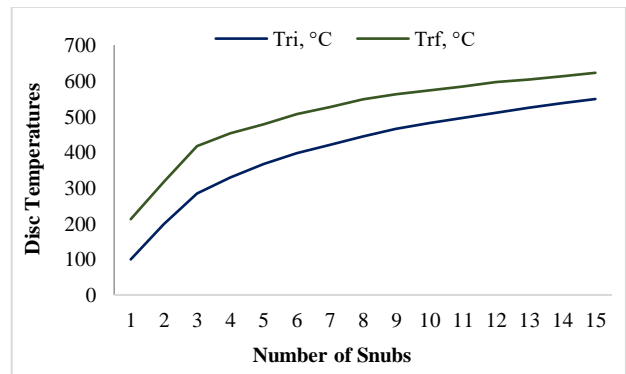


**Figure 4.** Disc's initial and final temperatures in repeated braking

Table 3 has showed that the temperature obtained at the end of a cycle decreased until the next cycle, that is, cooling occurred. However, the cooling that occurs between cycles is insufficient for the disc brake to reach its initial temperature. In the next cycle, the disc has started to heat up again before it can reach the initial temperature. This situation increased the energy accumulated on the disc, and the temperatures increased with the increase in the number of repetitive braking.

**Table 3.** Initial and final temperature values in repeated braking

Stop Number	T <sub>ri</sub> (°C)	T <sub>rf</sub> (°C)
1	100	212
2	198	316
3	284	417
4	329	452
5	367	478
6	397	507
7	421	526
8	444	548
9	465	562
10	482	574
11	496	584
12	511	595
13	525	604
14	537	612
15	549	622

### Steady State Thermal Analysis

Steady-state thermal analysis was carried out for the temperature ranges of 284-417 °C, 397-507 °C, 421-526 °C, and 496-584 °C. Close to each other visual results were obtained for these temperature ranges. It is given Table 4 the maximum and minimum temperature values obtained from thermal analysis for temperature ranges of 284-417 °C, 397-507 °C, 421-526 °C, and 496-584 °C. In the thermal analysis carried out in the temperature range of 284-417 °C, the temperature visuals at 0.008, 5.406, and 7.515<sup>th</sup> seconds, and the total heat flow visual at 7.515<sup>th</sup> second were shown in Fig. 5. Throughout braking analysis, the difference between the maximum and minimum temperature values were 56.46 °C at initial of braking, 33.18 °C in the middle, and 8.86 °C at end. When temperature drops were observed in cold region of the disc where the convection is more effective than in the outer radius of the disc, the maximum temperature value was obtained because friction occurs in the outer radius of the disc. The total heat flux was determined to be a minimum of 8.6727e-16 W/mm<sup>2</sup> and a maximum of 0.017641 W/mm<sup>2</sup>.

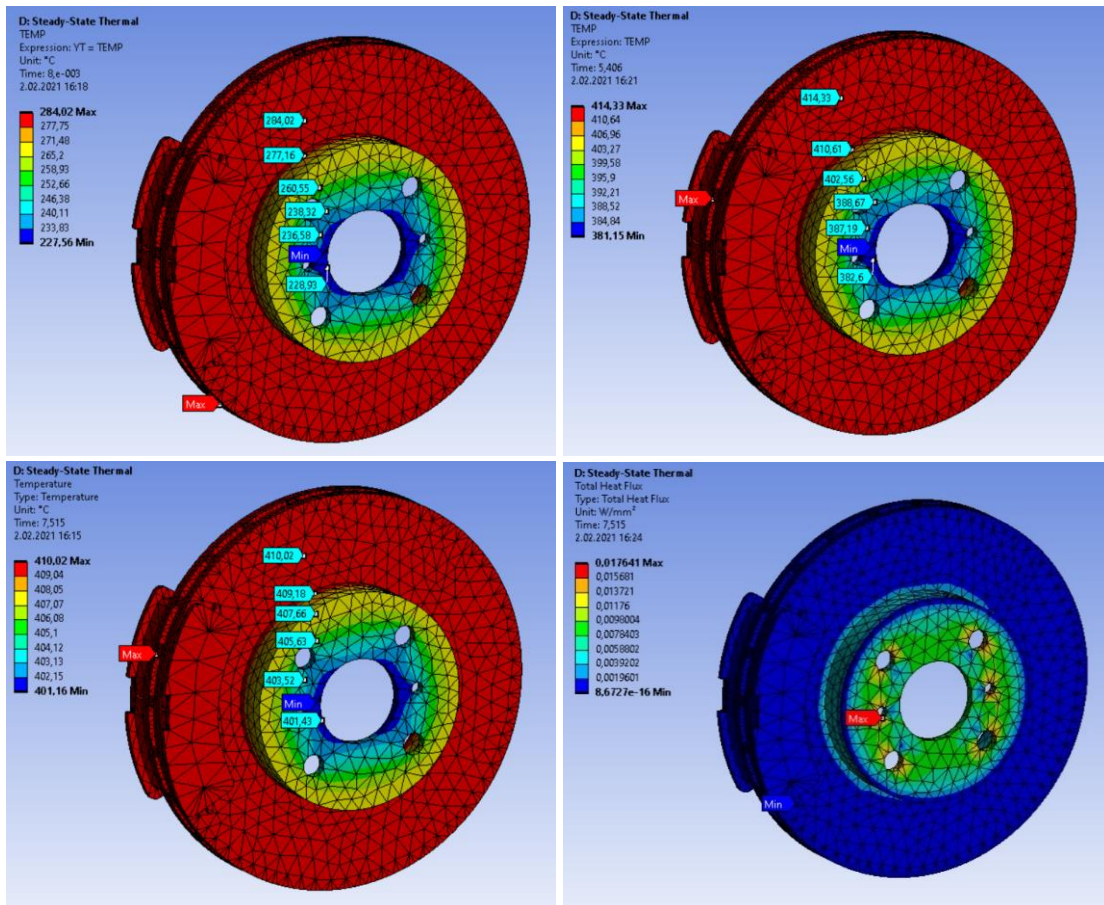


**Figure 5.** Temperature and total heat flux in thermal analysis in the temperature range of 284-417 °C

**Table 4.** The maximum and minimum temperature values

Temperature range (°C)	Initial of braking		5.406 <sup>th</sup> second of braking		End of braking	
	T <sub>max</sub> (°C)	T <sub>min</sub> (°C)	T <sub>max</sub> (°C)	T <sub>min</sub> (°C)	T <sub>max</sub> (°C)	T <sub>min</sub> (°C)
284-417	284.02	227.56	414.33	381.15	410.02	401.16
397-507	397.84	316.83	500.74	460.09	500.19	489.44
421-526	421.46	335.47	522.39	479.12	520.08	509.39
496-584	496.35	394.25	581.84	533.24	581.98	569.56

When the total heat flux visual was examined, the heat flux values were higher at the centre of the disc, while the minimum values were obtained in the outer radius of the disc. This situation demonstrated that the heat generated during braking moved away faster than the centre of the disc than the outer radius of the disc.

#### Experimental data and analysis data

Brake disc cooling is a complex phenomenon governed by conduction, convection, and radiation. Convection, one of these modes, is the most important mechanism of spreading heat from the brake disc while the vehicle is in motion. When the disc temperature rises above air temperature, energy (heat) transfer occurs towards air due to the temperature difference. For the temperature ranges on the brake discs during this process, the number of Prandtl varies very little. Therefore, it can be said that although convection is caused by the temperature difference between the brake disc and air in contact with it, it also depends on the dynamic of the flow near the disc surface. In the dynamic of flow, high velocity flows create large temperature gradients. That is, an upwards amount of heat is transported for high-speed streams than for low-velocity streams. The speed of the flow around the disc is affected by the angular velocity of the disc. This situation is reflected in the heat convection coefficient and affects the cooling amounts in the disc. When the vehicle starts braking from a certain speed, the decrease in angular velocity decreases the heat transfer coefficient. Low heat transfer coefficient values correspond to a lower level of energy transferred, especially for a disc. All of these have reflected in the temperature data obtained as a result of the analysis.

Experimental data and analysis data in the study conducted for the disc-pad pair are given in Fig. 6, temperature ranges of 284-417 °C, 397-507 °C, 421-526 °C, and 496-584 °C. It is determined that the amount of temperature drop at the beginning of braking is higher than the amount of temperature drop at the end of braking. This is explained by the fact that the heat transfer coefficient values are a function of the angular velocity. Because the heat convection coefficient value decreases as the angular velocity value decreases, compared to the beginning of braking decreases at the end of braking, the effect of convection on cooling.

When the experimental data and analysis data were compared for the temperature range of 284-417 °C, it was found that there was a difference of 3.25 °C at the initial of braking and 0.5 °C at the end of braking. Table 5 presents all of the differences between experimental and analysis data at the initial and the end of braking for the four temperature ranges.

At end of braking, it has been determined that in the decrease in temperature difference compared to the initial state, the convective effect is decreased at the rate of 91.22%. At the 5.406<sup>th</sup> second of braking, in the decrease in temperature difference compared to the initial state, the convection effect is decreased at the rate of 65.67%. At the 5.406<sup>th</sup> second of the braking, in the decrease in temperature difference compared to end of braking, the convection effect is decreased at the rate of 74.43%. Convective effect decrease rates in temperature difference drop are given in Table 6, comparatively for all temperature ranges.

**Table 5.** Difference between experimental and analysis temperatures

Temperature range (°C)	Initial of braking (°C)	End of braking (°C)
284-417	3.25	0.5
397-507	4.66	0.614
421-526	4.96	0.61
496-584	5.88	0.70

**Table 6.** Convective effect decrease rates in temperature difference drop

Temperature range (°C)	According to the initial of braking at the end of braking (%)	According to the initial of braking at 5.406 <sup>th</sup> second of braking (%)	According to the 5.406 <sup>th</sup> second of braking at the end of braking (%)
284-417	91.22	65.67	74.43
397-507	91.34	64.72	74.46
421-526	91.74	64.75	76.57
496-584	91.46	64.61	75.88

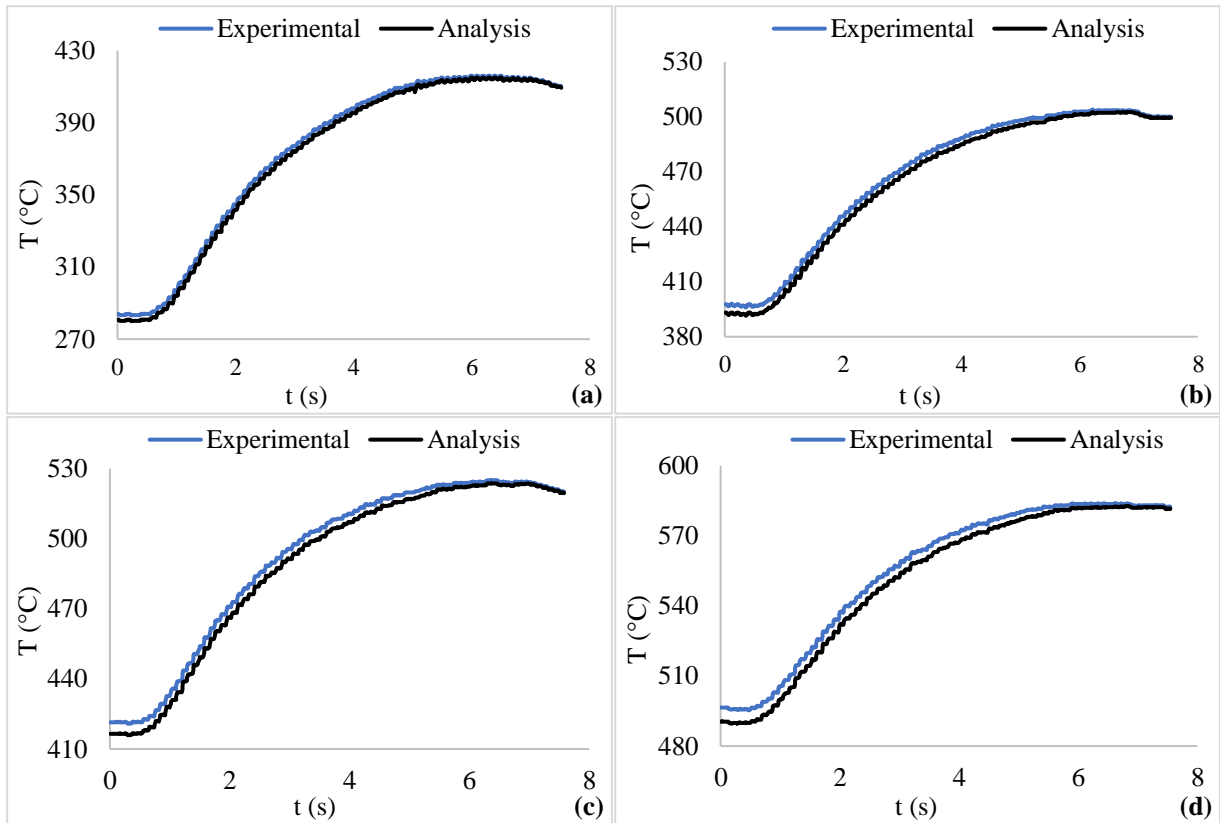


**Figure 6.** Experimental data and analysis data, 284-417 °C (a), 397-507 °C (b), 421-526 °C (c), and 496-584 °C (d)

## CONCLUSION

In the heat convection coefficient-angular velocity graphs, the break that occurred at a value of 23.85 rad/s showed that the flow passed from turbulent to laminar after a certain value of the Re number with the decrease in the velocity of the flow.

Since cold region of the disc is not exposed to friction, minimum temperature values have been observed. In the outer radius of the disc where friction occurred, the temperature has reached the maximum value.

In summary, it has been concluded that the impact of cooling by convection in the decline of the temperature difference at the end of braking compared to the initial state is between 91.22% and 91.74%.

It has been deduced that the cooling amounts at the initial of braking are higher than the cooling amounts at end of braking. This situation is explained by the fact that the heat transfer coefficient values are a function of the angular velocity.

While the total heat flux values reached their maximum in cold region of the disc, minimum values were obtained in the outer radius of the disc.

It has determined that the disc temperature increased as the number of repetitions increased because the disc's temperature could not return to its initial state with the cooling occurring between cycles in repeated braking.

## ACKNOWLEDGMENT

This article is derived from the MS thesis titled "*Investigation of The Effect of Disc-Pad Pair Temperature Distribution on Braking*" prepared by Cansu AY GÖKÇE under the advisor of Assistant Professor Abdullah DEMİR.

## REFERENCES

- Abhishek, C.B.N.S., Ramachandran, B. and Alekhya, G.N., 2020, Design and analysis of disc rotor brake under tribological behaviour of materials, *Materials Today: Proceedings* 33, 4298-4310.
- ANSYS, Mesh quality & advanced topics, 2015, ISO 9001:2008  
[https://www.academia.edu/16970000/MESH\\_QUALITY\\_AND\\_ADVANCED\\_TOPICS\\_ANSYS\\_WORKBENCH\\_16\\_0](https://www.academia.edu/16970000/MESH_QUALITY_AND_ADVANCED_TOPICS_ANSYS_WORKBENCH_16_0)
- Belhocine, A. and Bouchetara, M., 2012, Thermal Analysis of a Solid Brake Disc, *Applied Thermal Engineering*, 32, 59-67.
- Carlos, E.A. and Ferro, E., 2005, Technical overview of brake performance testing for original equipment and aftermarket industries in the US and European markets, *Link Technical Report FEV 2005-01*, 15-16.

Çengel, Y.A. and Ghajar, A.J., 2015, Heat and Mass Transfer. Fifth edition, McGraw-Hill Education, ISBN 978-0-07-339818-1, New York.

Day, A., 2014, Braking of Road Vehicles, ISBN: 978-0-12-397314-6, Elsevier, Oxford.

Demir, A., 2009, An Experimental Investigation on the Braking Performance of Coated Brake Discs. *Doctoral Thesis*, Kocaeli University, Institute of Pure and Applied Sciences, Kocaeli, Turkey.

Dhir, K.D., 2018, Thermo-mechanical Performance of Automotive Disc Brakes, *Materials Today: Proceedings*, 5(1), 1864-1871.

Dubale, H., Paramasivam, V., Gardie, E., Chekol, E.T., and Selvaraj, S.K., 2021, Numerical investigation of thermo-mechanical properties for disc brake using light commercial vehicle, *Materials Today: Proceedings*, 46, 7548-7555.

Jihan, Q., Wang, L. and Shui, Y., 2020, Thermal analysis of ventilated brake disc based on heat transfer enhancement of heat pipe, *International Journal of Thermal Sciences* 155, 106356.

Kishore, V.S.N., and Vineesh, K.P., 2021, Temperature evolution in disc brakes during braking of train using finite element analysis, *Materials Today: Proceedings* 41, 1078-1081.

Lee, K., 1999, Numerical Prediction of Brake Fluid Temperature Rise During Braking and Heat Soaking. *SAE Technical Paper Series*, 1999-01-0483.

Lewis, R.W., Nithiarasu, P. and Seetharamu, K.N., 2004, Fundamentals of the Finite Element Method for Heat and Fluid Flow. *John Wiley & Sons Ltd*, ISBN 0-470-84788-3, England.

Limpert, R., 2001, Brake Design and Safety. Third Edition, *Society of Automotive Engineers*, Warrendale.  
Mugilan, M., Devendra, K.S., Danish, M., and Prabu, S.S., 2022, Investigation on thermal analysis of disc brake using Autodesk Fusion 360, *Materials Today: Proceedings*, 65, 3707–3713.

Nathi, G.M., Charyulu, T.N., Gowtham, K., and Reddy, P.S., 2012, Coupled structural / thermal analysis of disc brake, *International Journal of Research in Engineering and Technology*, 1(4), 539-553.

Saiz, C.B., Ingrassia, T., Nigrelli, V., and Ricotta, V., 2015, Thermal stress analysis of different full and ventilated disc brakes, *Frattura ed Integrità Strutturale*, 34, 608-621.



## DİFÜZYON ABSORPSİYONLU SOĞUTMA SİSTEMİNDE CuO VE TiO<sub>2</sub> NANO PARTİKÜLLERİNİN ENERJİ VE EKSERJİ PERFORMANSINA ETKİSİ

Abdullah YILDIZ\*, Sinan SUNAL\*\*

Uşak Üniversitesi Mühendislik Fakültesi Makine Mühendisliği Bölümü, Uşak

\* [abdullah.yildiz@usak.edu.tr](mailto:abdullah.yildiz@usak.edu.tr), ORCID: 0000-0003-4831-0975

\*\* [sinan.sunal@gmail.com](mailto:sinan.sunal@gmail.com)

(Geliş Tarihi: 08.03.2022, Kabul Tarihi: 14.03.2023)

**Özet:** Difüzyon Absorpsiyonlu Soğutma (DAR) sisteminde performans artırmanın etkin yollarından biriside nano partikül kullanımıdır. Bu çalışmada, çalışma akışkanı olarak amonyak-su-helyum kullanan bir DAR sistemine ağırlıkça % 0,68 eklenen CuO ve TiO<sub>2</sub> nano partikülünün sistemin her bir ekipmanında meydana gelen enerji kaybı ve ekserji yıkımına, enerji ve ekserji performanslarına etkisi deneysel olarak araştırılmıştır. TiO<sub>2</sub> nano partikülünün sistemin çalışma basıncını düşürdüğü, CuO nano partikülünün sistem çalışma basıncında herhangi bir etki yaratmadığı gözlemlenmiştir. TiO<sub>2</sub> ve CuO nano partikülleri soğutma kapasitesini artırmıştır. TiO<sub>2</sub> ve CuO nano partikülü enerji performansını sırasıyla % 66,75 ve % 13,32 artırırken ekserji performansını sırasıyla %17,53 ve %3,42 azaltmıştır.

**Anahtar Kelimeler:** Difüzyon Absorpsiyonlu Soğutma, CuO, TiO<sub>2</sub>, performans, enerji, ekserji

### THE EFFECT OF CuO AND TiO<sub>2</sub> NANO PARTICLES ON ENERGY AND EXERGY PERFORMANCE IN DIFFUSION ABSORPTION REFRIGERATION SYSTEM

**Abstract:** One of the effective ways to increase performance in Diffusion Absorption Refrigeration (DAR) system is the use of nanoparticles. In this study, the effect of CuO and TiO<sub>2</sub> nanoparticles added 0.68 wt% to a DAR system using ammonia-water-helium as the working fluid on the energy loss and exergy destruction occurring in each equipment of the system, energy and exergy efficiencies was experimentally investigated. It has been observed that the TiO<sub>2</sub> nanoparticle reduces the operating pressure of the system, while the CuO nanoparticle does not have any effect on the system operating pressure. TiO<sub>2</sub> and CuO nanoparticles increased the cooling capacity. While TiO<sub>2</sub> and CuO nanoparticles increased the energy performance by 66.75% and 13.32%, respectively, they decreased the exergy performance by 17.53% and 3.42%, respectively.

**Keywords:** Diffusion Absorption Refrigeration, CuO, TiO<sub>2</sub>, performance, energy, exergy

#### SEMBOLLER

COP	enerji performans katsayısı	$\dot{Q}$	ısı transfer hızı [W]
$C_p$	özgül ısı [ $\text{Jkg}^{-1}\text{K}^{-1}$ ]	$s$	özgül entropi (J kg-1 K-1)
DAR	difüzyon absorpsiyon soğutma	$\dot{S}$	entropi [W]
$\dot{I}$	tersinmezlik [W]	$T$	sıcaklık [ $^{\circ}\text{C}$ , K]
$\dot{E}_x$	ekserji hızı [W]	$X$	çözeltideki amonyak kütle oranı
ExCOP	ekserji performans katsayısı	$\dot{W}$	elektrik tüketimi [W]
$h$	entalpi [ $\text{Jkg}^{-1}$ ]	$\rho$	yoğunluk [ $\text{kgm}^{-3}$ ]
$k$	ısı iletim katsayısı [ $\text{Wm}^{-1}\text{K}^{-1}$ ]	$\Psi$	akış ekserjisi (kullanılabilirlik) [ $\text{Jkg}^{-1}$ ]
$\dot{m}$	kütleli debi [ $\text{kgs}^{-1}$ ]	$\mu$	dinamik viskozite [ $\text{kgm}^{-1}\text{s}^{-1}$ ]
$P$	basıncı [bar]		

#### Alt indis

1a,2,3,..	sistemin tanımlı noktası	mass	kütle
bf	baz akışkan	nf	nano akışkan
buh	buharlaştırıcı	np	nano partikül
dest	yıkım	o	tanımlı ölü hal
elect	elektrik	out	çıkış
gen	üretim	ps	zengin çözelti
heat	ısı	rs	zayıf çözelti
ısıd	ısı değiştirici	saf	saflaştırıcı
ig	yardımcı gaz	soğ	soğurucu
in	giriş	yoğ	yoğurturucu

## GİRİŞ

Difüzyon Absorpsiyonlu Soğutma (DAR) sisteminin kullanılması çok eski yıllara uzanmaktadır. Elektrikli nadir kullanıldığı zamanlarda buzdolaplarında soğutma sistemi olarak ısı güç ile çalışan bu sistemler kullanılmıştır. Sonraki dönemlerde elektrik enerjisinin daha sık kullanılması ile birlikte bu sistem yerini kompresörlü soğutma sistemine bırakmıştır. Absorpsiyonlu soğutma sistemlerinde en sık kullanılan çalışma akışkanı LiBr-H<sub>2</sub>O ve NH<sub>3</sub>-H<sub>2</sub>O çözeltilisidir. DAR sistemlerinde kullanılan akışkanların çevreye herhangi bir zarar vermemesi, sistemde elektrik, yenilenebilir enerji, LPG ve doğalgaz gibi farklı enerji kaynaklarının kullanılması bu sistemin yaygınlaşmasında önemli bir rol oynamıştır. Ayrıca sessiz çalışma ortamı sağlaması ve parçaların hareketli olmaması bakım maliyeti ve sürecini olumlu yönde etkilemiş dolayısıyla bu soğutma sisteminin önemini arttırmıştır (Sunal, 2019).

Literatürde, DAR sistemlerinin enerji analizi üzerine birçok çalışma mevcuttur. Arslan ve Eğrican (2004) çalışma akışkanı olarak amonyak-su-helyum kullanan DAR sisteminin farklı ısı girdileri için (60 W, 70 W ve 80 W) enerji analizini yapmıştır. Sistem performansını 60 W, 70 W ve 80 W için sırasıyla 0,2338, 0,2364 ve 0,2254 olarak hesaplamışlardır. Özbaş (2009) çalışma akışkanı olarak amonyak-su-helyum kullanan DAR sistemini deneysel ve teorik olarak incelemiştir. Sistem performansını arttırmak amacıyla iki farklı tasarım geliştirmiştir. Ön soğutmalı sistemde yapısal değişiklik yaparak ön soğutmasız sistem (DAR2) ve ön soğutmalı sistemin absorber girişine yerleştirilen bir ejektörün kullanıldığı sistemlerin (DAR3) tasarımlarını ve imalatlarını yapmıştır. Elektrik enerjisi ile yapılan deneylerde iç ortam sıcaklığı olarak 3°C ile en iyi sonucu DAR3 sisteminde ulaşırlken, dolaşım oranının yüksek olmasından dolayı en iyi COP değeri DAR2 sisteminde % 27 olarak elde edilmiştir. Ayrıca ejektör kullanımı ile ön soğutmalı sistemin performansının % 26 arttığı gözlemlenmiştir. Chen vd. (1996) ısı değiştiricili yeni bir jeneratöre sahip DAR sistemi tasarlamış ve üretmiştir. Bu sistemin test sonuçlarını orijinal jeneratör tasarımına sahip DAR sistemi ile karşılaştırmıştır. Yeni tasarımın, COP değerini % 50 arttırdığı sonucuna ulaşmıştır. Srihkirin ve Aphornratana (2002) kabarcık pompası performansı için hava ve su kullanan basit bir deneyden elde sonuçları matematiksel modelden elde edilen sonuçlarla karşılaştırmışlardır. Sistem performansının kabarcık pompası özelliklerine ve evaporatör ve absorber kütle transfer performansına güçlü bir şekilde bağlı olduğunu ortaya koymuşlardır. Koyfman vd. (2003) çalışma akışkanı olarak organik çözücü ve hidroklorofloro karbon soğutucu akışkan çözeltisi kullanan DAR sistemindeki kabarcık pompasının performansını deneysel olarak araştırmıştır. Kabarcık pompasının performansının ısı girişine bağlı olarak değiştiğini gözlemiştir. Zohar vd. (2005) Electrolux Sweden tarafından üretilen yardımcı gaz olarak hidrojen

ve helyum kullanan amonyak-su çalışma akışkanlı DAR sistemi için termodinamik bir model geliştirmişler ve sistemin performansını bilgisayar simülasyonu ile parametrik olarak incelemişlerdir. Sistemin her bir ekipmanı için kütle ve enerji korunum denklemleri oluşturularak sayısal olarak çözmüşlerdir. Modeli, DAR sistemleri için daha önce yayınlanan deneysel verilerle karşılaştırılarak doğrulamışlardır. Farklı koşullar altında en iyi performansı, zengin çözelti için 0,2-0,3 ve zayıf çözelti için 0,1 amonyak kütle derişiminde elde etmişlerdir. Yardımcı gaz olarak helyum kullanan DAR sisteminin performans katsayısının hidrojen kullanan sistemden yaklaşık % 40 daha fazla olduğunu ortaya koymuşlardır. Zohar vd. (2007) yardımcı gaz olarak hidrojen kullanan amonyak-su çalışma akışkanlı DAR sistemi için termodinamik bir modele dayanarak, buharlaştırıcı girişinden önce yoğunlaşma alt soğutması olan ve olmayan, iki DAR sisteminin performansını karşılaştırmışlardır. İki çevrimin performansını bilgisayar simülasyonları ile parametrik olarak araştırmışlardır. Yoğuşma alt soğutmasız DAR sisteminin COP değerinin yoğunlaşma alt soğutmalı sisteme göre % 14-20 daha yüksek olduğunu bulmuşlardır. Zohar vd. (2008) birinci tasarımda; zayıf çözeltiye ısı aktarımı olmadan zengin çözeltiye ısı girişi, ikinci tasarımda; halka şeklindeki zayıf çözeltiye ısı transferi ile zengin çözeltiye ısı girişi ve üçüncü tasarımda ticari sistemlerde kullanılan bir konfigürasyon olan zayıf çözelti yoluyla zengin çözeltiye ısı girişi olan jeneratör ve kabarcık pompası tasarımlarında farklılık gösteren üç DAR sisteminin performansını sayısal olarak incelemişlerdir. Aynı ısı girişi için, ikinci tasarımın en yüksek seviyede ve birinci tasarımın en düşük seviyede soğutucu akışkanı ayırtırdığını tespit etmişlerdir. Üçüncü tasarımın, COP açısından ikinci tasarıma nazaran daha düşük performansla sahip olduğunu ortaya koymuşlardır. Birinci tasarımın, ısının doğrudan zengin çözeltiye verilmesine rağmen en düşük performansla sahip olduğunu ifade etmişlerdir. Jakob vd. (2008) enerji kaynağı olarak güneş enerjisi kullanan amonyak-su çalışma akışkanlı DAR sisteminin deneysel ve simülasyon sonuçlarını karşılaştırmıştır. Maksimum COP değerini 0,38 olarak bulmuşlar ve simülasyon sonuçlarının deney sonuçları ile uyumlu olduğunu ortaya koymuşlardır. Zohar vd. (2009) beş farklı soğutucu akışkan (R22, R32, R124, R125 ve R134a) ve organik soğurucu (DMAC - dimetilasetamid) sistemin enerji performansını, yardımcı gaz olarak helyum kullanan amonyak-su çalışma akışkanlı DAR sisteminin performansı ile sayısal olarak karşılaştırmışlardır. En yüksek performansı 0,298 olarak amonyak-su çalışma akışkanlı sistemde elde ederken en düşük performansı 0,136 olarak R32 çalışma akışkanlı sistemde hesaplamışlardır. Wang vd. (2011) ikili soğutucu R23-R134a, soğurucu olarak N,N-dimethylformamide (DMF) ve yardımcı gaz olarak helyum ile çalışan bir DAR sisteminin COP değerini teorik olarak araştırmışlardır. Teorik analizde, ısıtıcı gücü, kaynak sıcaklığı, çevre sıcaklığı, sistem basıncı, zengin çözelti derişim oranı, saflaştırıcının saflaştırma etkinliği ve soğutucuya katılan



helyum oranının performansa etkini incelemişlerdir. Sözen vd. (2012) DAR performans iyileştirmesi üzerine deneysel bir çalışma yapmışlardır. Deneysel, endüstride en yaygın kullanılan model olan ön soğutmalı sistem (DAR-1), ön soğutmasız sistem (DAR-2) ve DAR-1'den farklı olarak, DAR-1'in soğurucu girişine bir ejektörün yerleştirildiği sistem (DAR-1WE) olmak üzere üç DAR çevrimini incelemişlerdir. DAR-1WE çevriminin en yüksek performansa sahip olduğunu ve soğutma ortam sıcaklığını 3,2 °C'ye düşürdüğünü belirlemişlerdir. Başka bir deyişle, DAR-1WE sisteminin önceden belirlenmiş soğutma ortam sıcaklığına en az sürede ulaştığını ortaya koymuşlardır. Starace ve Pascalis (2012) DAR performansı için saflaştırıcı çıkışında saf amonyak kabulünün yapılmadığı yeni termodinamik modelin sonuçlarını Zohar vd. (2009) teorik sonuçları ile karşılaştırmışlardır. İki modelin tahminleri arasındaki farkın % 2 ile % 8,5 arasında değiştiğini ve bu farkın amonyak içeriğine ilişkin varsayımdaki ana farktan kaynaklandığı belirtmişlerdir. Starace ve Pascalis (2013) soğutma sistemleri tasarımı için yeni bir analitik model iyileştirmesi yapmıştır. % 70,1 H<sub>2</sub>O, % 27,9 NH<sub>3</sub> ve % 2.0 Na<sub>2</sub>CrO<sub>4</sub> karışımı ile doldurulmuş ve 11,5 bar helyum ile basınçlandırmış sisteminin analitik modelini, farklı ısıtıcı güçleri için deneylerle karşılaştırmıştır. Ölçüm ve modelden hesaplanan kütleli debileri karşılaştırmış ve zayıf karışım kütleli debisi ve COP açısından hataları tahmin etmiştir. Zayıf karışım sıcaklığında 1 K, zayıf karışım kütleli debisinde % 2,32 ve COP değerinde maksimum %5 mutlak hata bulmuş ve modelin doğruluğunu ortaya koymuştur. Mazouz vd. (2014) ticari bir DAR sisteminin soğutma kapasitesini değerlendirmek için kararlı hal ve dinamik olmak üzere iki alternatif deney yöntemini deneysel olarak karşılaştırmıştır. 42 W ısıtıcı gücü ve 185 °C jeneratör sıcaklığı için COP değerini 0,12 olarak hesaplamıştır. Ersöz (2015) jeneratöre sağlanan üç farklı ısı girişinin (62, 80 ve 115 W) DAR sisteminin enerji performansına etkisini deneysel olarak araştırmıştır. Saflaştırıcı, kondenser, absorber, çözelti ısı değiştiricisi ve borulardan çevreye olan enerji kayıplarını, evaporatörde kazanılan enerji kazancını ve enerji performansını irdelemiştir. En yüksek COP değerini 0,36 olarak 62 W ısı girişinde elde ederken en düşük COP değerini 0,30 olarak 115 W ısı girişinde elde etmiştir. Wang vd. (2017) düşük jeneratör sıcaklığında düşük soğutma sıcaklığı elde etmek için R23-R134a ve R23-R32-R134a gibi iki grup florür soğutucu çalışma akışkanı kullanan bir DAR sistemi üretmiştir. Soğurucu ve yardımcı gaz olarak DMF ve helyum kullanmıştır. R23-R134a çalışma akışkanlı DAR sisteminde soğutma sıcaklığı, R23 derişiminden veya helyum miktarlarından etkilenmezken R23-R32-R134a çalışma akışkanlı DAR sisteminde optimum bir R32 derişimi ve optimum bir basınç değeri oluşmuştur. Düşük sıcaklıklı soğutma uygulamalarında ve düşük dereceli ısı enerjisinin verimli kullanımında karışık florür soğutucu akışkanlarla çalışan DAR sisteminin umut verici bir potansiyele sahip olduğunu ortaya koymuşlardır. Soli vd. (2017) çalışma akışkanı olarak propilen/heksan, propilen/heptan, propilen/oktan ve propilen/nonan olmak

üzere dört farklı hidrokarbon kullanan DAR sisteminin teorik termodinamik fizibilite çalışmasını yapmışlardır. 150 °C'den düşük (fosil ve güneş enerjisi gibi) jeneratör sıcaklıklarında çalışan düşük güçlü (300 W) bir sistemi modellemişlerdir. Hesaplamalarda, kondenser ve absorber sıcaklıklarını 42 °C ve sistem toplam basıncını 17,5 bar olarak kabul etmişlerdir. Modelin doğruluğunu literatürden elde edilen sonuçlarla karşılaştırarak optimum çalışma koşullarını belirlemişlerdir. Adjidabe vd. (2017) elektrik ve içten yanmalı motorun egzoz gazından elde edilen ısı olmak üzere iki enerji kaynağı için çalışma akışkanı olarak H<sub>2</sub>O-NH<sub>3</sub>-H<sub>2</sub> kullanan bir DAR sisteminin dinamik yöntem kullanan deneysel olarak analiz etmiştir. Her iki enerji kaynağı için, buharlaşma sıcaklığının 3°C ve amonyak kaynatmak için gerekli minimum sıcaklığın 140°C civarında olması gerektiğini belirtmişlerdir. Adjidabe vd. (2017) bir DAR sisteminin performansını MATLAB ve EES yazılımı kullanılarak bilgisayar simülasyonu ile dinamik model geliştirerek sayısal ve deneysel olarak analiz etmişlerdir. Zamana bağlı sayısal sonuçlar, NH<sub>3</sub>-H<sub>2</sub>O-H<sub>2</sub> çalışma akışkanlı 0.04 m<sup>3</sup> ticari bir DAR sisteminden elde edilen deneysel verilerle doğrulanmıştır. Model ve deney sonuçları arasındaki kısmi hata her bir bileşenin tüm sıcaklıkları için % 15'i geçmemiştir ve uyumlu çıkmıştır. Sonuç olarak, buharlaşma sıcaklığının düşmeye başlaması için minimum başlangıç sıcaklığının 152 °C ve gerekli elektrik gücünün 63,8 W olduğunu ortaya koymuşlardır. Jemaa vd. (2017) ticari bir DAR sisteminin deneysel sonuçlarına bağlı analizini yapmışlardır. Sistemin her bir ekipmanının giriş ve çıkış, kabin ve ortam sıcaklıklarını sürekli olarak ölçmüşler ve farklı elektrik girdileri için test etmişlerdir. Kabinin toplam ısı transfer katsayısını hem teorik hem de deneysel yöntemden 0,2 W/°C olarak bulmuşlardır. Buharlaştırıcı toplam ısı transfer katsayısını, dinamik ve kararlı durum yöntemlerini kullanarak 0,3 W/°C olarak hesaplamışlardır. Son olarak, ünitenin soğutma kapasitesi ve COP değerini değerlendirmişlerdir. Bu sistemin istenen durumu sağlamak için gerekli ısıtma gücünün 35 W- 45 W aralığında olması gerektiğini ortaya koymuşlardır. Mansouri vd. (2018) kararlı koşullar altında çalışan düşük kapasiteli ticari DAR sisteminin deney sonuçlarını Aspen-Plus yazılımıyla geliştirilen modelin simülasyon sonuçları ile karşılaştırmıştır. Farklı ısı giriş test koşulları (46 W, 56 W ve 67 W) için DAR sisteminin optimum değerini, 0,159 COP değerine karşılık gelen 167 °C jeneratör sıcaklığında 46 W ısıtıcı gücünde elde etmiştir. Model tahminleri ile soğutma kapasitesi ve COP bakımından deneysel ölçümler arasındaki sapmaların % 1'den az olduğunu ifade etmişlerdir. Chaves vd. (2019) gövde boru buhar jeneratörü ile donatılmış ve amonyak- su-hidrojen çalışma akışkanı kullanan DAR sisteminin matematiksel modelini yapmışlardır. 80 W elektrik gücüne sahip ticari buzdolabı için model sonuçlarını deney sonuçları ile karşılaştırılarak doğrulamışlardır.

DAR sisteminin ekserji analizi üzerine literatürde çok sayıda çalışma bulunmamaktadır. Sözen ve Özalp (2003)

amonyak-su ile çalışan DAR sisteminde, ejektörün genellikle kondenser girişinde bulunduğunu, bu çalışmada, ejektörün soğurucu (absorber) girişine yerleştirilmesi durumunda enerji ve ekserji performansına etkisini araştırmıştır. Bu yeni durumda, enerji ve ekserji performansının sırasıyla % 49 ve % 56 oranında arttığını ve daha düşük jeneratör sıcaklıklarında çalıştığından dolayı dolaşım oranının % 57 azaldığını ortaya koymuşlardır. Düşük dolaşım oranı nedeniyle, sistem boyutlarının azaltılabileceğini ve sonuç olarak toplam maliyetin azalacağını ifade etmişlerdir. Isıtıcı ve soğutma sıcaklıkları sırasıyla 5-15 °C ve 1-3 °C arasında azalmıştır. Enjektörlü DAR sisteminin ekserji kaybının diğer bileşenlerden daha yüksek bir ekserji kaybına sahip olduğunu ve bu nedenle enjektörlü DAR soğurucusunun ekserji kaybını azaltmak için çok bölmeli bir absorber tasarlanabileceğini önermişlerdir. Ziapour ve Tavakoli (2011) amonyak-su-helyum çalışma akışkanlı difüzyon absorpsiyon soğutma ısı borusu (DARHP) çevriminin termodinamik analizi için EES yazılımını kullanarak bir bilgisayar kodu geliştirmişlerdir. DARHP sisteminin her bir ekipmanı için kütle ve enerji korunum denklemlerini ifade etmişler ve ekserji performansını bilgisayar simülasyonu ile parametrik olarak incelemişlerdir. Modeli, DARHP sistemi için önceden yayınlanmış deneysel verilerle karşılaştırılarak doğrulamışlardır. Farklı koşullar altında en iyi performansı, zengin çözelti bakımından 0,35 amonyak kütle derişimi ve zayıf çözelti bakımından 0,1 derişimde elde etmişlerdir. Ayrıca, maksimum ekserji kaybının termosifonda meydana geldiğini, evaporatör, kondenser ve soğurucudaki ekserji kayıplarının kısmen daha az olduğunu ortaya koymuşlardır. Ekserji performansının, artan evaporatör sıcaklığı ile arttığını ve artan termosifon sıcaklığı ile azaldığını ortaya koymuşlardır. Yıldız ve Ersöz (2013a) amonyak-su-helyum çalışma akışkanlı DAR sisteminin enerji ve ekserji analizlerini yapmışlardır. DAR sisteminin her bir ekipmanı için kütle, enerji ve ekserji dengesi içeren termodinamik model oluşturmuş ve bu modeli deney sonuçları ile karşılaştırmışlardır. Termodinamik analizlerde her bir ekipmanda meydana gelen enerji ve ekserji kayıplarını hesaplamışlar ve en yüksek enerji ve ekserji kaybının ısı değiştiricisinde meydana geldiğini ortaya koymuşlardır. Model ve deneysel çalışmalardan COP değerini 0,1858 olarak hesaplarlarken model ve deneysel ekserji performanslarını sırasıyla 0,0260 ve 0,0356 olarak hesaplamışlardır. Yıldız vd. (2014) DAR sistemlerinde yalıtımın enerji ve ekserji performansları üzerindeki etkilerini deneysel olarak araştırmışlardır. DAR sistemindeki çözelti ısı değiştirici ve saflaştırıcının bir kısmının yalıtılması durumunda enerji performansının % 38 ve ekserji performansının % 57 arttığını ortaya koymuşlardır. Yıldız (2016) elektrik ve LPG ile çalışan amonyak-su-helyum çalışma akışkanlı DAR sistemlerinin deneysel olarak enerji, ekserji ve termoeconomik analizlerini yapmıştır. Elektrikle çalışan DAR sisteminin enerji ve ekserji performanslarını sırasıyla 0,393 ve 0,1008, LPG ile çalışan DAR sistemlerinin enerji ve ekserji performans değerlerini sırasıyla 0,432 ve 0,1067 olarak

hesaplamıştır. LPG ve elektrik DAR sistemlerinin ekserjetik maliyetlerini sırasıyla 2,111 \$/h ve 1,284 \$/h olarak belirlemiştir. LPG ile çalışan DAR sisteminin termoeconomik ekserji maliyetinin, elektrikle çalışan DAR sisteminden % 64 daha yüksek olduğunu ortaya koymuştur. Taieb vd. (2016) çalışma akışkanı olarak amonyak-su-hidrojen kullanan, güneş enerjisi ile ısıtılan 200 °C sıcaklıktaki su ile çalıştırılan ve ortam havası ile soğutulan DAR sistemi için geliştirilmiş bir simülasyon model oluşturmuş ve farklı çalışma koşulları altında davranışını incelemiştir. İlk olarak, DAR sistemini 26 °C ortam hava sıcaklığı, 47 W kabarcık pompası ısı girişi ve 5 °C soğutulan ortam sıcaklığı sabit koşulları için modellemiştir. Bu koşullarda, soğutma kapasitesini 22,3 W ve COP değerini 0,126 olarak hesaplamıştır. Daha sonra, 15 °C ve 40 °C ortam hava sıcaklığı için model oluşturmuş ve COP değerlerini sırasıyla 0,138 ve 0,103 olarak belirlemiştir. En yüksek ekserji yıkımının hava soğutmalı saflaştırıcıda meydana geldiğini ve COP değerinin ortam hava sıcaklığına ve soğurucu verimliliğine önemli derecede bağlı olduğunu ortaya koymuştur.

Literatürde, DAR sistemlerinde nanopartikül kullanımı üzerine çok az sayıda çalışma olduğu görülmüştür. Sözen vd. (2014) DAR sisteminde amonyak-su çiftine Al<sub>2</sub>O<sub>3</sub> nano partikül ilavesinin sistem performansına etkisini deneysel olarak incelenmiştir. Nano partikül nedeniyle yüzey alanı ve akışkanın ısı kapasitesinin arttığını ve dolayısıyla ısı transferinde önemli bir iyileşme, jeneratörden daha iyi ısı soğurma ve soğutucunun soğutma/soğurma sıvısından daha hızlı buharlaşmasını sağladığını ortaya koymuştur. Ayrıca, daha kısa ısı transfer süreleri nedeniyle sistemin çalışma süresinin azaldığını ve istenen sıcaklığın daha hızlı elde edildiğini gözlemlemiştir. Sonuç olarak, nano akışkansız sistemin COP değerinin 0,213-0,280 arasında değişirken nano akışkanlı sistemin COP değerinin 0,225-0,295 arasında değiştiğini ve nano partikülün sistem performansını artırdığını ortaya koymuştur. Lee vd. (2014) amonyak-su çözeltisine nano boyutlu yağ damlacıklarının (N-decane) ve kararlı dağılım için yüzey aktif madde olarak C<sub>12</sub>E<sub>4</sub> (Polyoxyethylene lauryl ether) ve TWEEN20 (Polyoxyethylen sorbitan monolaurate, C<sub>58</sub>H<sub>114</sub>O<sub>26</sub>) ilavesinin DAR sistemi performansı üzerine etkisini araştırmışlardır. Nano akışkan ilavesinin COP değerini % 15 artırdığını ortaya koymuşlardır. Jiang vd. (2019) amonyak-su çalışma akışkanlı DAR sistemine ağırlıkça % 0,1, % 0,3 ve % 0,5 TiO<sub>2</sub> derişimli ve ağırlıkça % 0,5 TiO<sub>2</sub> ve ağırlıkça % 0,02 sodyum dodesil benzen ilavesi sonucu elde edilen dört farklı nano akışkanın sistem performansına etkisini deneysel olarak araştırmışlardır. TiO<sub>2</sub> nano parçacıklarının sistem üzerinde büyük etkilerinin olduğunu ve COP değerini % 27 artırdığını ortaya koymuşlardır. Ağırlıkça % 0,5 TiO<sub>2</sub> ve % 0,02 sodyum dodesil benzen ilaveli sistemin en iyi COP değerine sahip olduğunu belirlemişlerdir. Sonuç olarak, COP değerinin sadece eklenen nano partiküllere bağlı değil aynı zamanda temel akışkan içinde kararlı bir şekilde dağılmış nano partiküllerin sayısına güçlü bir

şekilde bağlı olduğunu ortaya koymuşlardır. Gürbüz vd. (2020) temel bir amonyak-su çalışma akışkanlı DAR sistemine ağırlıkça %1 ve %2 ZnOAl<sub>2</sub>O<sub>3</sub> ve TiO<sub>2</sub> nano parçacık ilavesinin DAR sisteminin enerji performansına etkisini deneysel ve sayısal olarak araştırmışlardır. DAR sisteminde çalışma sıvısı olarak nanoakışkanın kullanılmasının daha hızlı buharlaşmaya yardımcı olduğunu, bunun da çalışma süresini azalttığını ve jeneratördeki ısı transferini artırdığını ortaya koymuşlardır. Ağırlıkça %2 ZnOAl<sub>2</sub>O<sub>3</sub> nano parçacık ilavesi DAR sisteminin performansını %57 arttırmıştır. Sözen vd. (2021) geleneksel su-amonyak-helyum çalışma akışkanlı kullanan bir soğurmalı soğutma sisteminde ağırlıkça %1 ve %2 derişiminde MgOAl<sub>2</sub>O<sub>3</sub> nano partikül ilavesinin enerji ve ekserji performansına etkisini deneysel olarak araştırmıştır. %2 derişimli sistemin, geleneksel ve %1 derişimli çalışma akışkanlı sistemden sırasıyla % 37,4 % 24,5 daha iyi performans gösterdiğini ve %2 derişimli nano partikül ilavesinin ekserji performansını % 44,2 artırdığını ortaya koymuştur. Özbaş (2021) baz çalışma akışkanı olarak amonyak-su kullanan DAR sisteminde çalışma akışkanına ağırlıkça % 1 ve % 2 derişiminde FeOTiO<sub>2</sub> nano partikül ilavesinin sistem performansına etkisini deneysel olarak araştırmıştır. Ağırlıkça % 1 nanopartikül ilaveli sisteminin % 2 nano partikül ilaveli sistemden daha iyi performans gösterdiğini ve ağırlıkça % 1 nano partikül ilavesinin baz amonyak-su çalışma akışkanlı sistemin COP, sirkülasyon oranı ve iç sıcaklık değerini sırasıyla % 17, % 57 ve % 20 artırdığını ortaya koymuştur. Ayrıca, ekserji analizi sonucunda, baz çalışma akışkanına ağırlıkça % 1 nano partikül ilavesinin toplam ekserji kaybını % 4,5 azalttığını ifade etmiştir.

DAR sistemlerinin enerji analizi üzerine yoğun bir şekilde çalışılırken, ekserji analizi üzerine çok fazla çalışma bulunmamaktadır. Son yıllarda DAR sistemlerinin performansını arttırmaya yönelik nano partikül kullanımı ile ilgili çalışmalar devam etmektedir ve literatürde çok az çalışmaya rastlanmıştır. Bu çalışmada, amonyak-su-helyum çalışma akışkanlı bir DAR sistemine ağırlıkça % 0,68 eklenen CuO ve TiO<sub>2</sub> nano partikül ilavesinin enerji ve ekserji performansına etkisi deneysel olarak araştırılmıştır.

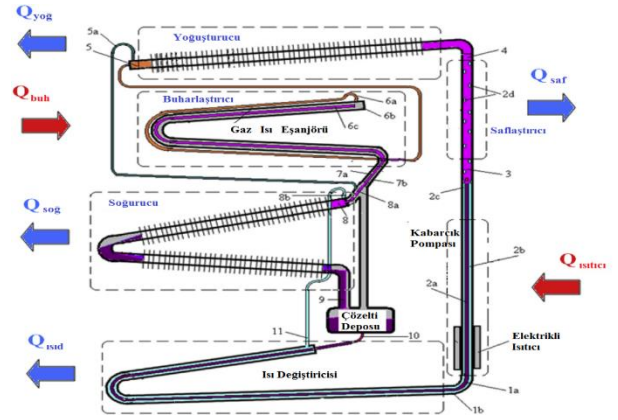
## DENEYSEL ÇALIŞMA

Bu çalışmada, Şekil 1'de verilen DAR sistemi tasarlanmış ve imal edilmiştir. Sisteme % 32 amonyak derişiminde 110 ml hacminde amonyak su çözeltisi ve yardımcı gaz olarak 11 bar basınçta helyum gazı şarj edilmiştir.



Şekil 1. Difüzyon Absorpsiyon Soğutma Sistemi

Şekil 2'de şematik olarak gösterildiği gibi DAR sistemi jeneratör-kabarcık pompası, saflaştırıcı, yoğunlaştırıcı, buharlaştırıcı, soğurucu, ısı değıştirici ekipmanlarından oluşmaktadır.



Şekil 2. DAR sisteminin şematik görünümü (Yıldız ve Ersöz, 2013)

Şekil 2'de görüldüğü gibi, DAR sisteminde amonyak buharı elektrikli ısıtıcı vasıtasıyla sağlanan ısı girişi ile kaynaticıdaki (1a) zengin çözeltiden ayrılır. Bu amonyak buharı ve amonyak bakımından derişimi azalan çözelti (fakir çözelti) kabarcık pompası içinde yükselir. Amonyak buharı saflaştırıcıya doğru ilerler (3 noktası) ve fakir çözelti ise 2a noktasına geri dönerek ısı değıştiriciden geçip soğurucuya gelir. Sistemde fakir çözeltinin ısı değıştiricisinden geçirilmesinin amacı kaynaticıda aldığı ısının bir miktarını çözünme işlemi için soğurucudan kaynaticıya gelen amonyak bakımından derişimi yüksek çözeltiye (zengin çözelti) vermesidir. Saflaştırıcıya gelindiğinde ise amonyak buharı içinde barındırdığı bir miktar su buharından çözünür. Burada gerçekleşen bu çözünme, saflaştırıcıdan çevreye olan ısı geçişi nedeniyle sıcaklığı düşerek su buharının yoğunlaşması şeklinde gerçekleşir. Yoğuşan su 2d noktasına geri dönerek kabarcık pompası çıkışındaki fakir çözelti ile birleşir. Amonyak buharı ise saflık derecesine yaklaşılarak yoğunlaştırıcıya gelir. Yoğunlaştırıcıya saflık derecesine yakın bir şekilde giren amonyak buharı 4 noktasında yoğunlaşarak sıvı faza geçiş yapar. Sıvı faza geçemeyen bir miktar amonyak buharı çözelti deposuna (5a noktası) ve sıvı fazdaki amonyak (5

noktası) ise buharlaştırıcıya gelir. Buharlaştırıcıda sıvı amonyak, yardımcı gaz olan helyum gazıyla karşılaşır. Bu karşılaşmada kısmi basıncı düşen amonyak, helyum gazı içinde yayılarak buharlaşmaya başlar. Helyum gazı karşılaşmanın olduğu sıcaklık değeri için belirli bir miktar amonyak buharını bünyesine taşır. Buharlaştırıcı içinde amonyak ilerlerken kısmi basıncı artar ve buharlaştırıcı çıkışında tamamen buhar fazına geçer. Amonyak buharı ve helyum karışımı soğurucuya gelir. Soğurucuda, amonyak ve helyum gazı karışımını, kaynatıcıdan gelen ve ısı değiştiriciden geçen fakir çözelti ile birleşir. Bu bölgede amonyak buharı helyum gazından ayrılır ve fakir çözelti tarafından soğurulur. Soğurucu çıkışında helyum gazı saf halde, fakir çözelti ise amonyak bakımından zenginleşerek zengin çözelti olarak çıkar. Zengin çözelti, çözelti deposuna girer ve oradan ısı değiştiricide ön ısıtmadan geçerek kaynatıcıya gelir. Böylece sistem çevrimi tamamlanmış olur. Sistem içinde her bir akışkan için üç ayrı çevrim meydana gelir. Bu çevrimler; soğurucu akışkan yani amonyak bakımından fakir olan su çevrimi, soğutucu akışkan (amonyak) çevrimi ve basınç dengeleyici olan yardımcı gaz (helyum gazı) çevrimi olarak açıklanabilir. Soğurucu akışkan çevrimi; kaynatıcı, ısı değiştirici ve soğurucu arasında meydana gelir. Soğutucu akışkan çevrimi; kaynatıcı, saflaştırıcı, yoğuşturucu, buharlaştırıcı, soğurucu, ısı değiştirici ve tekrar kaynatıcı arasında meydana gelir. Basınç dengeleyici yardımcı gaz çevrimi ise buharlaştırıcı ile soğurucu arasında gerçekleşir (Yıldız ve Ersöz, 2013b)

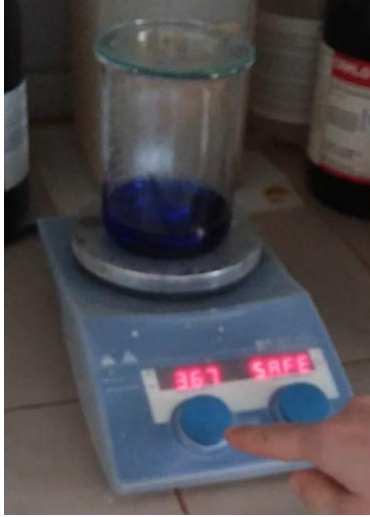
Nano partiküller, DAR sisteminde kaynatıcıdaki amonyak-su karışımından buhar fazındaki amonyanın daha hızlı ayrılmasını sağlamak amacıyla iş akışkanına içerisine eklenmektedir (Sözen vd., 2015). Bu çalışmada, DAR sistemlerinde yaygın olarak kullanılan  $\text{NH}_3\text{-H}_2\text{O-He}$  çalışma akışkanına ısı performansını artırmak amacıyla Tablo 1'de teknik ve termofiziksel özellikleri verilen CuO ve  $\text{TiO}_2$  nano partikülleri ilave edilmiştir.

**Tablo 1.** CuO ve  $\text{TiO}_2$  nano partiküllerinin teknik ve termofiziksel özellikleri (<https://nanografi.com>, Dağdevir ve Özceyhan, 2016, Khanafer ve Vafai , 2011)

Özellikler	Nano partikül	
	CuO	$\text{TiO}_2$
Saflık %	% 99,5	% 99,55
Renk	Siyah	Beyaz
Ortalama partikül boyutu (nm)	77	13
Özgül yüzey alanı ( $\text{m}^2\text{g}^{-1}$ )	20	60
Kütle Yoğunluğu ( $\text{gcm}^{-3}$ )	0,8	0,19
$\rho$ ( $\text{kgm}^{-3}$ )	6500	4100
$k$ ( $\text{Wm}^{-1}\text{K}^{-1}$ )	18	10,2
$C_p$ ( $\text{Jkg}^{-1}\text{K}^{-1}$ )	540	690

Bu çalışmada, baz çalışma akışkanı olarak  $\text{NH}_3\text{-H}_2\text{O-He}$  çözeltisi, yardımcı gaz olarak 11 bar basınçlandırılan helyum gazı ve enerji kaynağı olarak elektrik kullanan bir DAR sistemi tasarlanmıştır. Sisteme % 32 amonyak derişimi olan 110 ml amonyak-su çözeltisi konulmuştur. Çevreye olan ısı kayıplarının ihmal edilebilmesi için jeneratör-kabarcık pompası ve ısı eşanjörü yalıtılmıştır. Birinci aşamada, nano partikül ilavesi olmayan baz  $\text{NH}_3\text{-H}_2\text{O-He}$  çalışma akışkanlı sistemin deneyleri yapılmıştır. İkinci ve üçüncü aşamada sırasıyla 110 ml amonyak su çözeltisine sırasıyla ağırlıkça % 0,68 CuO nano partikülü ve ağırlıkça % 0,68  $\text{TiO}_2$  nano partikülü eklenmiştir. DAR sisteminin çalışması sırasında, çalışma akışkanına içerisine katılan nano partiküller, amonyak-su çözeltisi ile birlikte sistemin tüm bölümlerinde dolaşmaktadır. Nanoakışkan solüsyonunun kararlılığının artırılması için literatürde farklı yöntemler önerilmektedir. Bu yöntemlerden biri yüzey aktif madde eklenmesi metodu ile baz çalışma akışkanına nano partiküllerin arasındaki bağın artırılması ve dolayısıyla kararlılığın artırılması sağlanırken diğer yöntem ise çalışma akışkanının hazırlanması aşamasında ultrasonik dalgalar aracılığıyla ultrasonik banyo işlemi yapılmasıdır. Bu çalışmada, CuO ve  $\text{TiO}_2$  nano partikül ilaveli amonyak-su çözeltisine % 0,1 oranında AOT (Sodium bis-(2-ethylehexyl) sulfosuccinate) yüzey aktif maddesi eklenmiştir ve 24 saat boyunca ultrasonik çalkalama ile karışımı sağlanmıştır (Şekil 3) ve deneyleri gerçekleştirilmiştir. Hazırlanan  $\text{NH}_3\text{-H}_2\text{O-He+CuO}$  karışımı ve  $\text{NH}_3\text{-H}_2\text{O-He+TiO}_2$  sisteme şarj edilmiş ve yardımcı gaz olarak 11 bar ile sınırlandırılmış helyum gazı kullanılmıştır.

Tüm deneylerde sistem kontrol hacimlerinin (jeneratör-kabarcık pompası, saflaştırıcı, yoğuşturucu ve buharlaştırıcı) giriş-çıkış, soğutma odası ve ortam sıcaklıkları, sistemin çalışma basıncı ve enerji tüketimleri ve sıcaklık ölçümleri 5 dakika ara ile kaydedilmiştir, her bir deney yaklaşık 4 saat sürmüştür ve 10'ar defa tekrarlanmıştır.



(a) CuO nano akışkanı



(b) TiO<sub>2</sub> nano akışkanı



(c) Sisteme şarjı

Şekil 3. Nano akışkan karışımının yapılması ve sisteme şarj edilmesi

## TERMODİNAMİK ANALİZ

Termodinamik analizlerde aşağıdaki kabuller yapılmıştır.

- Boru hattındaki basınç düşüşleri ve hidrostatik basınçlar ihmal edilmiştir,
- Sıvı çözelti (2c) ve buhar kabarcıkları (3) kılcal borudan çıkmakta ve jeneratörü aynı sıcaklıkta terk etmektedir ( $T_{2c}=T_3$ ),
- Jeneratörden çevreye olan ısı kayıplarının ihmal edilebilmesi için jeneratör yalıtılmıştır,
- Buharlaştırıcı girişindeki amonyak su çözeltisi ve helyum adyabatik kabul edilmiştir,
- 5a noktasında hiçbir akışım olmadığı kabul edilmiştir,
- Ölçülen ortam sıcaklığı ölü hal sıcaklığı olarak kabul edilmiştir.

## Enerji Analizi

Enerji analizinde, DAR sisteminin her bir ekipmanı için kontrol hacimleri belirlenmiş ve ısı kayıpları, kazançları ve kapasitelerini içeren kütle ve enerji denge denklemleri elde edilmiştir. Her bir ekipman için yapılan analiz aşağıda verilmiştir.

### Jeneratör - kabarcık pompası

Jeneratör-kabarcık pompasına giren zengin çözeltiden ( $\dot{m}_{1a}$ ), soğutkanı buharlaştırarak ayırmak için elektrik direnci ile ısı girişi ( $\dot{Q}_{ısıtıcı}$ ) yapılmıştır. Amonyak buharı ( $\dot{m}_3$ ) kabarcık pompasından yükselerek saflaştırıcıya gelmektedir. Kabarcık pompasının çıkışındaki zayıf çözelti ise ( $\dot{m}_{2c}$ ) ısı değiştiricisine geri dönmektedir. Analizlerde, sıvı çözeltinin (2c) ve buhar kabarcıklarının (3) jeneratörü aynı sıcaklıkta ( $T_{2c}=T_3$ ) terk ettiği ve jeneratörden çevreye olan ısı kayıplarının ihmal edildiği

kabul edilmiştir. Jeneratör-kabarcık pompası için kütle ve enerji dengeleri aşağıda verilmiştir:

$$\dot{m}_{1a} = \dot{m}_3 + \dot{m}_{2c} \quad (1)$$

$$\dot{m}_{1a}X_{1a} = \dot{m}_3X_3 + \dot{m}_{2c}X_{2c} \quad (2)$$

$$\dot{m}_{1a}h_{1a} + \dot{Q}_{ısıtıcı} = \dot{m}_3h_3 + \dot{m}_{2c}h_{2c} \quad (3)$$

burada,  $\dot{m}$  çalışma akışkanının kütleli debisi ( $\text{kg s}^{-1}$ ),  $h$  özgül entalpi ( $\text{kJ kg}^{-1}$ ),  $\dot{Q}_{ısıtıcı}$  jeneratöre verilen elektrik gücü (W), X amonyak su karışımının kütle oranıdır (Jakob vd, 2008).

### Saflaştırıcı

Kaynatıcıdan çıkan buhar çok az miktarda soğurucu içerir ve dolayısıyla saf soğutucu değildir. Bu nedenle saflaştırıcıda kısmi yoğunlaşma ile saflaştırılır ve bu işlem ile neredeyse saf amonyak buharı elde edilir. Saf buharın kütleli debisi Eş. (4) ile saflaştırıcıdan çevreye atılan ısı miktarı ( $\dot{Q}_{saf}$ ) Eş. (6) ile hesaplanır;

$$\dot{m}_3 = \dot{m}_4 + \dot{m}_{2d} \quad (4)$$

$$\dot{m}_3X_3 = \dot{m}_4X_4 + \dot{m}_{2d}X_{2d} \quad (5)$$

$$\dot{m}_3h_3 = \dot{m}_4h_4 + \dot{m}_{2d}h_{2d} + \dot{Q}_{saf} \quad (6)$$

### Isı değiştirici

Isı değiştiricide, jeneratörden çıkan fakir çözelti (4), soğurucudan gelen düşük sıcaklıktaki zengin çözeltiye enerjisini aktarır. Isı değiştirici için kütle ve enerji dengeleri;

$$\dot{m}_{10} = \dot{m}_{1a} = \dot{m}_{rs} \quad (7)$$

$$\dot{m}_{1b} = \dot{m}_{11} = \dot{m}_{ps} \quad (8)$$

$$\dot{m}_{1b} = \dot{m}_{2c} + \dot{m}_{2d} \quad (9)$$

$$\dot{m}_{1b}X_{1b} = \dot{m}_{2c}X_{2c} + \dot{m}_{2d}X_{2d} \quad (10)$$

$$\dot{m}_{1b}h_{1b} = \dot{m}_{2c}h_{2c} + \dot{m}_{2d}h_{2d} \quad (11)$$

$$\dot{m}_{1b}h_{1b} + \dot{m}_{10}h_{10} = \dot{m}_{11}h_{11} + \dot{m}_{1a}h_{1a} + \dot{Q}_{ısıt} \quad (12)$$

### Yoğuşturucu

Amonyak buharı sistem basıncı ile aynı yüksek basınç değerinde yoğuşturucuya girer ve sıvıya dönüşür.

Yoğuşturucu için kütle ve enerji dengeleri aşağıda verilmiştir.

$$\dot{m}_4 = \dot{m}_5 \quad (13)$$

$$\dot{m}_4 h_4 = \dot{m}_5 h_5 + \dot{Q}_{yoğ} \quad (14)$$

### Buharlaştırıcı

Sistem basıncında yoğuşturucuyu terk eden sıvı amonyak, buharlaştırıcı girişine ulaşır ve burada ısı değiştirici boyunca soğurucudan gelen helyum gazı ile karışır. Sonuç olarak sıvı amonyakın kısmi basıncı düşer ve düşük sıcaklıkta buharlaşmaya başlar. Buharlaştırıcı için kütle ve enerji dengesi aşağıdaki gibi ifade edilir;

$$\dot{m}_{6a} + \dot{m}_{ig} = \dot{m}_{7b} \quad (15)$$

$$\dot{m}_{6a} h_{6a} + \dot{m}_{ig} h_{ig} + \dot{Q}_{buh} = \dot{m}_{7b} h_{7b} \quad (16)$$

### Soğurucu

Soğutucu buhar burada jeneratörden dönen zayıf çözelti tarafından emilir ve zengin çözelti, çözelti tankına akar. Helyum ve amonyak artıkları ise buharlaştırıcıya doğru akar. Soğurucu için kütle ve enerji dengeleri sırasıyla Eş. (17) ve (18) ile verilmiştir. Soğurucudan çevreye atılan ısı transfer hızı ( $\dot{Q}_{soğ}$ ) Eş. (19) ile hesaplanabilir;

$$\dot{m}_9 + \dot{m}_{ig} = \dot{m}_{7b} + \dot{m}_{8b} \quad (17)$$

$$\dot{m}_9 h_9 + \dot{m}_{ig} h_{ig} + \dot{Q}_{abs} = \dot{m}_{7b} h_{7b} + \dot{m}_{8b} h_{8b} \quad (18)$$

$$\dot{Q}_{soğ} = \dot{m}_{7b} h_{7b} + \dot{m}_{8b} h_{8b} - \dot{m}_9 h_9 - \dot{m}_{ig} h_{ig} \quad (19)$$

### Enerji performansı katsayısı (COP)

Enerji Performansı Katsayısı (COP), buharlaştırıcı tarafından çekilen ısı, sisteme verilen ısıtıcı gücü oranı olarak tanımlanır.

$$COP = \frac{\dot{Q}_{buh}}{\dot{Q}_{ısıtıcı}} \quad (20)$$

### Ekserji Analizi

Ekserji kavramı termodinamiğin birinci ve ikinci yasasına dayanmaktadır. Ekserji analizi, bir proseste bozulan enerji bölgelerini göstermektedir. Ekserji analizinin temel amacı, anlamlı verimleri (ekserji) ve ekserji kayıplarının nedenlerini ve gerçek büyüklüklerini belirlemektir. Bu çalışmada, ölçülen ortam sıcaklığı, ölü durum sıcaklığı ( $T_0$ ) olarak değerlendirilmiştir. Genel ekserji dengesi;

$$\dot{E}x_{heat} - \dot{E}x_{work} + \dot{E}x_{mass,in} - \dot{E}x_{mass,out} = \dot{E}x_{dest} \quad (21)$$

$$\Sigma \left(1 - \frac{T_0}{T_k}\right) \dot{Q}_k - \dot{W} + \Sigma \dot{m}_{in} \Psi_{in} - \Sigma \dot{m}_{out} \Psi_{out} = \dot{E}x_{dest} \quad (22)$$

Eş. (22)'de,  $\dot{Q}_k$ , k noktasında  $T_k$  sıcaklığındaki sınıra geçen ısı transfer hızı,  $\dot{W}$  iş ve  $\Psi$  özgül akış enerjisidir. Akan akışkan için özgül ekserji ve ekserji denklemleri sırasıyla Eş. (23) ve (24)'de verilmiştir.

$$\Psi = (h - h_0) - T_0(s - s_0) \quad (23)$$

$$\dot{E}x = \dot{m}(h - h_0) - T_0(s - s_0) \quad (24)$$

Eş. (23) ve (24)'de s entropi ( $\text{kJkg}^{-1}\text{K}^{-1}$ ) ve alt indis 0  $P_0$  ve  $T_0$  ölü hal durumundaki özellikleri göstermektedir.

Sisteme olan ısı transferi pozitif alındığında sistem için entropi üretimi Eş. (25) ile ifade edilebilir.

$$\dot{S}_{gen} = \Sigma \dot{m}_{out} S_{out} - \Sigma \dot{m}_{in} S_{in} - \Sigma \frac{\dot{Q}_k}{T_k} \quad (25)$$

Ekserji yıkımı için, ilk olarak entropi üretimi  $\dot{S}_{gen}$  hesaplanır ve Eş. (26) ile bulunabilir.

$$\dot{I} = \dot{E}x_{dest} = T_0 \dot{S}_{gen} \quad (26)$$

### Jeneratör - kabarcık pompası

Jeneratör-kabarcık pompası için ekserji yıkımı Eş. (27)'de verilmiştir.

$$\dot{I}_{ısıtıcı} = T_0 \left( \dot{m}_{3s} s_3 + \dot{m}_{2c} s_{2c} - \frac{\dot{Q}_{ısıtıcı}}{T_{ısıtıcı}} - \dot{m}_{1a} s_{1a} \right) \quad (27)$$

### Saflaştırıcı

Saflaştırıcı için ekserji yıkımı Eş. (28) ile hesaplanabilir.

$$\dot{I}_{saf} = T_0 \left( \dot{m}_4 s_4 + \dot{m}_{2d} s_{2d} + \frac{\dot{Q}_{saf}}{T_{saf}} - \dot{m}_3 s_3 \right) \quad (28)$$

### Isı değiştirici

Isı değiştirici için ekserji yıkımı aşağıda verilmiştir.

$$\dot{m}_{10} = \dot{m}_{1a} = \dot{m}_{rs} \quad (29)$$

$$\dot{m}_{1b} = \dot{m}_{11} = \dot{m}_{ps} \quad (30)$$

$$\dot{I}_{ıstıd} = T_0 \left( \dot{m}_{1a} s_{1a} + \dot{m}_{11} s_{11} + \frac{\dot{Q}_{ıstıd}}{T_{ıstıd}} - \dot{m}_{10} s_{10} - \dot{m}_{1b} s_{1b} \right) \quad (31)$$

$$\dot{I}_{ıstıd} = T_0 \left[ \dot{m}_{rs} (s_{1a} - s_{10}) + \dot{m}_{ps} (s_{11} - s_{1b}) + \frac{\dot{Q}_{ıstıd}}{T_{ıstıd}} \right] \quad (32)$$

### Yoğuşturucu

Yoğuşturucu için ekserji yıkımı aşağıdaki denklemden hesaplanır;

$$\dot{I}_{yoğ} = T_0 \left( \dot{m}_5 s_5 + \frac{\dot{Q}_{yoğ}}{T_{yoğ}} - \dot{m}_4 s_4 \right) \quad (33)$$

### Buharlaştırıcı

Buharlaştırıcı için ekserji yıkımı aşağıda verilmiştir;

$$\dot{I}_{buh} = T_0 \left( \dot{m}_{7b} s_{7b} - \dot{m}_{6a} s_{6a} - \dot{m}_{ig} s_{ig} - \frac{\dot{Q}_{buh}}{T_{buh}} \right) \quad (34)$$

### Soğurucu

Soğurucu için ekserji yıkımı aşağıdaki denklemden hesaplanır;

$$\dot{I}_{soğ} = T_0 \left( \dot{m}_9 s_9 + \dot{m}_{ig} s_{ig} + \frac{\dot{Q}_{soğ}}{T_{soğ}} - \dot{m}_{7b} s_{7b} - \dot{m}_{8b} \right) \quad (35)$$

## Diğer bileşenler

Diğer bileşenler için boru hatları ve çözelti deposu olarak ekserji yıkımı Eş. (36) ile hesaplanır;

$$\dot{I}_{diğer} = \dot{Q}_{diğer} \left( 1 - \frac{T_0}{T_{diğer}} \right) \quad (36)$$

## Ekserji performans katsayısı (ExCOP)

DAR sisteminin ekserji performansı (ExCOP), Eş. (37) ile belirlenir.

$$ExCOP = 1 - \frac{\dot{E}_{xykıtm}}{\dot{E}_{xgiren}} \quad (37)$$

## Nanoakışkanın Termodinamik Özellikleri

Bu çalışmada, baz çalışma akışkanı olarak amonyak-su kullanan bir DAR sisteminde, amonyak-su soğutucuna ağırlıkça %0,68 CuO ve TiO<sub>2</sub> nano partikülleri ilave edilmiştir. Daha sonra, nano partiküllerin arasındaki bağın ve kararlılığın artırılması için % 0,1 oranında AOT yüzey aktif maddesi ilavesi ile 24 saat boyunca ultrasonik çalkalama ile karışımı sağlanan NH<sub>3</sub>-H<sub>2</sub>O-He+CuO ve NH<sub>3</sub>-H<sub>2</sub>O-He+TiO<sub>2</sub> nano akışkanı elde edilmiştir.

Nano akışkanların yoğunluğu ( $\rho_{nf}$ ), özgül ısı kapasitesi ( $c_{p,nf}$ ), vizkozitesi ( $\mu_{nf}$ ) ve ısı iletkenliği sırasıyla Eş. (38), Eş. (39), Eş. (40) ve Eş. (41) ile hesaplanır (Khanfer ve Vafai, 2011):

$$\rho_{nf} = (1 - \phi_{np})\rho_{bf} + \phi_{np}\rho_{np} \quad (38)$$

$$c_{p,nf} = (1 - \phi_{np})c_{p,bf} + \phi_{np}c_{p,np} \quad (39)$$

$$\frac{\mu_{nf}}{\mu_{bf}} = \frac{1}{(1 - \phi_{np})^{2.5}} \quad (40)$$

$$\frac{k_{static}}{k_{bf}} = 1 + \frac{3 \left( \frac{k_{np}}{k_{bf}} - 1 \right) \phi_{np}}{\left( \frac{k_{np}}{k_{bf}} + 2 \right) - \left( \frac{k_{np}}{k_{bf}} - 1 \right) \phi_{np}} \quad (41)$$

Eş. (38), (39) ve (40)'da,  $\phi_{np} = V_{np}/(V_{np} + V_{bf})$  nano partikülün hacimsel derişimidir.

Nano akışkan çalışma akışkanı kullanan DAR sisteminin her bir ekipmanı için entalpi farkı, Eş. (42)'nin genişletilmesiyle Eş. (43)'den hesaplanabilir;

$$C_p = \left( \frac{\partial h}{\partial T} \right)_p \quad (42)$$

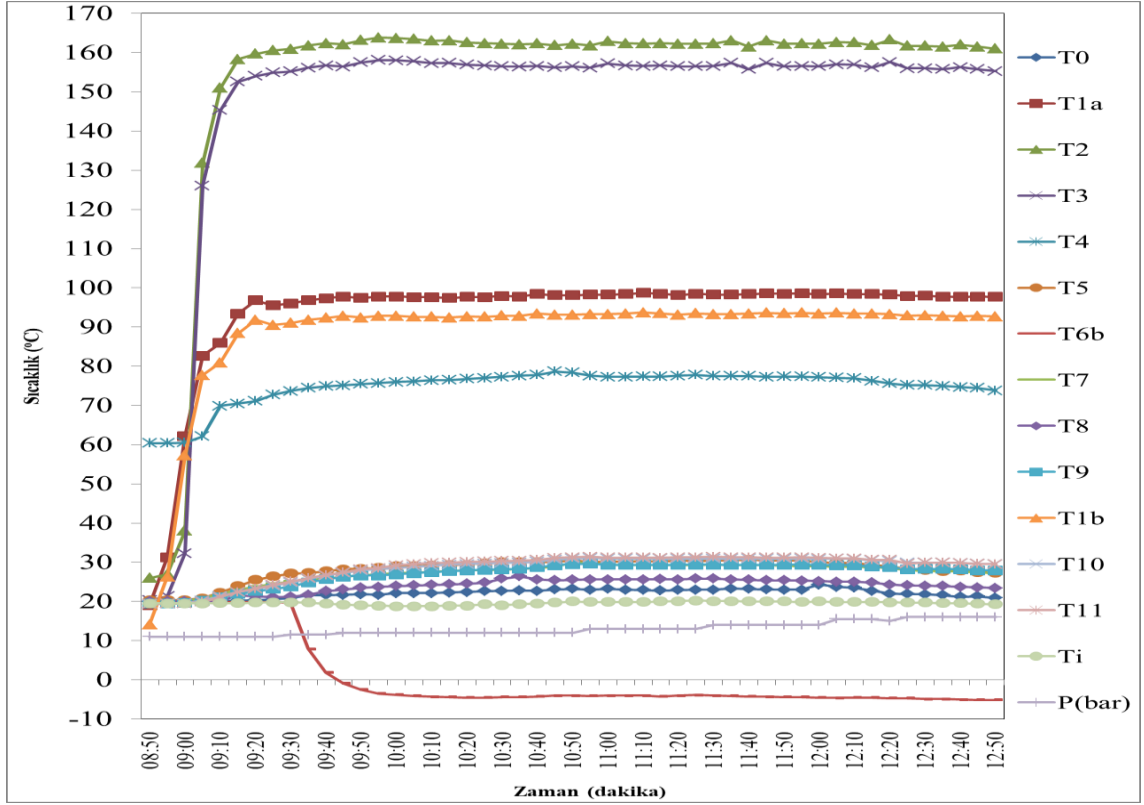
$$\Delta h = h_{out} - h_{in} = \int_{in}^{out} C_p dT \quad (43)$$

## BULGULAR

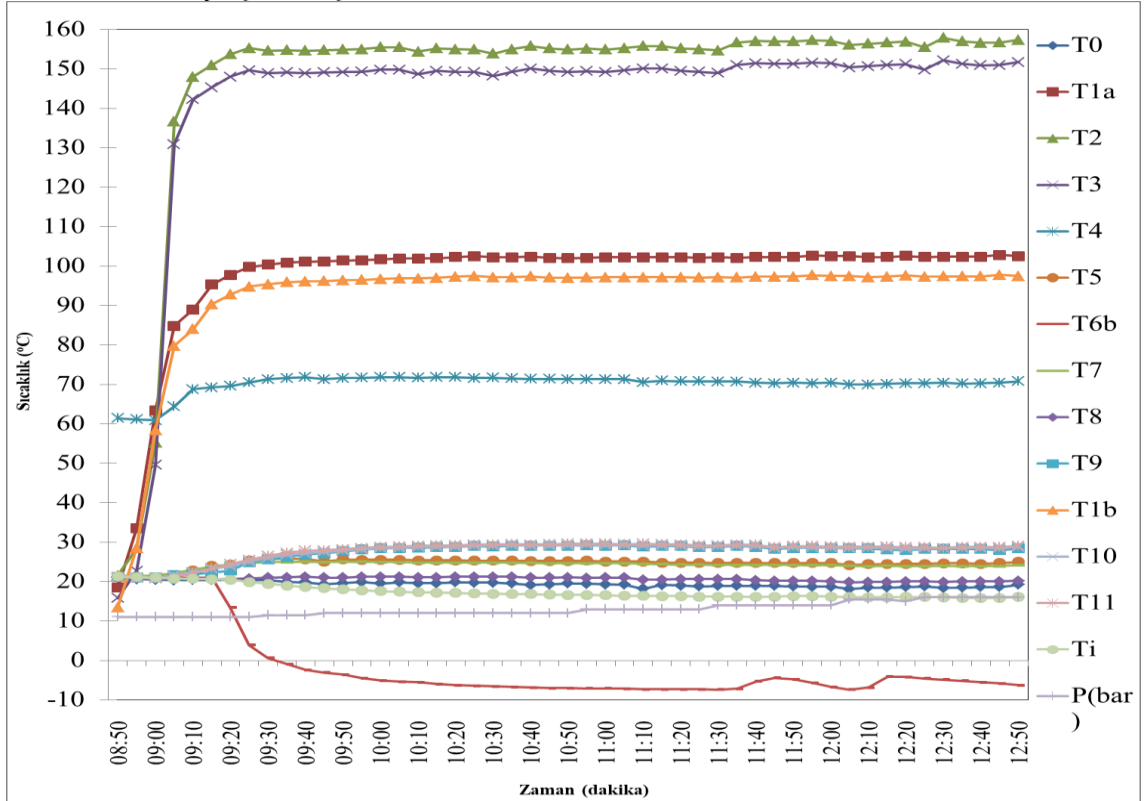
Literatürde DAR sistemlerinin deneysel enerji performansı üzerine birçok çalışma mevcut iken ekserji analizi üzerine fazla çalışma bulunmamaktadır. Son yıllarda DAR sistemlerinin performansını arttırmaya yönelik nano partikül kullanımı yaygınlaşmasına rağmen çalışma sayısı fazla değildir. Bu çalışmada, baz çalışma akışkanı olarak NH<sub>3</sub>-H<sub>2</sub>O-He kullanan sistem ile bu sisteme ilave edilen CuO nano partikülü ilave edilerek oluşturulan NH<sub>3</sub>-H<sub>2</sub>O-He+CuO nano akışkanı ve TiO<sub>2</sub> nano partikülü ilave edilerek oluşturulan NH<sub>3</sub>-H<sub>2</sub>O-He+TiO<sub>2</sub> nano çalışma akışkanı kullanan DAR sistemlerinin enerji ve ekserji analizleri yapılmıştır. Analizlerde, sistemin tüm bileşenleri için enerji kayıp-kazanç, ekserji kayıpları, enerji ve ekserji performansları hesaplanmış ve karşılaştırılmıştır.

DAR sistemlerinin karakteristiklerini belirlemenin en önemli yolu sıcaklık ve basınç ölçümüdür. NH<sub>3</sub>-H<sub>2</sub>O-He, NH<sub>3</sub>-H<sub>2</sub>O-He+CuO ve NH<sub>3</sub>-H<sub>2</sub>O-He+TiO<sub>2</sub> çalışma akışkanlı sistemler için deneyler yapılmıştır. Deneylerde, jeneratör-kabarcık pompası, saflaştırıcı, yoğunlaştırıcı, buharlaştırıcı, soğurucu ve ısı değıştirici giriş ve çıkış sıcaklıkları, ölü hal sıcaklığı olarak da değerlendirilen çevre ortam sıcaklığı (T<sub>0</sub>), ortalama kaynatıcı sıcaklığı (T<sub>1a</sub>), soğutulan ortam sıcaklığı ve sistem basıncı ölçülmüştür. Ölçülen veriler 4 saatlik süre boyunca 5'er dakika ara ile kaydedilmiştir.

NH<sub>3</sub>-H<sub>2</sub>O-He, NH<sub>3</sub>-H<sub>2</sub>O-He+CuO ve NH<sub>3</sub>-H<sub>2</sub>O-He+TiO<sub>2</sub> çalışma akışkanlı sistemler için ölçüm sonuçları sırasıyla Şekil 4, 5 ve 6'da verilmiştir.

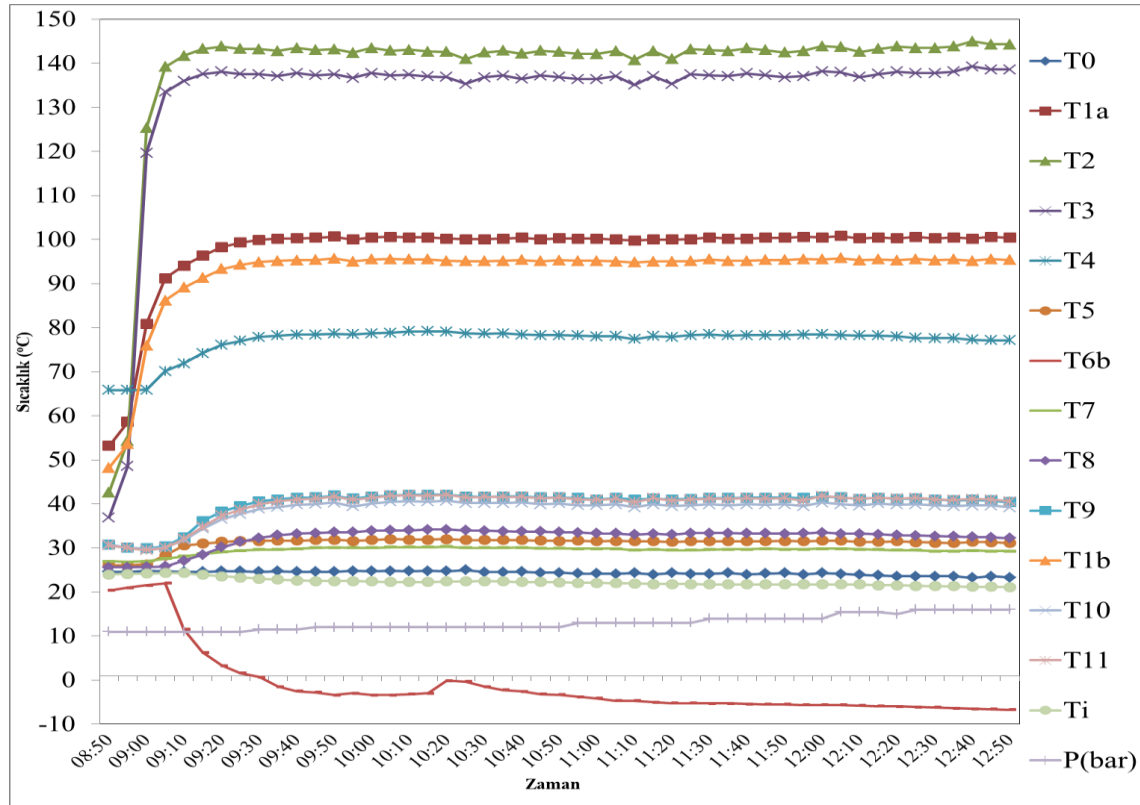


Şekil 4. NH<sub>3</sub>-H<sub>2</sub>O-He deney ölçüm sonuçları



Şekil 5. NH<sub>3</sub>-H<sub>2</sub>O-He+CuO deney ölçüm sonuçları





Şekil 6. NH<sub>3</sub>-H<sub>2</sub>O-He+TiO<sub>2</sub> deney ölçüm sonuçları

Şekil 4-6'da görüldüğü gibi, deneyler benzer çevre sıcaklığında (T<sub>0</sub>) yapılmıştır ve hesaplamalarda ortalama 21 °C olarak alınmıştır. En yüksek kaynatıcı giriş sıcaklığı (T<sub>1a</sub>) ve fakir çözelti ısı değiştirici giriş sıcaklığı (T<sub>1b</sub>) NH<sub>3</sub>-H<sub>2</sub>O-He+CuO çalışma akışkanını kullanan sistemde elde edilirken en düşük ortalama kaynatıcı giriş sıcaklığı NH<sub>3</sub>-H<sub>2</sub>O-He kullanan sistemde elde edilmiştir. Kaynatıcı ortalama sıcaklıklarının tam olarak ölçülememesi sebebiyle elde edilen yaklaşık veriler kullanılmıştır. Kaynatıcı çıkış sıcaklığı (T<sub>3</sub>), ortalama kaynatıcı sıcaklığından bir miktar düşüş göstermiştir ve saflaştırıcı giriş sıcaklığının kaynatıcı çıkış sıcaklığına eşit olduğu kabul edilmiştir. Kaynatıcıda elde edilen sıcaklıkların yarısından fazlası saflaştırıcıdan atılmıştır. Saflaştırıcı çıkış sıcaklığının yoğuşturucu giriş sıcaklığına eşit olduğu (T<sub>4</sub>) kabul edilmiştir. Safılık derecesine ulaşan amonyak yoğuşturucuya girmekte (T<sub>5</sub>) ve burada yoğuşarak sıvı faza geçiş yapmaktadır ve yoğuşma sırasında çevre ortama ısı atılmaktadır. Yoğuşma, NH<sub>3</sub>-H<sub>2</sub>O-He+CuO karışımında en düşük sıcaklıkta gerçekleşirken NH<sub>3</sub>-H<sub>2</sub>O-He+TiO<sub>2</sub> karışımında en yüksek sıcaklıkta gerçekleşmektedir. Buharlaştırıcının girişinde (6b noktası), sıvı amonyak helyumla karşılaşarak buharlaşmaya başlar. Deneylerde soğuma başlangıcı ve kararlı hale geçiş süresi NH<sub>3</sub>-H<sub>2</sub>O-He karışımında en düşük iken, NH<sub>3</sub>-H<sub>2</sub>O-He+TiO<sub>2</sub> karışımında en yüksek değere sahiptir. Soğuma başlama süresi, NH<sub>3</sub>-H<sub>2</sub>O-He, NH<sub>3</sub>-H<sub>2</sub>O-He+CuO, NH<sub>3</sub>-H<sub>2</sub>O-

He+TiO<sub>2</sub> çalışma akışkanlı sistemde sırasıyla 54., 45. ve 41. dakikada başlarken kararlı hale geçiş süreleri sırasıyla 119., 215. ve 143. dakika sonunda meydana gelmiştir. Buharlaştırıcı çıkışında (7 noktası) yardımcı gaz olan helyumla birlikte soğurucuya ulaşır. Buharlaştırıcı çıkış sıcaklığı (T<sub>7</sub>), NH<sub>3</sub>-H<sub>2</sub>O-He çalışma akışkanlı sistemde en düşük iken, NH<sub>3</sub>-H<sub>2</sub>O-He+TiO<sub>2</sub> çalışma akışkanlı sistemde en yüksek değere sahiptir. Soğurucu giriş sıcaklığı (T<sub>8</sub>) düştükçe suyun amonyağı emme kabiliyetinin arttığı bilinmektedir ve dolayısıyla en yüksek soğurucu giriş sıcaklığı NH<sub>3</sub>-H<sub>2</sub>O-He+TiO<sub>2</sub> çalışma akışkanlı sistemde elde edilmiştir. Soğurucu çıkış sıcaklığı (T<sub>9</sub>) en yüksek NH<sub>3</sub>-H<sub>2</sub>O-He+TiO<sub>2</sub> çalışma akışkanlı sistemde elde edilirken en düşük NH<sub>3</sub>-H<sub>2</sub>O-He+CuO çalışma akışkanlı sistemde elde edilmiştir. Isı değiştiricisi zengin çözelti giriş sıcaklığı (T<sub>10</sub>) ve ısı değiştirici çıkış fakir çözelti sıcaklığı en yüksek NH<sub>3</sub>-H<sub>2</sub>O-He+TiO<sub>2</sub> çalışma akışkanlı sistemde meydana gelirken en düşük NH<sub>3</sub>-H<sub>2</sub>O-He+CuO çalışma akışkanlı sistemde meydana gelmiştir.

NH<sub>3</sub>-H<sub>2</sub>O-He, NH<sub>3</sub>-H<sub>2</sub>O-He+CuO ve NH<sub>3</sub>-H<sub>2</sub>O-He+TiO<sub>2</sub> akışkan çiftlerinde kullanılan ortalama elektrik tüketimi 63 W olarak ölçülmüştür. Termodinamik analizlerde, enerji ve ekserji hesaplamalarında sistemin kararlı hale geçtikten sonra Tablo 2'de verilen ortalama sıcaklık değerleri kullanılmıştır.

**Tablo 2.** Termodinamik analizlerde kullanılan ortalama değerler

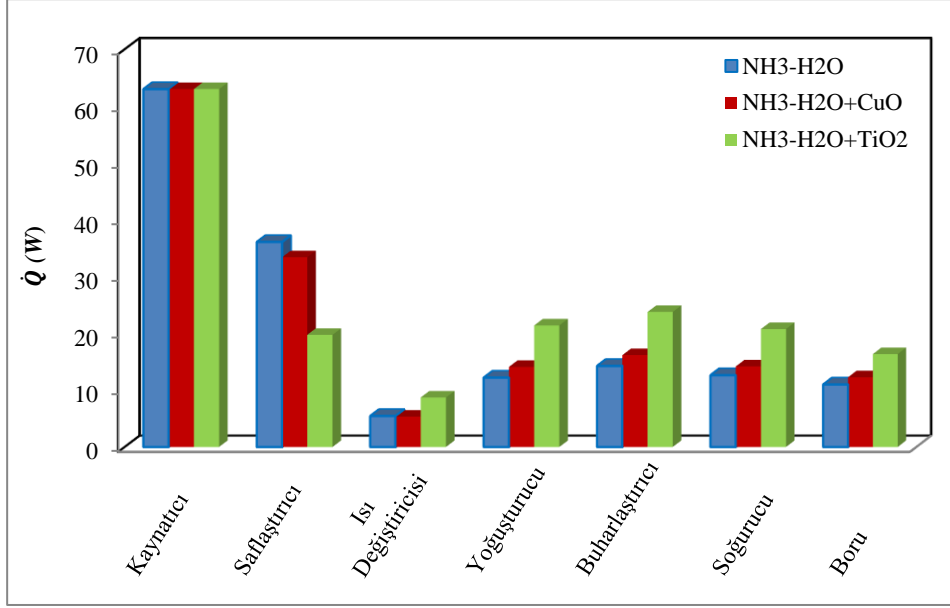
Ölçüm noktaları	NH <sub>3</sub> -H <sub>2</sub> O-He	NH <sub>3</sub> -H <sub>2</sub> O-He+CuO	NH <sub>3</sub> -H <sub>2</sub> O-He+TiO <sub>2</sub>
Çevre ortam sıcaklığı, T <sub>0</sub> (°C)	21	21	21
Kaynatıcı giriş sıcaklığı, T <sub>1a</sub> (°C)	98,24	100,56	100,37
Isı Değiştirici fakir çözelti giriş sıcaklığı, T <sub>1b</sub> (°C)	93,24	95,56	95,37
Ortalama kaynatıcı sıcaklığı, T <sub>2</sub> (°C)	161,49	156,75	143,23
Kaynatıcı çıkış-saflaştırıcı giriş sıcaklığı, T <sub>3</sub> (°C)	155,79	151,05	137,53
Saflaştırıcı çıkış-yoğuşturucu giriş sıcaklığı, T <sub>4</sub> (°C)	76	70,32	78,04
Yoğuşturucu çıkış- sıcaklığı, T <sub>5</sub> (°C)	29,58	24,57	31,41
Buharlaştırıcı giriş sıcaklığı, T <sub>6b</sub> (°C)	-4,39	-5,02	-5,76
Buharlaştırıcı çıkış sıcaklığı, T <sub>7</sub> (°C)	28,82	23,95	29,57
Soğurucu giriş sıcaklığı, T <sub>8</sub> (°C)	25,02	20,01	33,06
Soğurucu çıkış sıcaklığı, T <sub>9</sub> (°C)	29,02	28,1	41,17
Isı Değiştirici zengin çözelti giriş sıcaklığı, T <sub>10</sub> (°C)	30,59	28,45	39,74
Isı Değiştirici fakir çözelti çıkış sıcaklığı, T <sub>11</sub> (°C)	30,83	28,75	41,15
Sistem basıncı, P (bar)	13,00	13,00	12,02
Isıtıcı gücü, $\dot{Q}_{\text{ISITICI}}$ (W)	63	63	63

Çalışma akışkanlarının DAR çevrimin her bir noktasındaki termodinamik özellikleri, sıcaklık ve basıncın fonksiyonu olarak REFPROP 9.0 yazılımından elde edilmiştir. Kütle, enerji ve ekserji dengeleri ve termodinamik özellik denklemleri eş zamanlı olarak çözülmüştür. Tablo 2’de verilen ortalama sıcaklık ve

sistem basıncı değerlerine bağlı olarak her bir nokta için hesaplanan kütleli debi ve amonyak kütle derişim oranı değerleri Tablo 3’de ve her bir ekipman için enerji analiz eşitliklerinden bulunan ısı transfer hızı ( $\dot{Q}$ ) sonuçları Şekil 7’de verilmiştir.

**Tablo 3.** Deneysel olarak hesaplanan kütleli debi ve amonyak kütle derişim oranı

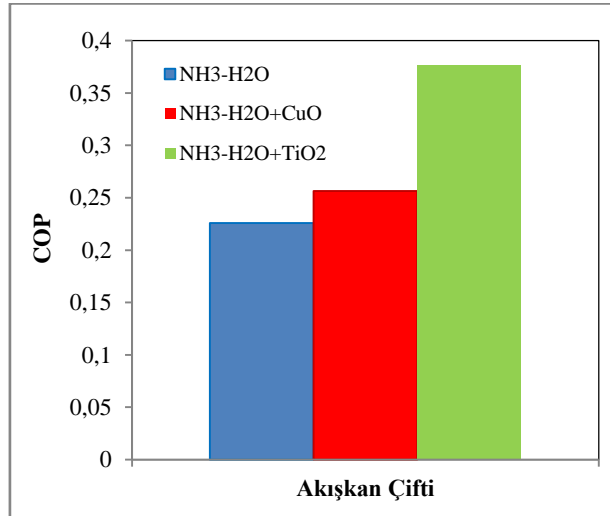
Noktalar	NH <sub>3</sub> -H <sub>2</sub> O-He		NH <sub>3</sub> -H <sub>2</sub> O-He+CuO		NH <sub>3</sub> -H <sub>2</sub> O-He+TiO <sub>2</sub>	
	X	$\dot{m}$ (kg s <sup>-1</sup> )	X	$\dot{m}$ (kg s <sup>-1</sup> )	X	$\dot{m}$ (kg s <sup>-1</sup> )
1 <sub>a</sub>	0,32	5,36942E-05	0,32	6,28820E-05	0,32	9,97040E-05
1 <sub>b</sub>	0,175	4,29559E-05	0,175	5,06597E-05	0,187	8,18209E-05
2 <sub>c</sub>	0,102	2,62169E-05	0,118	3,52686E-05	0,17	7,29018E-05
2 <sub>d</sub>	0,29	1,67390E-05	0,308	1,53911E-05	0,331	8,91903E-06
3	0,528	2,74773E-05	0,578	2,76134E05	0,728	2,68021E-05
4	0,899	1,07383E-05	0,918	1,22223E-05	0,926	1,78831E-05
5	0,899	1,07383E-05	0,918	1,22223E-05	0,926	1,78831E-05
6 <sub>a</sub>	0,899	1,07383E-05	0,918	1,22223E-05	0,926	1,78831E-05
7 <sub>a</sub>	0,899	1,20641E-06	0,918	1,09175E-06	0,926	1,4291E-06
8 <sub>a</sub>	0,899	1,20641E-06	0,918	1,09175E-06	0,926	1,42910E-06
8 <sub>b</sub>	0,175	4,29559E-05	0,175	5,06597E-05	0,187	8,18209E-05
9	0,32	5,36942E-05	0,32	6,28820E-05	0,32	9,97040E-05
10	0,32	5,36942E-05	0,32	6,28820E-05	0,32	9,97040E-05
11	0,175	4,29559E-05	0,175	5,06597E-05	0,187	8,18209E-05
$\dot{I}_g=m_{8a}=m_{7a}$	---	1,20641E-06	---	1,09175E-06	---	1,4291E-06



Şekil 7. DAR sisteminin her bir ekipmanı için ısı transfer hızı sonuçları

Şekil 7’de görüldüğü gibi aynı ısıtıcı gücü (63W) ve benzer çevre sıcaklığında, en yüksek enerji kaybı  $\text{NH}_3\text{-H}_2\text{O-He}$  ve  $\text{NH}_3\text{-H}_2\text{O-He+CuO}$  kullanan sistemde saflaştırıcıda meydana gelirken,  $\text{NH}_3\text{-H}_2\text{O-He+TiO}_2$  çalışma akışkanlı sistemde yoğuşturucuda meydana gelmiştir. En düşük enerji kaybı ise üç sistemde de ısı değiştiricide meydana gelmiştir. En yüksek soğutma yükü  $\text{NH}_3\text{-H}_2\text{O-He+TiO}_2$  çalışma akışkanlı kullanan sistemde 23,708 W olarak elde edilirken en düşük soğutma yükü  $\text{NH}_3\text{-H}_2\text{O-He}$  çalışma akışkanlı sistemde 14,23 W olarak elde edilmiştir. Saflaştırıcıda en yüksek enerji kaybı 36,049 W olarak  $\text{NH}_3\text{-H}_2\text{O-He}$  kullanan sistemde oluşurken, en düşük enerji kaybı 19,682 W olarak  $\text{NH}_3\text{-H}_2\text{O-He+TiO}_2$  çalışma akışkanlı sistemde meydana gelmiştir. Isı değiştiricide en yüksek enerji kaybı  $\text{NH}_3\text{-H}_2\text{O-He+TiO}_2$  kullanan sistemde 8,689 W olarak hesaplanırken en düşük enerji kaybı 5,326 W olarak  $\text{NH}_3\text{-H}_2\text{O-He+CuO}$  kullanan sistemde

hesaplanmıştır. Yoğuşturucudan çevreye atılan en yüksek ısı atımı  $\text{NH}_3\text{-H}_2\text{O-He+TiO}_2$  kullanan sistemde 21,334 W olarak gerçekleşirken en düşük ısı atımı 12,175 W olarak  $\text{NH}_3\text{-H}_2\text{O-He}$  çalışma akışkanlı sistemde gerçekleşmiştir. Soğutucuda meydana gelen en yüksek enerji kaybı 20,7 W olarak  $\text{NH}_3\text{-H}_2\text{O-He+TiO}_2$  çalışma akışkanlı sistemde oluşurken en düşük enerji kaybı 12,597 W olarak  $\text{NH}_3\text{-H}_2\text{O-He}$  kullanan sistemde oluşmuştur. Borularda meydana gelen en yüksek enerji kaybı  $\text{NH}_3\text{-H}_2\text{O-He+TiO}_2$  çalışma akışkanlı sistemde 16,303 W olarak hesaplanırken en düşük enerji kaybı 10,969 W olarak  $\text{NH}_3\text{-H}_2\text{O-He}$  kullanan sistemde hesaplanmıştır.



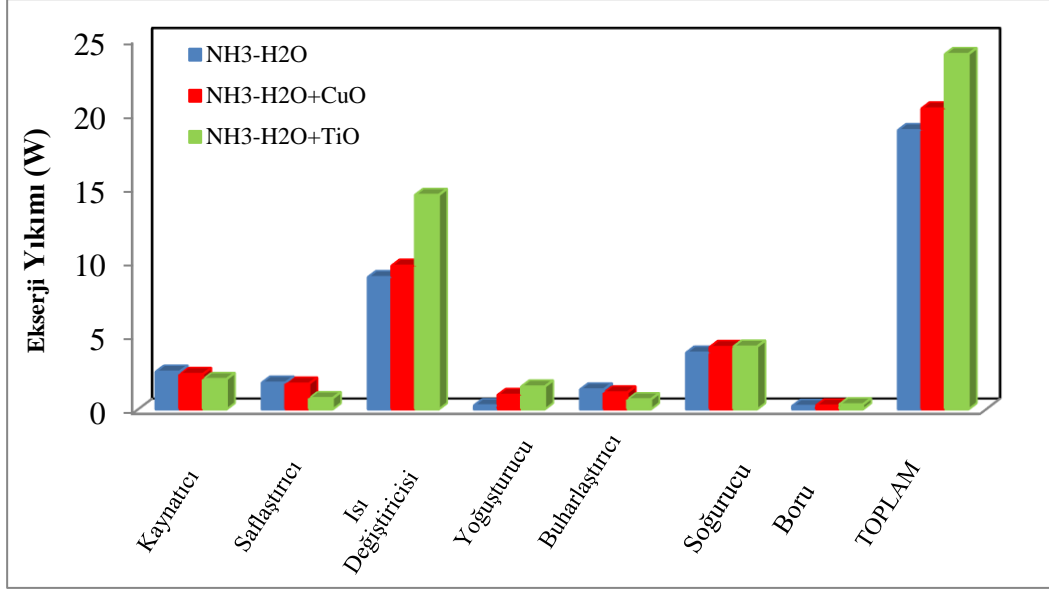
Şekil 8. Akışkan çiftlerin soğutma performans katsayısı

Şekil 8’de,  $\text{NH}_3\text{-H}_2\text{O-He}$ ,  $\text{NH}_3\text{-H}_2\text{O-He+CuO}$  ve  $\text{NH}_3\text{-H}_2\text{O-He+TiO}_2$  çalışma akışkanlı sistem için ortalama soğutma performans katsayısı (COP) değerleri verilmiştir.

Şekil 8’den görüldüğü gibi,  $\text{NH}_3\text{-H}_2\text{O-He}$ ,  $\text{NH}_3\text{-H}_2\text{O-He+CuO}$  ve  $\text{NH}_3\text{-H}_2\text{O-He+TiO}_2$  çalışma akışkanlı sistemlerin COP değeri sırasıyla 0,226, 0,256 ve 0,377 olarak hesaplanmıştır. Dolayısıyla, CuO nano partikülünün enerji performans katsayısını % 13,32 ve  $\text{TiO}_2$  nano partikülünün enerji performans katsayısını % 66,75 arttırdığı gözlemlenmiştir.

Elde edilen enerji analizi, enerji kullanım süreçlerinin tüm yönlerinin anlaşılması açısından tam olarak tek başına yeterli değildir. Bu yüzden DAR sisteminde enerji verimliliğini daha iyi anlayabilmek için termodinamiğin birinci ve ikinci yasalarına dayanan enerji ve ekserji analizlerinin yapılması gerekmektedir.

Şekil 9’da her bir ekipmanda meydana gelen ekserji yıkım değerleri karşılaştırılmıştır.

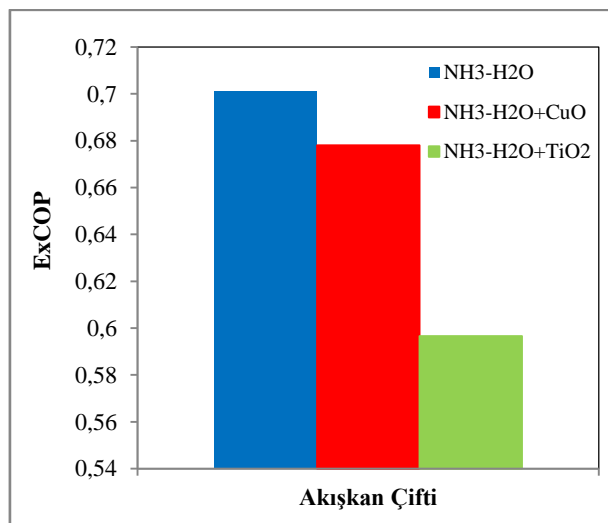


Şekil 9. Sistem ekipmanlarında oluşan ekserji yıkım değerleri

Şekil 9'da görüldüğü gibi aynı ısıtıcı gücü ve çevre sıcaklığında, üç sistem için de en yüksek ekserji yıkımı ısı değiştiricisinde meydana gelirken en düşük ekserji yıkımı ise için boru hattında meydana gelmektedir. Sıfırlatıcıda en büyük ekserji yıkımı NH<sub>3</sub>-H<sub>2</sub>O-He çalışma akışkanlı sistemde 1,787 W olarak hesaplanırken, en düşük ekserji yıkımı NH<sub>3</sub>-H<sub>2</sub>O-He+TiO<sub>2</sub> kullanan sistemde 0,743 W olarak hesaplanmıştır. Isı değiştiricisinde en yüksek ekserji yıkımı 14,448 W olarak NH<sub>3</sub>-H<sub>2</sub>O-He+TiO<sub>2</sub> kullanan sistemde hesaplanırken, en düşük ekserji yıkımı 8,896 W olarak NH<sub>3</sub>-H<sub>2</sub>O-He çalışma akışkanlı sistemde oluşmuştur. Yoğuşturucuda en büyük ekserji yıkımı NH<sub>3</sub>-H<sub>2</sub>O-He+TiO<sub>2</sub> kullanan sistemde 1,526 W olarak

bulunurken, en düşük ekserji yıkımı 0,259 W olarak NH<sub>3</sub>-H<sub>2</sub>O-He çalışma akışkanlı sistemde hesaplanmıştır. Buharlaştırıcıda en yüksek ekserji yıkımı NH<sub>3</sub>-H<sub>2</sub>O-He çalışma akışkanlı sistemde 1,328 W olarak bulunurken, en düşük ekserji yıkımı NH<sub>3</sub>-H<sub>2</sub>O-He+TiO<sub>2</sub> çalışma akışkanlı sistemde 0,669 W olarak hesaplanmıştır. Soğurucuda en yüksek ekserji yıkımı NH<sub>3</sub>-H<sub>2</sub>O-He+TiO<sub>2</sub> çalışma akışkanlı sistemde 4,215 W bulunurken, en düşük ekserji yıkımı 3,809 W olarak NH<sub>3</sub>-H<sub>2</sub>O-He çalışma akışkanlı sistemde bulunmuştur.

Şekil 10'da NH<sub>3</sub>-H<sub>2</sub>O-He, NH<sub>3</sub>-H<sub>2</sub>O-He+CuO ve NH<sub>3</sub>-H<sub>2</sub>O-He+TiO<sub>2</sub> çalışma akışkanlı sistem için bulunan ekserji performansı (ExCOP) değerleri verilmiştir



Şekil 10. Akışkan çiftlerinin ekserji performans değerleri

Şekil 10'da görüldüğü gibi, NH<sub>3</sub>-H<sub>2</sub>O-He, NH<sub>3</sub>-H<sub>2</sub>O-He+CuO ve NH<sub>3</sub>-H<sub>2</sub>O-He+TiO<sub>2</sub> çalışma akışkanlı sistemlerde sırasıyla ExCOP değeri 0,701, 0,678 ve 0,597 olarak hesaplanmıştır. Nano partikül ilavesi sistem ekipmanlarında daha yüksek ekserji yıkımına sebep olduğundan dolayı soğutma performans katsayısının (COP) aksine ekserji performansını düşürmüştür. CuO ve TiO<sub>2</sub> nano partikülü sistemin ekserji performansını sırasıyla % 3,42 ve % 17,53 azaltmıştır.

## TARTIŞMA VE ÖNERİLER

Bu çalışmada, NH<sub>3</sub>-H<sub>2</sub>O-He çalışma akışkanı kullanan DAR sisteminin performansı, benzer ısıtıcı gücü ve çevre sıcaklığında CuO ve TiO<sub>2</sub> nano partikülleri ilave edilen sistemlerin performansları ile deneysel olarak karşılaştırılmıştır.

Çalışmadan elde edilen sonuçlar aşağıda sıralanmıştır.

(1)  $\text{NH}_3\text{-H}_2\text{O-He}$ ,  $\text{NH}_3\text{-H}_2\text{O-He+CuO}$ ,  $\text{NH}_3\text{-H}_2\text{O-He+TiO}_2$  akışkan kullanan sistemler soğutmaya geçtikten sonra kararlı hale sırasıyla 119. dakika, 215. dakika ve 143. dakikadan itibaren geçmiştir.

(2)  $\text{NH}_3\text{-H}_2\text{O-He}$ ,  $\text{NH}_3\text{-H}_2\text{O-He+CuO}$  ve  $\text{NH}_3\text{-H}_2\text{O-He+TiO}_2$  kullanan sistemlerde ortalama elektrik tüketimi 63 W olarak ölçülmüştür.

(3)  $\text{TiO}_2$  nano partikülünün sistemin çalışma basıncını düşürdüğü,  $\text{CuO}$  nano partikülünün sistem çalışma basıncında herhangi bir etki yaratmadığı gözlemlenmiştir.

(4) En yüksek enerji kaybı  $\text{NH}_3\text{-H}_2\text{O-He}$  ve  $\text{NH}_3\text{-H}_2\text{O-He+CuO}$  çalışma akışkanlı sistemde saflaştırıcıda meydana gelirken,  $\text{NH}_3\text{-H}_2\text{O-He+TiO}_2$  çalışma akışkanlı sistemde yoğunlaştırıcıda meydana gelmiştir.

(5) En yüksek soğutma kapasitesi  $\text{NH}_3\text{-H}_2\text{O-He+TiO}_2$  akışkanlı sistemde elde edilirken, en düşük soğutma kapasitesi  $\text{NH}_3\text{-H}_2\text{O-He}$  çalışma akışkanlı sistemde elde edilmiştir.

(6) En yüksek enerji performansı  $\text{NH}_3\text{-H}_2\text{O-He+TiO}_2$  kullanılan sistemde elde edilirken, en düşük enerji

performansı  $\text{NH}_3\text{-H}_2\text{O-He}$  kullanan sistemde elde edilmiştir.

(7)  $\text{TiO}_2$  nano partikülünün soğutma performans katsayısını % 66,75,  $\text{CuO}$  nano partikülünün % 13,32 arttırdığı gözlemlenmiştir.

(8)  $\text{NH}_3\text{-H}_2\text{O-He}$ ,  $\text{NH}_3\text{-H}_2\text{O-He+CuO}$  ve  $\text{NH}_3\text{-H}_2\text{O-He+TiO}_2$  çalışma akışkanlı üç sistemde de en yüksek ekserji yıkımı ısı değiştiricisinde oluşurken, en düşük ekserji yıkımı borularda meydana gelmiştir.

(9) Soğutma performans katsayısının aksine en yüksek ekserji performansı  $\text{NH}_3\text{-H}_2\text{O-He}$  kullanan sistemde elde edilirken, en düşük ekserji performansı  $\text{NH}_3\text{-H}_2\text{O-He+TiO}_2$  çalışma akışkanlı sistemden elde edilmiştir.

(10)  $\text{CuO}$  nano partikülünün enerji performans katsayısının aksine ekserji performansını % 3.42 azalttığı,  $\text{TiO}_2$  nano partikülünün ekserji performansını % 17,53 azalttığı gözlemlenmiştir.

İlerleyen çalışmalarda farklı nano partiküllerin DAR sistemlerinde enerji ve ekserji performansı üzerinde etkileri termoeconomik açıdan da incelenebilir.

## KAYNAKLAR

Adjibade, M. I. S., Thiam, A., Awanto, C., Azilnon, D., 2017, Experimental analysis of diffusion absorption refrigerator driven by electrical heater and engine exhaust gas, *Case Stud. Therm. Eng.*, 10, 255–261.

Adjibade, M. I. S., Thiam, A., Awanto, C., Ndiogou, B. A., Sambou, V., 2017, Dynamic investigation of the diffusion absorption refrigeration system  $\text{NH}_3\text{-H}_2\text{O-H}_2$ , *Case Stud. Therm. Eng.*, 10, 468–474.

Arslan, M. E. ve Eğrican, A. N., 2004, Buzdolabı Uygulamasında Kullanılan Absorpsiyonlu Soğutma Sisteminin Termodinamik Analizi, *Tesisat Mühendisliği Dergisi*, 83, 53-63.

Chaves, F. D., Moreira, M. F. S., Koury, R. N., Machado, L., Cortez, M. F. B., 2019, Experimental study and modeling within validation of a diffusion absorption refrigerator, *Int. J. Refrigeration*, 101, 136–147.

Chen, J., Kim, K. J., Herold, K. E., 1996, Performance enhancement of a diffusion absorption refrigerator, *Int. J. Refrigeration*, 19, 208-218.

Dağdevir T., Özceyhan V., 2016, Thermal performance analyses of water based  $\text{CuO-TiO}_2$  hybrid nanofluid flow in a horizontal tube, *Journal of fCE – Scientific paper*, 4, 49-54.

Ersöz, M. A., 2015, Investigation the effects of different heat inputs supplied to the generator on the energy performance in diffusion absorption refrigeration systems, *Int. J. Refrigeration*, 54, 10-21.

Gürbüz, E. Y., Sözen, A., Keçebaş, A., Özbaş, E., 2020, Experimental and numerical investigation of diffusion absorption refrigeration system working with  $\text{ZnOAl}_2\text{O}_3$  and  $\text{TiO}_2$  nanoparticles added ammonia/water nanofluid, *Exp. Heat Transf.*, A head of print, 1-26.

İnternet, 2018, Nanografi, <https://nanografi.com> (07.10.2018 tarihinde erişilmiştir).

Jakob, U., Eicker, U., Schneider, D., Taki, A. H., Cook, M. J., 2008, Simulation and experimental investigation into diffusion absorption cooling machines for air-conditioning applications, *Appl. Therm. Eng.* 28, 1138-1150.

Jemaa, R. B., Mansouri, R., Boukholda, I., Bellagi, A., 2017, Experimental characterization and performance study of an ammonia–water–hydrogen refrigerator, *Int. J. Hydrogen Energ.*, 42, 8594-860.

Jiang W., Li S., Yang L., Du K., 2019, Experimental investigation on performance of ammonia absorption refrigeration system with  $\text{TiO}_2$  nanofluid, *Int. J. Refrigeration*, 98, 80-88.

- Khanafer K., Vafai K., 2011, A Critical Synthesis of Thermophysical Characteristics of Nano-Fluids, *Int. Journal of Heat and Mass Transfer*, 54, 4410-4428.
- Koyfman, A., Jelinek, M., Levy, A., Borde, I., 2003, An experimental investigation of bubble pump performance for diffusion absorption refrigeration system with organic working fluids, *Appl. Therm. Eng.*, 23, 1881-1894.
- Lee, J., Lee, K. R., Kang, Y. T., 2014, Development of binary nanoemulsion to apply for diffusion absorption refrigerator as a new refrigerant, *Energy*, 78, 693-700.
- Mansouri, R., Bourouis, M., Bellagi, A., 2018, Steady state investigations of a commercial diffusion-absorption refrigerator: Experimental study and numerical simulations, *Appl. Therm. Eng.*, 129, 725-734.
- Mazouz, S., Mansouri, R., Bellagi, A., 2014, Experimental and thermodynamic investigation of an ammonia/water diffusion absorption machine, *Int. J. Refrigeration*, 45, 83-91.
- Özbaş, E., 2009, Yayınımlı soğurmalı soğutma sistemi tasarımı, imali, deneysel ve teorik analizi ile performans iyileştirilmesi, Doktora tezi, Gazi Üniversitesi Fen Bilimleri Enstitüsü, Ankara, Türkiye.
- Özbaş, E., 2021, Energy and exergy analysis of using FeOTiO<sub>2</sub> nanofluid in diffusion absorption refrigeration systems, *Heat Transf. Res.*, 11-24.
- Srikhirin, P., Aphornratana, S., 2002, Investigation of a diffusion absorption refrigerator, *Appl. Therm. Eng.*, 22, 1181-1893.
- Soli, N., Hafsi, N. B., Chaouachi, B., 2017, Thermodynamic feasibility study of absorption diffusion machine working with hydrocarbons, *Int. J. Hydrogen Energ.*, 42, 8881-8887.
- Sözen, A., Menlik, T., Özbaş, E., 2012, The effect of ejector on the performance of diffusion absorption refrigeration systems: an experimental study, *Appl. Therm. Eng.*, 33-34, 44-53.
- Sözen, A., ve Özalp, M., 2003, Performance improvement of absorption refrigeration system using triple-pressure-level, *Appl. Therm. Eng.*, 23, 1577-1593.
- Sözen, A., Keçebaş, A., Gürbüz, E. Y., 2021, Enhancing the thermal performance of diffusion absorption refrigeration system by using magnesium aluminate spinel oxide compound nanoparticles: an experimental investigation, *Heat Mass Transfer*, 57, 1583-1592.
- Sözen, A., Özbaş, E., Menlik, T., Çakır M. T., Gürü, M., Boran, K., 2014, Improving the thermal performance of diffusion absorption refrigeration system with alimuna nanofluids: an experimental study, *Int. J. Refrigeration*, 44, 73-80.
- Sözen, A., Özbaş, E., Menlik, T., Çiftçi, E., İskender, Ü., 2015, Difüzyonlu absorpsiyonlu mini soğutucularda nanoakışkan kullanımının ekserji performansına etkisi, *Gazi Mühendislik Bilimleri Dergisi*, 99-118.
- Starace, G., Pascalis, L. D., 2012, An advanced analytical model of the diffusion absorption refrigerator cycle, *Int. J. Refrigeration*, 35, 605-612.
- Starace, G., Pascalis, L. D., 2013, An enhanced model for the design diffusion absorption refrigerators, *Int. J. Refrigeration*, 36, 1495-1503.
- Sunal, S., 2019, Difüzyon absorpsiyon soğutma sistemlerinde nanopartikül kullanımının ısı performansına etkisi, Yüksek Lisans tezi, Uşak Üniversitesi Fen Bilimleri Enstitüsü, Uşak, Türkiye.
- Taieb, A., Mejbri, K., Bellagi, A., 2016, Detailed thermodynamic analysis of a diffusion-absorption refrigeration cycle, *Energy*, 115, 418-434.
- Wang, S. K., Wang, J., Wang Q., Wang, Y. L., Zhao, J. Y., Chen, G. M., 2017, Experimental research on the performance of the diffusion absorption refrigerator with mixed fluoride refrigerants, *Int. J. Refrigeration*, 81, 50-59.
- Wang, Q., Gong, L., Wang, J. P., Sun, T. F., Cui, K., Chen, G. M., 2011, A numerical investigation of a diffusion absorption refrigerator operating with the binary refrigerant for low temperature applications, *Appl. Therm. Eng.*, 3, 1763-1769.
- Yıldız, A., ve Ersöz, M. A., 2013a, Energy and exergy analyses of the diffusion absorption refrigeration system, *Energy*, 60, 407-415.
- Yıldız, A., Ersoz, M. A., Gözmen, B., 2014, Effect of insulation on the energy and exergy performances in DAR systems, *Int. J. Refrigeration*, 44 161-167.
- Yıldız, A., 2016, Thermoeconomic analysis of diffusion absorption refrigeration systems, *Appl. Therm. Eng.*, 99, 23-31.
- Yıldız, A., Ersöz M., A., 2013b, Yayınımlı Soğurmalı Soğutma Sisteminin Deneysel İncelenmesi ve Soğutma Verimi Analizi, 11. Ulusal Tesisat Mühendisliği Kongresi, İzmir, 789-798.
- Ziapour B. M., ve Tavakoli M., 2011, Performance study on a diffusion absorption refrigeration heat pipe cycle, *Int. J. Therm. Sci.*, 50, 592-598.

Zohar, A., Jelinek, M., Levy, A., Borde, I., 2005, Numerical investigation of a diffusion absorption refrigeration cycle, *Int. J. Refrigeration*, 28, 515-525.

Zohar, A., Jelinek, M., Levy, A., Borde, I., 2007, The influence of diffusion absorption refrigeration cycle configuration on the performance, *Appl. Therm. Eng.*, 27, 2213-2219.

Zohar, A., Jelinek, M., Levy, A., Borde I., 2008, The influence of the generator and bubble pump configuration on the performance of diffusion absorption refrigeration (DAR) system, *Int. J. Refrigeration*, 20, 962-969.

Zohar, A., Jelinek, M., Levy, A., Borde, I., 2009, Performance of diffusion absorption refrigeration cycle with organic working fluids, *Int. J. Refrigeration*, 32, 1241-1246.



## ANALYSIS OF THERMAL CRACK FORMATION IN WATER-CHARGED AIR-COOLED HEAT EXCHANGERS FOR HEAVY-DUTY VEHICLES

İsmail Hakkı SAVCI

Ford Otosan Flow Performance Durability Department  
34885 Sancaktepe, İstanbul, Turkey  
isavci@ford.com.tr, ORCID: 0000-0002-7923-6061

(Geliş Tarihi: 27.04.2022, Kabul Tarihi: 12.02.2023)

**Abstract:** The non-uniform flow distribution at the inlet severely affects the thermal cycling loading of the water-charged air-cooled (WCAC) systems resulting in crack formation after periods and hence leakage in the internal coolant. These cracks are serious since having crucial effects on performance and durability. This work developed a custom thermal fatigue test rig and methodology to precisely determine the crack formation's location and cycle time in WCACs. The test rig was designed to reflect the vehicle's situation by simultaneously controlling the air and waterside of the WCAC continuously. The crack formation occurred by performing tests with different critical cycles on the test rig because a specific cycle was observed, and a thermal cycle profile was created. It was seen that the crack formation in the WCAC can be predicted at the same cycle time and exact location with this test rig compared to the vehicle tests. Moreover, the total cost, time, and man-hours per test decreased by 80 %, 75 %, and 60, % respectively, compared to traditional vehicle tests. Subsequently, the modified WCAC design was proposed to prevent non-uniform flow distribution at the inlet of the WCAC. The thermal fatigue tests of the modified WCAC design were tested in a developed test rig for stressful operating conditions. The results showed that the modified WCAC design is more robust than the old design. There was no crack formation in the modified WCAC design under various stressful operating conditions.

**Keywords:** WCAC, Heat-exchanger, Thermal Fatigue, Thermal Cracking, Automotive Applications

## AĞIR HİZMET ARAÇLARI İÇİN SU ŞARJLI HAVA SOĞUTMALI ISI DEĞİŞTİRİCİLERİNDE ISIL ÇATLAK OLUŞUMUNUN ANALİZİ

**Özet:** Girişteki muntazam olmayan akış dağılımı, su şarjlı hava soğutmalı (WCAC) sistemlerin termal döngü yüklemesini ciddi şekilde etkiler, bu da belirli çevrimlerden sonra çatlak oluşumuna ve dolayısıyla dahili soğutucuda sızıntıya neden olur. Bu çatlaklar, performans ve dayanıklılık üzerinde önemli etkilere sahip olduğundan ciddidir. Bu çalışmayla, WCAC'lerde çatlak oluşumunun yerini ve döngü süresini kesin olarak belirlemek için özel bir termal yorulma test donanımı ve metodolojisi geliştirildi. Test teçhizatı, WCAC'ın hava ve su tarafını aynı anda sürekli olarak kontrol ederek aracın durumunu yansıtacak şekilde tasarlanmıştır. Test teçhizatı üzerinde farklı kritik çevrimlerle testler yapılarak belirli çevrim sonucunda oluşam çatlak gözlemlenmiş ve termal çevrim profili oluşturulmuştur. Bu test düzeneği ile WCAC içerisindeki çatlak oluşumunun araç testlerine göre aynı çevrim süresinde ve tam lokasyonda tahmin edilebildiği görülmüştür. Ayrıca, geleneksel araç testlerine kıyasla test başına toplam maliyet, zaman ve adam-saat sırasıyla %80, %75 ve %60 azaldı. Daha sonra, WCAC girişinde üniform olmayan akış dağılımını önleyen için değiştirilmiş WCAC tasarımı geliştirildi. Modifiye edilmiş WCAC tasarımının termal yorulma testleri, zorlu çalışma koşulları için geliştirilmiş bir test profili ile test riginde test edilmiştir. Sonuçlar, değiştirilmiş WCAC tasarımının eski tasarıma göre daha sağlam olduğunu göstermiştir. Çeşitli zorlu çalışma koşulları altında değiştirilmiş WCAC tasarımında herhangi bir çatlak oluşumu olmamıştır.

**Anahtar Kelimeler:** WCAC, Eşanjör, Termal Yorulma, Termal Çatlama, Otomotiv Uygulamaları

### NOMENCLATURE

#### Abbreviations

EGR Engine Gas Recirculation  
ACAC Air Charged Air Cooler  
WCAC Water Charged Air Cooler

#### MAE

Mean Absolute Error

#### Subscripts

$u$  Velocity Related Value  
 $T$  Temperature  
BC Boundary Condition  
Symbols



$p$	Pressure
$\varepsilon$	Average Strain Magnitude
$M$	Mass Flow Meter
$t$	Non-dimensional Time

## INTRODUCTION

Although electric vehicles have emerged in daily life, motor vehicles are still the primary form of transportation in the world (Panchal et al., 2018). However, the environmental and social damages of exhaust emissions have reached critical degrees, resulting in stringent regulations by policymakers. Consequently, motor vehicle manufacturers have researched alternative solutions to release exhaust emission levels. Subasi et al. (2017) reported that the transportation sector, including rail, aviation, shipping, and road transportation is responsible for 30 % of global carbon dioxide emissions. One way to reduce exhaust emissions is by improving the efficiency of the engine cooling system. The efficient cooling produces lower smoke (particulate) emissions due to higher density and the air-fuel ratio (Edara et al., 2019). The purpose of the engine cooling system is to prevent the vehicle engine from overheating by keeping the engine at optimum operating temperature. Various novel architectures of cooling systems have been developed to improve the cooling system's efficiency and meet new emission regulations. The Water Charged Air Cooler (WCAC) and the Air Charged Air Cooler (ACAC) systems can be mentioned. These systems regulate the pressure and distribution of the exhaust gas at the inlet of the cooling loop. In ACAC systems, the primary and secondary fluids are air, whereas the primary fluid is air, and the secondary fluid is water in WCAC systems. WCACs are heat exchangers facilitating heat transfer between two fluids at different temperatures. WCACs use lower charge air temperatures than ACACs, which leads to lower temperatures for combustion gases and, therefore, produces lower NO<sub>x</sub> emissions (Lujan et al., 2016).

Furthermore, the WCAC improves the engine response in transient conditions by reducing the charge air volume between the compressor and the engine. Besides, the WCAC increases the engine's durability by reducing the temperature in the cylinders and the exhaust system (Broatch et al., 2008). The WCAC is located between the turbocharger and the engine air inlet manifold in heavy-duty engines. The WCAC and turbocharger are part of a high-tech induction system that increases engine combustion efficiency. The ambient air is compressed and heated in the turbocharger before it enters the WCAC. The compressed and warm air directs to the WCAC and is cooled by the cold ambient air flowing across the cooler fins. Since the cold air is denser than the warm air, the volumetric air rate entering the engine increases. Therefore, the power and engine efficiency

improvements and fuel consumption and exhaust emissions decrease (Burgold et al., 2012); (Arikan et al., 2008); (Savci et al., 2022). WCACs are operated in highly stressful environments, and consequently, the parts of the WCAC must be resistant to thermal load and vibration. Otherwise, system components may be damaged over time due to thermal fatigue (Torregrosa et al., 2008). The damage in the system reduces the boost pressure and increases the intake manifold temperature. Hence, the engine provides lower power and higher emission levels than the design values (Joshi et al., 2009); (Wang et al., 2011).

In the literature, many studies reported that the non-uniform flow distribution at the inlet of heat exchangers might escalate wall heat conduction longitudinally. Therefore, the non-uniform flow distribution at the inlet of heat exchangers may be one of the responsible mechanisms of thermal fatigue cracks in the device (Yaici et al., 2014); (Demirkesen et al., 2020); (Holland et al., 2015); (Salmon et al., 2017); (Vashahi et al., 2014); (Iwahori et al., 2013). There are several methods to determine the location of the thermal cracks in engine cooling systems. These models can be summarised in three chapters. First, one is to monitor sensor data, fuse data from the sensors, and predict cracks; the second is to develop a test rig and repeat the cracks into experimental studies. The third one is to create finite element methods. Joshi et al. (2009) developed a model to diagnose a fault in the intercooler of different engines. The authors monitored the status of the WCAC intercooler by analyzing the intake manifold temperature signal. They blocked the air flowing over the intercooler by varying degrees for different engine temperatures, pressure, and torque conditions. It was found that the model successfully predicted the failure of the intercooler. Haider et al. (2015) designed a test rig to investigate thermal stress in aluminum-brazed plate-fin heat exchangers due to the transient temperature profiles. The researchers designed a test rig to reflect extreme operating conditions calculated by developing a finite element method-based model. The results showed that the location of maximum stress in the finite element method model matched the cracks observed in the heat exchanger. In another study, Iwahori et al. (2013) developed a finite element model of a WCAC intercooler using the homogenization method.

Usman and Khan (2008) investigated the failure reasons of heat exchanger tubes experimentally using a tube material ASTM A213 grade T11. They found that the cracks across the tube axis are caused by thermal fatigue due to temperature variations causing stresses in the tube wall. They reported that the cyclic heating and cooling caused thermal fatigue, which resulted in circumferential cracks. They also said that longitudinal cracks occurred due to exposure to higher-than-permissible temperatures. In a recent study, Ali et al.

(2020) reviewed the common failures in heat exchangers due to elevated temperature values. They concluded that thermal fatigues are one of the leading causes of failures in heat exchangers. They stated that thermal fatigue could be attributed to the oscillation in temperature because of poor water circulation. Also, they reported that thermal fatigue due to a rise in temperature or localized overheating caused transverse cracking in serpentine. They concluded that design modifications are needed to prevent cracks due to thermal fatigue. Since WCACs are heat exchangers, the design of the WCAC is essential since it is exposed to high thermal stress rates and therefore has a high possibility of crack formation (Ali et al., 2020).

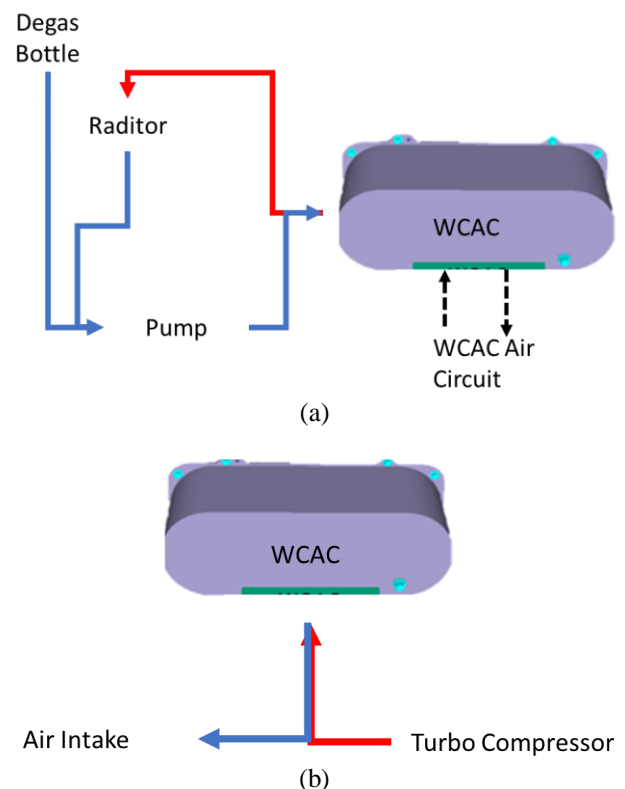
Consequently, several researchers attempted to modify the design of the intercoolers to prevent the thermal crack formation and increase the intercooler's lifetime. In a study by O'Connor and Trauger (1990), the effect of turbocharger outlet temperature on the durability of the charge air cooler was examined experimentally. They found that the elevated turbocharger outlet temperature resulted in higher strain magnitude and strain cycling of the charge air cooler. The design modifications in charge air coolers can help reduce the strain magnitudes. In another study, Kolb et al. (1998) proposed using a resilient tube to header joints and grommets seals between the tubes and headers in a charge air cooler to eliminate the high stresses in the device and consequently provide longer equipment life. They reported that the new charge air cooler design with the mentioned modifications did not show any leakage on the surface of the charge air cooler during vehicle tests. Mezher et al. (2013) analyzed the four-cylinder diesel engine to present the reflection characteristics of the intake of the WCAC intercooler. The results showed that the pipeline length between the intake manifold and intercooler has an essential effect on the system's thermal efficiency.

The above brief literature review indicates some studies to analyze crack formation due to thermal stress in heat exchangers. Furthermore, the literature review reveals that the non-uniform flow distribution at the inlet of heat exchangers is the dominant parameter of crack formation (Canyurt et al., 2022). However, there are limited studies to analyze crack formation due to thermal fatigue in WCAC intercoolers. The current study aims to design and validate an experimental setup to determine the crack formation's location and cycle time in WCAC intercoolers. Accordingly, the pre-existing WCAC intercooler design was modified to prevent crack formation due to thermal fatigue. The custom experimental setup was validated with vehicle test data. The proposed experimental setup can be an alternative to expensive and time-consuming traditional vehicle tests.

## MATERIALS AND METHODS

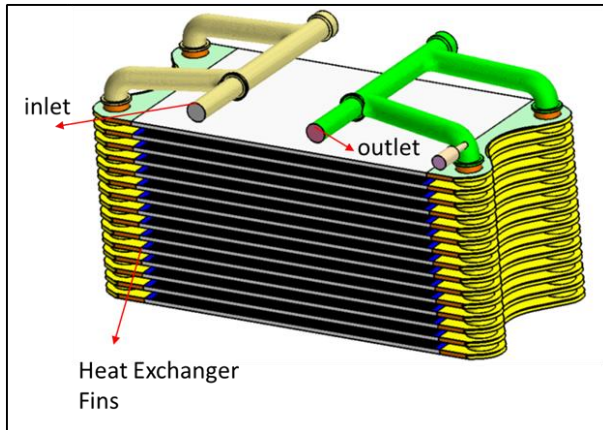
Water-charged air-cooled (WCAC) are specific heat exchangers used in particularly stressful conditions, such as internal combustion engines with turbochargers. When the turbocharger compresses the air, it is heated simultaneously, causing its density to decrease by cooling the combustion air with a charge air cooler before it is sent to the engine, the density of the air increases, allowing more air to enter the engine, increasing engine power and efficiency. The cooler in the engine is located between the turbocharger and the engine air intake manifold.

The cooler and turbocharger are part of a high-tech induction system that improves combustion efficiency. The turbocharger uses ambient air to compress it before entering the cooler. The ambient air flowing through the cooling fins cools the compressed air passing through the cooler. Cooled air is denser than warm air. Thus, when flowing to the intake side of the engine, the increased density increases horsepower, saves fuel, and reduces emissions. Figure 1 shows the WCAC cooling and air circuits schematically.



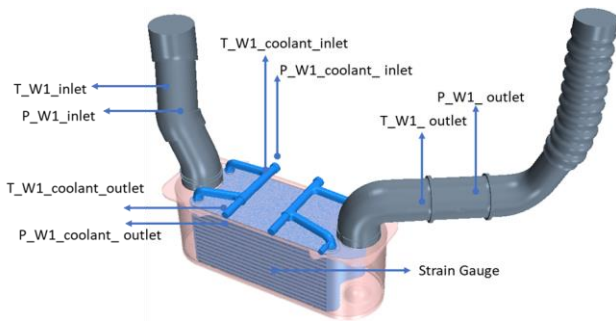
**Figure 1.** WCAC cooling circuit, (a) coolant circuit, (b) air circuit.

Integrating WCAC into the intake manifold is an ideal design solution that offers the best engine performance. The detailed schematic of the cooling part of the WCAC system can be shown in Figure 2. The main components of the cooling part are the fin, header, sidebar, and parting sheets. These components form a compact plate heat exchanger.



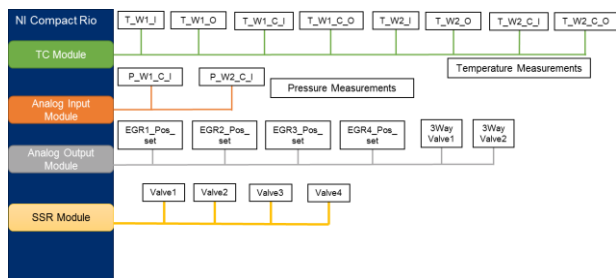
**Figure 2.** WCAC Cooling Part

Figure 3 shows the sensor instrumentation on the WCAC. The strain gauge is instrumented right side of the WCAC where the cracks occur.



**Figure 3.** Sensor Instrumentations

Figure 4 shows the temperature and pressure instrumentations on WCAC. The DSpace microautobox is used to control valves and the burner system. Due to the high temperature of the valve, the valve should be a cooling system, so the EGR valve is selected for this test bench. Sensor measurement is done by national instrument measurement cards.



**Figure 4.** Control Schematic of the WCAC Test Bench

During the vehicle tests on the heavy-duty truck engine, it was observed that the WCAC cooling part cracked due to thermal gradients in specific cycles under continuous thermal load. These cracks caused leaks in the intercooler. Figure 5 presents the average strain magnitude ( $\epsilon$ ) of the vehicle's durability test for four cycles of stressful and average conditions. It was observed that the crack formation started in the WCAC cooling part for the stressful operating condition. In

contrast, there was no evidence of a crack for the average operating condition for four cycles. The strain data in Figure 5 was used to construct the custom test rig to observe whether the test rig can simulate vehicle tests accurately. Cycle 1, cycle 2, cycle 3, and cycle 4 represent the tests applied to temperature profiles specified in Figure 6. The strain values are varied at 12 percent according to the average values.

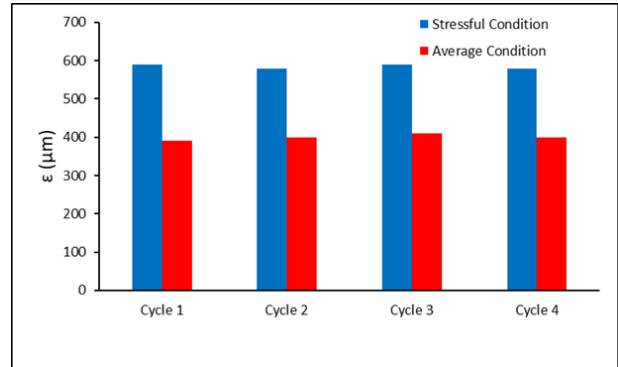
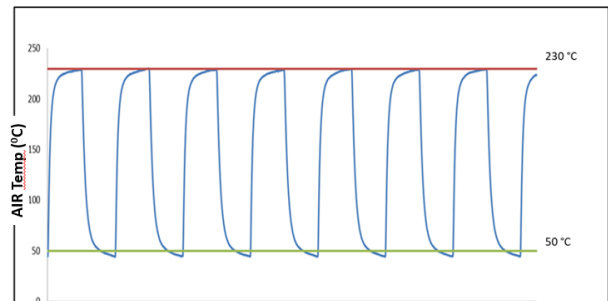
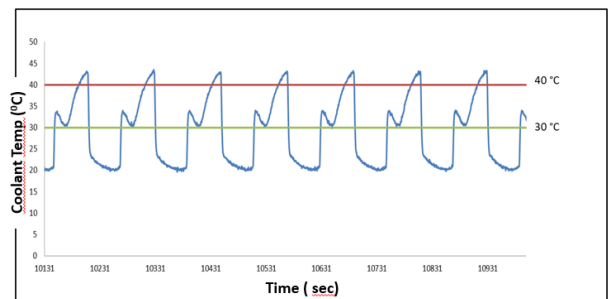


**Figure 5.** Average strain magnitude measurements for two different conditions from the vehicle test data

Furthermore, the temperature profiles of air and coolant sides were obtained for the stressful condition vehicle tests to reveal the maximum and minimum temperatures, in other words, boundary conditions of vehicle tests under variable thermal load to verify the custom test rig; please see Figures 6(a)-(b).



(a)



(b)

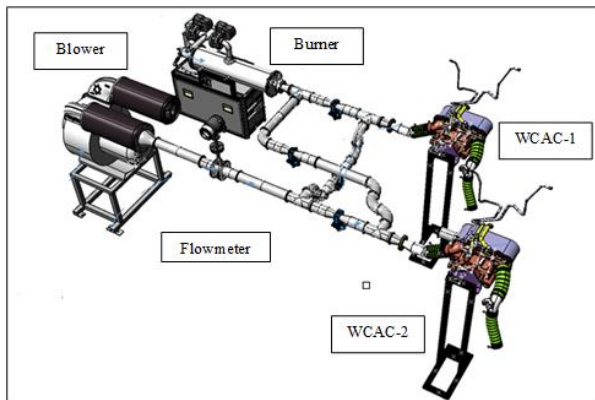
**Figure 6.** Temperature profile, (a) Airside, (b) Coolant side.

The boundary conditions of the test profile can be found in table 1. Figure 6a. red line represent BC1, green line represents BC2. Figure 6b red line represents BC3, and the green line represents BC4.

**Table 1.** Test parameters

		T	Unit	M	Unit
Hot Air	BC1	230	<sup>0</sup> C	1000	kg/h
Cold Air	BC2	50	<sup>0</sup> C	500	kg/h
Hot Water	BC3	40	<sup>0</sup> C	1000	l/h
Cold Water	BC4	30	<sup>0</sup> C	900	l/h

As mentioned above, the most effective way to find the main reasons for WCAC cracks is by performing vehicle tests. The vehicle test includes thermal fatigue tests with air and coolant flow cycles. However, the vehicle test could be more cost-effective due to many tests and parts requirements and maintenance of test types of equipment. Therefore, a custom test rig is designed to simulate the cooling mechanism of the engine completely. Figures 7(a)-(b) demonstrate the test rig's schematic drawing and photograph, respectively.



(a)

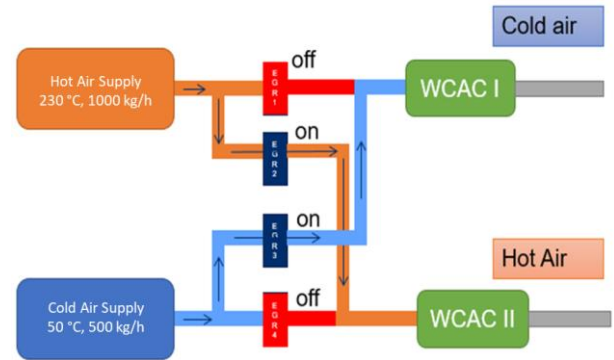


(b)

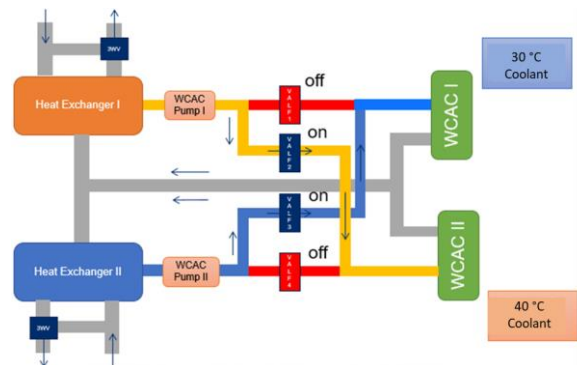
**Figure 7.** The WCAC test rig, (a) Schematic Drawing, (b) Photograph.

The test rig consists blower system for cold air supply, an AC motor with an inverter speed controller of 22 kW, a burner system with 400 kW which works with natural gas, the mass flowmeter (40-1500kg/h), a data acquisition system ( national instruments ) for measurement and data recording, solenoid valves to control coolant flow, EGR valves to control airflow and a three-way valve with a proportional controller to control the temperature of the coolant. As a result, two identical WCAC coolers can be tested simultaneously in the test rig, as shown in Figure 7 (a).

The test rig has two synchronic cycles: air and coolant cycles. These two loops are driven by four different EGR valves controlled by the data acquisition system. As can be seen from Figures. 8(a-b), WCAC-1 and WCAC-2 return the coolant with two different WCAC pumps. The positions of the valves are switched to direct the flow to the system at the desired condition. The flow enters the test bench from two entrances, as seen in Figures 8(a)-(b) below, and reaches the EGRs. After that, the flow goes to WCAC-1 or WCAC-2 according to the path assigned. The positions of EGRs are controlled for the cold airpath and hot air path in different ways. The cold air source is a blower, whereas the burner supplies the hot air to the test chamber.



(a)



(b)

**Figure 8.** The cycle diagram of the test rig, (a) air, (b) coolant.

The tests were conducted three times for two identical WCACs in cold flow and hot flow conditions separately to ensure the repeatability of tests. Therefore, experimental tests are always subject to some uncertainty. The uncertainty values for the measured parameters are obtained from sensor data sheets and are given in Table 2.

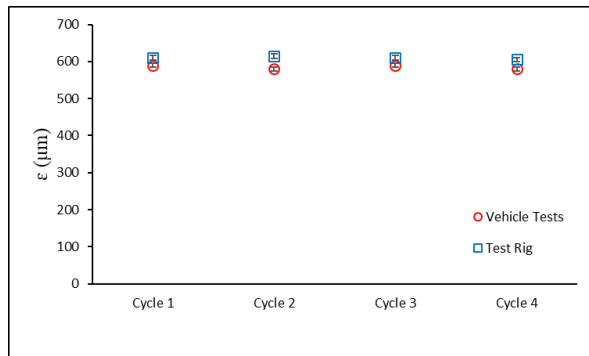
**Table 2.** Uncertainty values for the measured parameters

Measured parameter	The instrument	Uncertainty
Airflow rate	Mass flowmeter	±0.00001kg/s
Coolant flow rate	Mass flowmeter	±0.00001kg/s
The temperature of the air	K Thermocouple	±0.24 K

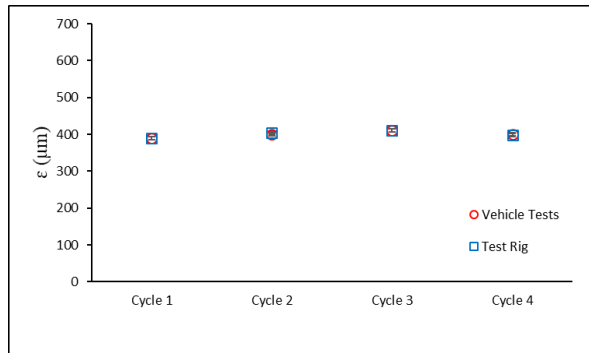
The temperature of the coolant	K Thermocouple	$\pm 0.24$ K
Pressure	Gauge Pressure	$\pm 0.01$ kPa
Strain	Strain gauge	$\pm 1$ %

## RESULTS AND DISCUSSION

Figure 9 (a) and (b) demonstrate the strain measurements on the WCAC cooling part with vehicle tests and develop a custom test rig for stressful and average conditions. After the development of the test rig, the tests were conducted to develop the measurement of the rig compared to vehicle tests. It can be seen that the strain measurements taken from the test rig are highly correlated with vehicle tests for four different cycles and two different conditions. For example, the Mean Absolute Error (MAE) of the two measurements at the stressful condition tests is in the range of 3.39 - 6.03 %, whereas it is 0.2 - 0.5 % at the average condition tests.



(a)

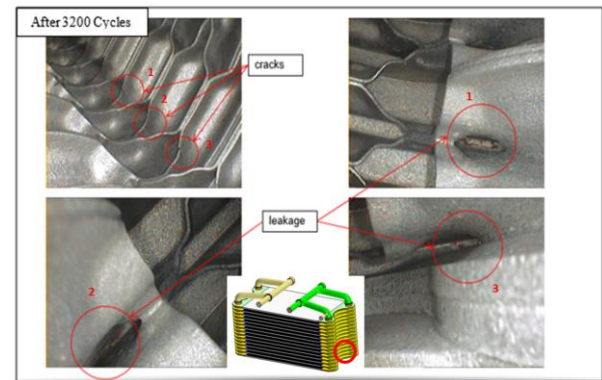


(b)

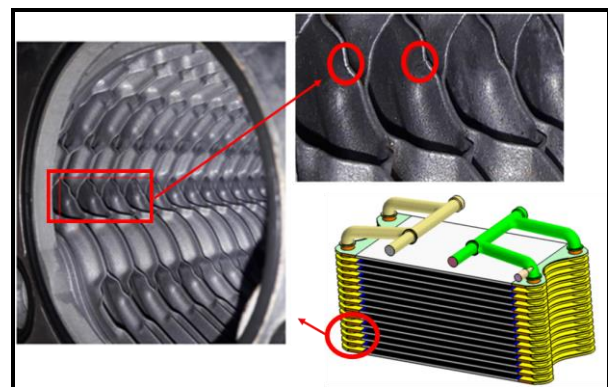
**Figure 9.** Verification of the test rig with vehicle tests for four different cycles, (a) Stressful Condition, (b) Average Condition

Subsequently, four critical cycles were determined and organized by engine heating-cooling data to characterize the same engine working conditions. At the end of each cycle, the WCACs were inspected periodically to detect crack formation using an endoscopic camera. According to the vehicle tests, the WCAC control cycle plan was defined with the four critical cycles. These are the 120th cycle, 240th cycle, 550th cycle, and 3200th cycle. The first inspection of the WCACs was conducted at the end of the 120th

cycle. It was seen that the corroded regions that have a crack formation possibility could be detected even at the lowest cycle. When the WCACs were inspected at the second cycle (240th cycle), it was observed that the corroded regions enlarged, and the leakage from the intercooler started. The WCACs damage was detected in the 240th cycle compared to the 120th cycle from the erosion point of view. The third inspection was performed at the end of the 550th cycle, and there was still no crack, but the corroded regions became quite large. Therefore, the test was continued to the end of the 3200th cycle. The visualization study showed deep crack regions, and the heavy coolant leakage on the metal existed at the end of the 3200th cycle. On the blades, there were cavitated regions, and the trails were widening. The leak's location was detected at the last stacked plate in the series of connection plates. The crack and leak detection images at the end of the 3200th cycle control are presented in Figures 10 (a)-(b).



(a)



(b)

**Figure 10.** The crack and leak detection images at the end of the 3200th cycle control, (a) left side of WCAC heat exchanger, (b) front right side of WCAC heat exchanger

At the end of the tests, the first crack formation was seen when the tests reached the 3200th cycle; in this cycle, the cracks were very sharp and deep such as 8 mm in length with 3 mm width and 5 mm depth. Cracks were observed in Figure 11 by using SEM (scanning electron microscope). The amount of leakage was high such as %5 percent, so WCAC became unusable. According to the test rig results, the cycle

time, strain magnitudes, and crack location are identical in the vehicle tests and the test equipment.

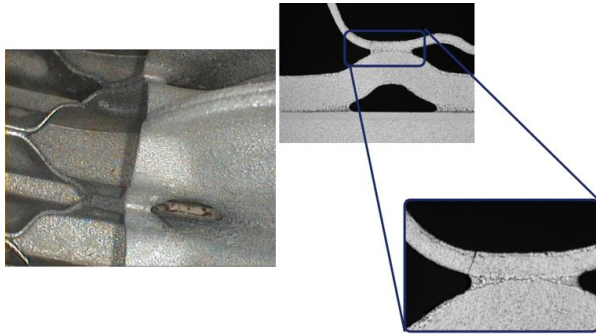


**Figure 11.** Cracks at the connection of the coolant and air (5mm depth, 10 mm length with 3 mm width)

Although vehicle tests are the most reliable method to detect WCAC cracks, the inconvenience, and high cost led us to investigate other techniques, as mentioned before (Moreira et al., 2019). Table 2 presents an infrastructure, operation, and engineering costs comparison between the two methods. In Table 2, the infrastructure cost has been taken from the refs. (Ahlin et al., 2004); (National2021); (Hertz2021) the engineering cost values have been obtained from the ref. (glassdoor2021). Moreover, the operational cost (electricity) has been taken from the Invest2021. On the other hand, the test duration comparison of the two methods is presented in Table 3. As can be observed from Tables 2 and 3, the test rig is a more cost-effective method compared to vehicle tests.

**Table 3.** Cost comparison of two methods

Cost Unit	Vehicle Tests	Test rig
Infrastructure (\$) (VehicleRent-TestRigCost)	60000	10000
EngineeringCost(\$/month)	7500	1000
OperationalCost (\$/month)	10000	2000
Total (\$+\$/month)	100000	16000

**Table 4.** Test duration comparison of two methods

Item	Vehicle Tests	Test rig
Time (days)	60	15
Man Hours (hour/test)	4	1.5

Consequently, the design of the WCAC part was modified by extending the length of the inlet tubes seven times the length of the diameter of the pipes to prevent non-uniform flow distribution at the inlet of the WCAC. This modification was chosen according to the literature survey presented in the introduction. The tests of the modified WCACs were conducted using the developed test rig for various stressful conditions. As a result, the modified WCAC part was found to be more robust than the old design, and there was no evidence of crack formation.

## CONCLUSIONS

This study developed a specialized thermal fatigue testing rig to determine crack formation's location and cycle time in WCAC parts as an alternative to vehicle testing. Test rig data were validated with differences of up to 5 percent compared to strain measurement, position, and thermal stress data from vehicle tests. Also, crack formation in WCACs was examined periodically with an endoscopic camera after each test for different critical cycles in the test setup. It has been observed that crack formation in WCACs differs by no more than 10 percent from the cycle time in the test rigs and the vehicle's cycle time. The location of the refraction obtained from the special test equipment developed is only 1 cm different from that obtained from the vehicle tests. In addition, the cost and test time between the two methods were compared, and it was seen that the test equipment method was 80% cost-effective compared to vehicle tests.

The literature survey conducted in this study revealed that the non-uniform flow distribution at the inlet of heat exchangers is the dominant parameter of crack formation. Therefore, the WCAC system was re-designed by increasing the length of the inlet tubes seven times the diameter of the pipes to prevent non-uniform flow distribution at the inlet. Finally, the modified WCAC system was tested under stressful operating conditions through the developed custom test rig. The results showed that the WCAC is more robust than the old design, and there was no evidence of crack formation until the 10000 cycles, even under stressful operating conditions.

## ACKNOWLEDGMENT

The author would like to thank Aydın Ayyıldız and Hakan Gokoglu for the technical support of this research.

## REFERENCES

- Ahlin, K., Granlund, J., and Lindstrom, F., 2004, Comparing road profiles with vehicle perceived roughness, *International Journal of Vehicle Design*, 36(2), 270-286.
- Ali, M., Ul-Hamid, A., Alhems, L. M., and Saeed, A., 2020, Review of common failures in heat exchangers–Part I: Mechanical and elevated temperature failures, *Engineering Failure Analysis*, 109, 104396.
- Arikan, K. B., 2008, *Identification of handling models for road vehicles*, Ph.D. Thesis, Middle East Technical University, Ankara, Turkey.
- Broatch, A., Luján, J. M., Serrano, J. R., and Pla, B., 2008, A procedure to reduce pollutant gases from Diesel combustion during the European MVEG-A cycle

- by using electrical intake air heaters. *Fuel*, 87(12), 2760-2778.
- Burgold, S., Galland, J. P., Ferlay, B., and Odillard, L., 2012, Modular Water Charge Air Cooling for Combustion Engines. *MTZ worldwide*, 73(11), 26-31. doi: <https://doi.org/10.1007/s38313-012-0237-z>.
- Canyurt, T. G., Ergin, S., Zeren, H. B., Savcı I. H., 2022, Experimental and numerical investigation on the urea-deposit formation at different severities in selective catalytic reduction systems, *Applied Thermal Engineering*, 214, 118884. doi: <https://doi.org/10.1016/j.applthermaleng.2022.118884>.
- Demirkesen, C., Colak, U., Savci, I. H., and Zeren, H. B., 2020, Experimental and Numerical Investigation of Air Flow Motion in Cylinder of Heavy Duty Diesel Engines', *Journal of Applied Fluid Mechanics*, 13(2), 537-547. doi: 10.29252/jafm.13.02.30369
- Edara, G., Murthy, Y. S., Nayar, J., Ramesh, M., and Srinivas, P., 2019, Combustion analysis of modified light-duty diesel engine under high-pressure split injections with cooled EGR. *Engineering Science and Technology, an International Journal*, 22(3), 966-978. doi: <https://doi.org/10.1016/j.jestch.2019.01.013>
- Internet, 2021, Hertz car, *car rental cost table*, <https://www.hertz.com/p/car-rental>.
- Holland, B., McKinley, T., and Storkman, B., 2015, Modeling Approach to Estimate EGR Cooler Thermal Fatigue Life, *SAE International Journal of Engines*, 8(4), 1724-1732. doi: <https://doi.org/10.4271/2015-01-1654>.
- Hoseinzadeh, S., and Heyns, P. S., 2020, Thermo-structural fatigue and lifetime analysis of a power plant's heat exchanger as a feedwater heater, *Engineering Failure Analysis*, 113, 104548. doi: <https://doi.org/10.1016/j.engfailanal.2020.104548>.
- Internet, 2022, Investment support and promotion agency of the Republic of Turkey, *Electricity Cost*, <http://www.invest.gov.tr>.
- Iwahori, K., Ohno, N., Okumura, D., and Muraki, T., 2013, The Large Scale Finite Element Analysis of a Charge Air Cooler Using a Homogenization Method. *SAE Technical Paper*, 01-1212.
- Joshi, A. A., James, S., Meckl, P., King, G., and Jennings, K., 2009, Assessment of charge-air cooler health in diesel engines using nonlinear time series analysis of intake manifold temperature. *Journal of dynamic systems, measurement and control*, 131(4), 041009-041020. doi: <https://doi.org/10.1115/1.3023142>.
- Kolb, J., Zhao, M., Lambert, M., and JuGer, J., 1998, Long Life, Heavy Duty, Air-to-Air Charge Air Cooler. *SAE transactions*, 107(2), 182-214.
- Kuehnel, W., Weise, S., Krueger, U., and Sekler, H., 2005, The Validation Process- One Key Element of Reliability Management. *SAE Technical Paper*, <https://doi.org/10.4271/2005-01-1778>.
- Laurent, M., Estevez, R., Fabrègue, D., and Ajax, E., 2016, Thermomechanical fatigue life prediction of 316L compact heat exchanger. *Engineering Failure Analysis*, 68, 138-149. doi: <https://doi.org/10.1016/j.engfailanal.2016.06.003>.
- Luján, J. M., Climent, H., Dolz, V., Moratal, A., Borges-Alejo, J., and Soukeur, Z., 2016, The potential of exhaust heat recovery for intake charge heating in a diesel engine transient operation at cold conditions. *Applied Thermal Engineering*, 105, 501-508. doi: <https://doi.org/10.1016/j.applthermaleng.2016.03.028>.
- Mezher, H., Migaud, J., and Raimbault, V., 2013, Optimized Air Intake for a Turbocharged Engine Taking into Account Water-Cooled Charge Air Cooler Reflective Properties for Acoustic Tuning. *SAE Technical Paper*, 1, 0575-0587. doi: <https://doi.org/10.4271/2013-01-0575>.
- Moreira, T.A., Colmanetti, A.R.A., and Tibiriçá, C.B., 2019, Heat transfer coefficient: a review of measurement techniques. *Journal of the Brazilian Society of Mechanical Sciences and Engineering*, 41, 264. doi: <https://doi.org/10.1007/s40430-019-1763-2>.
- Internet, 2022, National Instruments, *Technical Specifications*, <https://www.ni.com>.
- O'Connor, T. W., and Trauger, P. E., 1990, The Impact of Elevated Turbocharger Outlet Conditions on Charge Air Cooler Durability. *SAE Technical Paper, Truck and Bus Meeting, and Exposition*, Detroit, Michigan, USA.
- Internet, 2021, Glass Door , *Salaries*, [https://www.glassdoor.com/Salary/Ford-Motor-Company-Cost-Engineer-Salaries-E263\\_D\\_KO19,32.htm](https://www.glassdoor.com/Salary/Ford-Motor-Company-Cost-Engineer-Salaries-E263_D_KO19,32.htm) .
- Panchal, C., Stegen, S., and Lu, J., 2018, Review of the static and dynamic wireless electric vehicle charging system. *Engineering Science and Technology, an International Journal*, 21(5), 922-937. doi: <https://doi.org/10.1016/j.jestch.2018.06.015>.

- Ren, P., Li, Z., Wu, J., Guo, Y., and Li, W., 2017, Failure analysis of blots for diesel engine intercooler. *In Journal of Physics: Conference Series*, 842 (1), 012063-012071.  
doi: <https://doi.org/10.1088/1742-6596/842/1/012063>.
- Salmon, P., Könözsy, L., Temple, C., and Grove, S., 2017, Numerical investigation on various heat exchanger performances to determine an optimum configuration for charge air cooler, oil, and water radiators in F1 sidepods. *Applied Thermal Engineering*, 117,235-244.  
doi:<https://doi.org/10.1016/j.applthermaleng.2017.02.026>.
- Savci, I. H., Gul, M. Z., 2022, A methodology to assess mixer performance for selective catalyst reduction application in hot air gas burner. *Alexandria Engineering Journal*, 61(9), 6621-6633.  
doi: <https://doi.org/10.1016/j.aej.2021.12.011>
- Subasi, A., 2017, *Numerical and experimental investigation of boundary layer transition with active and passive flow control methods*. Ph.D. Thesis. Istanbul Technical University, Istanbul, Turkey.
- Torregrosa, A.J., Broatch, A., Olmeda, P. and Romero, C. 2008, Assessment of the influence of different cooling system configurations on engine warm-up, emissions, and fuel consumption. *International Journal of Automotive Technology*, 9(4), 447-458.  
doi: <https://doi.org/10.1007/s12239-008-0054-1>.
- Usman, A., and Khan, A. N. 2008, Failure analysis of heat exchanger tubes. *Engineering Failure Analysis*, 15(1-2), 118-128.  
doi: <https://doi.org/10.1016/j.engfailanal.2006.11.051>.
- Vashahi, F., Lee, M., Kim, J., Kim, D., and Baek, B. J., 2014, A numerical study on the thermal and strain characteristics of EGR cooler. *International Journal of Control and Automation*, 7(7), 241-252.  
doi: <https://doi.org/10.14257/ijca.2014.7.7.20>.
- Wang, C. C., Yang, K. S., Tsai, J. S., and Chen, Y., 2011, Characteristics of flow distribution in compact parallel-flow heat exchangers, part I: typical inlet header. *Applied Thermal Engineering*, 31(16), 3226-3234.  
doi:<https://doi.org/10.1016/j.applthermaleng.2011.06.004>.
- Yaïci, W., Ghorab, M., and Entchev, E., 2014, 3D CFD analysis of the effect of inlet air flow maldistribution on the fluid flow and heat transfer performances of plate-fin-and-tube laminar heat exchangers. *International Journal of Heat and Mass Transfer*, 74, 490-500.  
doi:<https://doi.org/10.1016/j.ijheatmasstransfer.2014.03.03>.
- Yu, C., Qin, S., Chai, B., Huang, S., and Liu, Y., 2019, The Effect of Compressible Flow on Heat Transfer Performance of Heat Exchanger by Computational Fluid Dynamics (CFD) Simulation. *Entropy*, 21(9), 829.  
doi: <https://doi.org/10.3390/e21090829>.





## DAMLACIK SAYISI VE DAMLACIKLAR ARASI YATAY MESAFENİN MAKSİMUM YAYILMA ALANI VE ISI TRANSFERİ PERFORMANSI ÜZERİNE ETKİLERİNİN SAYISAL İNCELENMESİ

Ahmet GÜLTEKİN\*, Nejdet ERKAN\*\*, Üner ÇOLAK\*\*\* ve Shunichi SUZUKI\*\*\*\*

\*İstanbul Sağlık ve Teknoloji Üniversitesi - Makine Mühendisliği Bölümü, İstanbul/Türkiye  
ahmet.gultekin@istun.edu.tr, ORCID: 0000-0002-1307-9016

\*\*United Kingdom Atomic Energy Authority, Rotherham/UK  
nejdet.erkana@ukaea.uk, ORCID: 0000-0001-9868-4305

\*\*\*İstanbul Teknik Üniversitesi - Enerji Enstitüsü, İstanbul/Türkiye  
unercolak@itu.edu.tr, ORCID: 0000-0001-9293-6065

\*\*\*\*The University of Tokyo - Department of Nuclear Engineering and Management, Tokyo/Japan  
s\_suzuki@n.t.u-tokyo.ac.jp, ORCID: 0000-0001-8441-5999

(Geliş Tarihi: 23.06.2022, Kabul Tarihi: 28.03.2023)

**Özet:** Damlacıkların katı bir yüzeye etki etmesi fenomeni çok sayıda endüstriyel uygulamalarda görülebilir. Damlacıkların sıcak bir yüzeye ve/veya diğer damlacıklarla etkileşimleri durumunda bu fenomen daha karmaşık hale gelmektedir. Katı bir yüzeye çok sayıda damlacık çarptığında, damlacıkların çarpma koşulları ve aralarındaki mesafeye bağlı olarak bir etkileşim meydana gelir. Bu etkileşim nedeniyle bir katman yükselmesi oluşur ve yüzeyde damlacık başına daha az yayılma gerçekleşir. Dolayısıyla, ortaya çıkan hidrodinamik ve ısı transferi değişimleri tek damlacık etkileşimlerinden oldukça farklıdır. Sprey soğutma olgusunda meydana gelen fiziksel mekanizmaları anlama ve modelleme ile ilgili zorluklar, damlacıkların rastlantısallığından ve izlenemez davranışlarından kaynaklanmaktadır. Bu nedenle, karmaşık yapı basitleştirilerek çoklu damlacıkların etkileşimleri sıvıların hacmi (VOF) metodu kullanılarak sayısal olarak incelenmiştir. Bu çalışmanın amacı, damlacık sayısının ve damlacık çarpma koşullarının yüzeyden gerçekleşen ısı transferi performansına etkisini incelemektir.

**Anahtar Kelimeler:** Çoklu damlacık etkileşimleri, ısı transfer performansı, sprey soğutma, VOF metodu.

## NUMERICAL INVESTIGATION OF THE EFFECTS OF DROPLET NUMBER AND HORIZONTAL DISTANCE ON MAXIMUM SPREADING AREA AND HEAT TRANSFER PERFORMANCE

**Abstract:** The phenomenon of droplets impact on a solid surface can be seen in many industrial applications. This phenomenon becomes more complex when droplets interact with a hot surface and/or other droplets. After multiple droplet impingement on a solid surface, an interaction occurs depending on the impact conditions of the droplets and the distance between them. This interaction leads to an uprising layer which causes lesser spreading area per droplet on solid surface. The hydrodynamic outputs and heat transfer activities of the droplets are very distinct from single droplet cases due to this interaction. Difficulties in understanding and modeling the physical mechanisms that take place in the spray cooling phenomenon arise from the randomness and untraceable behavior of the droplets. Therefore, the complex structure has been simplified and the interactions of multiple droplets have been numerically investigated using the volume of fluid (VOF) method. The aim of this study is to examine the effect of droplet number and droplet impact conditions on the heat transfer performance from the surface.

**Keywords:** Multiple droplet interactions, heat transfer performance, spray cooling, VOF method.

### SEMBOLLER

A Yayılma alanı [ $m^2$ ]

$\bar{A}$  Boyutsuz yayılma alanı [ $= \frac{A}{ND_0^2}$ ]

$D_0$  İlk damlacık çapı [mm]

$d_h$  Damlacıklar arası yatay mesafe [mm]

$\bar{d}_h$  Boyutsuz yatay mesafe [ $=d_h / D_0$ ]

$d_v$  Damlacıklar arası dikey mesafe [mm]

$\bar{d}_v$  Boyutsuz dikey mesafe [ $=d_v / D_0$ ]

$D_s$  Yayılma çapı [mm]

$H_s$  Katman yüksekliği [mm]

$\bar{H}_s$  Boyutsuz katman yüksekliği [ $=H_s / D_0$ ]

N Damlacık sayısı

$q''$  Isı akısı [ $W/m^2$ ]

T Sıcaklık [ $^{\circ}C$ ]

t zaman [s]

$U_0$  Damlacık başlangıç hızı [m/s]

We Weber sayısı [ $= \rho u_0^2 D_0 / \sigma$ ]

$\alpha$	VOF hacim oranı
$\beta$	Boyutsuz yayılma çapı [=D <sub>s</sub> / D <sub>0</sub> ]
$\mu$	Dinamik viskozite [Ns/m <sup>2</sup> ]
$\rho$	yoğunluk [kg/m <sup>3</sup> ]
$\sigma$	Yüzey gerilimi [N/m]
$\tau$	Boyutsuz zaman [= tu <sub>0</sub> /D <sub>0</sub> ]

## GİRİŞ

Katı bir yüzeye damlacık çarpması olgusu, mürekkep püskürtmeli yazıcı (Castrejón-Pita *vd.*, 2008; de Gans *vd.*, 2004), içten yanmalı motorlarda yakıt enjeksiyon işlemi (Panão ve Moreira, 2005), sprej kaplama (Pasandideh-Fard *vd.*, 2002; Soltani-Kordshuli ve Eslamian, 2017) ve sprej soğutma sistemleri (Bostanci *vd.*, 2012; Cheng *vd.*, 2015; Mehdizadeh ve Chandra, 2006; Shahmohammadi *vd.*, 2018; Silk *vd.*, 2006) gibi çeşitli endüstriyel uygulamalarda görülebilir. Literatürde, tek damlacık ile ısıtılmış katı yüzey etkileşimleri hakkında çok sayıda deneysel (Akao *vd.*, 1980; Breitenbach *vd.*, 2017; Hatakenaka *vd.*, 2019; Jung *vd.*, 2016; Lee *vd.*, 2020; Pasandideh-Fard *vd.*, 2001; Tran *vd.*, 2012; Tran *vd.*, 2013) ve sayısal çalışmalar (Margarinos *vd.*, 2014; Nikolopoulos *vd.*, 2007; Pournaderi ve Pishevar, 2012; Reyhanian *vd.*, 2017; Taghilou ve Hassan, 2014; Villegas *vd.*, 2016; Z. Wang *vd.*, 2016; Xiong ve Cheng, 2018) bulunmaktadır. Damlacıkların sıcak yüzeylere çarpmasıyla ilgili güncel çalışmalar hakkında ayrıntılı bilgiler Liang ve Mudawar (2017) tarafından yapılan kapsamlı derleme makalesinde bulunmaktadır.

Yüzey sıcaklığı, hem damlacık dinamiklerini hem de ısı transfer performansını etkilemekte hayati bir rol oynamaktadır. Ayrıca, yayılma alanı miktarı sıvı lamel ile yüzey arasındaki temas alanını belirler, bu yüzden sprej soğutma sırasında ısı transferini etkileyen diğer önemli bir parametredir. Yayılma alanı, damlacık çarpmasının başlangıç kinetik enerjisi ve viskoz yayılmadan kaynaklanan enerji kayıpları ile yüksek oranda ilişkilidir. Damlacık çarpmasının kinetik enerjisi, yüzeye temasın ilk aşamalarında sıvının radyal hareketine dönüştürülür. Damlacık yüzey boyunca genişlediğinde, damlacığın kinetik enerjisi viskoz kuvvetler tarafından kısmen dağılır. Sonunda, damlacık maksimum yayılma alanına ulaştığında, yüzey gerilimi deformasyonun neden olduğu arayüz enerjisinde sıvının kalan kinetik enerjisini biriktirerek genişlemeyi yavaşlatır. Bu noktada, damlacık dairesel bir lamel şeklini alarak maksimum yayılma alanına ulaşır. Birçok araştırmacı, damlacığın maksimum yayılma çapını sayısal yöntemler veya enerji dengesini kullanarak tahmin etmeye çalışmıştır (Clanet *vd.*, 2004; Huang ve Chen, 2018; Ukiwe ve Kwok, 2005).

Diğer damlacıklarla etkileşim varsa bu durum daha karmaşık hale gelir. Ancak, literatürde çoklu damlacık etkileşimleri ile ilgili sınırlı sayıda çalışma bulunmaktadır. Cossali *vd.* (2003), sıcak yüzey üzerinde eşzamanlı üçlü damlacık çarpmasından sonraki damlacık etkileşimlerini incelemek için deneyler yapmıştır. Buhar

kabarcıklarının büyümesinin ve ayrılmasının, geçiş kaynama rejiminde çok sayıda küçük ikincil damlacıklara neden olduğunu belirtmişlerdir. Başka bir çalışmada, Cossali *vd.* (2005), sıcak yüzeylere çoklu damlacık çarpması için yüzey malzemesinin ikincil damlacık atomizasyonu üzerindeki etkilerini araştırdı. İkincil damlacık morfolojisinin yüzey malzemesinden güçlü bir şekilde etkilendiğine dikkat çektiler. Ersoy ve Eslamian (2020), farklı renklerde sıvılar kullanarak kuru ve ıslak yüzeylere yüksek Weber sayısına sahip damlacık çiftleri uygulayarak damlacıklar arası oluşan etkileşim nedeniyle oluşan katman yüksekliğinin zamanla değişimini deneysel olarak incelediler. Katı yüzeye damlacık çifti etkisi uygulandığında üç farklı tip katman yükselmesi formu gözlemlenildi. Liang *vd.* (2019) ortam sıcaklığında eşzamanlı olmayan ve eşzamanlı durumlar için damlacık çiftini deneysel olarak araştırdılar. Eşzamanlı olmayan durumları etkileşim türüne göre üç ana alt duruma ayırdılar. Gültekin *vd.* (2021) aynı anda birden fazla damlacık elde etmek için bir damlacık üretim ve kontrol sistemi geliştirmişlerdir. Geliştirdikleri bu deney düzeneği ile Shadowgraph yöntemini kullanarak farklı çarpma koşullarına ve konfigürasyonlara sahip tek ve çoklu damlacıkların ısıtılmış yüzeylerle etkileşimlerini incelemişlerdir. Katman yüksekliğinin, damlacıklar arası mesafe azaldıkça ve damlacık Weber sayısı arttıkça arttığını belirtmişlerdir. Ayrıca, damlacıklar arası yatay mesafenin artmasıyla, yayılan sıvı lameller viskoz kuvvetlere karşı daha fazla enerji kaybettiğinden dolayı zayıf bir katman yükselmesinin oluşmasına neden olduğunu vurgulamışlardır. Başka bir çalışmada, Gültekin *vd.* (2020) parçacık görüntü hız ölçümü (PIV) ve gölge grafiği (Shadowgraph) yöntemlerini eş zamanlı olarak kullanmıştır. PIV yöntemi ile farklı sıcaklıklarda safir cam üzerinde damlacıkların içindeki radyal hız değişimi incelenmiştir. Radyal hız değişiminin, nispeten geniş bir yayılma yarıçapı aralığında doğrusal olduğu gözlemlenmiştir. Ancak zamanla kılcal ve viskoz kuvvetlerin etkisiyle, radyal hız profilinin dış bölgelerinde nonliner şekil aldığı gözlemlenmiştir. Ek olarak damlacık çifti içindeki yayılma hızları, PIV yöntemi kullanılarak ortam sıcaklığında incelenmiştir. Etkileşim bölgesinde yukarı doğru bir akış nedeniyle oluşan katman yükselmesinin ekstra bir durgunluk noktasına neden olduğu gözlemlenmiştir.

Nümerik olarak yapılan çoklu damlacık araştırmalarının çoğunda, Lattice Boltzmann, Level Set ve Volume of Fluid (VOF) gibi çeşitli yöntemler kullanılmıştır. Li *vd.* (2016) bir Lattice Boltzmann modeli kullanarak sıvı film üzerindeki yatay ve dikey mesafelere sahip damlacık çifti etkisini inceledi. Eşzamanlı olmayan damlacık çiftlerinin etkileşimi nedeniyle oluşan katman yüksekliğini ve yönünü değiştirerek asimetriye neden olacağını belirtmişlerdir. Wang *vd.* (2018) akan bir sıvı film üzerine eşzamanlı bir damlacık çifti çarpmasıyla ısı transfer davranışını sayısal olarak araştırdı. Asimetrisinin daha önemli hale geldiğini ve damlacıklar arasındaki mesafe kısaldıkça çarpma alanındaki ısının uzaklaştırılmasının daha belirgin olduğunu gösterdiler.

Liang *vd.* (2018) ısı transferi sürecini dikkate almadan sıvı film üzerine eşzamanlı çoklu damlacık çarpmasını sayısal olarak inceledi. Ayrıca, bir sıvı film üzerine çoklu damlacık çarpması için tek fazlı (Liang *vd.*, 2019a) ve iki fazlı (Liang *vd.*, 2019b) ısı transfer davranışını göz önünde bulundurarak incelemişlerdir. Bir sıvı film üzerine çoklu damlacık çarpması ile çarpma bölgesindeki ısı transfer katsayısının, filmin etkilenmeyen bölgesinden çok daha büyük olduğunu belirtmişlerdir.

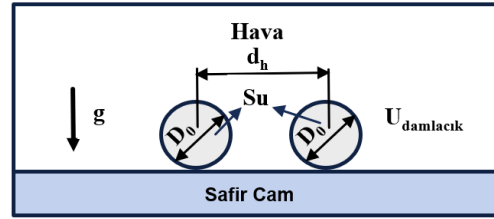
Literatürde bulunan çalışmaların çoğu tek damlacık etkileşimlerine odaklanırken, birden çok damlacığın etkileşimiyle ilgili oldukça sınırlı sayıda çalışma bulunmaktadır. Katı yüzeye tek bir damlacık çarptıktan sonra damlacık yayılmaya başlar ve dairesel yapıda ince bir sıvı film oluşur. Bununla birlikte, katı bir yüzeye birden çok sayıda damlacık çarpması sonucu, çarpma koşulları ve damlacıkların arasındaki mesafeye bağlı olarak bir etkileşim meydana gelmektedir. Bu etkileşim nedeniyle damlacık başına daha az yayılma gerçekleşir. Dolayısıyla ortaya çıkan hidrodinamik ve ısı transferi değişimleri tek damlacık etkileşimlerinden oldukça farklıdır. Sprey soğutma olgusunda gerçekleşen fiziksel mekanizmalar ve modelleme ile ilgili zorluklar, damlacıkların rastlantısallığından ve izlenemez davranışlarından kaynaklanmaktadır. Bu sebeple, karmaşık yapı basitleştirilerek az ve bilinen sayıda damlacıkların etkileşimlerinin incelenmesi gereklidir. Bu makalenin amacı, damlacık çarpma koşullarının yanı sıra çoklu damlacıklar için damlacık sayısı ve damlacıklar arası yatay mesafenin ısı transferi davranışı üzerindeki etkilerini araştırmaktır. Bu nedenle VOF metodu kullanılarak 3 boyutlu sayısal bir model geliştirilmiş ve deneysel sonuçlarla doğrulanmıştır. Doğrulanmış sayısal modelle farklı konfigürasyonlara sahip çoklu damlacık etkileşimleri parametrik olarak incelenmiştir. Tek damlacık çarpması referans alınarak çoklu damlacık etkileşimlerinde soğutma verimliliği ve yüzeyden gerçekleşen ısı transferi performans kaybının değişimi damlacık sayısı ve aralarındaki yatay mesafe için belirlenerek literature katkı sağlanmıştır.

## SAYISAL MODEL

Katı bir yüzey üzerine çoklu damlacık çarpmaları durumunda, damlacıklar arası etkileşim olgusu, damlacık çarpma koşullarına bağlı olarak meydana gelir. Bu etkileşim nedeniyle, damlacık hidrodinamiği ve ısı transferi davranışları, tek damlacık çarpmasından oldukça farklıdır. Bu nedenle, bu problemi doğası gereği 2 boyutlu sayısal modeller ile incelemek yeterli değildir. Katı yüzey üzerine düşen çoklu damlacıklar, bir hesaplamalı akışkanlar dinamiği (CFD) programı olan Star-CCM + programı kullanılarak modellenmiştir. Bu yazılımı kullanarak çok fazlı akışları da içeren çeşitli mühendislik problemleri modellenebilir ve simüle edilebilir.

Ağ yapısı analizi için farklı ağ durumuyla 16 mm × 16 mm × 5 mm'lik hesaplama alanı kullanılmıştır. Farklı sayıda (1,875 × 10<sup>6</sup>, 7,5 × 10<sup>6</sup> ve 10 × 10<sup>6</sup>) ağ sayılarına

sahip modeller sonuçların ağdan bağımsız olduğundan emin olmak için incelenmiştir (Gultekin, 2021). Yüzey sınırına yakın bölgelerde ağ yapısı daha yoğun uygulanırken, yüzeyden uzaklaştıkça daha seyrek bir ağ yapısı kullanılmıştır. Başka bir deyişle, yüzeyden uzaklaştıkça modelin arayüz yakalamada hata miktarı artmaktadır. Damlacıkların yüzeyde kapladığı alan ve damlacık etkileşimi sırasında oluşan arayüzü yakalamak için yeterli ağ çözünürlüğüne sahip (7,5 × 10<sup>6</sup>) grid seçilmiştir. Kullanılan modelde boyutu 20 µm ile 40 µm arasında değişen dörtgen hücre ağ yapısı kullanılmıştır. Hesaplama alanının genel bir şematik gösterimi Şekil 1'de verilmiştir.



Şekil 1. Hesaplama alanı genel bir şematik gösterimi.

Damlacıkların ve havanın bulunduğu araştırma alanında VOF methodu kullanılarak arayüz takibi gerçekleştirilmiştir. Akışkanlar arasında keskin bir arayüz sağlamak amacıyla “Yüksek Çözünürlüklü Arayüz Yakalama (HRIC)” seçeneğini aktif hale getirmek için VOF metodunda konveksiyon 2. dereceye ayarlanmıştır. Tüm damlacıkların başlangıçta küresel olduğu ve safir yüzeyin üzerine yerleştirildiği varsayılmıştır, burada damlacıkların bulunduğu hacim sıvı olarak belirtilmiştir ve çarpma hızı başlangıç hızı verilerek simülasyonlar başlatılmıştır. Safir katı yüzey kaymaz duvar koşulu olarak modellenmiştir. Modellerde kullanılan alanların fiziksel özellikleri Tablo 1'de verilmiştir.

Tablo 1. Sayısal çalışmada kullanılan alanların fiziksel özellikleri.

	Özellikler	Birim	Değer
Su	Yoğunluk	[kg/m <sup>3</sup> ]	998
	Dinamik viskozite	[Ns/m <sup>2</sup> ]	0,001
	Yüzey gerilimi	[N/m]	0,072
	Özgül ısı kapasitesi,	[kJ/(kg K)]	4,18
Safir cam	Yoğunluk	[kg/m <sup>3</sup> ]	3980
	Özgül ısı kapasitesi	[kJ/(kg K)]	1134
	Termal iletkenlik	[W/(m K)]	32,5
	Termal yayılım	[m <sup>2</sup> s]	2,79 × 10 <sup>-5</sup>

STAR-CCM+'da arayüz takibi için Hirt ve Nichols (1981) tarafından önerilen damlacık-yüzey etkileşiminin simülasyonu için uygun olan VOF yaklaşımı kullanılmıştır. VOF yöntemi, havacılık, otomotiv ve denizcilik sektörlerinde bulunan karmaşık geometriler ve hareketli arayüz sınırları içeren problemleri simüle etmek için oldukça etkili bir yöntemdir. Ayrıca, kaynama veya yoğunlaşma gibi faz değişikliği içeren akışları simüle etmek için yaygın olarak kullanılır. VOF yönteminde, akış alanı

hücrelere bölünür ve her hücrenin içindeki sıvı iki veya daha fazla fazdan oluşan bir karışım olarak ele alınır. Her zaman adımında, her hücredeki her fazın hacim oranı hesaplanır. Hacim oranı  $\alpha$ , VOF yönteminde Eş. (1) şeklinde tanımlanır:

$$\alpha = \frac{\text{Sıvı fazın hacmi}}{\text{Kontrol hacminin toplam hacmi}} \quad (1)$$

burada  $\alpha$  sıvı fazda 1, gaz fazında 0 ve arayüzde 0 ile 1 arasında değerlerdir. VOF yönteminin diğer sayısal yöntemlerden farkı, sıvı özelliklerinin hücrenin  $\alpha$  değerine göre güncellendiği iki faz (gaz-sıvı) için sadece bir momentum denkleminin çözülmesidir. Gaz-sıvı için süreklilik ve momentum denklemleri Eş.(2) ve Eş. (3) ile verilmiştir.

$$\begin{aligned} \nabla \cdot \mathbf{u} &= 0 \quad (2) \\ \frac{\partial \rho \mathbf{u}}{\partial t} + \nabla \cdot (\rho \mathbf{u} \mathbf{u}) &= -\nabla p + \nabla \cdot \mu (\nabla \mathbf{u}) + \mathbf{f}_\sigma + \rho \mathbf{g} \quad (3) \end{aligned}$$

burada  $\mathbf{f}_\sigma$  ve  $\mathbf{g}$ , sürekli yüzey kuvveti modeli (Brackbill *vd.*, 1992) tarafından hesaplanan arayüzde sıvıya etki eden yüzey gerilimi ve yerçekimi kuvvetleri içindir. Bu modelde sıvı ve gazların tamamen karışmadığı varsayılmaktadır. Arayüzde sıvıya etki eden yüzey gerilimi Eş. (4) ile verilmiştir.

$$\mathbf{f}_\sigma = \sigma \kappa \mathbf{n}, \quad \kappa = -\nabla \cdot \left[ \frac{\nabla \alpha}{|\nabla \alpha|} \right], \quad \mathbf{n} = \nabla \alpha \quad (4)$$

burada  $\kappa$ , arayüzün ortalama eğriliğidir ve  $\mathbf{n}$ , arayüze normal ve sıvıdan gaza yönlendirilmiş birim vektördür. Eş. (3)'de, bulunan sıvı yoğunluğu  $\rho$  ve viskozite  $\mu$  Eş. (5) ve Eş. (6) ile tanımlanır:

$$\rho = \alpha \rho_{sıvı} + (1 - \alpha) \rho_{gaz} \quad (5)$$

$$\mu = \alpha \mu_{sıvı} + (1 - \alpha) \mu_{gaz} \quad (6)$$

Safir yüzey içindeki enerji korunumu denklemi Eş. (7) ile ifade edilir:

$$\rho_s c_s \frac{\partial T}{\partial t} = \nabla \cdot (k_s \nabla T) \quad (7)$$

burada  $\rho_s$ ,  $c_s$  ve  $k_s$  sırasıyla safir yüzeyin yoğunluğunu, ısı kapasitesini ve termal iletkenliğini gösterir. Sayısal çalışmalarda adaptif zaman adımı kullanılmıştır. Adaptif zaman adımı Courant – Friedrichs – Lewy (CFL) kriterlerine göre belirlendi. Bu kriterde Courant sayısı Eş. (8) ile tanımlanır:

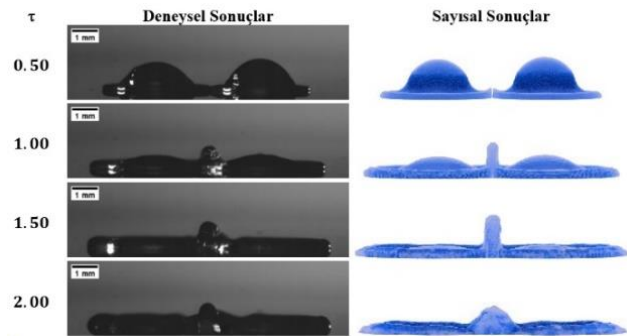
$$\text{Courant sayısı} = U \frac{\Delta t}{\Delta x} \quad (8)$$

burada U hızın büyüklüğü,  $\Delta t$  zaman aralığı ve  $\Delta x$  ağ elemanları arasındaki mesafedir. Courant sayısı 1'den küçük veya 1'e eşit olmalıdır, aksi takdirde sonuçlar yakınsamayacağından problem doğru bir şekilde çözülmeyecektir. Sonuçların yakınsaması için zaman

aralığı azaltılabilir veya daha kötü bir ağ yapısı seçilebilir. Sayısal çalışmalarımızda Courant sayısı 0,5 alınarak adaptif zaman adımı uygulandı. Ayrıca, gevşeme faktörü 0,9 ve maksimum iç iterasyonu 5 olarak uygulandı.

## Sayısal Modelin Doğrulanması

Çoklu damlacık etkileşimleri için 3 boyutlu sayısal modeller geliştirilip deneysel verilerle (Gultekin, 2021) doğrulanmıştır. Şekil 2'de, ortam sıcaklığında katı bir yüzey ile damlacık çiftinin etkileşiminin deneysel ve sayısal sonuçlarını görsel olarak karşılaştırmaktadır. Şekillerden görülebileceği gibi, farklı boyutsuz zaman aralıkları için öngörülen damlacık çifti görselleri ile shadowgraph görüntüleri arasında büyük bir uyum olmasına rağmen, tam olarak örtüşme gerçekleşmemiştir. Sayısal model tahmini hesaplamasında bazı sınırlamalar vardır: Bir modelin karmaşıklığına bakılmaksızın bazı basitleştirmeler kaçınılmazdır; mükemmel bir model elde edilemez. Oluşturduğumuz modelde damlacıkların yüzeye çarpmadan önceki durumu tam küre olarak kabul edilmiştir. Ancak, görüntülerde elde edilen damlacıkların dairesellik oranı 0,90 civarındadır. Spesifik bir problem için mükemmel bir model kabul edilebilse bile, başlangıç ve sınır koşulları ve model parametreleri sonsuz hassasiyetle bilinmedikçe, tahmin sonuçları yine de hatalar içerir.



Şekil 2. Ortam sıcaklığında katı bir yüzey ile damlacık çiftinin şekilsel değişiminin deneysel ve sayısal olarak karşılaştırılması. (Gultekin, 2021).

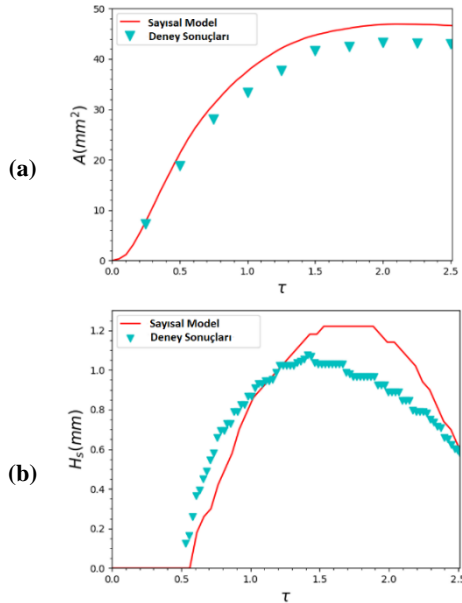
Modellemede kullanılan verilerin doğruluğu, görüntü analizi yöntemlerindeki hatalar, görüntü çözünürlüğündeki belirsizlikler ve damlacıkların yüzeye çarpmadan önceki dairesellik oranındaki değişim gibi faktörlerden kaynaklanabilir. Özellikle, damlacıkların çapları, hızları ve aralarındaki mesafeler gibi verilerin doğruluğu, deneylerde elde edilen görüntülerden görüntü analizi yöntemleri kullanılarak elde edilmiş olmasına rağmen, görüntü çözünürlüğündeki belirsizlikler ve rastgelelik gibi faktörler nedeniyle bazı sapmalar oluşabilir. Bu faktörlerin ve bileşik etkilerinin tam örtüşme olmamasının muhtemel nedenleri olduğu değerlendirilebilir. Damlacık çiftinin dinamik çarpma koşulları Tablo 2'de verilmiştir. ImageJ programı (Schneider *vd.*, 2012) kullanılarak deneysel sonuçlardan damlacık çapları, çarpma hızları, dikey ve yatay mesafeler elde edilmiştir. Elde edilen bu değerler sayısal

modele uygulanmıştır. Bu parametreler, başlangıçtaki ortalama damlacık çapı kullanılarak  $\bar{d}_h = \frac{d_h}{D_0}$ ,  $\bar{d}_v = \frac{d_v}{D_0}$  boyutsuzlandırılmıştır. Boyutsuz zaman  $\tau$  ( $\tau = tu_0/D_0$ ) olarak tanımlanmıştır. Ayrıca, boyutsuz Weber sayısı, damlacık kinetik enerjisinin yüzey gerilimine oranını temsil eder ve  $We = \rho u_0^2 D_0 / \sigma$  şeklinde tanımlanır.

**Tablo 2.** Ortam sıcaklığında damlacık çiftinin çarpma koşulları.

Parametreler	Damlacık çifti	
Damlacık çapları [mm]	2,23	2,25
Damlacık hızları [m/s]	1,13	1,13
We	40	40
$\bar{d}_h$	1,80	
$\bar{d}_v$	0,02	

Modelimizi nicel verilerle doğrulamak için, ilk olarak, Şekil 3 (a)'da gösterildiği gibi, damlacık çifti için yayılma alanının boyutsuz zamanla değişimi karşılaştırılarak oldukça iyi bir uyum olduğu görüldü. Daha sonra Şekil 3 (b)'de gösterildiği gibi katman yüksekliğinin boyutsuz zamanla değişimi de karşılaştırılmıştır. Sayısal olarak tahmin edilen katman yüksekliğinin değişimi ile deneysel sonuçlar arasında büyük benzerlikler olmasına rağmen, sayısal model katman yüksekliğini biraz fazla tahmin etmektedir. Şekillerden de görüldüğü gibi sayısal veriler ile deneysel veriler arasında oldukça iyi bir uyum bulunmaktadır.



**Şekil 3.** (a) Yayılma alanının boyutsuz zamanla değişimi ve (b) katman yüksekliğinin boyutsuz zamanla değişiminin deneysel ve sayısal karşılaştırılması. (İşaretler deneysel sonuçları temsil ederken düz çizgiler sayısal sonuçları temsil etmektedir.) (Gultekin, 2021).

## SONUÇLAR VE TARTIŞMA

Sıcak yüzeyden gerçekleşecek olan ısı transferi damlacıkların yüzeyde yayılması ile doğrudan bağlantılıdır. Damlacıkların yüzeyde yayılması ise damlacık çapı, damlacık hızı, damlacıklar arası mesafe ve sıvının fiziksel özellikleri gibi faktörlere bağlıdır. Weber sayısı arttıkça damlacıkların yüzeyde yayılma

alanı artmaktadır. Bu yüzden, sadece damlacık çaplarının etkisini görmek için aynı Weber sayısında farklı damlacık çapları için (Gultekin, 2021) numaralı çalışmamızda karşılaştırıldı. Weber sayısını aynı tutmak için damlacıkların başlangıç hızları farklı alındı. Yayılma faktörünün başlangıçta tüm durumlar için hemen hemen aynı davranışı gösterdiği gözlemlendi. Belli bir noktadan sonra daha küçük damlacık çapları için yayılma faktörünün daha yüksek olduğu gözlemlendi. Başka bir deyişle, daha yüksek çarpma hızına sahip damlacıkların, aynı Weber sayıları için daha geniş yayılma alanına neden olduğu görüldü. Bu makale kapsamında damlacık çapları ile ilgili bir çalışma yapılmamıştır. Eşzamanlı çoklu damlacıklarda çarpma hızı, damlacıklar arası yatay mesafe ve damlacık sayısı incelenmiştir.

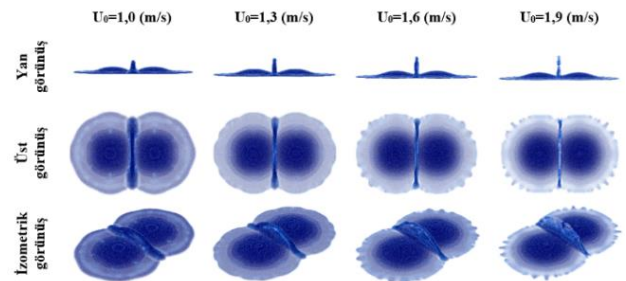
## Eşzamanlı Damlacık Çifti için Çarpma Hızının Etkisi

Katı yüzeye eşzamanlı damlacık çifti çarpmalarında damlacık çarpma hızının etkisini görmek için, farklı ilk çarpma hızları karşılaştırıldı. Parametrik incelemeler için damlacık çifti çarpma koşulları Tablo 3'te verilmiştir.

**Tablo 3.** Eşzamanlı damlacık çiftlerinde çarpma hızının etkisini araştırmak için kullanılan damlacık parametreleri.

Parametreler	Değer
Damlacık çapı [mm]	2,30
Damlacık hızı [m/s]	1,0-1,3-1,6-1,9
Weber sayısı	32 – 115
Yüzey sıcaklığı	130
$\bar{d}_h$	1,6

Farklı çarpma hızları için katı yüzeye damlacık çifti etkileşimleri  $\tau=1$  zamanında Şekil 4'te verilmiştir. En düşük çarpma hızı durumunda, orta bölgedeki etkileşim, damlacıkların başlangıçta sahip olduğu düşük kinetik enerjisi yüzünden minimum katmanyüksekliğine yol açar. Weber sayısı arttıkça, damlacığın hidrodinamik davranışı da benzer bir davranış gösterir, ancak daha büyük başlangıç kinetik enerjisi nedeniyle katmanyüksekliğinin şiddeti artar. Bir noktadan sonra, Weber sayısı arttıkça katman yüksekliği kararlılığını kaybeder ve ayrılmalar gerçekleşir.

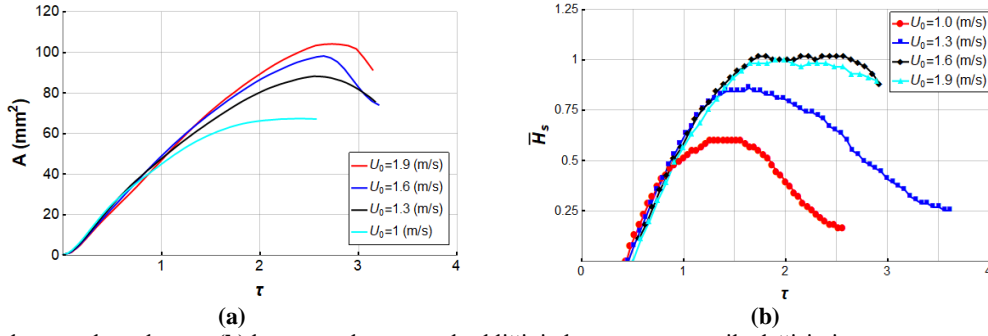


**Şekil 4.** Farklı çarpma hızları için  $\tau=1$  anında eşzamanlı damlacık çifti etkileşimleri.

Şekil 5 (a) ve (b), farklı çarpma hızlarına sahip damlacık çiftleri için toplam yayılma alanı ve boyutsuz katman yüksekliğinin zamanla değişimini göstermektedir. Efektif toplam yayılma alanı değerleri, tüm durumlar için büyük ölçüde  $\tau=1$ 'e kadar benzerdir. Bu değerlerde olan benzerlik,  $\tau=2$  anında  $U_0=1,6$  (m/s) ve  $U_0=1,9$  (m/s)

devam ederken, düşük çarpma hızlarına sahip durumlarda yayılma süreci bittiği ve gerileme süreci başladığı için farklı bir eğilim göstermektedir. Şekil 5 (b), boyutsuz katman yüksekliğinin zamanla değişimini göstermektedir. Şekilden görülebileceği gibi, düşük çarpma hızı durumlarında, boyutsuz yükselen levha, yerçekimi etkisi nedeniyle maksimum yüksekliğe

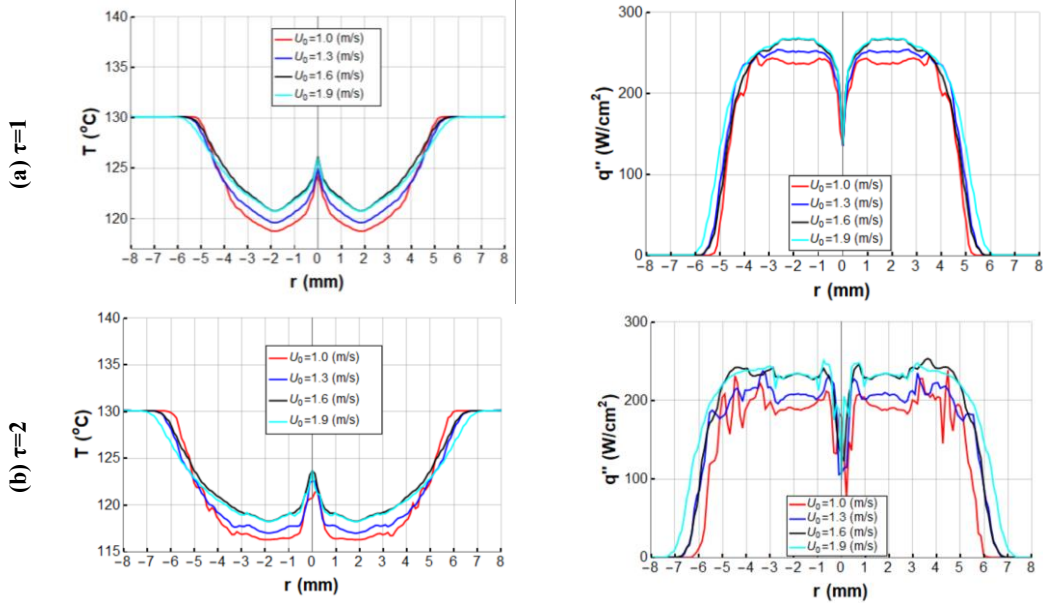
ulaştıktan sonra tekrardan düşmeye başlar. Yüksek çarpma hızı durumlarında, bir noktada oluşan yükselti kararlılığını kaybederek parçalanmaya başlar. Katman yükselmesinde parçalanma gerçekleştikten sonra kopan parçaların yükselmesi dikkate alınmamıştır. Bütünlüğü sağlayan kısımdaki yükseklik dikkate alınmıştır.



Şekil 5. (a) Toplam yayılma alanı ve (b) boyutsuz katman yüksekliğinin boyutsuz zaman ile değişimi.

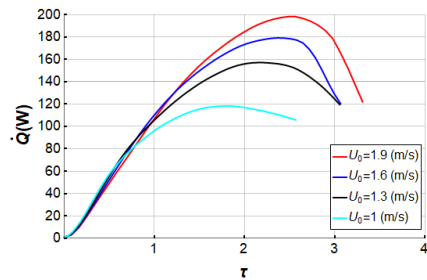
Damlacık çarpma hızının etkisini daha iyi görmek için, sıcaklık dağılımları ve ısı akısı değişimleri Şekil 6'da gösterilmiştir. Etkileşimin ilk aşamasında etki alanı çok küçük olmasına rağmen, ısıtılan yüzey ile damlacıklar arasındaki büyük sıcaklık farkları nedeniyle yüzey sıcaklığı hızla düştüğü ve birim alan başına oluşan ısı transferinin daha yüksek olduğu görülmüştür. En düşük

çarpma hızı durumunda yüzey sıcaklığında daha belirgin bir düşüş gözlemlenmiştir. Bunun nedeni, çarpma hızı azaldıkça boyutsuz zamanın aynı değere ulaşmasının daha fazla zaman almasıdır. Yüksek çarpma hızındaki damlacık çiftlerin yüzey üzerindeki termal etkileri büyük ölçüde benzerdir.



Şekil 6. Farklı çarpma hızları için damlacık çiftleri için yüzey sıcaklık dağılımları ve ısı akısı değişimleri (a)  $\tau=1$  ve (b)  $\tau=2$ .

Şekil 7, farklı çarpma hızlarına sahip eşzamanlı damlacık çiftlerinin yüzeyde yayılmasıyla gerçekleşen ısı transferinin boyutsuz zamanla değişimini göstermektedir. Isı transferinin boyutsuz zamanla değişimi, yayılma alanının zamanla değişimi ile benzer davranışlar göstermiştir. Beklendiği gibi çarpma hızı arttıkça yüzeydeki yayılma alanı arttığı için yüzeyden oluşan ısı transferi de artmaktadır.



**Şekil 7.** Farklı çarpma hızlarına sahip damlacık çiftlerinin yüzeyde yayılmasıyla gerçekleşen ısı transferinin boyutsuz zamanla değişimi.

### Eşzamanlı Damlacık Çifti için Damlacıklar Arası Yatay Mesafenin Etkisi

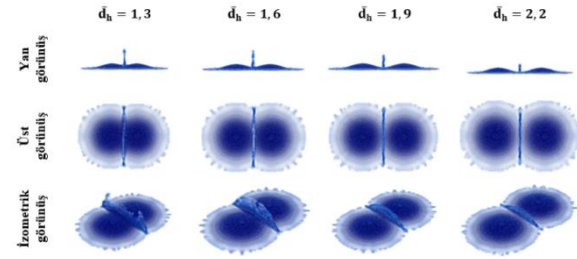
Damlacıklar arası yatay mesafe, damlacıklar arası oluşan etkileşimin şiddetini etkileyen en önemli faktörlerden biridir. Damlacık çifti etkileşimlerinde damlacıklar arası yatay mesafenin etkisini görmek için farklı yatay mesafeler karşılaştırılmıştır. Parametrik incelemeler için damlacık çifti çarpma koşulları Tablo 4'te verilmiştir.

**Tablo 4.** Eşzamanlı damlacık çiftlerinde damlacıklar arası yatay mesafenin etkisini araştırmak için kullanılan damlacık parametreleri.

Parametreler	Değerler
Damlacık çapı [mm]	2,30
Damlacık hızı [m/s]	1,9
Weber sayısı	115
Yüzey sıcaklığı	130
$\bar{d}_h=1$	1,3 - 1,6 - 1,9 - 2,2

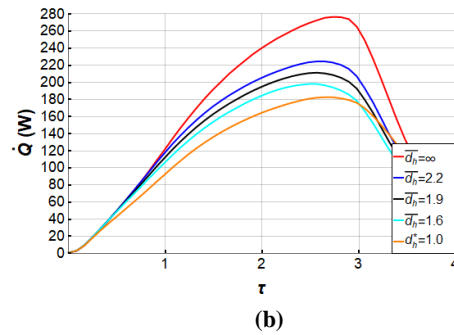
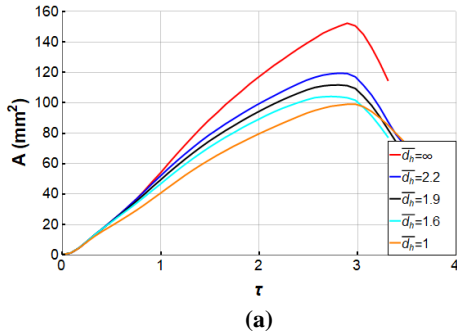
Farklı yatay mesafeler için  $\tau=1$  anında damlacık çifti etkileşimleri Şekil 8'de verilmiştir. Beklendiği gibi, aralarındaki yatay mesafe ne kadar küçük olursa, damlacıklar yüzeydeki yayılma sürecinde birbirleriyle o kadar hızlı etkileşime girdiği görülmüştür. Daha büyük yatay mesafeler için, lameller viskoz yayılım nedeniyle

daha fazla enerji kaybederek daha zayıf katman yüksekliğine neden olmuştur.



**Şekil 8.** Damlacıklar arası farklı yatay mesafeler için  $\tau=1$  anında eşzamanlı damlacık çifti etkileşimleri.

Şekil 9, farklı yatay mesafelere sahip damlacık çiftleri için yüzeyde gerçekleşen toplam yayılma alanı ve yüzeyden gerçekleşen ısı transferinin boyutsuz zamanla değişimini göstermektedir. Damlacıklar arasındaki yatay mesafe azaldıkça etkileşimin büyüklüğü artmakta ve yüzeyde kaplanan yayılma alanı ve ısı transferi azalmaktadır. Efektif toplam yayılma alanları,  $\tau=2$ 'de  $\bar{d}_h=2.2$  ve  $\bar{d}_h=1$  konfigürasyonları için sırasıyla tek damlacık konfigürasyonundan %14,5 ve %32 daha azdır. Bu değerler  $\tau=3$ 'te sırasıyla %22 ve %34'tür. Isı transferinin değişimi için benzer davranışlar gözlenir ve performans kaybı değerleri hemen hemen aynıdır. Bu nedenle damlacıklar arası etkileşim olgusunun özellikle damlacık çarpmasından sonraki ilk aşamalarda soğutma verimini güçlü bir şekilde etkilediği söylenebilir.

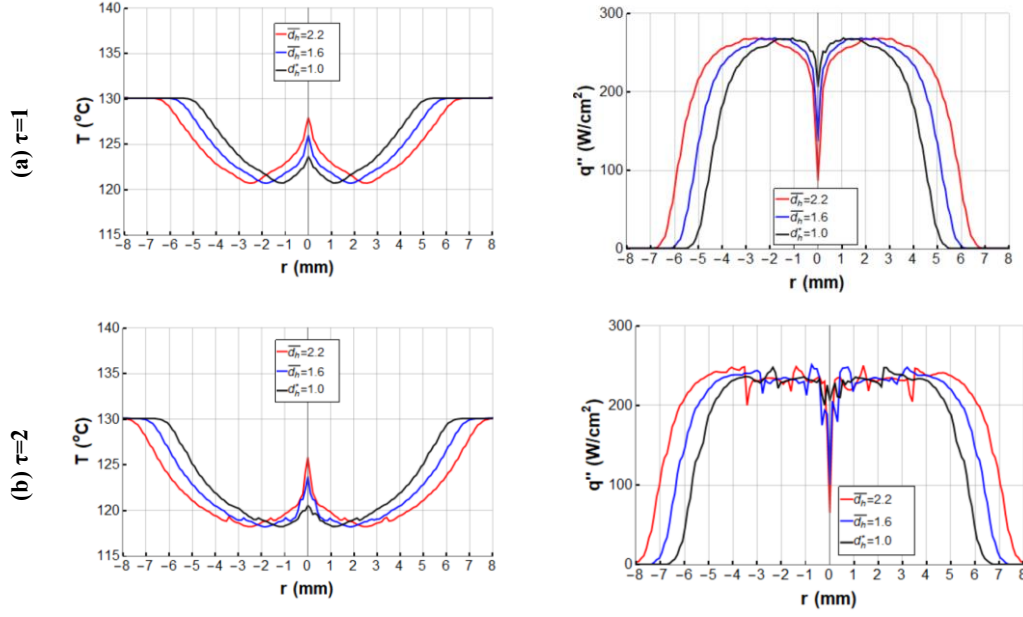


**Şekil 9.** Farklı yatay mesafelere sahip damlacık çiftleri için yüzeyde gerçekleşen (a) toplam yayılma alanı ve (b) ısı transferinin boyutsuz zamanla değişimi.

Eşzamanlı damlacık çiftleri için yatay mesafenin sıcaklık dağılımları ve ısı akısı davranışı üzerindeki etkisi Şekil 10'da gösterilmektedir. Damlacıklar arasındaki yatay mesafe arttıkça etkileşim daha fazla geciktiğinden dolayı damlacıklar katı yüzey üzerinde daha fazla yayılmıştır ve ısıtılan yüzeyden daha fazla ısı akısı oluştuğu görülmüştür.

İncelenen koşullarda safir camdan gerçekleşen ısı akısı  $250 \text{ W/cm}^2$  mertebelerinde olduğu görülmüştür. Bunun yanında, elektronik cihazlardaki sprej soğutma uygulamalarındaki ısı akısı, uygulamanın özel koşullarına bağlı olarak büyük ölçüde değişebilir. Bu

koşullar elektronik cihazın boyutu ve tipi, soğutucu sprejin özellikleri ve sprejin akış hızı ve basıncı gibi faktörlere bağlı olarak önemli ölçüde değişebilir. Bunun yanında ısı akısı, yüzeyin sıcaklığı ve soğutucu akışkanın sıcaklık farkına ve yüzeyde kullanılan malzemenin ısı iletkenliğine bağlı olduğundan uygulama sırasında büyük ölçüde değişebilir. Daha yüksek sıcaklığa ve ısı iletkenliğe sahip metal yüzeylerden çok daha fazla oranda ısı akısı gerçekleşecektir. Ayrıca, farklı yüzey morfolojileri kullanılarak sprej soğutma uygulamalarındaki gerçekleşen ısı akıları,  $1000 \text{ W/cm}^2$  mertebelerine ulaşabilmektedir.



Şekil 10. Farklı yatay mesafelere sahip damlacık çiftleri için yüzey sıcaklık dağılımları ve ısı akısı değişimleri (a)  $\tau=1$  ve (b)  $\tau=2$ .

### Eşzamanlı Çoklu Damlacık Etkileşimleri için Damlacık Sayısının Etkisi

Sprey soğutma için damlacıklar arası hiçbir etkileşimin olmadığı en optimum durumu varsaydığımızda, her bir damlacık tek bir damlacık gibi yayılır, o zaman toplam yayılma alanı, tek bir damlacık için oluşan yayılma alanının damlacık sayısı (N) çarpımıyla elde edilir. Ancak, çoklu damlacıklar katı bir yüzeye çarptığında, damlacık parametrelerine (damlacık hızı, damlacıklar arası mesafe, damlacık sayısı vb.) bağlı olarak damlacıklar birbirine yeterince yakınsa damlacıklar arasında bir etkileşim gerçekleşir. Damlacıkların hidrodinamik ve ısı transferi davranışları, bu etkileşim nedeniyle tek damlacık durumlarından oldukça farklıdır. Bu etkileşim, katı yüzey üzerinde damlacık başına daha küçük yayılma alanına neden olur. Bu nedenle, katı yüzeye aynı anda çarpan çoklu damlacıklar için yayılma alanını tahmin etmek için Gultekin (2021) doktora tezinde Eş. (9) ve Eş. (10) ifadelerini önermiştir.

$$A_{ND} = NA_{SD} - (N - 1)A_i \quad (9)$$

burada N damlacık sayısıdır,  $A_{SD}$  tek damlacık için yayılma alanıdır ve  $A_i$  etkileşim nedeniyle oluşan alan kaybıdır. Bu denklemi boyutsuz hale getirerek ve düzenleyerek aşağıdaki şekilde tekrar yazabiliriz.

$$\bar{A}(\tau) = \frac{A_{toplamlam}(\tau)}{ND_0^2} = \pi \frac{\beta^2(\tau)}{4} \left[ 1 - \frac{2 * (N - 1)}{\pi N} \left( \cos^{-1} \left( \frac{\bar{d}_h}{\beta(\tau)} \right) - \sqrt{\left( \frac{\bar{d}_h}{\beta(\tau)} \right)^2 - \left( \frac{\bar{d}_h}{\beta(\tau)} \right)^4} \right) \right] \quad (10)$$

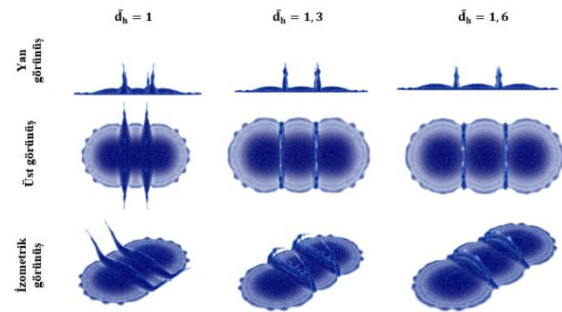
Denklemden görülebileceği gibi, etkin yayılma alanı, damlacık çarpma koşullarına ve damlacık sayısına ve

damlacıklar arasındaki yatay mesafeye bağlıdır. Bu nedenle, eşzamanlı üçlü damlacık durumları için farklı yatay mesafeler incelenmiştir. Parametrik incelemeler için üçlü damlacık konfigürasyonları çarpma koşulları Tablo 5'de verilmiştir.

Tablo 5. Eşzamanlı üçlü damlacık konfigürasyonlarında damlacıklar arası yatay mesafenin etkisini araştırmak için kullanılan damlacık parametreleri.

Parametreler	Değerler
Damlacık çapı [mm]	2,30
Damlacık hızı [m/s]	1,9
Weber sayısı	115
Yüzey sıcaklığı	130
$\bar{d}_h$	1- 1,3- 1,6

Farklı yatay mesafeler için katı yüzeye üçlü damlacık çarpması Şekil 11'de verilmiştir. Genel olarak damlacık çifti ile benzer hidrodinamik davranışlar gözlenmiştir.

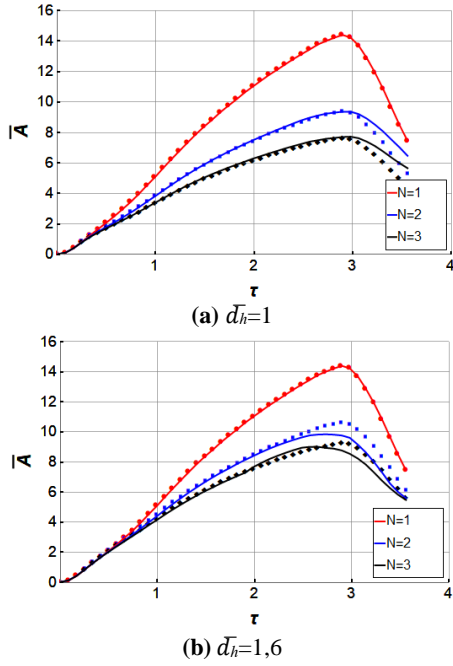


Şekil 11. Damlacıklar arası farklı yatay mesafeler için  $\tau=1$  anında eşzamanlı üçlü damlacık konfigürasyonu etkileşimleri.

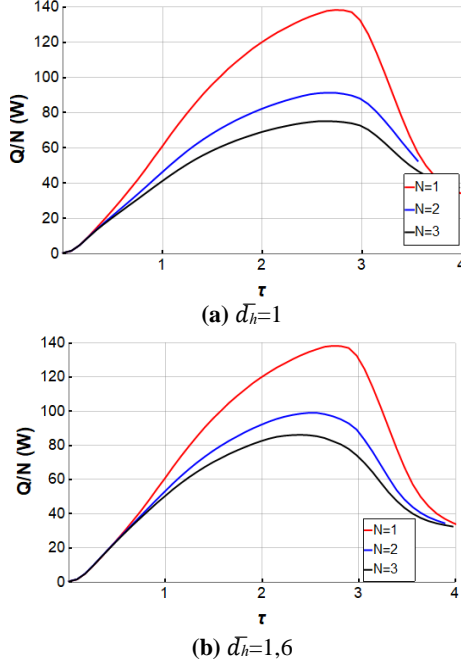
Şekil 12, farklı sayıda damlacık konfigürasyonları için boyutsuz yayılma alanının boyutsuz zamanla değişimi için sayısal sonuçların ve önerilen ifadenin karşılaştırmasını göstermektedir. Önerilen analitik model genellikle  $\tau \approx 2,5$ 'e kadar hesaplama sonuçlarıyla



uyumludur. Ayrıca, farklı sayıda damlacık çarpması için damlacık başına yüzeyden oluşan ısı transferinin değişimi Şekil 13'te verilmiştir.



**Şekil 12.** Farklı damlacık sayıları için boyutsuz yayılma alanının boyutsuz zamanla değişimi. Düz çizgiler hesaplama sonuçlarını temsil ederken semboller denklem (10)'u temsil etmektedir. (a)  $\bar{d}_h=1$  (b)  $\bar{d}_h=1,6$ .



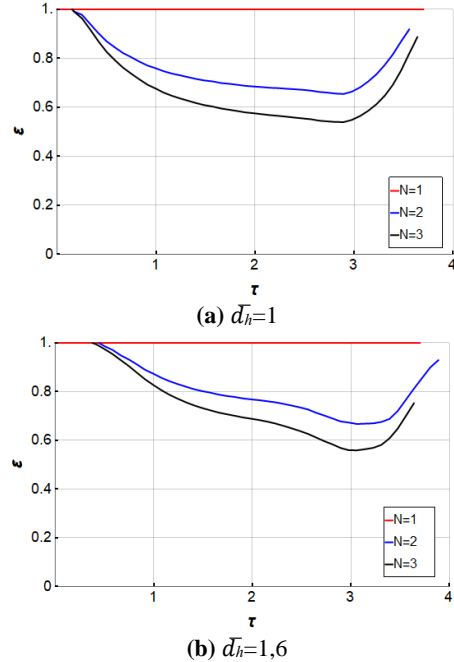
**Şekil 13.** Farklı sayıda damlacık çarpması için damlacık başına yüzeyden gerçekleşen ısı transferinin zamanla değişimi (a)  $\bar{d}_h=1$  (b)  $\bar{d}_h=1,6$ .

Tek damlacık etkisini referans alarak çoklu damlacık sayısının soğutma verimliliği üzerindeki etkisini incelemek istersek. Çoklu damlacıklar için soğutma verimi performansını, N tane damlacıkların çarpışmasından kaynaklanan toplam ısı transferinin, N

sayıda tek bir damlacığın çarpışmasından oluşan toplam ısı transferine oranlayarak Eş.(11) ifadesiyle tanımlanabilir.

$$\epsilon = \frac{Q_{ND}}{N * Q_{SD}} \quad (11)$$

Etkileşimin olmadığı spray soğutma için en uygun koşul varsayıldığında, her bir damlacık tek bir damlacık gibi yayılır ve  $\epsilon$  bire gider. Etkileşimlerin tamamen baskın hale geldiği tersi durumda ise  $1/N$ 'ye yakınsar. Şekil 14 (a) ve (b), farklı damlacık sayısına sahip konfigürasyonlar için sırasıyla  $\bar{d}_h = 1$  ve  $\bar{d}_h = 1,6$  durumlarında soğutma verimliliği performansının boyutsuz zamanla değişimini göstermektedir. Önceki bölümlerde de bahsedildiği gibi, damlacıklar arasındaki yatay mesafe ne kadar kısaysa, etkileşim daha erken gerçekleşir. Soğutma verimliliği performansı büyük ölçüde damlacık sayısına ve çoklu damlacıklar arasındaki yatay mesafeye bağlıdır. Damlacık çifti ve üçlü damlacık konfigürasyonlarının  $\bar{d}_h = 1$  ve  $\tau=1$  durumunda soğutma verimlilikleri sırasıyla 0,76 ve 0,67'dir. Bu değerler  $\tau=3$  anında sırasıyla 0,66 ve 0,54 değerleridir. Boyutsuz yatay mesafe 1,6 olduğunda,  $\tau=1$  için damlacık çifti ve üçlü damlacık konfigürasyonları durumunda soğutma verimleri sırasıyla 0,87 ve 0,82'dir. Bu değerler  $\tau=3$  anında sırasıyla 0,67 ve 0,56 değerleridir. Bu nedenle, özellikle damlacık çarpışmasından sonraki ilk aşamalarda, etkileşim olgusunun soğutma verimini güçlü bir şekilde etkilediği söylenebilir.

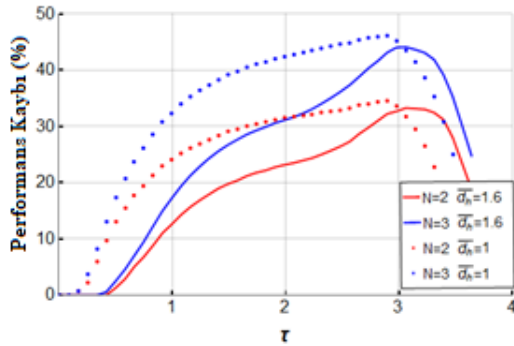


**Şekil 14.** Farklı damlacık sayısına sahip konfigürasyonlar için sırasıyla (a)  $\bar{d}_h=1$  ve (b)  $\bar{d}_h=1,6$  durumlarında soğutma verimliliği performansının boyutsuz zamanla değişimi.

Aynı şekilde performans kaybı (%) Eş. (12) ifadesiyle tanımlanabilir.

$$\text{Performans Kaybı (\%)} = \left(1 - \frac{\dot{Q}_{ND}}{N * \dot{Q}_{SD}}\right) * 100 \quad (12)$$

Şekil 15, farklı sayıda damlacık ve yatay mesafeler için performans kaybının değişimini göstermektedir. Şekilden görülebileceği gibi, çoklu damlacık etkileşimi olgusu, özellikle damlacık çarpmasından sonraki ilk aşamalarda soğutma performansını güçlü bir şekilde etkiler. Damlacık çifti ve üçlü damlacık konfigürasyonlarında  $\bar{d}_h=1$  ve  $\tau=1$  anında performans kayıpları sırasıyla %24 ve %33'tür. Bu değerler  $\tau=3$ 'te sırasıyla %34 ve %46'dır. Boyutsuz yatay mesafe 1,6 olduğunda,  $\tau=1$  için damlacık çifti ve üçlü damlacık konfigürasyon durumunda performans kayıpları sırasıyla %13 ve %18'dir. Bu değerler  $\tau=3$ 'te sırasıyla %33 ve %44'tür.



**Şekil 15.** Farklı sayıda damlacık ve yatay mesafeler için performans kaybının zamanla değişimi. Düz çizgiler  $\bar{d}_h=1.6$  için hesaplama sonuçlarını temsil ederken, noktalar  $\bar{d}_h=1$  için hesaplama sonuçlarını temsil etmektedir.

## SONUÇLAR

Sprey soğutma sırasında sıcak bir yüzeye etkileyen çoklu damlacıkların birbirleri ile etkileşimlerinin yüzeyden olan ısı transferi performansına etkisi sayısal yöntemlerle incelenmiştir. Sayısal incelemelerde Star CCM+ yazılımı kullanılmış olup ara yüz takibi için VOF yöntemi kullanılmıştır. Bu çalışma kapsamında, damlacık çarpma hızı, damlacıklar arasındaki yatay mesafe ve damlacık sayısı gibi parametreler incelenmiştir. Damlacıklar arasındaki yatay mesafe kısaldıkça etkileşimin büyüklüğü artar ve yüzeyde kaplanan yayılma alanı ve ısı transferi azalır. Efektif yayılma alanları,  $\tau=2$ 'de sırasıyla  $\bar{d}_h=2.2$  ve  $\bar{d}_h=1$  konfigürasyonları için tek damlacık konfigürasyonundan % 14,5 ve % 32 daha azdır. Bu değerler  $\tau=3$ 'te sırasıyla % 22 ve % 34'tür.

Tek bir damlacık için yayılma faktörünün değişimini hesaba katarak katı yüzey üzerinde eş zamanlı etki eden birden çok damlacık için damlacık başına yayılma alanını tahmin etmek için matematiksel bir ifade önerilmiştir. Damlacık sayısının soğutma performansına etkisini görmek için, tek bir damlacık için soğutma performansının değişimi referans alınarak bir ifade tanımlandı. Etkileşimin özellikle çoklu damlacık etkileşiminden sonraki ilk aşamalarda soğutma

performansını güçlü bir şekilde etkilediği bulunmuştur. Damlacık çifti ve üçlü damlacık konfigürasyonları ( $\bar{d}_h=1$  ve  $\tau=3$  durumunda) performans kayıpları sırasıyla %34 ve %46'ya varmaktadır. Boyutsuz yatay mesafe 1,6 olduğunda, soğutma performansları sırasıyla çift damlacık çifti ve üçlü konfigürasyonlarda %33 ve %44'tür.

## TEŞEKKÜR

Bu çalışma, Japonya Atom Enerjisi Ajansı tarafından Nükleer Enerji Bilimi ve Teknolojisi ve İnsan Kaynakları Geliştirme Projesi kapsamında finansal olarak desteklenmiştir. Ayrıca, ilk yazara Türkiye Bilimsel ve Teknolojik Araştırma Kurumu (TÜBİTAK/2214-A-Yurt Dışı Doktora Sırası Araştırma Burs Programı) tarafından mali destek sağlanmıştır.

## KAYNAKLAR

Akao, F., Araki, K., Mori, S., Moriyama, A., 1980, Deformation Behaviors of a Liquid Droplet Impinging Onto Hot Metal Surface, *Transactions of the Iron and Steel Institute of Japan*, 20, 737–743, doi.org/10.2355/isijinternational1966.20.737

Bostanci, H., Rini, D.P., Kizito, J.P., Singh, V., Seal, S., Chow, L.C., 2012, High heat flux spray cooling with ammonia : Investigation of enhanced surfaces for CHF. *International Journal of Heat and Mass Transfer*, 55, 3849–3856, doi.org/10.1016/j.ijheatmasstransfer.2012.03.040

Brackbill, J.U., Kothe, D.B., Zemach, C., 1992, A continuum method for modeling surface tension, *Journal of Computational Physics*, 100, 335–354, doi.org/10.1016/0021-9991(92)90240-Y

Breitenbach, J., Roisman, I. V., Tropea, C., 2017, Heat transfer in the film boiling regime : Single drop impact and spray coolin, *International Journal of Heat and Mass Transfer*, 110, 34–42, doi.org/http://dx.doi.org/10.1016/j.ijheatmasstransfer.2017.03.004

Castrejón-Pita, J.R., Martin, G.D., Hoath, S.D., Hutchings, I.M., 2008, A simple large-scale droplet generator for studies of inkjet printing, *Review of Scientific Instruments*, 79, doi.org/10.1063/1.2957744

Cheng, W., Zhang, W., Jiang, L., Yang, S., Hu, L., 2015, Experimental investigation of large area spray cooling with compact chamber in the non-boiling regime, *Applied Thermal Engineering*, 80, 160–167, doi.org/10.1016/j.applthermaleng.2015.01.055

Clanet, C., Béguin, C., Richard, D., Quéré, D., 2004, Maximal deformation of an impacting drop, *Journal of Fluid Mechanics*, 517, 199–208, doi.org/10.1017/S0022112004000904

- Cossali, G.E., Marengo, M., Santini, M., Bergamo, U., 2005, Effects of wall effusivity on secondary droplet atomisation from single and multiple drop impact onto heated surfaces, *Proceedings of the 20th ILASS - Europe Meeting*, pp. 1–6, Orleans, France.
- Cossali, G., Marengo, M., Santini, M., 2003, Multiple drop impact on heated surface, *Proceedings of the 9th ICLASS*, Sorrento, Italy.
- de Gans, B.-J., Duineveld, P.C., Schubert, U.S., 2004, Inkjet Printing of Polymers: State of the Art and Future Developments, *Advanced Materials*, 16, 203–213, doi.org/10.1002/adma.200300385
- Ersoy, N.E., Eslamian, M., 2020, Central uprising sheet in simultaneous and near-simultaneous impact of two high kinetic energy droplets onto dry surface and thin liquid film, *Physics of Fluids*, 32, 012108, doi.org/10.1063/1.5135029
- Gultekin, A., 2021, *Experimental and numerical investigation of single and multiple droplet interactions with high-temperature surfaces*, Ph.D. Thesis, Istanbul Technical University, Istanbul, Türkiye.
- Gultekin, A., Erkan, N., Colak, U., Suzuki, S., 2020, PIV measurement inside single and double droplet interaction on a solid surface, *Experiments in Fluids*, 61, 1–18, doi.org/10.1007/s00348-020-03051-0
- Gultekin, A., Erkan, N., Ozdemir, E., Colak, U., Suzuki, S., 2021, Simultaneous multiple droplet impact and their interactions on a heated surface, *Experimental Thermal and Fluid Science*, 120, 110255, doi.org/10.1016/j.expthermflusci.2020.110255
- Hatakenaka, R., Breitenbach, J., Roisman, I. V., Tropea, C., Tagawa, Y., 2019, Magic carpet breakup of a drop impacting onto a heated surface in a depressurized environment, *International Journal of Heat and Mass Transfer*, 145, 118729, doi.org/10.1016/j.ijheatmasstransfer.2019.118729
- Hirt, C.W., Nichols, B.D., 1981, Volume of fluid (VOF) method for the dynamics of free boundaries, *Journal of Computational Physics*, 39, 201–225, doi.org/10.1016/0021-9991(81)90145-5
- Huang, H.M., Chen, X.P., 2018, Energetic analysis of drop's maximum spreading on solid surface with low impact speed, *Physics of Fluids*, 30, doi.org/10.1063/1.5006439
- Jung, J., Jeong, S., Kim, H., 2016, Investigation of single-droplet/wall collision heat transfer characteristics using infrared thermometry, *International Journal of Heat and Mass Transfer*, 92, 774–783, doi.org/10.1016/j.ijheatmasstransfer.2015.09.050
- Lee, S.H., Harth, K., Rump, M., Kim, M., Lohse, D., Fezzaa, K., Je, J.H., 2020, Drop impact on hot plates: Contact times, lift-off and the lamella rupture, *Soft Matter*, 16, 7935–7949, doi.org/10.1039/d0sm00459f
- Liang, G., Mudawar, I., 2017, Review of drop impact on heated walls. *International Journal of Heat and Mass Transfer*, 106, 103–126, doi.org/10.1016/j.ijheatmasstransfer.2016.10.031
- Liang, G., Yu, H., Chen, L., 2019a, Interfacial phenomena in impact of droplet array on solid wall, *Acta Mechanica*, 231, 305–319, doi.org/doi.org/10.1007/s00707-019-02542-4
- Liang, G., Zhang, T., Chen, L., Chen, Y., Shen, S., 2019b, Single-phase heat transfer of multi-droplet impact on liquid film, *International Journal of Heat and Mass Transfer*, 132, 288–292, doi.org/10.1016/j.ijheatmasstransfer.2018.11.145
- Liang, G., Zhang, T., Chen, Y., Chen, L., Shen, S., 2019c, Two-phase heat transfer of multi-droplet impact on liquid film, *International Journal of Heat and Mass Transfer*, 139, 832–847, doi.org/10.1016/j.ijheatmasstransfer.2019.05.055
- Liang, G., Zhang, T., Yu, H., Chen, H., Shen, S., 2018, Simultaneous Impact of Multiple Droplets on Liquid Film, *Journal of Industrial and Engineering Chemistry*, 65, 51–61, doi.org/doi.org/10.1016/j.jiec.2018.04.011
- Li, L., Jia, X., Liu, Y., Su, M., 2016, Simulation of double droplets impact on liquid film by a simplified lattice Boltzmann model, *Applied Thermal Engineering*, 98, 656–669, doi.org/10.1016/j.applthermaleng.2015.12.050
- Margarinos, I., Nikolopoulos, N., Marengo, M., Antonini, C., Gavaises, M., 2014, VOF simulations of the contact angle dynamics during the drop spreading: Standard models and a new wetting force model, *Advances in Colloid and Interface Science*, 212, 1–20, doi.org/http://dx.doi.org/10.1016/j.cis.2014.07.004
- Mehdizadeh, N.Z., Chandra, S., 2006, Boiling during high-velocity impact of water droplets on a hot stainless steel surface, *Proceedings of the Royal Society A: Mathematical, Physical and Engineering Sciences*, 462, 3115–3131, doi.org/10.1098/rspa.2006.1722
- Nikolopoulos, N., Theodorakakos, A., Bergeles, G., 2007, A numerical investigation of the evaporation process of a liquid droplet impinging onto a hot substrate, *International Journal of Heat and Mass Transfer*, 50, 303–319, doi.org/10.1016/j.ijheatmasstransfer.2006.06.012
- Panão, M.R.O., Moreira, A.L.N., 2005, Flow characteristics of spray impingement in PFI injection systems, *Experiments in Fluids*, 39, 364–374,

doi.org/10.1007/s00348-005-0996-2

Pasandideh-Fard, M., Aziz, S.D., Chandra, S., Mostaghimi, J., 2001, Cooling effectiveness of a water drop impinging on a hot surface, *International Journal of Heat and Fluid Flow*, 22, 201–210, doi.org/10.1016/S0142-727X(00)00086-2

Pasandideh-Fard, M., Pershin, V., Chandra, S., Mostaghimi, J., 2002, Splat shapes in a thermal spray coating process: Simulations and experiments, *Journal of Thermal Spray Technology*, 11, 206–217, doi.org/10.1361/105996302770348862

Pournaderi, P., Pishavar, A.R., 2012, A numerical investigation of droplet impact on a heated wall in the film boiling regime, *Heat and Mass Transfer/Waerme- und Stoffuebertragung*, 48, 1525–1538, doi.org/10.1007/s00231-012-0999-5

Reyhanian, E., Hassan, M., Chini, S.F., 2017, Investigation of 2D drop evaporation on a smooth and homogeneous surface using Lattice Boltzmann method, *International Communications in Heat and Mass Transfer*, 89, 64–72, doi.org/http://dx.doi.org/10.1016/j.icheatmasstransfer.2017.09.019

Schneider, C.A., Rasband, W.S., Eliceiri, K.W., 2012, NIH Image to ImageJ: 25 years of image analysis, *Nature Methods*, 9, 671–675, doi.org/10.1038/nmeth.2089

Shahmohammadi, M., Zhao, J., Yu, K.N., 2018, Investigation of droplet behaviors for spray cooling using level set method, *Annals of Nuclear Energy*, 113, 162–170, doi.org/10.1016/j.anucene.2017.09.046

Silk, E.A., Kim, J., Kiger, K., 2006, Spray cooling of enhanced surfaces: Impact of structured surface geometry and spray axis inclination, *International Journal of Heat and Mass Transfer*, 49, 4910–4920, doi.org/10.1016/j.ijheatmasstransfer.2006.05.031

Soltani-Kordshuli, F., Eslamian, M., 2017, Impact dynamics and deposition of pristine and graphene-doped PEDOT:PSS polymeric droplets on stationary and vibrating substrates, *Experimental Thermal and Fluid Science*, 89, 238–248, doi.org/10.1016/j.expthermflusci.2017.08.019

Taghilou, M., Hassan, M., 2014, Lattice Boltzmann model for thermal behavior of a droplet on the solid surface, *International Journal of Thermal Sciences*, 86, 1–11, doi.org/10.1016/j.ijthermalsci.2014.06.006

Tran, T., Staat, H.J.J., Prosperetti, A., Sun, C., Lohse, D., 2012, Drop Impact on Superheated Surfaces, *Physical Review Letters*, 036101, 1–5, doi.org/10.1103/PhysRevLett.108.036101

Tran, T., Staat, H.J.J., Susarrey-arce, A., Foertsch, T.C., Van Houselt, A., Gardeniers, H.J.G.E., Prosperetti, A., Lohse, D., Sun, C., 2013, Droplet impact on superheated micro-structured surfaces, *Soft Matter*, 3272–3282, doi.org/10.1039/c3sm27643k

Ukiwe, C., Kwok, D.Y., 2005, On the Maximum Spreading Diameter of Impacting Droplets on Well-Prepared Solid Surfaces, *Langmuir*, 21, 666–673, doi.org/10.1021/la0481288

Villegas, L.R., Alis, R., Lepilliez, M., Tanguy, S., 2016, A Ghost Fluid / Level Set Method for boiling flows and liquid evaporation: Application to the Leidenfrost effect, *Journal of Computational Physics*, 316, 789–813, doi.org/10.1016/j.jcp.2016.04.031

Wang, Y., Wang, X., Wang, T., Yan, W., 2018, Asymmetric heat transfer characteristics of a double droplet impact on a moving liquid film, *International Journal of Heat and Mass Transfer*, 126, 649–659, doi.org/10.1016/j.ijheatmasstransfer.2018.05.161

Wang, Z., Xing, Y., Liu, X., Zhao, L., Ji, Y., 2016, Computer modeling of droplets impact on heat transfer during spray cooling under vibration environment, *Applied Thermal Engineering*, 107, 453–462, doi.org/10.1016/j.applthermaleng.2016.06.176

Xiong, W., Cheng, P., 2018, 3D lattice Boltzmann simulation for a saturated liquid droplet at low Ohnesorge numbers impact and breakup on a solid surface surrounded by a saturated vapor, *Computers and Fluids*, 168, 130–143, doi.org/doi.org/10.1016/j.compfluid.2018.03.082



## EFFECTS OF ROUGHNESS ELEMENTS ON V-CORRUGATED ABSORBER PLATE SOLAR AIR HEATERS

Hussain SHAWISH\* and Murat ÖZDENEFE\*\*

\*Eastern Mediterranean University, Department of Mechanical Engineering  
Famagusta, North Cyprus via Mersin 10, Turkey

hussain.shawish@emu.edu.tr, ORCID: 0000-0001-9930-5258

\*\*Eastern Mediterranean University, Energy Research Center  
Famagusta, North Cyprus via Mersin 10, Turkey

murat.ozdenefe@emu.edu.tr, ORCID: 0000-0002-8905-0885

(Geliş Tarihi: 20.08.2022, Kabul Tarihi: 31.03.2023)

**Abstract:** Solar air heaters (SAHs) generally have low thermal efficiency, hence numerous research has been done to enhance their performance and to widen their applications. Although there has been extensive research on them, adding roughness elements on the corrugations of V-corrugated absorber plate SAHs to enhance their performance have not been investigated. Hence this work is an effort to address this gap by performing a numerical study to investigate the thermal performance enhancement caused by attaching transverse and longitudinal fins on 60° V-corrugated absorber plate SAH. It is also aimed to investigate the effect of same roughness elements on simple flat plate SAH. ANSYS Fluent program was utilized to simulate and analyze the three-dimensional airflow through the SAHs. The simulations were performed for three different Reynolds numbers; 4000, 8000 and 12000. The effects of adding fins on the outlet air temperature, Nusselt number and friction factor were analyzed and discussed. The results indicated that addition of roughness in the form of transverse and longitudinal fins offered enhancement in the thermal performance, leading the corrugated plate-longitudinal fins SAH to achieve the maximum outlet air temperature (315.3 K) and the flat plate-transverse fins SAH to attain the highest Nusselt number (58.4). For the V-corrugated SAH, transverse fins enhanced the Nusselt number by 17% compared to the smooth case, while the longitudinal fins offered 4 degrees increase in the outlet temperature. For the flat SAH on the other hand, transverse fins enhanced the Nusselt number by 26% as compared to the smooth case, while the longitudinal fins resulted in 2 degrees increase in the outlet temperature.

**Keywords:** solar air heater, thermal performance, numerical investigation

## PÜRÜZLÜLÜK ELEMANLARININ V-KAT LEVHALI GÜNEŞ HAVA ISITICILARINA ETKİLERİ

**Özet:** Güneş enerjili hava ısıtıcıları, genellikle düşük ısı verimliliğe sahiptir. Dolayısıyla bu cihazların performansını artırmak ve uygulamalarını çoğaltmak için birçok araştırma yapılmıştır. Yapılan kapsamlı çalışmalara rağmen, pürüzlülük elemanlarının V-kat levhalı güneş hava ısıtıcılarının soğurucusuna eklenmesinin performans üzerine etkisi incelenmemiştir. Dolayısıyla bu çalışma, 60° V-kat levhalı güneş enerjili hava ısıtıcısının soğurucusuna pürüzlülük elemanlarının (enine ve boyuna uzanan kanatçıklar) eklenmesinin sağladığı ısı performans artışını sayısal yaklaşım kullanarak incelemeyi hedeflemektedir. Aynı pürüzlülük elemanlarının düz levhalı güneş hava ısıtıcısına eklenmesi halinde oluşacak etkiyi araştırmak ayrıca amaçlanmıştır. Çalışmada cihazlardan geçen hava akışının üç boyutlu simülasyonunu ve analizini gerçekleştirmek için ANSYS Fluent yazılımı kullanılmıştır. Simülasyonlar üç farklı Reynolds sayısı için yapılmıştır (4000, 8000 ve 12000). Kanatçıkların çıkış hava sıcaklığı, Nusselt sayısı ve sürtünme katsayısı üzerindeki etkileri analiz edilmiş ve tartışılmıştır. Enine ve boyuna kanatçık biçimindeki pürüzlülük elemanlarının eklenmesinin, ısı performans artışı sağladığı ve V-kat levhalı boyuna kanatçıklı cihazın en yüksek çıkış havası sıcaklığına (315.3 K), bunun yanında düz levhalı enine kanatçıklı cihazın en yüksek Nusselt sayısına (58.4) ulaştığı belirlenmiştir. V-kat levhalı cihaz için, enine kanatçıklar Nusselt sayısını %17 artırırken, boyuna kanatçıklar çıkış sıcaklığında 4 derecelik artış sağlamıştır. Düz levhalı cihaz için ise enine kanatçıklar Nusselt sayısını %26 artırırken, boyuna kanatçıklar çıkış sıcaklığında 2 derecelik artışa neden olmuştur.

**Anahtar Kelimeler:** güneş enerjili hava ısıtıcıları, ısı performans, sayısal inceleme

### NOMENCLATURE

$A_s$	Surface Area of the Absorber [m <sup>2</sup> ]	$e/D$	Relative Roughness Height
$c_p$	Specific Heat [J/kg.K]	$g_x$	Gravitational Acceleration Component in the X Direction [m/s <sup>2</sup> ]
$D_h$	Hydraulic Diameter [m]	$g_y$	Gravitational Acceleration Component in the Y Direction [m/s <sup>2</sup> ]

$g_z$	Gravitational Acceleration Component in the Z Direction [m/s <sup>2</sup> ]
$h$	Coefficient of Heat Transfer [W/m <sup>2</sup> .K]
$k$	Thermal Conductivity [W/m.K]
$L$	SAH Length [m]
$\dot{m}$	Air Mass Flow Rate [Kg/s]
$Nu$	Nusselt Number [=hL/k]
$P$	Pressure [Pa]
$P/e$	Relative Roughness Pitch
$Pr$	Prandtl Number
$q$	Heat Flux [W/m <sup>2</sup> ]
$Re$	Reynolds Number [=vρD/μ]
$T_\infty$	Air Temperature Far From Absorber Plate [K]
$T_i$	Inlet Air Temperature [K]
$T_o$	Outlet Air Temperature [K]
$T_o^*$	Non-dimensional Temperature [K]
$T_p$	Average Absorber Plate Temperature [K]
$T_w$	Wall Temperature of the Absorber Plate [K]
$u$	Velocity in the X Direction [m/s]
$v$	Velocity in the Y Direction [m/s]
$\bar{v}$	Mean Velocity of Air [m/s]
$W$	SAH Width [m]
$w$	Velocity in the Z Direction [m/s]
$f$	Friction Factor [=ΔPD <sub>h</sub> /0.5Lρv <sup>2</sup> ]
$\mu$	Viscosity of Air [N.s/m <sup>2</sup> ]
$\rho$	Density [kg/m <sup>3</sup> ]
RNG	Re-Normalization Group
SAH	Solar Air Heater
SIMPLE	Semi-Implicit Method for Pressure Linked Equations

## INTRODUCTION

One of the simplest methods to exploit solar energy is via solar air heaters (SAHs) (Parsa et al., 2021). SAHs are low-cost, eco-friendly solar thermal systems that convert incident solar energy into useful thermal energy (Amit Kumar & Layek, 2021; Parsa et al., 2021). They are predominantly used for space heating and drying applications (Surendhar et al., 2021). The conventional SAH is composed of an absorbing plate made normally from a metallic material that absorbs the incident radiation, a channel or duct attached to the absorber through which air passes, glazing cover to decrease loss of heat from the absorber while allowing solar radiation to pass, thermal insulation at sides and back of the collector to reduce the thermal losses and a fan to provide means of airflow inside the duct (Saxena et al., 2015). Figure 1 provides an illustrative diagram of a conventional SAH (Tyagi et al., 2012). The incident radiation is absorbed by the absorber and this causes an increase in the absorber's temperature. When air flows over the plate, forced convection is generated and the flowing air starts to absorb heat from the plate which causes its temperature to rise, then this hot air is conveyed by a duct to provide heating for the desired purpose (Singh Bisht et al., 2018).

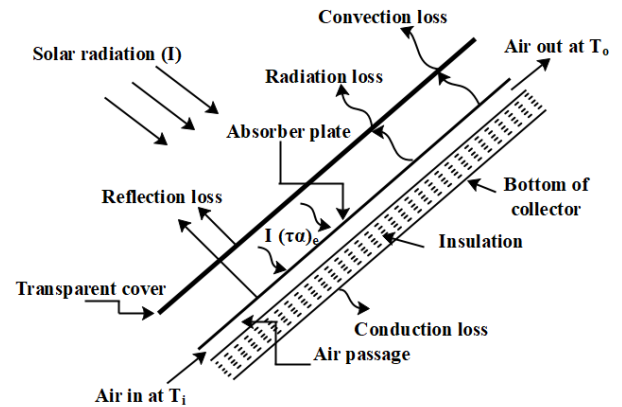


**Figure 1.** Longitudinal section of a conventional SAH (Tyagi et al., 2012).

Since the working fluid in these systems is air, freezing and boiling does not occur. However, the thermal efficiency of such systems is generally low because of the low heat transfer coefficient values encountered and the poor thermal capacity of air (Ghritlahre et al., 2019). The low heat transfer coefficient is a result of the formation of a laminar viscous layer on the absorber plate causing thermal resistance to heat transfer. Thus the addition of artificial roughness to the absorber plate to break up this layer and generate turbulent flow is a common way to enhance heat transfer coefficient hence the efficiency (Arunkumar et al., 2020). On the other hand, the addition of roughness increases the frictional losses resulting in a higher power requirement for moving the air (Arunkumar et al., 2020).

The thermal and friction characteristics of a shot blasted V-corrugated absorber SAH were studied experimentally by Poongavanam et al. (2018). In their experiments, the authors investigated varying flow rates. The results showed an increase in the mean efficiency as air flow rate increases and the efficiency value in the proposed SAH were higher compared to a smooth flat absorber SAH. In addition, a decrease in friction factor was observed with the increase of mass flow rate. Handoyo et al. (2016) numerically investigated the performance of a V-corrugated absorber SAH with delta-shaped obstacles attached to its backplate. The authors studied the effect of varying obstacles spacing ratio and they achieved optimal Nusselt number and friction factor values at spacing ratio of 1. Analysis on a V-corrugated SAH with twisted tape inserts suspended in the air channel between the absorber and backplate was performed by Farhan et al. (2021). The authors reported a considerable increase in the efficiency as compared to the conventional V-corrugated SAH. Prasad and Saini (1988) studied experimentally the performance in a flat plate SAH with a transverse wire roughness element. The authors investigated the impact of varying relative roughness height on coefficient of heat transfer and friction factor. The results showed that as the relative roughness height increases, the average Nusselt number and friction factor also increase. Performance of a flat plate SAH with transverse wedge-shaped rib roughness geometry was

studied experimentally by Bhagoria et al. (2002). They found an increase in Nusselt number and friction factor with increased relative roughness height. Saini and Saini (1997) tested a flat absorber SAH with expanded metal mesh. They investigated the effect of varying flow rate. The authors found an increase in Nusselt number with rising flow rates, but on the other hand the friction factor decreases. Momin et al. (2002) studied experimentally the performance of a flat absorber SAH with V-shaped roughness geometry. They also found an increase in the performance with increasing relative roughness height for this fin geometry. The effects of different relative roughness height and flow rates on the thermal and friction characteristics of a SAH with dimple-shape roughness were investigated experimentally by Saini and Verma (2008). The results showed good agreement with other studies in the literature. Performance of a SAH with square-sectioned transverse ribs as roughness was studied numerically by Yadav and Bhagoria (2014). They investigated the effects of relative roughness pitch and relative roughness height. A flat plate having discrete multi-V-rib with staggered rib roughness was investigated numerically by Kumar and Kim (2015). The authors studied the effects on performance associated with different relative width ratios for varying Reynolds numbers. The results showed that with an increase in relative width ratios the thermal performance also increased up to an optimum value. Performance of flat plate SAH with inclined circular ribs as the roughness element was studied by Kumar and Varun (2014). The authors investigated the effect of inclination angle and roughness height for different Reynolds numbers. Jin et al (2015) numerically studied a flat absorber SAH with multi V-shaped ribs as roughness. The computations were performed for different roughness parameters to study their effect on Nusselt number and friction factor. Yadav et al. (2014) analyzed numerically the thermal and friction characteristics of a flat absorber SAH with equilateral triangular sectioned rib roughness. The parameters discussed in their study were relative roughness height and relative roughness pitch. A numerical and experimental investigation was performed by Gawanda et al. (2016) to study the performance of a flat absorber SAH having chamfered square ribs attached to the absorber. The authors found an increase in Nusselt number and friction factor with increasing chamfer angle.

Ample of studies have been reported in the literature on the effect of adding different types of fins and roughness geometries to flat absorber plates, however studies investigating the effect of combining artificial roughness elements with the corrugated absorber plates are very few. Handoyo et al. (2016) and Farhan et al. (2021) studied the effects of adding obstacles to the V-corrugated SAHs, however in their studies the obstacles were not attached to the corrugations, rather they were either inserted in the channel between the corrugations and back plate or attached to the back plate. Poongavanam et al. (2018) on the other hand used shot-blasting to create roughness on the corrugations of the V-corrugated SAH. However, the roughness they created

are at micron scale. To the best knowledge of the authors, studies investigating thermal and friction characteristics of V-corrugated absorber plate SAH with fins attached directly to the absorber plate do not exist. Therefore, this work strives to numerically investigate and compare the effect of different roughness geometries and airflow rates on the thermal performance of V-corrugated absorber plate SAH with groove angle of 60°. A further purpose of this work is to employ the same roughness geometries and airflow rates in ordinary flat absorber plate SAH and compare the results.

## METHODOLOGY

In the current study a numerical analysis is conducted to investigate the thermohydraulic performance of different types of solar air heaters. ANSYS Fluent CFD code is used to simulate the three-dimensional fluid flow and heat transfer characteristics of the SAHs. This section describes the particulars of the computational domain, grid generation, governing equations, boundary conditions and turbulence model selection.

### Computational Domain

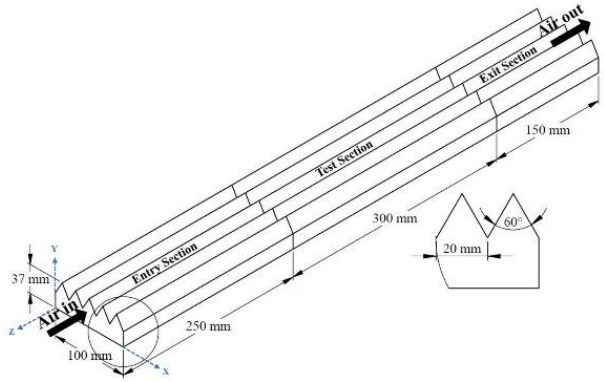
In the present study, 6 different SAHs were modeled and simulated. The six SAHs considered in the simulations were for two different types of SAHs; 60° V-corrugated absorber and flat absorber SAHs. For each type, 3 different designs; smooth plate, plate with transverse fins and plate with longitudinal fins were considered. For each SAH, the computational domain corresponds to the 3D geometry generated by SolidWorks software which is then exported to ANSYS. The length of the considered SAHs is divided into entrance, test and exit sections as proposed in ASHRAE standard 93-2003 (ASHRAE Standard, 2003). A summary of the general geometrical parameters used in the construction of the SAHs is presented in Table 1.

**Table 1.** General geometric parameters considered for the SAHs.

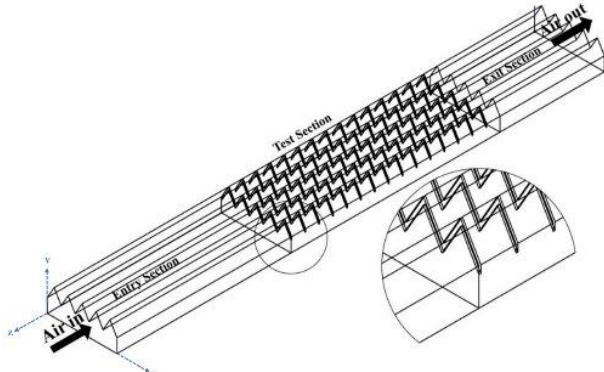
<b>Entrance section</b>	250 mm
<b>Test Section</b>	300 mm
<b>Exit Section</b>	150 mm
<b>Width (W)</b>	100 mm
<b>Hydraulic Diameter (D<sub>h</sub>)</b>	33.33 mm

Two roughness elements i.e. transverse and longitudinal fins were selected since they correspond to different heat transfer enhancement aspects. The transverse fins generate more turbulence in the flow and eliminate the viscous sub-layer, which results in higher heat transfer coefficients. On the other hand, the longitudinal fins mainly offer more surface area, so more air is in contact with the heated surface. The cross-section of both fins is a rectangle having 1mm thickness and 2mm height. Furthermore, all the SAHs are modeled as a single flow duct with its top wall representing the absorber plate of the SAH and the roughness is attached to the bottom side of this absorber plate in the case of roughened SAHs.

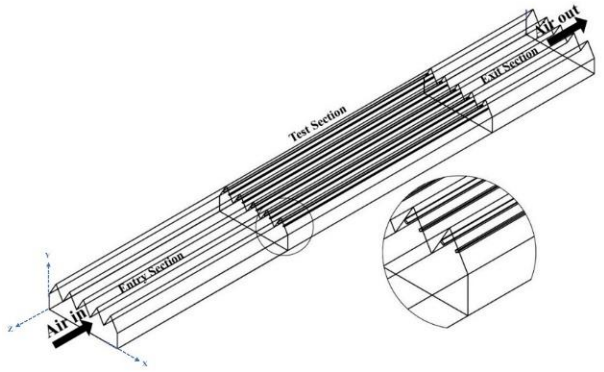
The generated 3D models are illustrated in Figures 2A-F. To reduce the computational time, only half of each SAH was considered in the simulations since all SAHs have a symmetry plan at  $x=W/2$ . This significantly reduces the number of elements in the mesh and the time required of each simulation while getting the same result as the full SAH case. The working fluid through the whole analysis is air, and the flow is assumed to be 3 dimensional, steady and incompressible. The walls of the SAHs' duct and the absorber plate are assumed to be made of aluminum. Table 2 lists the properties of the materials used in the simulations.



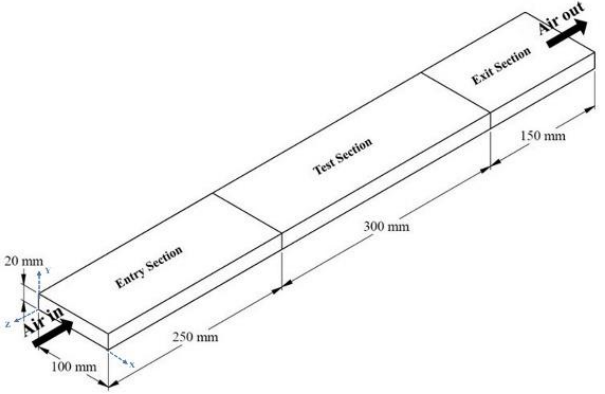
a. Corrugated plate-smooth SAH



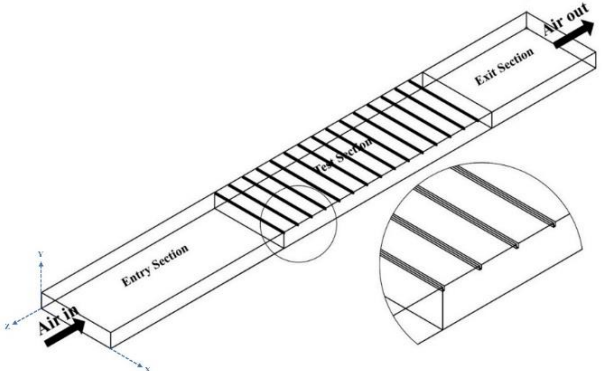
b. Corrugated plate-transverse fins SAH



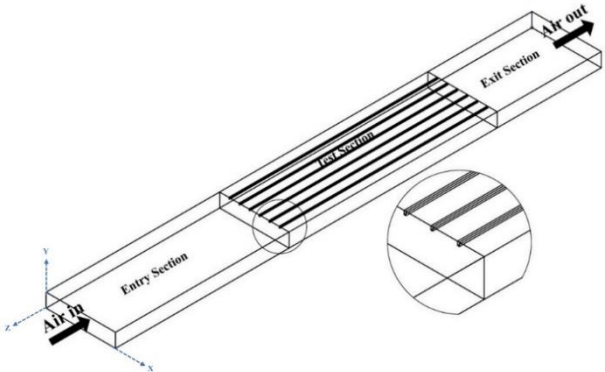
c. Corrugated plate-longitudinal fins SAH



d. Flat plate-smooth SAH



e. Flat plate-transverse fins SAH



f. Flat plate-longitudinal fins SAH

Figure 2. Generated three-dimensional models



**Table 2.** Properties of materials used in the simulations

Material	Density $\rho$ (kg/m <sup>3</sup> )	Thermal Conductivity $k$ (W/m.K)	Specific Heat $c_p$ (J/kg.K)	Viscosity $\mu$ (N.s/m <sup>2</sup> )	Prandtl Number Pr
Air	1.117	0.0262	1007	1.857e-5	0.71
Aluminum	2719	202.4	871	-	-

### Grid Generation

In this study, a non-uniform mesh with prism layers was created for the flow domain of all SAHs using ANSYS meshing. A Mesh independence check was conducted to examine the independency of the generated results from the mesh. Taking the corrugated plate-transverse fins SAH as an example, four meshes with an increasing number of elements from 1457397 to 2503811 corresponding to a decrease in the element size were tested. It was found that a mesh with 1863402 number of elements offered the optimum computational time with less than 1% variation in the results from the mesh with 2503811 elements. Figure 3 shows the generated mesh for the corrugated plat-transverse fins SAH.

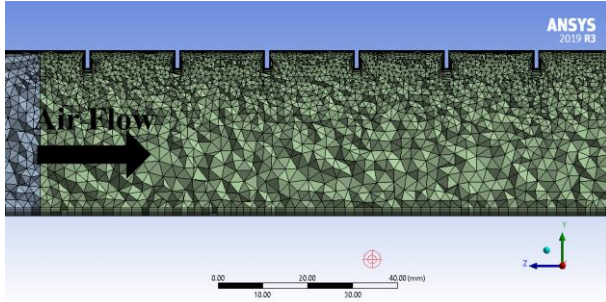


**Figure 3.** Non-uniform mesh generated for corrugated plate-transverse fins SAH.

### Governing Equations

In this work, the aim is to investigate the effect of adding roughness on various parameters such as outlet air temperature, Nusselt number and friction factor that represent the performance of the SAHs. The governing equations of fluid flow are continuity, momentum and energy equations, which can be written as follows (Jiji, 2009):

Continuity equation:

$$\frac{\partial \rho}{\partial t} + u \frac{\partial \rho}{\partial x} + v \frac{\partial \rho}{\partial y} + w \frac{\partial \rho}{\partial z} + \rho \left[ \frac{\partial u}{\partial x} + \frac{\partial v}{\partial y} + \frac{\partial w}{\partial z} \right] = 0 \quad (1)$$

Momentum equations:

$$\rho \frac{Du}{Dt} = \rho g_x - \frac{\partial p}{\partial x} + \frac{\partial}{\partial x} \left[ \mu \left( 2 \frac{\partial u}{\partial x} - \frac{2}{3} \nabla \cdot \vec{V} \right) \right] \quad (2)$$

$$+ \frac{\partial}{\partial y} \left[ \mu \left( \frac{\partial u}{\partial y} + \frac{\partial v}{\partial x} \right) \right] + \frac{\partial}{\partial z} \left[ \mu \left( \frac{\partial w}{\partial x} + \frac{\partial u}{\partial z} \right) \right]$$

$$\rho \frac{Dv}{Dt} = \rho g_y - \frac{\partial p}{\partial y} + \frac{\partial}{\partial y} \left[ \mu \left( 2 \frac{\partial v}{\partial y} - \frac{2}{3} \nabla \cdot \vec{V} \right) \right] + \frac{\partial}{\partial z} \left[ \mu \left( \frac{\partial v}{\partial z} + \frac{\partial w}{\partial y} \right) \right] + \frac{\partial}{\partial x} \left[ \mu \left( \frac{\partial u}{\partial y} + \frac{\partial v}{\partial x} \right) \right] \quad (3)$$

$$\rho \frac{Dw}{Dt} = \rho g_z - \frac{\partial p}{\partial z} + \frac{\partial}{\partial z} \left[ \mu \left( 2 \frac{\partial w}{\partial z} - \frac{2}{3} \nabla \cdot \vec{V} \right) \right] + \frac{\partial}{\partial x} \left[ \mu \left( \frac{\partial w}{\partial x} + \frac{\partial u}{\partial z} \right) \right] + \frac{\partial}{\partial y} \left[ \mu \left( \frac{\partial v}{\partial z} + \frac{\partial w}{\partial y} \right) \right] \quad (4)$$

Energy equation:

$$\rho c_p \left( \frac{\partial T}{\partial t} + u \frac{\partial T}{\partial x} + v \frac{\partial T}{\partial y} + w \frac{\partial T}{\partial z} \right) = k \left( \frac{\partial^2 T}{\partial x^2} + \frac{\partial^2 T}{\partial y^2} + \frac{\partial^2 T}{\partial z^2} \right) + \mu \Phi$$

Where

$$\Phi = 2 \left[ \left( \frac{\partial u}{\partial x} \right)^2 + \left( \frac{\partial v}{\partial y} \right)^2 + \left( \frac{\partial w}{\partial z} \right)^2 \right] + \left[ \left( \frac{\partial u}{\partial y} + \frac{\partial v}{\partial x} \right)^2 + \left( \frac{\partial v}{\partial z} + \frac{\partial w}{\partial y} \right)^2 + \left( \frac{\partial w}{\partial x} + \frac{\partial u}{\partial z} \right)^2 \right] - \frac{2}{3} \left( \frac{\partial u}{\partial x} + \frac{\partial v}{\partial y} + \frac{\partial w}{\partial z} \right)^2 \quad (5)$$

These equations are solved numerically using ANSYS Fluent software. The SIMPLE algorithm was used to handle the coupling in the pressure and velocity fields and the RNG k- $\epsilon$  model was selected as the turbulence model for the simulations. The residuals in the solution of  $10^{-3}$  in momentum and continuity equation and  $10^{-6}$  for energy equation were selected as the convergence criterion. These models were selected based on the validation and application done in previous studies (Gawande et al., 2016; Jin et al., 2015; Anil Kumar & Kim, 2015; Yadav & Bhagoria, 2014). The obtained results from the simulations for the heat transfer coefficient, temperature distribution and pressure are employed to find the aforementioned performance parameters using the following expressions: The average Nusselt number is defined as

$$Nu = \frac{h D_h}{k} \quad (6)$$

Where  $h$  is the average coefficient of heat transfer between the absorber plate and air,  $D_h$  is the hydraulic

diameter of the SAH and  $k$  is the thermal conductivity of air.

The average coefficient of heat transfer  $h$  is obtained by surface integrals at the absorber plate and it is defined as

$$h = \frac{q}{T_w - T_\infty} \quad (7)$$

Where  $q$  is the wall heat flux,  $T_w$  is the wall temperature and  $T_\infty$  is the air temperature far away from the wall.

The average friction factor is defined as

$$f = \frac{(\Delta p/L)D_h}{\frac{1}{2}\rho\bar{v}^2} \quad (8)$$

Where  $\Delta p$  is the pressure difference between the inlet and outlet of the SAH,  $L$  is the length of the SAH,  $\rho$  is the density of air and  $\bar{v}$  is the mean air velocity.

Figure 4 presents a flow chart of the methodology that has been followed to generate the results using ANSYS Fluent software.

### Boundary Conditions

In the present simulations, the walls in the computational domain were assigned to no-slip condition. At the inlet, a uniform velocity corresponding different Reynolds numbers was applied normal to the boundary with 300 K as the inlet temperature of the air. Three different Reynolds numbers; 4000, 8000 and 12000 were considered. For the outlet, a pressure-outlet condition was assigned where the pressure is equal to the atmospheric pressure. The surface of the absorber plate was assigned with constant heat flux while all other surfaces are assumed to be adiabatic. Moreover, a symmetry boundary condition was applied to the symmetry plane at  $x=W/2$ . Table 3 presents a summary of the boundary conditions used.

**Table 3.** Boundary conditions used in the computational domain.

Surface	Assigned boundary condition
inlet	Velocity-inlet
outlet	Pressure-outlet
Absorber Plate	Heat flux
Side and bottom walls of the test section	Adiabatic
Walls of entry and exit sections	Adiabatic
Symmetry plane at $x=W/2$	Symmetry

### Transport Equations for Renormalization-Group (RNG) k-ε Turbulence Model

The RNG k-ε model was derived using a statistical technique called renormalization group theory. It is similar in form to the standard k-ε model but includes some refinements. The RNG model has an additional term in its ε equation that improves the accuracy for rapidly strained flows. Also, the RNG model includes the

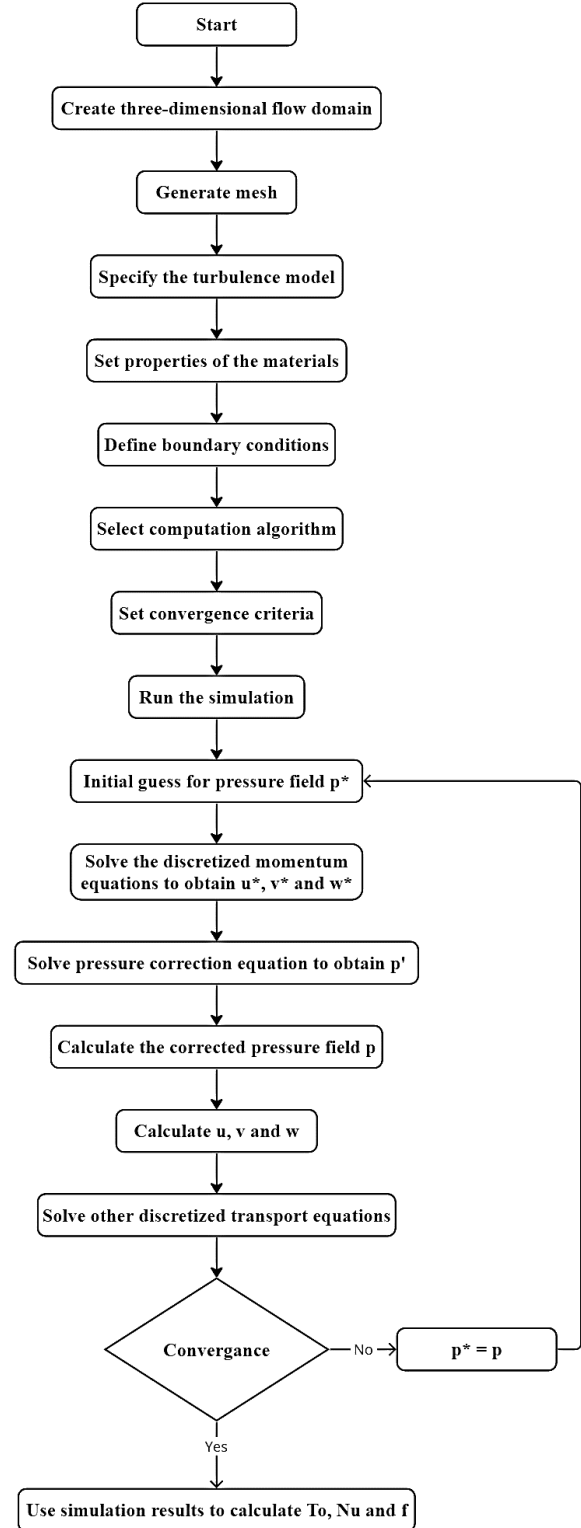


**Figure 4.** Flow chart of the followed methodology

effect of swirl on turbulence, thus improving the accuracy for swirling flows (ANSYS FLUENT 15, 2013; Yakhot & Smith, 1992). The modeled turbulent kinetic energy,  $k$ , and its rate of dissipation  $\varepsilon$ , are obtained from the following transport equations for the RNG  $k$ - $\varepsilon$  turbulence model (ANSYS FLUENT 15, 2013; Yadav & Bhagoria, 2014)

$$\begin{aligned} \frac{\partial}{\partial t}(\rho k) + \frac{\partial}{\partial x_i}(\rho k u_i) \\ = \frac{\partial}{\partial x_j} \left( \alpha_k \mu_{eff} \frac{\partial k}{\partial x_j} \right) + G_k \\ + G_b - \rho \varepsilon - Y_M + S_k \end{aligned} \quad (9)$$

$$\begin{aligned} \frac{\partial}{\partial t}(\rho \varepsilon) + \frac{\partial}{\partial x_i}(\rho \varepsilon u_i) \\ = \frac{\partial}{\partial x_j} \left( \alpha_\varepsilon \mu_{eff} \frac{\partial \varepsilon}{\partial x_j} \right) + C_{1\varepsilon} \frac{\varepsilon}{k} (G_k + C_{3\varepsilon} G_b) \\ - C_{2\varepsilon} \rho \frac{\varepsilon^2}{k} - R_\varepsilon + S_\varepsilon \end{aligned} \quad (10)$$

In these equations,  $G_k$  represents the generation of turbulence kinetic energy due to the mean velocity gradients and is evaluated by

$$G_k = -\overline{\rho u_i' u_j'} \frac{\partial u_j}{\partial x_i} \quad (11)$$

$G_b$  is the generation of turbulence kinetic energy due to buoyancy and is expressed as

$$G_b = \beta g_i \frac{\mu_t}{Pr_t} \frac{\partial T}{\partial x_i} \quad (12)$$

$Y_M$  represents the contribution of the fluctuating dilatation in compressible turbulence to the overall dissipation rate and is defined as

$$Y_M = 2\rho \varepsilon M_t^2 \quad (13)$$

The quantities  $\alpha_k$  and  $\alpha_\varepsilon$  are the inverse effective Prandtl numbers for  $k$  and  $\varepsilon$  respectively.  $S_k$  and  $S_\varepsilon$  are user-defined source terms.

$\mu_{eff}$  represents the effective turbulent viscosity and is given by

$$\mu_{eff} = \mu + \mu_t$$

where  $\mu_t = \rho C_\mu \frac{k^2}{\varepsilon}$  (14)

The default values of the model constants  $C_{1\varepsilon}$ ,  $C_{2\varepsilon}$ ,  $\alpha_k$ ,  $\alpha_\varepsilon$  and  $C_\mu$  are equal to 1.42, 1.68, 1.39, 1.39 and 0.0845 respectively.

## Validation of the CFD Model

The selected turbulence model is validated by comparing the average Nusselt number values predicted by the CFD model to the values obtained using Dittus-Boelter equation (see Eq. 15) (Incropera & DeWitt, 2007) for smooth SAHs as presented in Figure 5. This is analogous to the validation method used in literature (Yadav & Bhagoria, 2014; Anil Kumar & Kim, 2015). It is clear in the figure that predicted results for corrugated plate are closely agreeing with the results of Dittus-Boelter equation, while the results for the flat plate are overpredicted to a certain extent. The average error in Nusselt number values for corrugated plate smooth and flat plate smooth SAHs from the Dittus-Boelter equation was 9.52% and 32.7% respectively while the average absolute difference was +2.38 and +8.45 respectively.

$$Nu_s = 0.0243 Re_D^{0.8} Pr^{0.4} \quad (15)$$

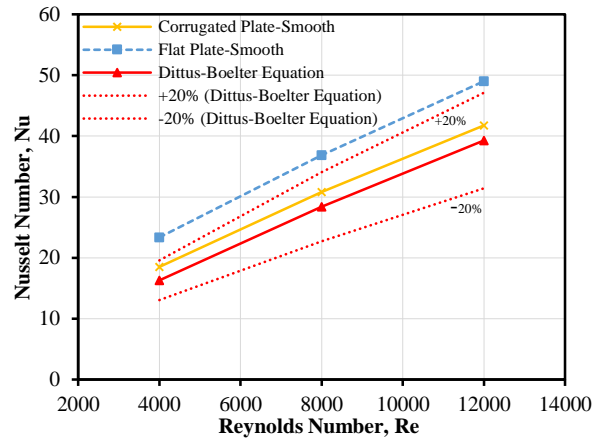


**Figure 5.** Comparison between the predicted Nusselt number with Dittus-Boelter Equation at different Reynolds numbers

## RESULTS AND DISCUSSIONS

Thermohydraulic performance of considered SAH designs i.e., 60° V-corrugated and flat absorber plate with different roughness elements are investigated numerically to reveal the effect of roughness elements on the performance. Outlet air temperature, Nusselt number and friction factor are three principal parameters that are examined and discussed. The results are presented for varying Reynolds numbers. In addition to the results obtained in this study, the available experimental results for Nusselt number and friction factor existing in the literature are also presented as an attempt to further validate the current study. Due to the difficulty of finding studies employing the identical geometric and operating conditions as used in this study, the authors considered available data from research works on flat plate SAHs employing same general aim and range of Reynolds number for the comparisons. Bhagoria et al. (Bhagoria et al., 2002) and Momin et al. (Momin et al., 2002) used the concept of adding roughness to enhance the performance of SAHs which is analogous to the aim of the current study. Bhagoria et al. used wedge shaped, whereas Momin et al. employed V-shaped roughness elements

that are transversely attached to the absorber plate. The range of the Reynolds number considered in their work (2500 to 18000) is similar to the range employed in the present study (4000 to 12000).

### Outlet air Temperature

The average outlet air temperature at different Reynolds numbers is presented in Figure 6 for different SAHs considered in this study. For all SAHs, the graph shows a decrease in the outlet temperature of air with increasing Reynolds numbers.

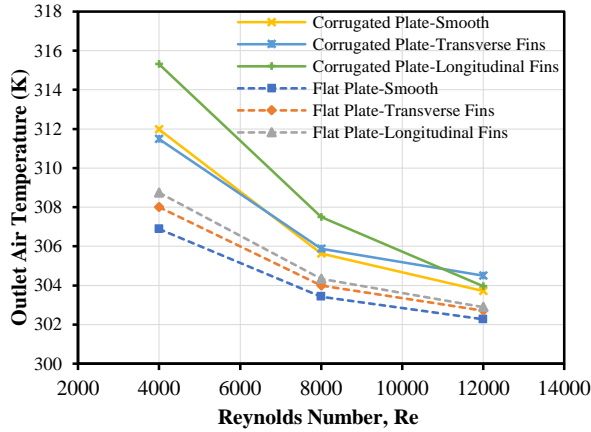


**Figure 6.** Outlet air temperature against Reynolds number for different SAHs

For V-corrugated SAHs, a maximum outlet temperature of 315.32 K was obtained in longitudinal fins case at Re=4000, while the minimum was 303.7 K in the smooth case corresponding to Re=12000. In addition, it can be seen from the graph that corrugated plate SAHs achieved higher outlet temperatures than flat plate SAHs for the considered Reynolds numbers. This is mainly because the corrugated absorber plate offers considerably more heat transfer surface area than the flat absorber plate, leading more air to be in direct contact with the absorber which results in higher outlet temperatures. Further investigation of the plot shows that at Re=12000, the corrugated plate-transverse fins SAH achieved higher outlet temperature than the corrugated plate-longitudinal fins. This observation raises the idea that at higher Reynolds numbers the effect of increasing the coefficient of heat transfer by transverse fins to achieve higher outlet temperatures surpasses the effect of higher surface area offered by the longitudinal fins.

For flat absorber plate SAHs, the maximum outlet temperature was obtained in the longitudinal fins case which corresponds to 308.7 K at Re=4000, while the minimum value of outlet temperature was 302.3 K in the smooth case for Re=12000. This result is akin to the case of V-corrugated plate. Moreover, it is noted that for all Reynolds numbers considered the SAH with longitudinal fins maintained the highest outlet temperatures among other flat plate SAHs.

To be able to draw general conclusions regarding considered SAHs' effect on the outlet air temperature it is useful to nondimensionalize the air temperature. In this study non-dimensional temperature is defined as the ratio of the actual temperature rise from inlet to outlet to the maximum possible temperature rise (which is the plate temperature minus inlet temperature) as given in equation 16. Hence greater non-dimensional temperature indicates that the outlet air temperature is closer to its maximum possible value which is the plate temperature. Figure 7 displays the relation between the non-dimensional temperature ( $T_o^*$ ) and Reynolds number for various SAH configurations. SAHs with transverse fins achieved better non-dimensional temperature compared to other configurations. For the first data point (Re=4000), flat plate-transverse fins achieved higher value of non-dimensional temperature compared to corrugated plate-transverse fins case. The non-dimensional temperature can be thought as a performance metrics indicating how effective a certain SAH is achieving the potential maximum temperature increase across the SAH. Hence, higher value of non-dimensional temperature for flat plate-transverse fins compared to corrugated plate-transverse fins for the first data point (Re=4000) means that at this Reynolds number flat plate-transverse fins better utilized the available potential. However, it must be said that the difference is 0.009 which is inconsequential. Since the corrugated plate-transverse fins SAH results in higher outlet temperature, the only reason for having higher dimensionless temperature at Re= 4000 in flat plate-transverse fins case is due to its much lower plate temperature (meaning its potential maximum temperature rise is low) than its counterpart, i.e. corrugated plate-transverse fins case. The variations in  $T_o^*$  values among the other SAHs (corrugated plate smooth, corrugated longitudinal fins, flat plate smooth and flat plate longitudinal fins) are minimal, making it difficult to draw a conclusive remarks regarding which is better. However, it can be said that corrugated plate smooth and corrugated longitudinal fins performed slightly better than their flat plate counterparts.

$$T_o^* = \frac{T_o - T_i}{T_p - T_i} \quad (16)$$

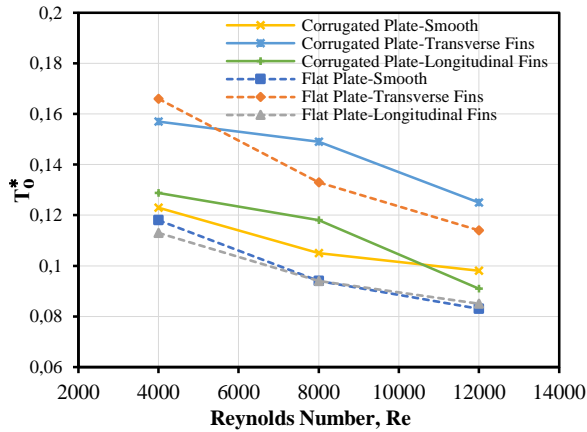


**Figure 7.** Non-dimensional outlet air temperature against Reynolds number

### Nusselt Number

The average Nusselt number at different Reynolds numbers is presented in Figure 8 for different SAHs. It also presents Nusselt number results from the selected experimental studies for comparison. It is seen that the trends of Nusselt number obtained in the current numerical study is in good agreement with the experimental data. It should be noted that the experimental data are not meant for one to one comparison with the data obtained from the present study since the configuration used in the experimental studies are not identical to the configurations used in the current study. The graph shows that for all SAHs considered, increasing Reynolds number causes increase in Nusselt number due to the accompanied decrease in the thickness of the laminar sub-layer. For V-corrugated SAHs, the highest value of Nusselt number was obtained in transverse fins case which correspond to 45.8 at  $Re=12000$ . The transverse fins act as turbulators, they break the laminar sub-layer and generate secondary flow and reattachment region after the fin resulting in higher Nusselt numbers. In addition, the vortex flow generated by the fin contribute to the enhancement of local heat transfer by mixing and transporting the low temperature fluid in mid-duct to be in contact with the heated absorber plate. Figure 9 presents the velocity contour and reattachment region generated in the corrugated plate-transverse fins SAH. The lowest Nusselt number with value of 15.7 occurred in the longitudinal fins case at  $Re=4000$ .

It is important to note that the increase in Nusselt number alone is not the only factor to consider when evaluating the performance of a SAH. The overall thermal performance of the system, as well as the associated increase in friction factor, should also be taken into account. The results of this study suggest that the SAH with longitudinal fins was able to achieve a higher outlet temperature despite having lower Nusselt number values compared to the transverse fins SAH. This highlights the need for a balance between heat transfer enhancement and pressure drop in the design of SAHs. The next section

of the paper provides further discussion on the friction factor.

For flat absorber SAHs, the highest Nusselt number was achieved in transverse fins case at  $Re=12000$  with a value of 58.4. On the other hand, a Nusselt number of 19 corresponding to the minimum value was obtained in longitudinal fins case at  $Re=4000$ .

It is noted that for all Reynolds numbers considered the transverse fins case maintained the highest Nusselt numbers, while the longitudinal fins case produced the lowest values of Nusselt number. Therefore, it is apparent that the addition of roughness largely had the same effect on Nusselt number for both the flat and corrugated absorbers. Further investigation of the results suggests that the increase in Nusselt number that the transverse fins achieve over the smooth absorber SAH is higher in the case of flat absorber SAH than in the case of corrugated absorber SAH. This means that the difference in Nusselt number between the plate with transverse fins and smooth plate is considerably higher in the flat absorber plate SAH. Moreover, the decreases in average Nusselt number encountered by the addition of longitudinal fins was higher in the flat plate.

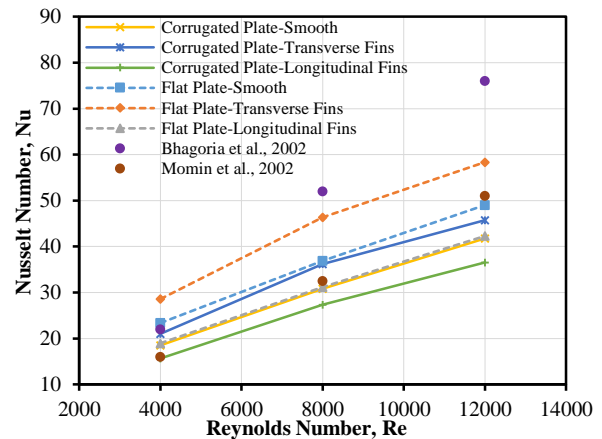


**Figure 8.** Nusselt number against Reynolds number for different SAHs

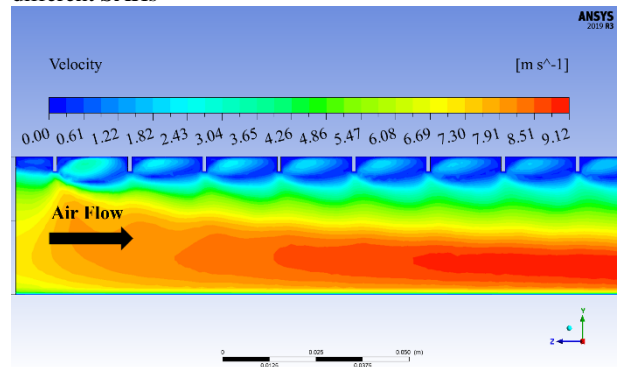


**Figure 9.** Contour of air velocity for corrugated plate-transverse fins SAH at  $Re=12000$

### Friction Characteristics

The average friction factor at different Reynolds numbers is plotted in Figure 10 for different SAHs. It can be observed that average friction factors are decreasing with increasing Reynolds number. It is thought that the

decrease in the friction factor is due to the termination of the laminar sub-layer encountered at rising Reynolds number.

For V-corrugated SAHs, the highest friction factor with value of 0.028 was achieved in transverse fins case as expected since the transverse fins have high flow resistance causing the pressure drop to increase. The smooth and longitudinal fins cases had close results for the average friction factor as seen in the graph. The minimum average friction factor occurred in the smooth case at  $Re=12000$ .

The friction factor represents a good reflection of the pumping power requirements of the SAHs since they share the same geometric characteristics; hydraulic diameter, length, etc. Generally, the addition of fins causes higher pressure-drop and hence higher pumping power. Therefore, the goal in SAH systems is to increase the outlet air temperature while keeping the pressure drop as low as possible. The addition of transverse fins on the corrugated plate resulted in an average friction factor of 0.0245 which is almost 2 folds that of the smooth case, while offering 1 degree increase in the outlet temperature compared to the smooth plate. On the other hand, the longitudinal fins generated an average friction factor of 0.0123 which is slightly higher than the that of the smooth case while offering up to 4 degrees increase in the outlet temperature as compared to the smooth plate. Therefore, the longitudinal fins represent a better alternative, since it resulted in higher outlet temperature with half of the pumping power requirement for the transverse fins.

For flat absorber SAHs, the maximum friction factor value occurred in transverse fins case at  $Re=4000$ , while the lowest value of the average friction factor occurred in the longitudinal fins case at  $Re=12000$ . The findings showed that for the average friction factor, the addition of fins had a similar effect in both flat absorber plate and corrugated absorber plate. Furthermore, a thorough investigation of the results suggests that the increase in the average friction factor caused by attaching transverse fins to a corrugated absorber is higher than the flat absorber case.

Figure 10 also presents the results of the friction factor from selected experimental studies for comparison. It can be observed that the trends of the friction factor obtained in the current numerical study match well with the experimental data.

In addition, Figure 10 shows a decrease in the friction factor by addition of longitudinal fins for the flat plate SAH, also the corrugated plate-smooth and corrugated plate-longitudinal fins achieved lower friction factor values than their flat plate counterparts. Although all SAHs were assigned with same uniform air velocity (hence the same Reynolds number) at the inlet section, the test sections' velocity distribution are different for different SAHs due to their geometrical differences

(smooth, transverse fins, longitudinal fins) in the air channel. As illustrated in Figure 10, the friction factor is function of Reynolds number which is dependent on the velocity and higher Reynolds number (higher velocity) means lower friction factor. Addition of longitudinal fins to the flat plate SAH resulted higher velocities in the test section compared with the smooth one which is the reason for lower friction factor. This phenomenon can be observed in Figure 11. Similarly, corrugated plate smooth SAH experienced higher velocities than flat plate smooth SAH as shown in Figure 12 causing lower friction factor in corrugated plate smooth SAH. On the other hand, corrugated plate-longitudinal fins, and flat plate-longitudinal fins SAHs had similar velocity distribution in the test section as shown in Figure 13, which led to close friction factor values.

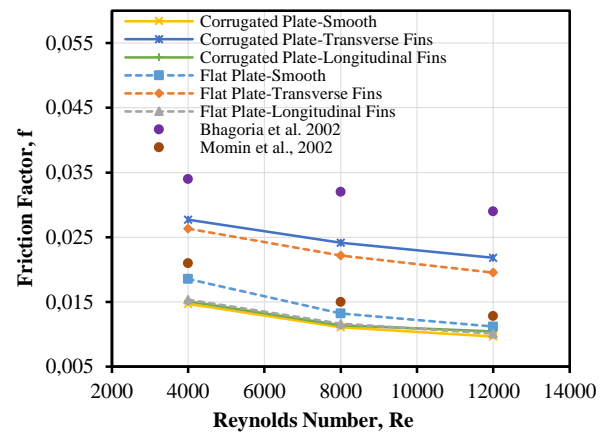


Figure 10. Friction factor against Reynolds number for different SAHs

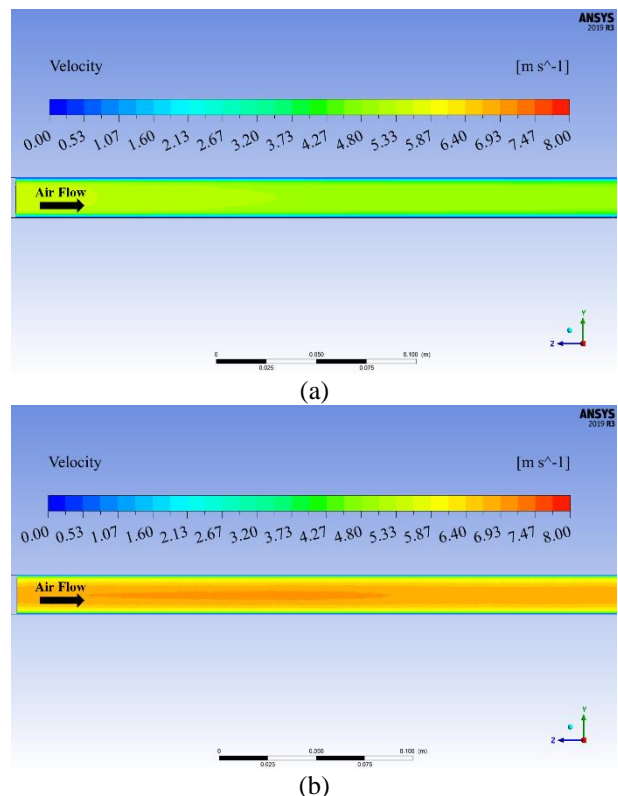
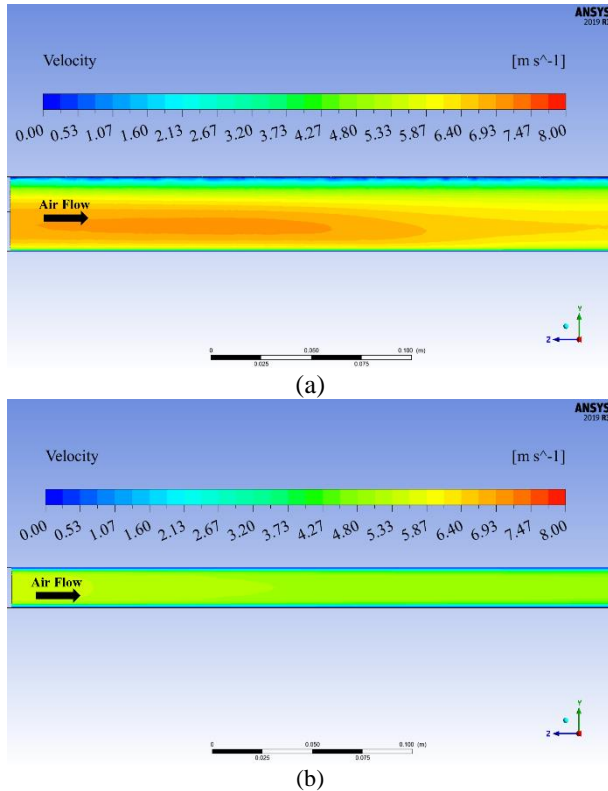
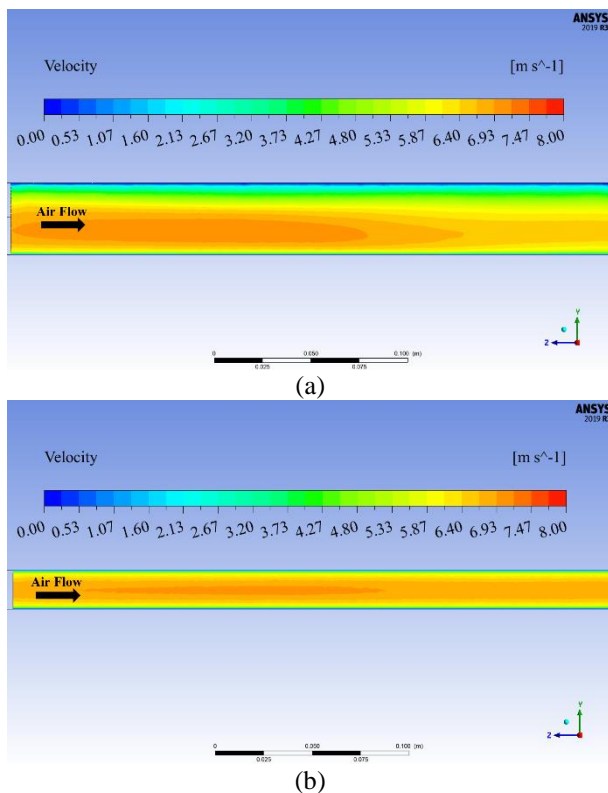


Figure 11. Velocity contour in the test section of (a) Flat plate-smooth (b) Flat plate-longitudinal fins SAHs



**Figure 12.** Velocity contour in the test section of (a) Corrugated plate-smooth (b) Flat plate-smooth SAHs



**Figure 13.** Velocity contour in the test section of (a) Corrugated plate-longitudinal fins (b) Flat plate-longitudinal fins SAHs

Figure 14 shows the pressure drop at different Reynolds numbers for the considered SAHs. It is seen from the

figure that the pressure drop increases as Reynolds number increases. For different types of SAHs the pressure drop results follow similar fashion as the friction factor results, e.g. the maximum pressure drop and friction factor occurred in corrugated plate-transverse fins case, whereas minimum pressure drop and friction factor occurred in corrugated plate-smooth case. Simply it can be said that configuration with higher friction factor resulted in higher pressure drop.

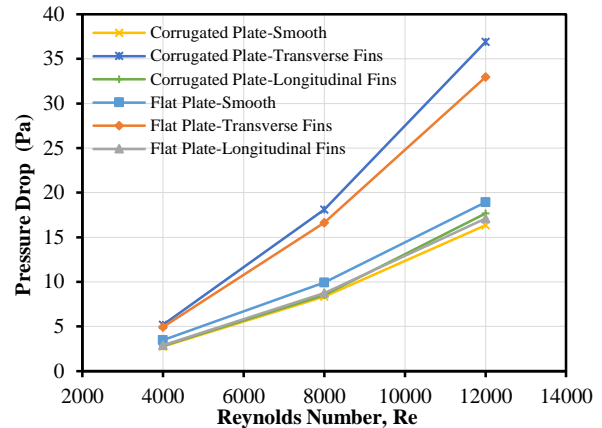


**Figure 14.** Pressure drop against Reynolds number for different SAHs.

## CONCLUSION

The objective of this work is to numerically investigate the thermohydraulic performance of six SAHs; corrugated plate-smooth, corrugated plate-transverse fins, corrugated plate-longitudinal fins, flat plate-smooth, flat plate-transverse fins and flat plate-longitudinal fins, at different Reynolds numbers. Simplified three-dimensional model of each SAH was constructed by SolidWorks software, then the model was exported to ANSYS Fluent software to simulate and analyze the fluid flow inside the SAHs. The required setting and methods for solving the governing equations and to model turbulence were set. An appropriate mesh was generated for each SAH and required boundary conditions were assigned to the different surfaces in the computational domain.

The results showed that the maximum outlet air temperature was 315.32 K in the corrugated plate-longitudinal fins SAH at Re=4000, while the minimum outlet air temperature was 302.27 K in the flat plate-smooth SAH at Re=12000. In addition, the findings showed a considerable improvement in the average Nusselt number by attaching transverse fins to the absorber plate. The highest obtained average Nusselt number was 58.37 in the flat plate-transverse fins SAH at Re=12000, while the minimum average Nusselt number occurred in the corrugated plate-longitudinal fins SAH with a value of 15.67 at Re=4000. Similarly, a noticeable friction factor increase was found in SAHs with transverse fins. The maximum average friction factor was 0.0277 in the corrugated plate-transverse fins SAH at Re=4000. On the other hand, the minimum average

friction factor was obtained in the smooth corrugated plate SAH at  $Re=12000$  and with a value of 0.0097.

The corrugated plate-longitudinal fins SAH was found to be the most effective configuration. It was able to achieve the highest outlet temperature with lower friction factor values. Moreover, the addition of each roughness elements; transverse fins and longitudinal fins is observed to have generally a similar effect on the thermohydraulic performance of the two SAHs types considered. The results show that the enhancement in Nusselt number that the transverse fins provide compared to the smooth absorber SAH is greater in the case of the flat absorber SAH than in the case of the corrugated absorber SAH. In addition, the results suggest that the average friction factor is increased more by attaching transverse fins to a corrugated absorber than to a flat absorber.

The manufacturing aspect of the proposed SAHs with roughness elements is important to consider as it could result in added cost which may not be justified by the improvement in performance. Therefore, further investigation is needed to fully understand the feasibility of implementing the proposed SAH configurations in practical systems, which is out of the scope of the current study. However, the authors suggest the use of thermally conductive adhesives as a potential practical solution for attaching roughness elements to a corrugated absorber. This could be investigated in future work.

## REFERENCES

- ANSYS, 2013, *Ansys Fluent Theory Guide 15.0*, ANSYS Inc., Canonsburg.
- Arunkumar, H. S., Vasudeva Karanth, K., and Kumar, S., 2020, Review on the design modifications of a solar air heater for improvement in the thermal performance, *Sustainable Energy Technologies and Assessments*, 39, 100685.
- Bhagoria, J. L., Saini, J. S., and Solanki, S. C., 2002, Heat transfer coefficient and friction factor correlations for rectangular solar air heater duct having transverse wedge shaped rib roughness on the absorber plate, *Renewable Energy*, 25(3), 341–369.
- Farhan, A. A., Issam M. Ali, A., and Ahmed, H. E., 2021, Energetic and exergetic efficiency analysis of a v-corrugated solar air heater integrated with twisted tape inserts, *Renewable Energy*, 169, 1373–1385.
- Gawande, V. B., Dhoble, A. S., Zodpe, D. B., and Chamoli, S., 2016, Experimental and CFD-based thermal performance prediction of solar air heater provided with chamfered square rib as artificial roughness, *Journal of the Brazilian Society of Mechanical Sciences and Engineering*, 38(2), 643–663.
- Ghritlahre, H. K., Chandrakar, P., and Ahmad, A., 2019, A Comprehensive Review on Performance Prediction of Solar Air Heaters Using Artificial Neural Network. In *Annals of Data Science*, 8, 405–449.
- Handoyo, E. A., Ichsani, D., Prabowo, and Sutardi., 2016, Numerical studies on the effect of delta-shaped obstacles' spacing on the heat transfer and pressure drop in v-corrugated channel of solar air heater, *Solar Energy*, 131, 47–60.
- Incropera, F. P., and DeWitt, D. P., 2007, *Fundamentals of Heat and Mass Transfer* (Sixth Edition), Wiley, New York.
- Jiji, L. M., 2009, *Heat convection* (Second Edition), Springer, New York.
- Jin, D., Zhang, M., Wang, P., and Xu, S., 2015, Numerical investigation of heat transfer and fluid flow in a solar air heater duct with multi V-shaped ribs on the absorber plate, *Energy*, 89, 178–190.
- Kumar, Amit, and Layek, A., 2021, Energetic and exergetic based performance evaluation of solar air heater having winglet type roughness on absorber surface, *Solar Energy Materials and Solar Cells*, 230, 111147.
- Kumar, Anil, and Kim, M. H., 2015, Effect of roughness width ratios in discrete multi V-rib with staggered rib roughness on overall thermal performance of solar air channel, *Solar Energy*, 119, 399–414.
- Kumar, M., and Mr, V., 2014, A Computational Fluid Dynamics Investigation of Solar Air Heater Duct Provided with Inclined Circular Ribs as Artificial Roughness, *Bonfring International Journal of Industrial Engineering and Management Science*, 4, 115–120.
- Momin, A.-M. E., Saini, J., and Solanki., S., 2002, Heat transfer and friction in solar air heater duct with V-shaped rib roughness on absorber plate. *International Journal of Heat and Mass Transfer*, 45(16), 3383–3396.
- Parsa, H., Saffar-Avval, M., and Hajmohammadi, M. R., 2021, 3D simulation and parametric optimization of a solar air heater with a novel staggered cuboid baffles, *International Journal of Mechanical Sciences*, 205, 106607.
- Poongavanam, G. K., Panchabikesan, K., Leo, A. J. D., and Ramalingam, V., 2018, Experimental investigation on heat transfer augmentation of solar air heater using shot blasted V-corrugated absorber plate, *Renewable Energy*, 127, 213–229.
- Prasad, B. N., and Saini, J. S., 1988, *Effect of artificial roughness on heat transfer and friction factor in a solar air heater*. 41(6), 555–560.
- Saini, R. P., and Saini, J. S., 1997, Heat transfer and friction factor correlations for artificially roughened



ducts with expanded metal mesh as roughness element, *International Journal of Heat and Mass Transfer*, 40(4), 973–986.

Saini, R. P., and Verma, J., 2008, Heat transfer and friction factor correlations for a duct having dimple-shape artificial roughness for solar air heaters, *Energy*, 33(8), 1277–1287.

Saxena, A., Varun, and El-Sebaai, A. A., 2015, A thermodynamic review of solar air heaters, *Renewable and Sustainable Energy Reviews*, 43, 863–890.

Singh Bisht, V., Kumar Patil, A., and Gupta, A., 2018, Review and performance evaluation of roughened solar air heaters, *Renewable and Sustainable Energy Reviews*, 81, 954–977.

ASHRAE, 2003, *Methods of testing to determine the thermal performance of solar collectors*, American Society of Heating, Refrigerating, and Air-Conditioning Engineers, Atlanta.

Sureandhar, G., Srinivasan, G., Muthukumar, P., and Senthilmurugan, S., 2021, Performance analysis of arc rib fin embedded in a solar air heater, *Thermal Science and Engineering Progress*, 23, 100891.

Tyagi, V. V., Panwar, N. L., Rahim, N. A., and Kothari, R., 2012, Review on solar air heating system with and without thermal energy storage system, *Renewable and Sustainable Energy Reviews*, 16(4), 2289–2303.

Yadav, A. S., and Bhagoria, J. L., 2014a, A CFD based thermo-hydraulic performance analysis of an artificially roughened solar air heater having equilateral triangular sectioned rib roughness on the absorber plate, *International Journal of Heat and Mass Transfer*, 70, 1016–1039.

Yadav, A. S., and Bhagoria, J. L., 2014b, A numerical investigation of square sectioned transverse rib roughened solar air heater. *International Journal of Thermal Sciences*, 79, 111–131.

Yakhot, V., and Smith, L. M., 1992, The renormalization group, the  $\epsilon$ -expansion and derivation of turbulence models, *Journal of Scientific Computing*, 7(1), 35–61.



## GEOMETRIC OPTIMIZATION OF A NANOSTRUCTURED W-SiO<sub>2</sub>-W SELECTIVE EMITTER WITH TEMPERATURE DEPENDENT EMISSIVITY FOR THERMOPHOTOVOLTAIC APPLICATIONS

Eslem Enis ATAĞ<sup>a\*</sup>, Elif Begüm ELÇİOĞLU<sup>b\*\*</sup>, Tuba OKUTUCU-ÖZYURT<sup>c\*\*\*</sup>

<sup>a</sup> Middle East Technical University, Department of Mechanical Engineering, 06800, Ankara, Turkey

<sup>b</sup> Eskişehir Technical University, Department of Mechanical Engineering, 26555 Eskişehir, Turkey

<sup>c</sup> İstanbul Technical University, Energy Institute, Renewable Energy Division, 34469, İstanbul, Turkey

\* eatak@metu.edu.tr, ORCID: 0000-0002-6866-5207

\*\* ebelcioglu@eskisehir.edu.tr, ORCID: 0000-0002-1005-4294

\*\*\* okutucuozyurt@itu.edu.tr, ORCID: 0000-0003-4248-8043

(Geliş Tarihi: 15.09.2022, Kabul Tarihi: 31.03.2023)

**Abstract:** Metal-Insulator-Metal (MIM) nanostructures provide tunable multiple absorption/emission peaks desirable for spectroscopy, light sensing and thermophotovoltaic (TPV) applications. The efficiency of TPV systems can be improved by employing MIM emitters with resonators that allow high emission above PV cell bandgap and low emission elsewhere. Although there have been attempts to design MIM emitters for TPV systems, a comprehensive study that investigates and optimizes different resonator shapes is lacking. In this study, broadband TPV emitters with W-SiO<sub>2</sub>-W nanostructures are optimized for pairing with GaSb PV cells. A numerical approach is followed utilizing finite-difference time-domain method and particle swarm optimization scheme, MIM emitters with four resonator shapes: disk, square, pyramid, and cone are dimensionally optimized to attain an emissivity spectrum that overlaps with high quantum efficiency region of the GaSb cell. The optimized emitters are compared for efficiency, power output, material consumption, as well as their optical response to temperature and angular effects. At an emitter temperature of 1600 K, electrical power outputs of 2.335-2.418 W·cm<sup>-2</sup> and spectral efficiencies of 56.2-57.6% are obtained. It is found that flat resonators tend to achieve similar performance to that of pointy resonators with shorter heights. Among the considered shapes, disk emitter demonstrates the highest efficiency with minimum material consumption. Compared to a plain W emitter at the same temperature, the disk MIM emitter exhibits significantly higher spectral efficiency and electrical power output (34% and 215% respectively). The results demonstrate the successful use of nano-elements in TPV systems, and the potential for fabricating and realizing such structures.

**Keywords:** Metal-insulator-metal, selective emitter, surface plasmon polariton, magnetic polariton, nanostructure, thermal radiation harvesting, particle swarm optimization.

## SICAKLIĞA BAĞLI YAYINIM GÖSTEREN NANOYAPILI W-SiO<sub>2</sub>-W SEÇİCİ YAYICININ TERMOFOTOVOLTAİK UYGULAMALAR İÇİN GEOMETRİK OPTİMİZASYONU

**Özet:** Metal-yalıtkan-metal (MIM) nanoyapılar, ışık algılama, spektroskopisi ve termofotovoltaik (TPV) uygulamalar için arzu edilen, ayarlanabilir soğurma/yayma spektrumu oluşturur. TPV sistemlerin verimliliği, PV hücrenin bant aralığı enerjisi üzerinde yüksek, altında düşük yayma sağlayan rezonatörlerin yayıcıda kullanımıyla iyileştirilebilir. Daha önce MIM yapıların TPV yayıcı olarak tasarlanma girişimleri olmasına rağmen, farklı rezonatör şekillerinin optimizasyonu ve kapsamlı incelenmesi eksiktir. Bu çalışmada, GaSb PV hücre ile eşleştirilmek üzere, W-SiO<sub>2</sub>-W nanoyapılı geniş bant TPV yayıcılar optimize edilmiştir. Zamanda sonlu farklar yöntemi ve parçacık sürü optimizasyonu kullanılarak, disk, kare, piramit ve koni olmak üzere dört rezonatör şeklinin boyutları, emisivitelerinin GaSb hücrenin kuantum verimliliğiyle spektral olarak eşleşmesi için nümerik olarak optimize edilmiştir. Optimize edilen yayıcılar; verim, güç çıktısı, harcanan malzeme miktarı, yayma açısı ve sıcaklık değişimine karşı optik davranışları bakımından karşılaştırılmıştır. 1600 K yayıcı sıcaklığında, 2.335-2.418 W·cm<sup>-2</sup> aralığında elektriksel güç çıktısı ve %56.2-57.6 aralığında spektral verim elde edilmiştir. Düz yapıli rezonatörlerin, sivri yapıli rezonatörlerle benzer performanslara, daha alçak boyutta nanoyapılarla ulaştığı gözlenmiştir. İncelenen şekiller arasında, disk rezonatör kullanan yayıcıların en yüksek verime en az malzeme kullanımı ile eriştiği gözlenmiştir. Disk rezonatörlü yayıcının, aynı sıcaklıkta düz W yayıcıya göre, oldukça yüksek spektral verim ve elektriksel güç çıktısı sağlayacağı

gösterilmiştir (sırasıyla, %34 ve %215). Çalışmanın sonuçları, nano elamanların TPV sistemlerde başarılı kullanım ve üretim potansiyelini göstermektedir.

**Anahtar Kelimeler:** Metal-yalıtkan-metal, seçici yayıcı, yüzey plazmon polariton, manyetik polariton, nanoyapı, ısı radyasyon harmanlaması, parçacık sürü optimizasyonu.

## NOMENCLATURE

$E$	Electric field intensity [V m <sup>-1</sup> ]
$E_g$	Bandgap energy [eV]
$E_{\lambda,b}$	Spectral blackbody radiation [W m <sup>-2</sup> μm <sup>-1</sup> ]
$E_{in}$	In-band radiation [W m <sup>-2</sup> ]
$E_{total}$	Total emissive power [W m <sup>-2</sup> ]
$EQE$	External quantum efficiency
$F$	Objective function
$FF$	Fill factor
$J$	Current density [A m <sup>-2</sup> ]
$J_0$	Reverse saturation current density [A cm <sup>-2</sup> ]
$J_{sc}$	Short circuit current density [A cm <sup>-2</sup> ]
$P_{el}$	Electrical power output [W cm <sup>-2</sup> ]
$T_E$	Emitter temperature [K]
$T_C$	TPV cell temperature [K]
$V_{oc}$	Open circuit voltage
$c$	Speed of light in vacuum [2.998×10 <sup>8</sup> m s <sup>-1</sup> ]
$d$	Diameter or base width of the resonator [nm]
$h$	Height of the resonator [nm], Planck's constant [6.626×10 <sup>-34</sup> m <sup>2</sup> kg s <sup>-1</sup> ]
$k$	Wave vector [m <sup>-1</sup> ]
$k_b$	Boltzmann constant [8.617×10 <sup>-5</sup> eV K <sup>-1</sup> ]
$n$	Ideality factor
$t$	Thickness of the dielectric layer [nm]
$q$	Charge of an electron [1.602×10 <sup>-19</sup> C]
$x$	Position of the particle
$v$	Velocity of the particle
$\Lambda$	Period of the nanostructure [μm]
$\alpha_\lambda$	Spectral absorptivity
$\beta$	Amendment factor
$\epsilon_\lambda$	Spectral emissivity
$\eta_E$	Emitter (spectral) efficiency
$\eta_{TPV}$	Thermophotovoltaic system efficiency
$\lambda_g$	Wavelength of radiation corresponding to the bandgap energy of the cell [μm]
$v$	Normalized open circuit voltage
$\rho_\lambda$	Spectral reflectivity

## INTRODUCTION

The ever-growing need for energy in the world directs researchers to look for alternative ways to convert energy. Thermophotovoltaic (TPV) conversion is among the promising candidates. A TPV system converts infrared radiation emitted by a thermal source (emitter) directly into electrical power by means of a photovoltaic (PV) cell (receiver). Silicon (Si) and Gallium antimonide (GaSb) are among the two most popular PV cells used in TPV prototypes (Ferrari, et al., 2014), while the low bandgap of GaSb ( $E_g = 0.72$  eV) (Adachi, 2013) makes it more suitable compared to Si ( $E_g = 1.12$  eV) for TPV systems with currently attainable emitter temperatures.

The biggest obstacle in development of efficient TPV systems is the spectral mismatch between the thermal

emission of the emitter and the PV cell bandgap. An ideal emitter should mainly emit photons with energies higher than or equal to the bandgap of the cell, i.e., in-band photons. TPV system prototypes with GaSb cells usually employ silicon carbide (SiC) or tungsten (W) based emitters (Ferrari, et al., 2014). SiC emitters, although generating a certain amount of power, have very low efficiency due to their high infrared emissivity. W is a suitable selective emitter for GaSb cells since it has high emissivity in the in-band region of the cell. Spectral selectivity can also be achieved by imprinting nanostructures on materials surface. Nanopatterning is usually applied to reduce reflectivity and increase the absorptivity/emissivity of materials (Atak, et al., 2022; Bandiera, et al., 2008; Deinega, et al., 2011; Yüksel, et al., 2015; Sai & Yugami, 2004). Among nanostructured materials, metal-insulator-metal (MIM) configurations were shown to further create multiple plasmonic resonances that allows tunable absorption/emission peaks (Aydın, et al., 2011; Yokoyama, et al., 2016; Lee, et al., 2008; Sakurai, et al., 2015) which exhibits high utility for TPV emitters. A MIM nanostructure is a tri-layer metamaterial consisting of metallic base layer (reflector), a dielectric spacer, and periodically placed metallic patches (resonators) on top. Several researchers employed MIM structures to design selective TPV emitters (Wang & Zhang, 2012; Woolf, et al., 2014; Song, et al., 2016), solar absorbers (Han, et al., 2016; Han, et al., 2017), and TPV cells (Isobe & Hanamura, 2019). MIMs consisting of W and SiO<sub>2</sub> were shown to produce broadband and high emissivity/absorptivity in the available region of GaSb related cells. For example, Wang and Zhang (Wang & Zhang, 2012) designed a TPV emitter with W base, SiO<sub>2</sub> spacer, and W strips (W-SiO<sub>2</sub>-W) which showed near unity absorption in the range 0.73-1.83 μm. Zhang, et al. (2021) designed a W-SiO<sub>2</sub>-W absorber with W strips with trapezoidal profile that showed high absorption between 0.55-1.9 μm. However, the one-dimensional grating structure causes polarization dependence of the emissivity, and resonators as tall as 2300 nm are used. Zhao, et al. (2013) reported a similar emitter design with square resonators, showing polarization independent and high emissivity between 0.7-1.8 μm. Han, et al. (2017) fabricated W-SiO<sub>2</sub>-W based solar absorber with disk resonators that showed an absorptivity over 90% between 0.5–1.75 μm, which remained unchanged for incidence angles up to 40°. Zhao and Fu (2016), numerically investigated a multilayer periodic SiO<sub>2</sub>-W-SiO<sub>2</sub>-W grating and achieved high emissivity suitable for InGaSb cells. The performance of their design is similar to that of MIMs; however, its structure is challenging in terms of fabrication.

Recent W based emitter designs encountered in the literature have room for improvement. A major issue is that the optical properties of W are mostly evaluated at

room temperature and considered in the same way to design selective emitters (Yüksel, et al., 2015; Wang & Zhang, 2012; Song, et al., 2016; Zhao, et al., 2013; Sakurai & Matsuno, 2019; Celanovic, et al., 2008; Blandre, et al., 2019), although the spectral emissivity of W varies greatly with temperature (Touloukian & DeWitt, 1970; Roberts, 1959). Feasible TPV systems should be operated at high temperatures (>1000 K) to generate enough power for use. Temperature dependence of spectral emissivity of W has considerable effect on the efficiency estimation of TPV systems (Atak, 2021). As an exception, the emitter design of Silva-Oelker et al. (2018) does take high temperature optical properties of W into account in their design. However, the one-dimensional periodic structure of the emitter makes the emissivity polarization-dependent and uses W resonators as tall as 1  $\mu\text{m}$  to reduce this dependency. This presents a fabrication challenge, similar to that of Zhang, et al. (2021). The most important issue is that the majority of MIM studies focus on one resonator type, which are usually disks or square patches. There is limited number of MIM studies with pointy resonators such as trapezoids (Zhang, et al., 2021), pyramids (Zheng, et al., 2019) and truncated pyramids (Dang, 2020), but they are not explored and optimized for TPV applications, and their performance is not compared to MIMs with other resonator shapes. In addition to the optical and thermal performance, the amount of material consumption is also affected by the shape of the resonators, which is important for large scale fabrication. Thus, a comprehensive study on the effect of shape on the performance of TPV emitters should be performed.

Considering aforementioned gaps in the literature, the objective of the present study is to optimize W and  $\text{SiO}_2$  based MIM emitters with differently shaped resonators, to be paired with GaSb cells, and systematically investigate the effect of resonator shape on the emitter performance. The parameter optimized in this work is the shape of the nano-elements, and the evaluation includes the following four homeomorphic resonator shapes: squares, disks, pyramids, and cones. The optimizations are performed to achieve high efficiency and power output at elevated temperatures. The optimized structures are compared in terms of spectral efficiency, power output, TPV system efficiency, material consumption, as well as optical response to the changes in the emission temperature and angles.

## MATERIAL AND METHOD

### Material

In this study, GaSb is selected as the TPV cell material, due to its low bandgap and maturity of systems with GaSb cells. GaSb has a direct bandgap of 0.72 eV (Adachi, 2013), which corresponds to the energy of a photon at a wavelength of 1.72  $\mu\text{m}$ . According to Wien's Displacement Law, in order to have thermal radiation peak at this wavelength, a blackbody should be heated up to 1680 K. In this work, W is selected as the metal base,

due to its high melting temperature (3695 K) and low evaporation rate in vacuum at temperatures up to 2000 K (Gombert, 2003), exhibiting high temperature stability.

In MIM designs, weakly absorbing dielectric oxides are usually used as the dielectric layer.  $\text{SiO}_2$  is chosen as the dielectric spacer in this work due to its high transmissivity of the light in the visible and near infrared range and high melting temperature (1983 K). MIMs composed of W and  $\text{SiO}_2$  have been successfully fabricated as TPV emitters (Sakurai & Matsuno, 2019), and solar absorbers (Han, et al., 2017). Kim et al. (2017) has shown that a TPV emitter composed of multiple W and  $\text{SiO}_2$  thin layers were stable at 1300 K although they displayed delamination spots at 1400 K. Compared to the design of Kim et al. (2017), the MIM structure considered in this work has fewer layers, hence it is expected to be more resistant to delamination at higher working temperatures. In this study, the MIM designs to be optimized are composed of a W substrate,  $\text{SiO}_2$  dielectric layer, and periodically spaced W resonators on top.

### Method

An ideal broadband TPV emitter has an emissivity of 1 above the bandgap and 0 below the bandgap as given in Eq (1). However, obtaining an emissivity spectrum with a sharp cut-off is challenging, if not impossible. In order to maximize in-band radiation with high utility, researchers usually try to obtain a peak emissivity at around the bandgap.

$$\varepsilon(\lambda) = \begin{cases} 1, & 0 < \lambda \leq \lambda_g \mu\text{m} \\ 0, & \lambda > \lambda_g \mu\text{m} \end{cases} \quad (1)$$

Having a peak emissivity at  $\lambda_g$  results in considerable emission for  $\lambda > \lambda_g$ , which in turn decreases the overall efficiency. Other than the bandgap, one alternate parameter for TPV emitter design is the external quantum efficiency (*EQE*) of the cell. *EQE* is defined as the number of electron-hole pairs created per incident photon. In PV cell applications, *EQE* peak does not always overlap with the bandgap. For example, GaSb has a bandgap of 1.72  $\mu\text{m}$ , but GaSb cell produced by JX Crystals (JXC) has its peak *EQE* (which is around 80%) centered at  $\lambda = 1.5 \mu\text{m}$  and has nonzero values up to 1.80  $\mu\text{m}$  (Fraas, et al., 2002). A selective emitter matching the high *EQE* region would have less out-of-band radiation while maximizing the electrical power output. For wavelengths below 0.6  $\mu\text{m}$ , the *EQE* of GaSb is low and the amount of radiation emitted by TPV emitters at attainable temperatures (1000-2000 K) is negligible. Therefore, the high emissivity region is set as 0.6-1.8  $\mu\text{m}$ . The emissivity for wavelengths longer than 1.8  $\mu\text{m}$  should be suppressed to keep the out-of-band radiation low. With these considerations, an objective function was developed to maximize the emissivity of the emitter within the high external quantum efficiency region of the

GaSb cell while suppressing the out-of-band radiation. The objective function ( $F$ ) is defined in Eq. (2).

$$F = \frac{\int_{0.6}^{1.8} E_{\lambda,b} \varepsilon_{\lambda}(\lambda) d\lambda}{\int_{0.6}^{1.8} E_{\lambda,b} d\lambda} - \frac{\int_{1.8}^5 E_{\lambda,b} \varepsilon_{\lambda}(\lambda) d\lambda}{\int_{1.8}^5 E_{\lambda,b} d\lambda} \quad (2)$$

In order to prevent additional emissivity peaks, the long wavelength limit of the low emissivity region is taken as 5  $\mu\text{m}$ . In this context,  $F$  is a measure of the selectivity of the emitter, where high in-band emissivity and low out-of-band emissivity maximizes its value. For an ideal emitter,  $F$  should be unity. A similar optimization method is previously used in the optimization of MIM emitters for the GaSb cell where the designed emitter showed both higher emitter efficiency and higher in-band radiation than frequently used emitters such as silicon carbide (SiC) and W (Atak, et al., 2021).

In the current design of W-SiO<sub>2</sub>-W emitter, the bottom W layer is assumed to be optically thick, i.e., the transmission through it is assumed zero. By Kirchhoff's law, for a body at equilibrium, the emissivity and the absorptivity should be equal at all wavelengths. Therefore, the spectral emissivity can be calculated using Eq. (3):

$$\varepsilon_{\lambda} = \alpha_{\lambda} = 1 - \rho_{\lambda} \quad (3)$$

The calculation of reflectivity from nanostructured surfaces requires Maxwell's equations to be solved. For this purpose, a numerical algorithm, the Finite-Difference Time-Domain (FDTD) method is employed. Originally developed by Yee (1996), FDTD aims to solve for the interaction of electromagnetic radiation with arbitrarily complex geometries, by discretizing the Maxwell's curl equations. FDTD method is widely employed in nano-photonics research.

In Figure 1, the four MIM designs and the computational domain of a disk MIM structure are given. A plane light source is incident normal to the  $x$ - $y$  plane. The  $x$  and  $y$  boundary conditions are periodic, since the nanostructure design repeats in both directions. The  $z$  boundary conditions are set as stretched coordinate perfectly matched layer (PML) in order to prevent reflections from the boundaries. This set of boundary conditions is frequently employed in the simulation of periodic nanostructures (Yüksel, et al., 2015; Sakurai, et al., 2014) and shown to be consistent with experiments (Matsuno & Sakurai, 2017).

In the simulations, optical properties SiO<sub>2</sub> are taken from Palik's Handbook (Palik, 1998) since the emissivity of SiO<sub>2</sub> is low and shows negligible temperature dependence (Rozenbaum, et al., 1999). The temperature of W is taken to be 1600 K since it was previously shown that W-based TPV emitters can be operated around similar temperatures (Fraas, et al., 2000). In order to account for the change in the emissivity with temperature, the Drude model by Roberts (1959) is used. In order to validate the method, Silva-Oelker et al.'s (2018), W-HfO<sub>2</sub>-W design with rectangular W strips is studied using FDTD, and the results are compared with those of Silva-Oelker et al. acquired by rigorous coupled-wave analysis (RCWA) method. Silva-Oelker et al.'s (2018) study is chosen for validation since the temperature of W in their design (1680 K) is similar to that of the present study. For accurate results, the mesh step should be at least ten times smaller than the smallest wavelength being simulated (Deinega, et al., 2011). Since wavelengths shorter than 500 nm are not in the scope of this work, the mesh step should be smaller than 50 nm. It is seen that the results converge to a constant value at 5 nm mesh size and decreasing the mesh size further did not improve the results, hence it is used for the rest of the simulations. The result of the present FDTD simulation is compared to the RCWA results of Silva-Oelker et al. (2018), in Figure 2.

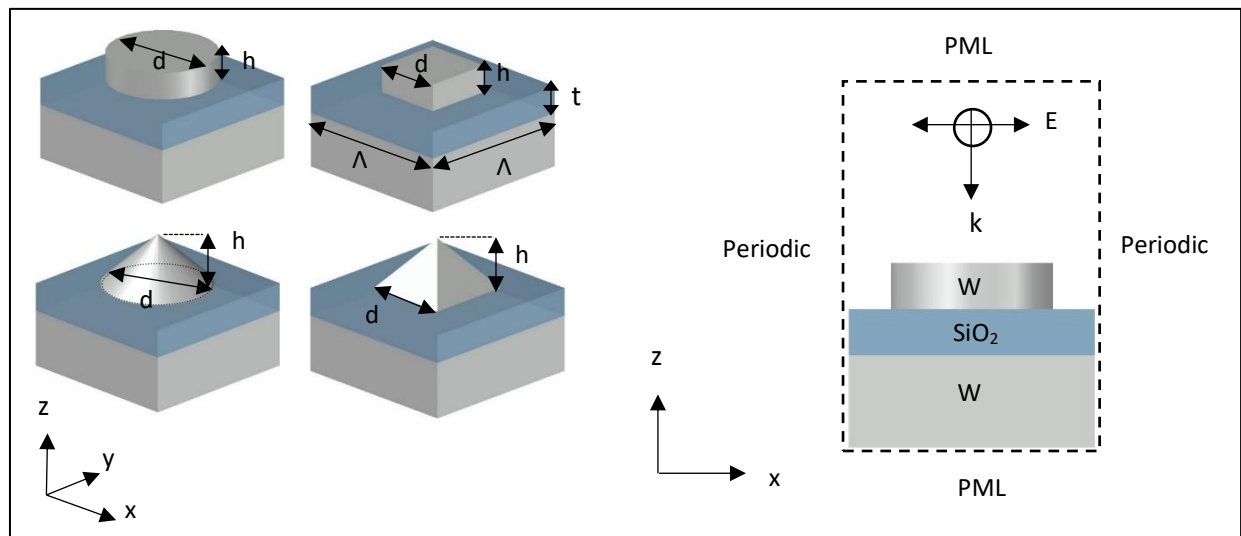


**Figure 1.** The MIM designs and the computational domain of a disk MIM structure.

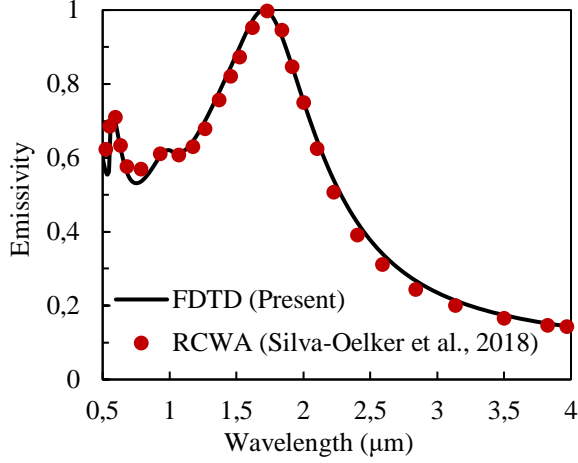


**Figure 2.** Emissivity of W-HfO<sub>2</sub>-W emitter with rectangular W strips of Silva-Oelker et al. (2018) obtained by RCWA and the present FDTD Simulation

The emissivity spectrum for TM polarized light predicted by FDTD (in the present work) is in good agreement with RCWA results of Silva-Oelker et al. (2018) with a maximum deviation of 9.1%, hence the model is validated.

In another study of W based MIM emitters (Silva-Oelker, et al., 2019), the polarization averaged spectral emissivity is found to be a good approximation of the hemispherical emissivity. Hence, in this study, majority of the FDTD simulations are performed considering normal emissivity.

### Optimization

The objective function,  $F$  defined earlier by Eq. (2) is formed to maximize emitter emissivity within the high external quantum efficiency region of the GaSb cell and suppress the out-of-band radiation. In order to find the nanostructure parameters yielding the highest  $F$  given by Eq. (2), Particle Swarm Optimization (PSO) is employed. PSO is a stochastic optimization algorithm designed by Kennedy and Eberhart (1995). In PSO, firstly, possible solutions called “particles” are generated, then these particles are moved in the solution space until maximum number of generations or a given convergence criterion is achieved. The movements of particles are affected both by their personal best positions and the best positions attained by the other particles. A mathematical description of the velocity ( $v$ ) and the position ( $x$ ) of each particle at each iteration are given in Eqs. (5a, 5b) (Shi & Eberhart, 1998). With this iterative process, eventually, all particles are expected to gather around the global best position, similar to bees swarming around the region with highest flower density.

$$v = w \cdot v + c_1 r_1 (p_{best} - x) + c_2 r_2 (g_{best} - x) \quad (5a)$$

$$x = x + v \quad (5b)$$

In Eqs. (5a) and (5b)  $w$  is the inertia factor,  $c_1$  and  $c_2$  are weights,  $r_1$  and  $r_2$  are random coefficients,  $p_{best}$  is the personal best position a particle has encountered, and  $g_{best}$  is the global best position encountered by all particles. In this work,  $w = 0.729$  and  $c_1 = c_2 = 1.494$  are used as recommended by Robinson and Rahmat-Samii (2004) for electromagnetics.

In this optimization scheme, the position ( $x$ ) vector is multidimensional with each dimension representing an optimization parameter. Since each additional parameter increases the computational time exponentially, it is important to assess the impact of each parameter and optimize those with higher impact. The main physical mechanism behind achieving broadband high emissivity with MIM structures is exciting surface plasmon polariton (SPP) and magnetic polariton (MP) resonances close to each other on the spectrum. In Wang and Wang (2013), it was shown that SPP resonance depends on the period, while MP resonance depends on the resonator width. In fact, the cut-off wavelength around 1.8  $\mu\text{m}$  remained unchanged between periods of 0.5-0.8  $\mu\text{m}$ . In other studies, cut-off wavelengths between 1.57-1.83  $\mu\text{m}$  were achieved for periods of 0.5-0.6  $\mu\text{m}$  (Han, et al., 2017; Zhao, et al., 2013; Sakurai & Matsuno, 2019; Khorrami & Fathi, 2019). In a previous study on optimization of W-SiO<sub>2</sub>-W emitters with periods of 0.4-0.8  $\mu\text{m}$ , it was shown that using 0.4  $\mu\text{m}$  period creates a dip in the emissivity spectra due to the two main resonances being too far apart on the spectrum (Atak, 2021). In the same study, it was also seen that minimum resonator height is obtained at 0.6  $\mu\text{m}$  period. Therefore, in the present work, a period of 0.6  $\mu\text{m}$  is used. Since MP resonance, which determines the cut-off wavelength depends on the resonator width, it is varied between zero and the period for the optimizations performed in this study. The width is equated to base length for square bases and diameter for circular bases. In Wang and Wang (2013), it was observed that the absorptivity in general increases with the resonator height, however, the peak at the MP resonance begins to decrease after 150 nm. In the same study, the thickness of the spacer layer is varied between 30-150 nm. It was seen that the peak absorptivity increased with SiO<sub>2</sub> thickness up to 80 nm, beyond which it decreased. In Khorrami and Fathi (2019) it was shown that the emissivity was enhanced gradually by increasing the thickness of the SiO<sub>2</sub> layer from 30 nm to 110 nm. Considering these findings, the range of resonator height and SiO<sub>2</sub> layer thickness are set to 0-200 nm for the optimization.

In summary, in order to obtain the emissivity profile giving maximum  $F$ , there are three parameters to be optimized: resonator width ( $d$ ), resonator height ( $h$ ), and the thickness of the dielectric layer ( $t$ ). Within the scope of this study, PSO procedures are followed separately for each shape. The solution space is three dimensional with parameters  $t$ ,  $d$ , and  $h$ . For each optimization, 10 random particles are generated initially. These particles are moved through the solution space for 10 generations, and evaluated according to  $F$  given in Eq (2).

## Performance Evaluations

For this study, three metrics are considered to evaluate the performance of TPV systems: the emitter efficiency, the TPV system efficiency (radiation-to-electricity efficiency), and the electrical power output. For the scope of this study, the view factor losses are ignored since emitter and cell are very close and parallel to each other. The performance evaluations are based on the normal emissivity since the emitter and cell usually directly face each other in TPV systems and the selectivity of W-SiO<sub>2</sub>-W structures is largely independent of angles (Han, et al., 2017). The in-band radiation is defined as the emissive power of the emitter within the wavelength range 0- $\lambda_g$ , as in Eq. (6).

$$E_{in} = \int_0^{\lambda_g} \varepsilon_\lambda(\lambda) E_{\lambda,b}(\lambda, T_E) d\lambda \quad (6)$$

The total emissive power radiated from an emitter is defined as in Eq. (7):

$$E_{total} = \int_0^{\infty} \varepsilon_\lambda(\lambda) E_{\lambda,b}(\lambda, T_E) d\lambda \quad (7)$$

The spectral emissive power of a blackbody ( $E_{\lambda,b}$ ) is given by Planck's law (Incropera, et al., 2011) as in Eq. (8):

$$E_{\lambda,b}(\lambda, T_E) = \frac{C_1}{\lambda^5 [\exp(C_2/\lambda T_E) - 1]} \quad (8)$$

where  $C_1 = 3.742 \times 10^8 \text{ W } \mu\text{m}^4 \text{ m}^{-2}$  and  $C_2 = 1.439 \times 10^4 \text{ W } \mu\text{m K}$ .

The emitter efficiency ( $\eta_E$ ), also called the spectral efficiency (Fraas, et al., 2003) is defined as the ratio of in-band radiation to the total emissive power of the emitter at a given temperature (Chubb, 2007), and shown in Eq. (9).

$$\eta_E = \frac{E_{in}}{E_{total}} = \frac{\int_0^{\lambda_g} \varepsilon_\lambda(\lambda) E_{\lambda,b}(\lambda, T_E) d\lambda}{\int_0^{\infty} \varepsilon_\lambda(\lambda) E_{\lambda,b}(\lambda, T_E) d\lambda} \quad (9)$$

The overall efficiency of the TPV system depends both the emitter and the TPV cell. The TPV system efficiency ( $\eta_{TPV}$ ), as in Eq. (10), can be calculated by dividing the electrical power output to the radiative power of the emitter. It should be noted that this efficiency assumes a view factor of unity.

$$\eta_{TPV} = \frac{P_{el}}{E_{total}} \quad (10)$$

The electrical power output ( $P_{el}$ ) from a TPV cell is a certain fraction (the fill factor,  $FF$ ) of the product of open circuit voltage ( $V_{oc}$ ) and the short circuit current ( $J_{sc}$ ) (Chubb, 2007) as in Eq. (11):

$$P_{el} = FF \cdot J_{sc} \cdot V_{oc} \quad (11)$$

The maximum current occurs when the TPV cell is short circuited. This is called the short circuit current density,

$J_{sc}$  (also known as the photocurrent density) and is calculated using Eq. (12) (Cai, et al., 2020).

$$J_{sc} = \frac{q}{hc} \int_0^{\lambda_g} \varepsilon_\lambda(\lambda) \cdot EQE(\lambda) \cdot E_{\lambda,b}(\lambda, T_E) \lambda d\lambda \quad (12)$$

In Eqs. (6), (9) and (12),  $\lambda_g$  of GaSb cell is taken to be 1.80  $\mu\text{m}$ , since JXC standard GaSb cells show nonzero  $EQE$  up to this value, meaning that current is generated even after the known bandgap of GaSb. When there is no current present, maximum possible voltage is achieved. This is called the open circuit voltage ( $V_{oc}$ ) defined in Eq. (13) (Iles, et al., 1996):

$$V_{oc} = \frac{nk_B T_c}{q} \ln \frac{J_{sc}}{J_0} \quad (13)$$

In Eq. (13),  $n$  is the ideality factor that is assumed to be 1. The reverse saturation current density ( $J_0$ ), also known as the dark current, is the current flowing when there is no light present.  $J_0$  depends on the material as well as the temperature of the cell. In the case of GaSb cell, an expression for  $J_0$  in units  $\text{A}/\text{cm}^2$  is derived by Fraas et al. (1991) as in Eq. (14):

$$J_0 = 1.84 \cdot 10^{-3} T_c^3 \exp\left(\frac{-E_g}{k_B T_c}\right) \quad (14)$$

Then, the fill factor (Eq. (15)) is calculated by (Qiu, et al., 2006):

$$FF = \beta \frac{v - \ln(v + 0.72)}{v + 1} \quad (15)$$

where  $v$  is the normalized open circuit voltage given as in Eq. (16) (Iles, et al., 1996):

$$v = \frac{V_{oc}}{nk_B T_c / q} \quad (16)$$

In Eq. (15),  $\beta$  is the amendment factor which accounts for cell parasitic losses. In the present work,  $\beta = 0.96$  is used as recommended by Qiu et al. (2006). In Eqs. (13), (14) and (16), the cell temperature ( $T_c$ ) is assumed to be 300 K. In Eqs. (6), (9) and (12), considering the JXC standard GaSb cells,  $\lambda_g$  is taken as 1.8  $\mu\text{m}$  in order to accurately calculate the power.

## RESULTS AND DISCUSSION

The optimum parameters found by PSO, the volumes of the resonators and the corresponding  $F$  values are presented in Table 1. All of the emitters converged to similar values of  $F$ , with almost identical SiO<sub>2</sub> thicknesses. However, the volume of the resonator varied from shape to shape. Cone and pyramid resonators tend to have smaller widths while having greater heights compared to disk and square ones.

**Table 1.** The optimized nanostructure parameters and corresponding values of objective function,  $F$ 

Resonator Shape	SiO <sub>2</sub> Thickness (nm)	Resonator Height (nm)	Resonator Width (nm)	Resonator Volume (nm <sup>3</sup> )	$F$
Disk	112	28	322	2.28×10 <sup>6</sup>	0.714
Square	113	36	276	2.74×10 <sup>6</sup>	0.715
Cone	113	93	344	2.88×10 <sup>6</sup>	0.710
Pyramid	113	105	285	2.84×10 <sup>6</sup>	0.711

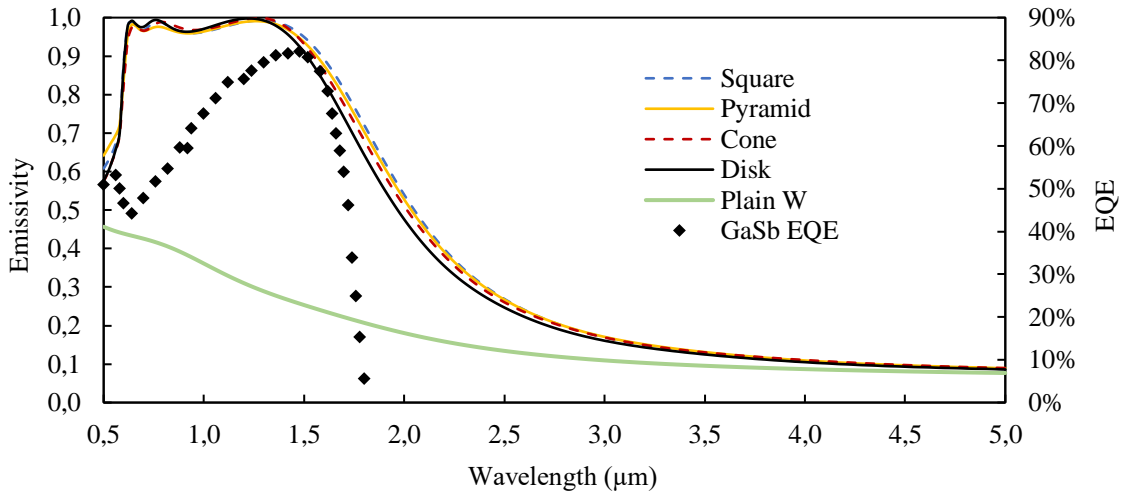
The smallest resonator height and volume are obtained with the disk resonator. The height of the disk resonator is 28 nm which is smaller than the resonators of similar W based MIM emitters/absorbers (Wang & Zhang, 2012; Song, et al., 2016; Han, et al., 2016; Han, et al., 2017; Zhao, et al., 2013; Sakurai & Matsuno, 2019; Silva-Oelker, et al., 2018; Wang & Wang, 2013; Khorrami & Fathi, 2019). It is seen that cone and pyramid structures tend to become taller compared to disk and square, in order to achieve similar  $F$ . Among the four shapes, pyramid is the tallest with 105 nm height, which is still much smaller compared to a similar W-SiO<sub>2</sub>-W design with trapezoidal resonators (Zhang, et al., 2021).

In Figure 3, spectral emissivity of optimized MIM emitters with the four resonator shapes are shown in addition to the spectral emissivity of plane W at 1600 K and  $EQE$  of GaSb (Fraas, et al., 2002). It is seen that MIM emitters regardless of the resonator shape can be optimized to demonstrate high spectral selectivity. Compared to plain W emitter, W-SiO<sub>2</sub>-W configurations have substantially higher emissivity in the in-band region, whereas emissivity becomes almost identical to that of plain W around 5  $\mu$ m. All four emitters showed emissivity peaks at similar wavelengths, two peaks at 0.64  $\mu$ m, 0.78  $\mu$ m and a third peak between 1.22-1.28  $\mu$ m.

Although the emitters are optimized to be used at 1600 K, it is useful to see how their selectivity is affected by temperature. In Figure 4, the emissivity spectra of W-

SiO<sub>2</sub>-W emitters at temperatures of 300 K, 1100 K, and 1600 K are shown. The optical properties of W at room temperature were taken from Palik's Handbook (Palik, 1998) while Drude model of Roberts (1959) is used for higher temperature considerations. It is seen that the locations of emissivity two leftmost peaks around are the same at all temperatures, however the rightmost peak shifts towards lower wavelengths with increasing temperature. The shift of the third peak between 300 K and 1600 K temperatures is about 440-460 nm for disk, square and cone resonators, and 360 nm for the pyramid. It can be said that the selectivity of pyramid resonators is less prone to changes in the temperature compared to other shapes.

Next, the change in the emissivity spectra with the angle of emission (the angle between emission and the surface normal) is investigated. In Figure 5, the emissivity spectra of the selective emitter at different angles are shown. The angular emissivity values are calculated by averaging TM and TE polarizations. It can be seen that all emitters preserve high selectivity at the angle of emission 30°. Although the emissivity at the leftmost two peaks decreases with the increasing angle, the third peak remains relatively unchanged. This can be explained by the excitation of MP around this wavelength. It should be noted that the rightmost peak of the cone emitter undergoes a slight shift towards higher wavelengths at 30°, dissimilar to the others.

**Figure 3.** Comparison of the emissivity spectra of MIM emitters with different shapes, and plain W at 1600 K



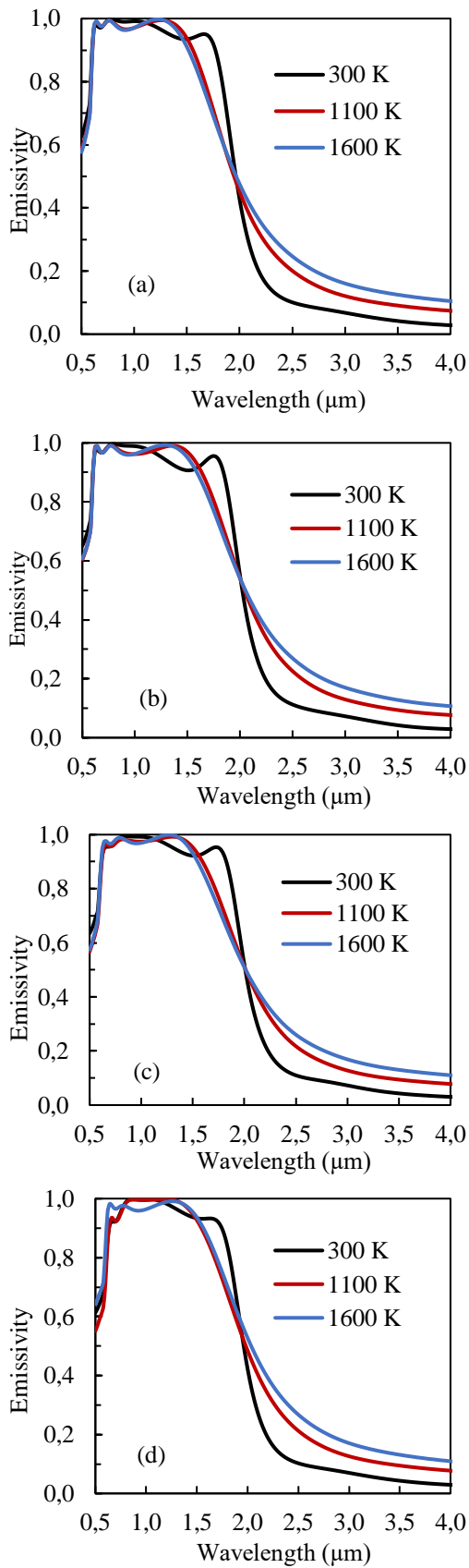


**Figure 4.** The emissivity spectra of optimized W-SiO<sub>2</sub>-W emitters with disk (a), square (b), cone (c), and pyramid (d) resonators at different temperatures

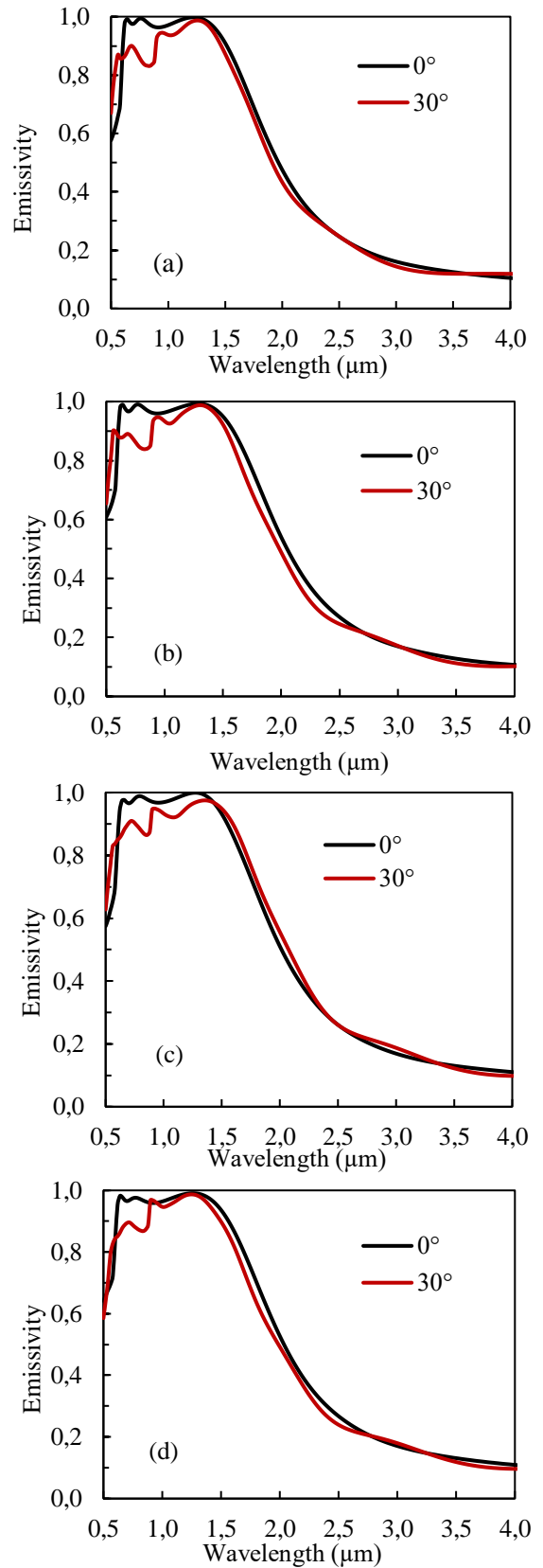


**Figure 5.** Spectral emissivity of the MIM emitter at different emission angles, for disk (a), square (b), cone (c), and pyramid (d) resonators

**Table 2.** The spectral efficiency, TPV efficiency and power output for the investigated emitters at 1600 K paired with GaSb cells. The top four rows list the optimized emitters of the present study.

Emitter	$\eta_E$	$P_{el}$ (W cm <sup>-2</sup> )	$\eta_{TPV}$
Disk MIM	57.62%	2.335	16.53%
Square MIM	56.31%	2.418	16.18%
Cone MIM	56.63%	2.381	16.26%
Pyramid MIM	56.23%	2.392	16.14%
Plain W	42.93%	0.741	11.20%
Blackbody	24.58%	2.605	7.01%
Ideal Emitter	100.00%	2.605	28.53%

Considering normal emissivity spectra, the emitter efficiency, TPV efficiency and power output are presented in Table 2 for optimized MIM and other emitters at 1600 K paired with GaSb cells. The emissivity spectrum of the ideal emitter is given by Eq. (1) with  $\lambda_g$  taken as 1.8  $\mu\text{m}$  to cover all the wavelengths with nonzero quantum efficiency. It is observed that on average,  $\eta_{TPV}$  is less than 30% of  $\eta_E$ , which means that most of the in-band radiation does not contribute to the electrical power. This loss can be attributed to thermalization, surface recombination, and other intrinsic cell losses. The highest TPV efficiency is obtained with the disk resonator, while the highest power output is obtained from square resonator. The difference in efficiency and power output results can be explained by the difference in emissivity after the third peak towards the out of band region as observed from Figure 3. Compared to the planar W emitter at the same temperature, the MIM emitter with disk resonator demonstrates 215.1% higher power and 34.2% higher spectral efficiency.

Although the efficiency and power outputs are similar, the disk resonator can be argued to be the most advantageous in terms of fabrication. Since it has the shortest height among others, its top-down fabrication requires less material and has shorter sputtering time. The volume of the disk is 17% smaller compared to the square resonator which is closest to disks resonator in terms of volume. That means it is also advantageous in terms of bottom-up fabrication. Therefore, we consider the configuration with the disk resonator for further investigations.

In Figure 6, considering temperature dependent emissivity, the efficiency of the TPV system with GaSb cell and optimized disk emitter is presented compared to the ideal and the blackbody emitters in the temperature range 1000 - 1800 K. For validation, the efficiency of a TPV system with blackbody emitter and JXC GaSb cell calculated by Sakurai and Matsuno (2019) is presented as well. It is seen that the efficiency of the optimized emitter is 2-6 times of that of the

blackbody emitter and within 24-65% of the ideal emitter.

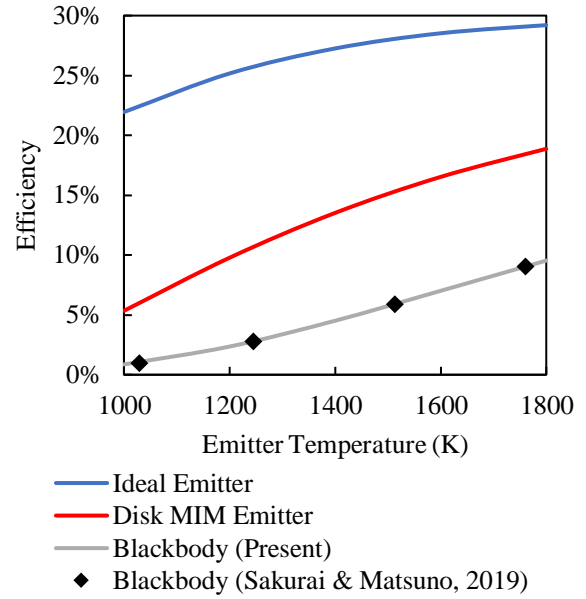


**Figure 6.** TPV system efficiencies for the MIM emitter, the ideal emitter, and the blackbody emitter in the range 1000 - 1800 K.

The efficiency values obtained by ideal, selective, and blackbody emitters tend to get closer as the temperature increases. This can be explained by the shifting of the peak emissive power towards lower wavelengths according to Wien's Displacement Law. With increased temperature, the ratio of in-band radiation to the total emissive power increases for all emitters considered. It should be noted that the ideal emitter in this context does not represent the ultimate attainable efficiency with a predetermined cell, rather, it represents maximum attainable efficiency while keeping the power output at maximum. In Figure 7, the power outputs at different emitter temperatures are presented for the selective emitter and blackbody emitter. Between emitter temperatures of 1000-1800 K, the emitter optimized in this study has a power output of 0.043-5.261 W cm<sup>-2</sup> that is about 87-90% of that of a blackbody.

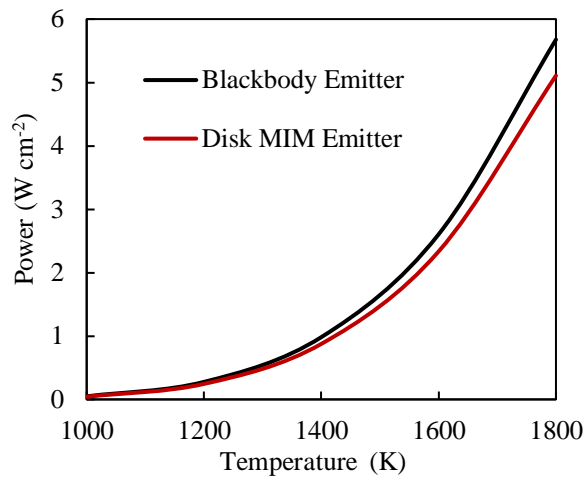


**Figure 7.** Electrical power outputs from TPV systems with the selective emitter and blackbody at different temperatures

## CONCLUSIONS

In this study, an improved selective emitter design is proposed in order to work optimally with a standard GaSb TPV cell. MIM emitters based on W-SiO<sub>2</sub>-W structure with different resonator shapes are optimized and their performances are compared. The nanostructures considered in this work are disks, squares, cones, and pyramids. During the design of the MIM selective emitter, first, an objective function was developed to maximize the emissivity of emitter within the high external quantum efficiency region of the GaSb cell while suppressing out-of-band radiation. By using this objective function with the FDTD method and PSO algorithm, the resonator width, height and the thickness of the SiO<sub>2</sub> layer of the W-SiO<sub>2</sub>-W emitters with four different resonator shapes are optimized. The performance of each emitter is compared by their spectral efficiency, TPV system efficiency, power output, material consumption, as well as the optical response to changes in temperature and emission angle. As a result of the optimization, the SiO<sub>2</sub> thicknesses converged to almost the same value for all emitters, however the dimensions of W resonators varied depending on the shape. Increasing the temperature is shown to cause the shifting of the cut-off wavelength towards lower wavelengths, with the selectivity of pyramid being affected the least. Increasing the angle of emission is shown to decrease the emissivity at short wavelengths but it does not change the emissivity peak near the cut-off wavelength, with the exception of cone resonators. However, the differences in the response of resonators to the angle and temperature effects are not significant enough to reach robust conclusions. At 1600 K, with normal emissivity, spectral efficiencies between 56.23-57.62% and electrical power outputs of 2.335-2.418 W cm<sup>-2</sup> are obtained. Since the emissivity of MIM structures are minimally affected by the emission angles, hemispherical emissivity is expected to be similar to that of normal emissivity. Although the performances are similar, it was found that the flat type of resonators have smaller heights and volumes

compared to pointy resonators, making them preferable for fabrication. Among all designed emitters, the disk emitter is found to be the most efficient while having the smallest volume, hence material consumption. At 1600 K, the MIM emitter with disk resonators demonstrated 57.62% spectral efficiency and 2.335 W cm<sup>-2</sup> power output, that is 34% more efficient and produces 215% more electrical power compared to plain W emitter at the same temperature. The findings of this work may provide insights on the development and fabrication of efficient selective TPV emitters and solar absorbers which are expected to operate at high temperatures.

## ACKNOWLEDGEMENTS

The first author's graduate education was partially supported by the Scientific and Technological Research Council of Turkey (TUBITAK) through 2210-C National MSc/MA Scholarship Program in the Priority Fields in Science and Technology.

## REFERENCES

- Adachi, S., 2013, *Optical constants of crystalline and amorphous semiconductors: numerical data and graphical information*, Springer Science and Business Media.
- Atak, E. E., 2021, *Investigation of Nanostructured Surfaces for Thermophotovoltaic Applications*, Master's Thesis, Middle East Technical University, Ankara, Turkey.
- Atak, E. E., Elçioğlu, E. B. and Okutucu-Özyurt, T., 2020, Nanostructured silicon design for effectively capturing infrared radiation for near-field TPV applications. *NanoRad 2020 4th International Workshop on Nano-Micro Thermal Radiation*, Shanghai, China.
- Atak, E. E., Okutucu-Özyurt, T. and Elçioğlu, E. B., 2021, Metal-Insulator-Metal Selective Emitter Design with an Emissivity Matching with Gasb Thermophotovoltaic Cell. *Proceedings of CHT-21 ICHMT International Symposium on Advances in Computational Heat Transfer*. Begel House Inc.
- Aydın, K., Ferry, V. E., Briggs, R. M. and Atwater, H. A., 2011, Broadband polarization-independent resonant light absorption using ultrathin plasmonic super absorbers. *Nature communications*, 2(1), pp. 1-7.
- Bandiera, S., Jacob, D., Muller, T., Marquier, F. Laroche, M.; Greffet, J. J., 2008, Enhanced absorption by nanostructured silicon. *Applied Physics Letters*, 93(19).
- Blandre, E., Vaillon, R. and Drévilion, J., 2019. New insights into the thermal behavior and management of thermophotovoltaic systems. *Optics Express*, 27(25).

- Cai, Q., Chen, P., Cao, S., Ye, Q., Wu, X., 2020, Performance Analysis of GaSb Cell and Thermophotovoltaic System Under Near-Field Thermal Radiation. *International Journal of Thermophysics*, 41(12), pp. 1-15.
- Celanovic, I., Jovanovic, N. and Kassakian, J., 2008, Two-dimensional tungsten photonic crystals as selective thermal emitters. *Applied Physics Letters*, 92(15).
- Chubb, D., 2007, *Fundamentals of thermophotovoltaic energy conversion*, Elsevier, Amsterdam, The Netherlands.
- Dang, P. T., 2020, Efficient broadband truncated-pyramid-based metamaterial absorber in the visible and near-infrared regions. *Crystals*, 10(9), p. 784.
- Deinega, A., Valuev, I., Potapkin, B. and Lozovik, Y., 2011, Minimizing light reflection from dielectric textured surfaces. *JOSA A*, 28(5), pp. 770-777.
- Ferrari, C., Melino, F., Pinelli, M., Spina, P. R., Venturini, M., 2014, Overview and status of thermophotovoltaic systems. *Energy Procedia*, Volume 45, pp. 160-169.
- Fraas, L. M., Avery, J. E., Gruenbaum, P. E., Sundaram, V. S., Emery, K., Matson, R., 1991, Fundamental characterization studies of GaSb solar cells, In *Conference Record of the Twenty-Second IEEE Photovoltaic Specialists Conference-1991*. pp. 80-84.
- Fraas, L. M., Avery, J. E., Huang, H. X. and Martinelli, R. U., 2003, Thermophotovoltaic system configurations and spectral control. *Semiconductor Science and Technology*, 18(5), p. S165.
- Fraas, L. M., Avery, J. E. and Nakamura, T., 2002, Electricity from concentrated solar IR in solar lighting applications, In *Conference Record of the Twenty-Ninth IEEE Photovoltaic Specialists Conference*, pp. 963-966.
- Fraas, L., Samaras, J., Avery, J. and Minkin, L., 2000, *Antireflection coated refractory metal matched emitters for use with GaSb thermophotovoltaic generators*. pp. 1020-1023.
- Gombert, A., 2003, An overview of TPV emitter technologies. *AIP conference proceedings*, 653(1), pp. 123-131.
- Han, S., Shin, J., Jung, P., Lee, H., Lee, B. J., 2016, Broadband Solar Thermal Absorber Based on Optical Metamaterials for High-Temperature Applications. *Advanced Optical Materials*, 4(8), pp. 1265-1273.
- Han, X., He, K., He, Z. and Zhang, Z., 2017, Tungsten-based highly selective solar absorber using simple nanodisk array. *Optics express*, 25(24), pp. A1072-A1078.
- Iles, P. A., Chu, C. and Linder, E., 1996, The influence of bandgap on TPV converter efficiency. *AIP Conference Proceedings*, February, 358(1), pp. 446-457.
- Incropera, F. P., Lavine, A. S., Bergman, T. L. and DeWitt, D. P., 2011, *Fundamentals of heat and mass transfer*, New York, Wiley.
- Isobe, K. and Hanamura, K., 2019, Selective absorption of a thermophotovoltaic cell using a thin semiconductor and a top fishnet-structured electrode. *International Journal of Heat and Mass Transfer*, Issue 134, pp. 807-814.
- Kennedy, J. and Eberhart, R., 1995, Particle swarm optimization, in *Proceedings of ICNN'95-international conference on neural networks*. Vol. 4, pp. 1942-1948, IEEE.
- Khorrani, Y. and Fathi, D., 2019, Broadband thermophotovoltaic emitter using magnetic polaritons based on optimized one-and two-dimensional multilayer structures. *JOSA B*, 36(3), pp. 662-666.
- Kim, J. H., Jung, S. M. and Shin, M. W., 2017, High-temperature degradation of one-dimensional metallodielectric (W/SiO<sub>2</sub>) photonic crystal as selective thermal emitter for thermophotovoltaic system. *Optical Materials*, Issue 72, pp. 45-51.
- Lee, B. J., Wang, L. P. and Zhang, Z. M., 2008, Coherent thermal emission by excitation of magnetic polaritons between periodic strips and a metallic film. *Optics Express*, 16(15), pp. 11328-11336.
- Matsuno, Y. and Sakurai, A., 2017, Perfect infrared absorber and emitter based on a large-area metasurface. *Optical Materials Express*, 7(2), pp. 618-626.
- Palik, E. D., 1998, *Handbook of optical constants of solids*. Academic press.
- Qiu, K., Hayden, A. C. S., Mauk, M. G. and Sulima, O. V., 2006, Generation of electricity using InGaAsSb and GaSb TPV cells in combustion-driven radiant sources. *Solar energy materials and solar cells*, 90(1), pp. 68-81.
- Roberts, S., 1959. Optical properties of nickel and tungsten and their interpretation according to Drude's formula. *Physical Review*, 114(1), p. 104.
- Robinson, J. and Rahmat-Samii, Y., 2004. Particle swarm optimization in electromagnetics. *IEEE*

*transactions on antennas and propagation*, 52(2), pp. 397-407.

Rozenbaum, O., Meneses, D. D. S., Auger, Y., Chermanne, S., Echegut, P., 1999, A spectroscopic method to measure the spectral emissivity of semi-transparent materials up to high temperature. *Review of scientific instruments*, 70(10), pp. 4020-4025.

Sai, H. and Yugami, H., 2004, Thermophotovoltaic generation with selective radiators based on tungsten surface gratings. *Applied Physics Letters*, 85(16).

Sakurai, A. and Matsuno, Y., 2019, Design and fabrication of a wavelength-selective near-infrared metasurface emitter for a thermophotovoltaic system. *Micromachines*, 10(2), p. 157.

Sakurai, A., Zhao, B. and Zhang, Z. M., 2014, Resonant frequency and bandwidth of metamaterial emitters and absorbers predicted by an RLC circuit model. *Journal of Quantitative Spectroscopy and Radiative Transfer*, Volume 149, pp. 33-40.

Sakurai, A., Zhao, B. and Zhang, Z. M., 2015, Effect of polarization on dual-band infrared metamaterial emitters or absorbers. *Journal of Quantitative Spectroscopy and Radiative Transfer*, Issue 158, pp. 111-118.

Shi, Y. and Eberhart, R., 1998, A modified particle swarm optimizer. In *1998 IEEE international conference on evolutionary computation proceedings. IEEE world congress on computational intelligence* (Cat. No. 98TH8360) pp. 69-73, IEEE.

Silva-Oelker, G., Jerez-Hanckes, C. and Fay, P., 2018, Study of W/HfO<sub>2</sub> grating selective thermal emitters for thermophotovoltaic applications. *Optics express*, 26(22).

Silva-Oelker, G., Jerez-Hanckes, C. and Fay, P., 2019, High-temperature tungsten-hafnia optimized selective thermal emitters for thermophotovoltaic applications. *Journal of Quantitative Spectroscopy and Radiative Transfer*, Volume 231, pp. 61-68.

Song, J., Si, M., Cheng, Q. and Luo, Z., 2016, Two-dimensional trilayer grating with a metal/insulator/metal structure as a thermophotovoltaic emitter. *Applied optics*, 55(6), pp. 1284-1290.

Touloukian, Y. S. and DeWitt, D. P., 1970, *Thermophysical Properties of Matter-The TPRC Data Series. Volume 7. Thermal Radiative Properties-Metallic Elements and Alloys*. New York, Springer.

Wang, H. and Wang, L., 2013, Perfect selective metamaterial solar absorbers. *Optics express*, 21(106), pp. A1078-A1093.

Wang, L. P. and Zhang, Z. M., 2012, Wavelength-selective and diffuse emitter enhanced by magnetic polaritons for thermophotovoltaics. *Applied Physics Letters*, 100(6), p. 063902.

Woolf, D., Hensley, J., Cederberg, J. G., Bethke, D. T., Grine, A. D., Shaner, E. A., 2014, Heterogeneous metasurface for high temperature selective emission. *Applied Physics Letters*, 105(8), p. 081110.

Yee, K., 1966, Numerical solution of initial boundary value problems involving Maxwell's equations in isotropic media, *IEEE Transactions on antennas and propagation*, 14(3), pp. 302-307.

Yokoyama, T., Dao, T. D., Chen, K., Ishii, S., Sugavaneshwar, R. P., Kitajima, M., Nagao, T., 2016, Spectrally Selective Mid-Infrared Thermal Emission from Molybdenum Plasmonic Metamaterial Operated up to 1000° C. *Advanced Optical Materials*, 4(12), pp. 1987-1992.

Yüksel, A., Heltzel, A. and R.Howell, J., 2015, Design and Optimization of Thermal Selective Emitters for High-Efficiency Thermophotovoltaic (TPV) Power Generation. In *Energy Sustainability, Vol. 56840, p. V001T10A003*). American Society of Mechanical Engineers. San Diego.

Zhang, W. W., Qi, H., Yin, Y. M. and Ren, Y. T., 2021, Tailoring radiative properties of a complex trapezoidal grating solar absorber by coupling between SPP and multi-order MP for solar energy harvesting. *Optics Communications*, Volume 479.

Zhao, B., Wang, L., Shuai, Y. and Zhang, Z. M., 2013, Thermophotovoltaic emitters based on a two-dimensional grating/thin-film nanostructure. *International Journal of Heat and Mass Transfer*, Issue 67, pp. 637-645.

Zhao, Y. and Fu, C., 2016, Numerical simulation on the thermal radiative properties of a 2D SiO<sub>2</sub>/W/SiO<sub>2</sub>/W layered grating for thermophotovoltaic applications. *Journal of Quantitative Spectroscopy and Radiative Transfer*, Volume 182, pp. 35-44.

Zheng, P., Sujan, K. and Nianqiang, W., 2019, Converting plasmonic light scattering to confined light absorption and creating plexcitons by coupling a gold nano-pyramid array onto a silica-gold film. *Nanoscale horizons*, 4(2), pp. 516-525.



## MİKROALG VE MİKROALG – ETANOL KARIŞIMLARI KULLANIMININ MOTOR PERFORMANS VE EMİSYONLARI ÜZERİNE BİR İNCELEME

Göneç DURAN\*, Muhammed DÖNMEZ\*\* ve Cumali İLKİLİÇ\*\*\*

\*Bursa Uludağ Üniversitesi Mühendislik Fakültesi Otomotiv Mühendisliği Bölümü, 16059 Nilüfer, Bursa  
gonenccuran@uludag.edu.tr, ORCID: 0000-0001-8545-7621

\*\*Bursa Uludağ Üniversitesi Mühendislik Fakültesi Otomotiv Mühendisliği Bölümü, 16059 Nilüfer, Bursa  
muhammeddonmez@uludag.edu.tr, ORCID: 0000-0002-9046-4989

\*\*\*Fırat Üniversitesi Teknoloji Fakültesi Otomotiv Mühendisliği Bölümü, 23100 Elâzığ  
cumilkilic@firat.edu.tr, ORCID: 0000-0001-5651-7621

(Geliş Tarihi: 17.03.2022, Kabul Tarihi: 04.04.2023)

**Öz:** Sanayileşme, taşıt sayısı ve popülasyonda olan artışla beraber, artan fosil yakıt kullanımı enerji gereksinimi ve emisyon gibi sorunlara sebep olmaktadır. Bu çalışmada içten yanmalı motorlarda kullanılabilir biyoyakıt üretimi, mikroalg yağı, sodyum metilat katalizörü eşliğinde metanol ile transesterifikasyon yapılarak gerçekleştirilmiştir. Günümüz trend çalışmalarında yer alan mikroalgler ekilebilir tarım alanlarının kullanılmasına gerek duymayan büyüme ortamı ve iyi hammadde/yağ dönüşüm oranından dolayı tercih edilmiştir. Ayrıca elde edilen biyoyakıtın, farklı oranlarda etanol ile karışım elde edilerek yakıtların motor performansı ve emisyonlar üzerine olan etkisi incelenmiştir. Deneysel tam yükte 1000-3000 d/dk motor devir aralığında gerçekleştirilmiştir. Motordaki maksimum tork 1800 d/dk elde edilirken en yüksek güç ise 2600 d/dk'da elde edilmiştir. %15 oranında etanol ile karıştırılmış biyodizel için dizele göre 1800 d/dk'da torkta %0.86 artış elde edilirken, 2600 d/dk'da güçte %0.42 azalma olmuştur. Mikroalg biyoyakıtı ve etanol karışımli yakıtların yanması sonucu ortaya çıkan emisyon değerleri dizel yakıt kullanımına göre oldukça düşmüştür. Bu bağlamda insana ve çevreye zararlı emisyonlar, özellikle küresel ısınmaya sebep olan karbondioksit emisyonu önemli ölçüde azalmıştır.

**Anahtar Kelimeler:** etanol, mikroalg, biyodizel, chlorella protothecoides, metil ester.

## AN INVESTIGATION ON ENGINE PERFORMANCE AND EMISSIONS OF USING MICROALGAE AND MICROALGAE-ETHANOL BLENDS

**Abstract:** Increasing use of fossil fuels with the increase in industrialization, number of vehicles and population causes problems such as energy requirement and emissions. In this study, biodiesel production was carried out by transesterification using microalgae oil, methanol, and sodium methylate as catalyst which can be used in internal combustion engines. In today's trend studies of Microalgae has been preferred because of its growth environment that does not require the use of arable land and its good raw material/oil conversion ratio. In addition, the effect of fuels on engine performance and emissions was investigated by obtaining a mixture of obtained biodiesel and ethanol at different rates. Experiments were carried out at full load in the engine speed range of 1000-3000 rpm. The maximum engine torque is obtained at 1800 rpm, while the maximum power is obtained at 2600 rpm. For biodiesel mixed with 15% ethanol, there was a 0.86% increase in torque at 1800 rpm compared to diesel, and a decrease of 0.42% in power at 2600 rpm. The emission values resulting from the combustion of biodiesel and ethanol blended fuels have decreased considerably compared to the use of diesel fuel. Thus, emissions harmful to humans and the environment, especially carbon dioxide emissions that cause global warming, have decreased significantly.

**Keywords:** ethanol, microalgae, biodiesel, chlorella protothecoides, methyl ester.

### SEMBOLLER

TSE	: Türk Standartları Enstitüsü	C <sub>2</sub> H <sub>5</sub> OH	: Etanol
EN	: Avrupa Birliği Standartları	EGS	: Egzoz Gazı Sıcaklığı
ISO	: Uluslararası Standart Organizasyonu	ÖYT	: Özgül Yakıt Tüketimi
BG	: Beygir güç	HC	: Hidrokarbon
NaOH	: Sodyum Hidroksit	CO	: Karbonmonoksit
KOH	: Potasyum Hidroksit	CO <sub>2</sub>	: Karbondioksit
NaOCH <sub>3</sub>	: Sodyum Metilat	O <sub>2</sub>	: Oksijen
		IAK	: Işık Absorban Katsayısı

## GİRİŞ

Dünya genelinde fosil yakıtlarının ciddi miktardaki azalışıyla beraber ani ve olağan fiyat değişimleri yeni ve yenilenebilir enerji kaynak arayış çalışmalarına yönlendirmektedir. Genellikle taşıma araçlarında kullanılan enerjilerin günden güne azalmasına karşılık alternatif çözümler gerekmektedir. Hibrit ve elektrikli araçların verimli kullanımını yaygınlaştırma ve geliştirme çalışmalarıyla birlikte, petrol kullanan araçlarda kompleks değişikliklere gidilmeden kullanılabilir uygulamalar bulunmaktadır. En yaygın uygulama olan biyodizel yakıtı; yağlardan elde edilmektedir. Bu bağlamda, yakın geçmişin yağ keşfi olan mikroalglerden elde edilen ve temel gıda olarak kullanılmayan bu yağ ile ilgili çalışmalar büyük önem arz etmektedir (Çakmak ve Özcan, 2021; Yeşilyurt vd, 2018). Mikroalglerin yüksek oranda yağ içeriğinden dolayı verimli biyoyakıt üretimleri sağlanabilmektedir. Ekonomik ve yenilenebilir oluşundan dolayı enerji kaynağı olarak kullanılabilmesi için pek çok çalışmalar yapılmaktadır (Pandey vd, 2014; Chisti, 2007).

Birçok bitki türlerinden farklı olarak mikroalgler doğal koşullarda suda ve karada yaşayabilirler. Kolay, hızlı üreyebilen ve fotosentez yapan pek çok çeşitli türleri bulunmaktadır. Mikroalgleri üretmek için ekin toprakları ve tatlı sular gibi özel ortamlar gerekmemektedir (Harun vd, 2011; Nagarajan vd, 2017). Ortalama hasat miktarı yüksek verimli olup küçük ölçekli optimum alanlarda büyük hacimde yetiştirilmektedir (Mota vd, 2022; Oni vd, 2022).

Mikroalglerin en cazip olan özelliklerinden biri ise yağ olarak depo edebilen, sentez sonucu oluşan ürünleridir (Ianda vd, 2022; Rajak vd, 2022). Mikroalgler dizel motorlarda organik nitelik taşıyan ve çevreye duyarlı biyoyakıt olarak kullanılabilir (Chhandama vd, 2021; Oni vd, 2021). %90'dan fazla yağ elde edilebilen mikroalgler, fotobiyoreaktör veya küçük arazilerde üretilebilmesi önemli bir hammadde potansiyeli oluşturmaktadır. Bu bağlamda çoğu bitkiden daha verimli biyoyakıt üretilme yeteneğine sahiptir (Rajak vd, 2022; Ge vd, 2022; Li vd, 2022). Mikroalg kullanımı posa artığı oluşturmamaktadır.

Gıda, ek takviye ürün, gübreleme ve kozmetik gibi endüstrilerde de kullanılmaktadır (Ganesan vd, 2022). Ayrıca klorofil taşıyan mikroalgler, fotosentez ile yüksek oranda CO<sub>2</sub> kullanarak küresel ısınmayı ve karbon ayak izi atıklarını önlemede büyük ölçekte destek olmaktadır (Jakob vd, 2022; Viguera vd, 2016; Farooq vd, 2022).

Biyoyakıtlar, hammadde olarak pek çok doğal yağların transesterifikasyon ile reaksiyonu sonucunda üretilen, yenilenebilir bir yakıt çeşididir (Rasim vd, 2015; İlkılıç vd, 2011; Wong vd, 2022). Ev tipi ve endüstriyel atık

yağların geri dönüşümünden de büyük ölçekte üretilmektedir (Kass vd, 2022; Karthikeyan ve Prathima, 2016). Önemli bir değişikliğe gidilmeden direkt olarak biyodizel ya da dizel-biyodizel karışımları kullanılmaktadır (Wu vd, 2019; Kontses vd, 2019; Lebedevas vd, 2021; Ushakov ve Lefebvre, 2019).

Etanol, bitkilerden elde edilen alkol çeşidi olup kimyasal formülü C<sub>2</sub>H<sub>5</sub>OH'tır (Ladanai ve Vinterback, 2009; Yılmaz ve Sanchez, 2012). Ulaştırma endüstrisinde de kullanılan etanolün, yakıt karışımlarına eklenebilmesi için en az %99.5 saflıkta, sudan uzaklaştırılmış olarak kullanılması gerekmektedir (Kwanchareon vd, 2007; Lui vd, 2016).

Biyoyakıtlar günümüz ve yakın gelecek için büyük avantaj sağlamaktadır (Hussan vd, 2013; Jafari vd, 2021). Biyodizel çalışmalarında termik verimliliğin yüksek olması da önem arz etmektedir (Çelik vd, 2016; Şahin ve Durgun, 2016). Biyoyakıtların sorunsuz bir şekilde verimli çalışması için yanma parametreleri üzerine pek çok çalışma yapılmaktadır (Gongora vd, 2022; Yesilyurt vd, 2020, Jacob vd, 2007, Alkidas, 2007).

Biyoyakıt kullanım oranının artırılması, petrol tüketimi ve çevre kirletici gazları azaltıcı etkisiyle hibrit motor geçiş süreci planlamasında büyük önem arz etmektedir.

Bu çalışma ile ülkemizin petrol kullanım ihtiyacını ve dışa bağımlılığı azaltacak çevre dostu yerli üretimi desteklemek hedeflenmiştir. Mevcut dizel motorlarında tasarımsal bir değişiklik yapılmadan mikroalglerin yakıt olarak kullanılması ve TS EN 14214 standardında biyoyakıt üretilip ve belirli oranlarda etanol ile karışımlarının bir dizel motorda kullanılabilirliği araştırılmıştır.

## MATERYAL VE METOD

Bu bölümde mikroalglerden yüksek verimli biyoyakıtı geliştirmek için kullanılan üretim yöntemi ve prosesinden bahsedilmiştir. Ayrıca mikroalg biyoyakıtının uygunluğu ve değerlerinin tespiti için yapılan akredite analiz deney sonuçları yer almaktadır. Son ürün olan biyoyakıt ile (ve) biyoetanol karışım yakıtlarının, egzoz emisyon deneyleri ve motor performans ölçümlerinde kullanılan test düzeneği yer almaktadır. Bu çalışmada mikroalg türü olan *Chlorella protothecoides*'lerden (Heterotrofik) elde edilen yağdan transesterifikasyon yöntemi kullanılarak biyoyakıt üretilmiştir. Mikroalg yağının yağ asidi profili Tablo 1'de verilmiştir. Palmitik yağ asidi oranının yüksek oluşu metil ester üretiminin kapasitif verimliliğine işaret etmiştir. Su barındırmayan alkali katalizör ve metanol kullanılarak transesterifikasyon reaksiyonu Şekil 1'de gösterilen düzenek ile gerçekleştirilmiştir. Mikroalg yağından elde edilen biyoyakıt eldesi ester oranını arttırmak amacıyla

çeşitli varyasyon numuneleri analiz edilmiştir. Yüksek verimli transesterifikasyon reçetesi ar-ge laboratuvarlarında geliştirilerek son ürün biyoyakıt üretimi gerçekleştirilmiştir.

**Tablo 1.** Mikroalg yağ asit profili

Yağ Asidi Profili (%)			
Yağ Asidi	C Bileşimi	Kimyasal Formülü	Yüzdesel Oranı (%)
Stearik	C 18:0	C <sub>18</sub> H <sub>36</sub> O <sub>2</sub>	2
Palmitik	C 16:0	C <sub>16</sub> H <sub>32</sub> O <sub>2</sub>	51
Diğer	-	-	1
Oleik	C 18:1	C <sub>18</sub> H <sub>34</sub> O <sub>2</sub>	39
Linoleik	C 18:2	C <sub>18</sub> H <sub>32</sub> O <sub>2</sub>	7



**Şekil 1.** Transesterifikasyon düzeneği

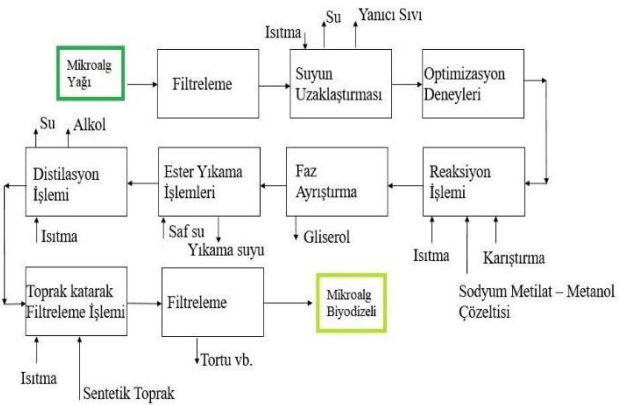
Bu çalışmada kullanılan mikroalg yağının özellikleri Tablo 2'de gösterilmiştir.

**Tablo 2.** Mikroalg yağ özellikleri

Organik Kaynak:		
Chlorella protothecoides / Heterotrofik Mikroalgler		
Yetiştirme Yöntemi:		
Yüksek Teknoloji Piramid Fotobiyoreaktörü		
Özellikler	Yağ Değerleri	Birimi
Viskozite	3,6	mm <sup>2</sup> /s
Isıl Değer	45.8	MJ/kg
Su	140	mg/kg
İyot	67	mg. iyot/100g
Karbon Kalıntısı	0,1	%(m/m)
Fosfor	0,0008	%(mg/kg)
Asit Sayısı	0,2	mg KOH/g
Sülfür	2	mg/kg
Renk	Yeşilimtrak / Açık Sarı	-
Görünüş	Berrak	-
Yoğunluk	912	kg/m <sup>3</sup>
Özgül ağırlık	0,91 – 0,92	-

Toplam Kirlilik	2	mg/kg
Peroksit Değeri	0,5	-
Parlama Noktası	220	°C

Endüstriyel ve de geleneksel katalizörlerden olan, zor çözülen sodyum hidroksit (NaOH) ve diğer taraftan daha fazla oranda potasyum hidroksit (KOH) kullanımı çeşitli maliyetler ve sorunlar içermektedir. Gaz kromatografisi analizlerinde ester sayısı sonuçlarının yüksek çıkması farklı bir katalizör olan sodyum metilatı (NaOCH<sub>3</sub>) cazip hale getirmiştir. NaOCH<sub>3</sub> kullanılmasıyla faz ayrılma süresi yaklaşık olarak %80 oranında azalmıştır. Yapılan ön deneylerde en uygun yağ/alkol oranı, reaksiyon sıcaklığı, süresi ve katalizör oranı tespiti ile son ürün biyoyakıt üretimi gerçekleştirilmiştir. Mikroalglerden biyodizel üretimi Şekil 2'deki aşamalara göre yapılmıştır.



**Şekil 2.** Biyodizel üretim akış şeması

Filtrasyon işleminde kullanılan kil toprak adımı, çeşitli safsızlıkları (büyük hücreli yağ asitleri, aromatik bileşikler vb.) gözeneklerinde absorban edebilme yeteneği sayesinde geleneksel biyodizel üretim akışına dahil edilmiştir. Transesterifikasyon işleminin uygulama literatürüne ve endüstriye, verimli biyodizel eldesi için katkı sağlayacak bu adım Şekil 3'te gösterilen distilasyon işleminden hemen sonra %0.3 oranda katılmıştır. Bu adımla yakıt berraklaşmış olup metil ester oranı iyileştirilmiş ve temiz yakıtın saflığı artırılmıştır.

TSE standart deney metotlarına göre; ester içeriği, iyot ve asit sayısı tayini, sabun ve su tayini, yoğunluk ve viskozite tayini, setan sayısı, kirlilik ve parlama noktası tayinleri, soğuk filtre tıkanma noktasının tayini (SFTN), akma-bulutlanma noktası tayini, ısıl değer ve bakır şerit korozyon standart deney metotları uygulanmış ve akredite sonuçlar elde edilmiştir.





(a) (b)

Şekil 3. (a) Kil toprak eklenmesi, (b) Aktif metil esterleşme

Motor performans ve emisyon testleri TS1231 ve TS ISO 3930 standartları içeriğine göre deney düzeneği kurulmuştur. Elektrikli dinamometre kullanılarak bilgisayar kontrollünde motor testleri gerçekleştirilmiştir. Tek silindirli dizel motorun stabil çalışma sıcaklık aralığına ulaşması için dizel yakıtı kullanılmıştır. Deney yakıtlarının tam yükte 400 devir artırılarak 1000-3000 d/dk'da emisyon ve performans etkileri incelenmiştir.

Motor testlerinde, torku 83 Nm, maksimum gücü 26 kW ve maksimum devri 5000 d/dk olan T-T Elektric marka dinamometre kullanılmıştır. Motor testleri standart kapsamında tolerans belirsizlikleri aralığında gerçekleşmiştir. Hata payına göre çoklu tekrarlanmıştır. Bu kapsamda, tekrarlı testler sonuçlarının aritmetik ortalamaları alınmıştır. M100 yakıtı, mikroalg yağından elde edilen saf biyoyakıtı temsil etmektedir. %99,8 saflıkta, hacimsel olarak %5, %10 ve %15 oranlarında etanol ile karıştırılmıştır. Deneyde kullanılan yakıtlar Tablo 3'te gösterilmiştir.

Tablo 3. Mikroalg biyoyakıtı ve karışım yüzdeleri

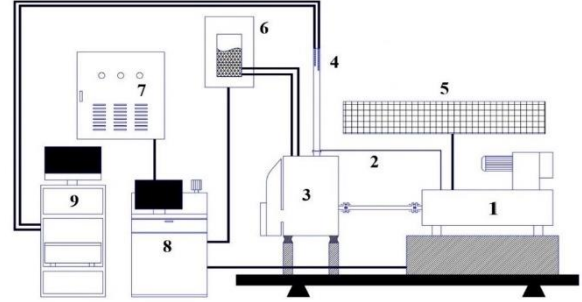
Yakıtlar	Mikroalg Biyodizel Oranı	Etanol Oranı	Dizel Yakıt Oranı
M100	%100	-	-
ME15	%85	%15	-
ME10	%90	%10	-
ME5	%95	%5	-
Dizel	-	-	%100

Tablo 4. Yakıtların termo-fiziksel özellikleri

Özellikler	Dizel	Etanol	M100	ME5	ME10	ME15
Saflık (% v/v)	-	>99,8	98,9	98,94	99	99,05
Setan Sayısı	min 51	13	57,3	56,1	55,8	54,7
Isıl Değer (MJ/kg)	42,7	29,7	40,9	40,7	40,5	40,2
Yoğunluk 15°C'de (kg/m3)	820-845	789	880	877,1	874,2	871,4
Viskozite 40 °C'de (mm <sup>2</sup> /s)	2-4,5	1,13	4,35	4,024	3,698	3,378

Deney yakıtlarının özellikleri TSE EN 14214 standartlarına uygun aralıklarda olup mikroalg biyoyakıtı ve mikroalg-etanol karışımıyla elde edilen yakıtların termo-fiziksel özellikleri Tablo 4'te sunulmuştur.

Test düzeneğinin Şekil 4'te şematik görünümü verilmiştir.



Şekil 4. Deney düzeneği şematik görünüm

Şekil 4'teki şematik görünümde sırasıyla; Dinamometre, EGS ölçer, Dizel motor, Emisyon ölçüm probrları, Rezistans, Yakıt haznesi, Güç ünitesi, Test ve ölçüm kontrol ünitesi, Emisyon test cihazı yer almaktadır.

Yapılan motor performans testlerinde güç ve tork, ayrıca özgül yakıt tüketimi, EGS (egzoz gazı sıcaklığı) kontrol panelinde anlık olarak hesaplanmıştır. Emisyonları testlerinde HC, CO, CO<sub>2</sub>, IAK (ışık absorban katsayısı) ve is yoğunluğu ölçülmüştür.

Tek silindirli dizel motoru olan Antor Lombardini 4 LD 640 deney motorunda testler yapılmıştır (İnternet 1, 2022). Test düzeneğinde kullanılan tek silindirli dizel motorun teknik spesifikasyonları Tablo 5'te listelenmiştir.

**Tablo 5.** Motorun teknik özellikleri

Özellik	Değer
Sıkıştırma oranı	17:1
Maksimum güç	13 BG
Soğutma sistemi	Hava Soğutmalı
Silindir hacmi	638 cm <sup>3</sup>
Maksimum motor devri	3000 d/dk
Püskürtme sistemi	Direkt
Çap x Strok	95 x 90 mm
Silindir sayısı	1
Maksimum tork (1800 d/dk)	3,5 Kg.m

Egzoz gazları emisyonları için TS ISO 3930 standardına göre kalibreli Mobydic 5000 cihazı kullanılmıştır (İnternet 2, 2022). Bu cihazın teknik özellikleri Tablo 6'da sunulmuştur. Egzoz gazı sıcaklık değişimlerini belirlemek amacıyla motorun egzoz çıkışı ile egzoz tahliye bağlantı arasına bir ısı çift bağlanmıştır.

**Tablo 6.** Egzoz gazı emisyon test cihazı teknik özellikleri

Ölçüm	Birim	Ölçüm Değerleri	Hassasiyet
HC	ppm	0-20000	1
CO	% Vol	0-10	0.02
CO <sub>2</sub>	% Vol	0-20	0.02
Partikül	mg/m <sup>3</sup>	0-1000	0.01
IAK	1/m	0-20	0.01

Deneylerde net kalibrasyon, çevre şartları, gözlem, veri işleme ve çoklu test cihazlarından dolayı çeşitli hatalar ve genel bariz belirsizlikler olmaktadır. Bu nedenle, bu çalışmada Holman (2012) tarafından önerilen belirsizlik analizi kullanılmıştır. Tablo 7'de belirsizlik analizi sonuçları görülmektedir.

**Tablo 7.** Hesaplanan sonuçların belirsizlikleri

Hesaplanan değerler	Birim	Belirsizlik (%)
Motor Torku	Nm	±1.64
Motor Gücü	kW	±1.8
Yakıt Tüketimi	g/s	±1.6
Özgül Yakıt Tüketimi	g/kWh	±2
Dinamometre - Yük	g	±1.15
Süre	s	±0.5
Devir Göstergesi	rpm	±5
Egzoz gazı sıcaklığı	°C	±2
İs koyuluğu	1/m	±0.1
CO	ppm	±2
CO <sub>2</sub>	%	±4
HC	ppm	±2

Bu tablodaki belirtilen sonuçlara göre, deney düzeneğinin genel belirsizliği ±%2.1-2.6 kayıplar aralığında hesaplanmıştır. Test belirsizliği için kabul edilebilir olup, sistemin genel belirsizliği de kabul edilebilir sınıır içerisinde.

## BULGULAR VE TARTIŞMA

Elde edilen biyoyakıtın, gerçek anlamda verimli bir biyodizel oluşunun tespiti için metil ester tayini yapılmaktadır. Bu bağlamda mikroalg biyoyakıtı Petrol Analiz Laboratuvarında TSE EN 14214 standardına akredite uygunluğu onaylanmıştır.

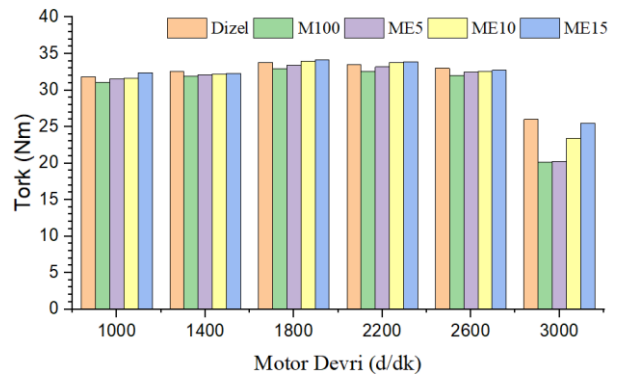
Mikroalg biyoyakıtının sonuç raporu Tablo 8'de verilmiştir. Bu çalışmada geliştirilen reçetenin, biyoyakıtın %98.9 gibi yüksek verimli ester içeriğine sahip oluşu yeni yapılacak ve geliştirilecek benzer çalışmalar adına literatüre önemli bir katkı sağlamıştır.

Ayrıca deney yakıtlarının yanması sonucu ortaya çıkan emisyonlar ve egzoz gazı sıcaklıkları ölçülmüştür. Test sonuçları çoklu yapılan testlerin aritmetik ortalaması alınarak elde edilmiştir.

Bütün deney yakıtları kullanımında 1800 d/dk'da maksimum tork noktasına varılmıştır. Tam yükte farklı devirlerde motor torku Şekil 5'te verilmiştir. Bu devirde maksimum tork %85 mikroalg biyodizel + %15 etil alkol olan ME15 yakıtında 33.8 Nm ölçülürken dizel yakıt için motor torku 34.2 Nm ölçülmüştür.

Motor devirlerinde elde edilen motor torku değerlerinin ortalaması alındığında dizele göre M100 kullanımında %4.6, ME5 yakıtında %3.7 ve ME15 kullanımında %0.8, ME15'de %0.86 azalış ölçülmüştür.

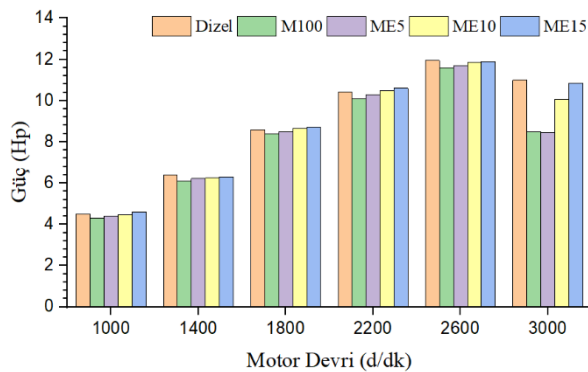
Motor devrinin 2600 d/dk'dan 3000 d/dk'ya çıkmasıyla mekanik verim değişimi meydana gelmektedir. Sürtünme kayıplarının artması ve volümetrik verimin azalması ile torkta düşüş olmaktadır. Bu düşüş dizele göre daha yüksek viskoziteye sahip olan mikroalg biyodizeli için daha fazla olmuştur. Mikroalg biyoyakıtına etanol ilave edilmesiyle yakıtın viskozitesinin azalmaktadır. Dolayısıyla motor devri 2600 d/dk'dan 3000 d/dk'ya çıktığında motor torkundaki düşüş azalmaktadır.

**Şekil 5.** Tam yükte motor torku değişimleri

**Tablo 8.** Mikroalg biyodizeli TS EN 14214 analiz sonuçları

Özellik	Kullanılan DeneY Yöntemi	Sınır Değerleri TS EN 14214		Ölçüm Değeri	Birim
		En az	En çok		
Ester içeriđi	TS EN 14103	96.5	-	<b>98.9</b>	% (m/m)
Viskozite (40°C)	TS 1451 EN ISO 3104	3.5	5	<b>4.35</b>	mm <sup>2</sup> /s
Yođunluk (15°C)	TS EN ISO 12185	860	900	<b>880</b>	kg/m <sup>3</sup>
Akma Noktası	TS 1233 ISO 3016	-	-	<b>-18</b>	°C
Isıl Deđer	TS 1740	35	-	<b>40.9</b>	MJ/kg
Toplam Kirlilik	TS EN 12662	-	24	<b>4.2</b>	mg/kg
Parlama noktası	TS EN ISO 3679	101	-	<b>182</b>	°C
Su içeriđi	TS 6147 EN ISO 12937	-	500	<b>182.76</b>	mg/kg
Setan Sayısı	TS EN 15195	51	-	<b>57.2</b>	-
Asit sayısı	TS EN 14104	-	0.5	<b>0.21</b>	mg KOH/g
İyot sayısı	TS EN 14111	-	120	<b>103</b>	g. iyot/100 g
Sabun Tayini	TS 5038	-	-	<b>0</b>	≈ % (m/m)
Bulutlanma Noktası	TS 2834 EN 23015	-	-	<b>-11</b>	°C
SFTN	TS EN 116	-	+5 Yaz -15 Kış	<b>-16</b>	°C
Bakır şerit korozyonu	TS 2741 EN ISO 2160	Sınıf 1		<b>1A</b>	Derece

Motor gücü Şekil 6'da gösterilen motor torku, dizel yakıtına kıyasla mikroalg biyoyakıtı, ME5 ve ME10 yakıtları için azalırken, ME15 yakıt kullanımında ise yakın sonuçlar gözlemlenmiştir.

**Şekil 6.** Tam yükte motor gücü değışimleri

Etanol oranı biyoyakıt karışımında arttıkça güç değerleri artmıştır. DeneY yakıtları için en yüksek motor güçleri 2600 d/dk'da elde edilmiştir. Bu devirde deneY yakıtları için elde edilen güç değerleri ME15'te 11.9 BG ortalamasında iken; ME10 yakıt karışımı kullanımında 11.87 BG ölçülmüştür. Yakıt ME5 yakıtı kullanımında 11.7 BG ve M100 deneY yakıtında ise 11.6 BG'dir. Dizel kullanımında bu durum 11.95 BG'dir.

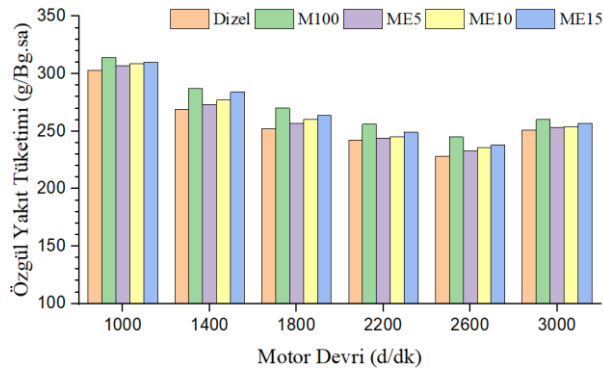
Dizele göre M100 biyoyakıtının düşük ısıl değeri ve yüksek viskozitesinden dolayı yanma kötüleştirmiştir. Yüksek saflığa sahip etanol katılması karışımın parlama noktasını ve ısıl değeri azaltmıştır. Bu duruma karşılık, yakıt karışımında etanol miktarı artıkça yoğunluk ve viskozite azaldığından iyi bir atomizasyon elde edilmekte olup ve buna bađlı olarak enjektörden daha verimli püskürtme sağlanabilmektedir (Zaharin vd, 2017; Gongora vd, 2022).

Yüksek setan sayısına sahip biyoyakıtta etanol ilave edilerek setan sayısı azalmış ve tutuşma gecikme süresi ise artmıştır. Bu ilaveyle viskozite azaltılarak atomizasyonda iyileşme ve elde edilen homojenize karışım sağlanmıştır.

Karışımındaki oksijen zenginliği ile tutuşma gecikmesi kısalmıştır. Ayrıca bu sayede yanma verimi artırılmış ve güç artışı sağlanmıştır.

Motor gücü, karışımının oranlarına bağlı olarak etanol ilavesiyle dizel kullanımdaki efektif güce yaklaşmıştır (Jafari vd, 2021; Zafarin vd, 2017; Wong vd, 2022). Motorun tam yükte ve 1000-3000 d/dk'da özgül yakıt tüketimleri Şekil 7'de görülmektedir. Deney devir aralığında M100 yakıtının 1000 d/dk'da özgül yakıt tüketimi (ÖYT) 314 g/BG.h olmuştur. 2600 d/dk'da tüm yakıtlar için ÖYT en az seviyelere ulaşmıştır.

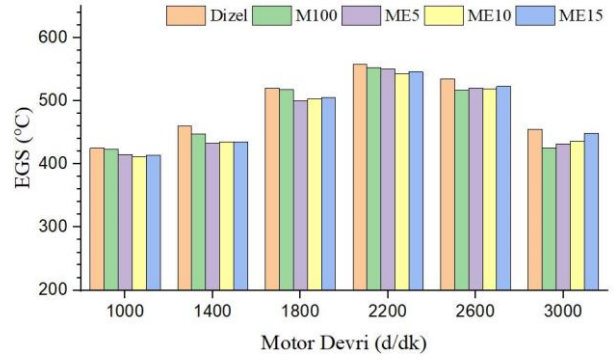
Motor deney devirlerinde elde edilen özgül yakıt tüketimleri dizele göre M100'de %5.6, ME5 yakıtında %2.46, Yakıt ME10'da %3.1 ve ME15 kullanımında ise %3.7 fazladır. Mikroalg biyodizeline etanol ilavesi ile ısıl değerine karşılık yakıtın viskozitesi iyileşmiştir (Noorollahi vd, 2018; Neel vd, 2008). Özgül yakıt tüketimi motorun devrine ve etanol oranına bağlı olarak değişmektedir.



Şekil 7. Özgül yakıt tüketimi

Artan motor devrine bağlı olarak egzoz gazı sıcaklığında artış olmakta ve 2200 d/dk'dan sonra da sıcaklık düşmektedir. Maksimum egzoz gazı sıcaklığı dizel kullanımında 558 °C, en düşük sıcaklık ise M100 için 426 °C 3000 d/dk'da ölçülmüştür.

Saf mikroalg biyodizeline etanol eklenerek elde edilen yakıt karışımlarının oksijen yoğunluğunun zengin olmasından dolayı tutuşma gecikmesi süresi kısılırken, termal verimi artmıştır (Al-lwayzy ve Yusaf, 2017). Şekil 8'de egzoz gazı sıcaklık değişimleri verilmiştir.



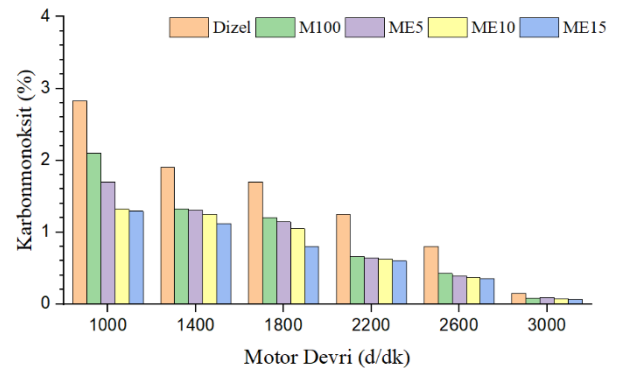
Şekil 8. Egzoz gazı sıcaklık değişimleri

Kısmi yanma sonucu oluşan, canlıya ve çevreye zararlı olan karbonmonoksit (CO) emisyonlarının değişimleri Şekil 9'da verilmiştir.

Hidrokarbonların (HC) oksijenle (O<sub>2</sub>) oksidasyonu yeterli seviyede olmayınca tam yanma olmamakta ve CO emisyonu oluşmaktadır (Zui vd, 2011; Ushakov ve Lefebvre, 2017). CO oluşumunun en önemli nedeni hava-yakıt karışımının yeteri düzeyde homojen olmaması veya bölgesel farklılıkların kısmi yanmaya sebep olmasından dolayı olduğu bilinmektedir. Fakir karışimli yanmalarda ise CO miktarı az olmaktadır (Rajak vd, 2022; Subbaiah vd, 2010).

Maksimum torkun elde edildiği devirde dizele göre CO emisyonlarında M100 için %30 Yakıt ME5'te %32.5, ME10'te %42 ve ME15 yakıtında %52 oranlarında azalma meydana gelmiştir.

Mikroalg biyodizelin moleküler yapısında oksijen bulunması ve setan sayısı verimli bir yanmaya işaret etmiş, dizel yakıtına göre CO emisyonlarında düşüşe neden olmuştur. Etanol bünyesinde daha fazla oksijen içermesi ve daha az karbon bulunmasından dolayı, karışımda etanol oranı artıkça CO emisyonlarında azalma olmuştur.



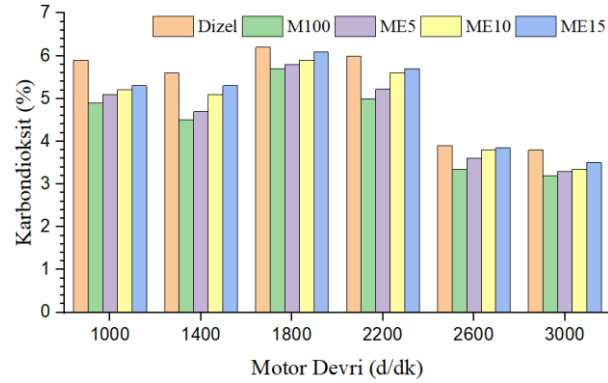
Şekil 9. CO emisyon değişimleri

Hidrokarbonların tam yanmasıyla birlikte karbondioksit (CO<sub>2</sub>) gazı oluşmaktadır. Karbondioksit gazının atmosferde belli bir seviyeden fazla olması sera etkisi gösterdiğinden küresel ısınmaya sebep olarak iklim

değişimi üzerinde büyük bir etkiye sebep olmaktadır (Oni vd, 2021; Viguera vd, 2016).

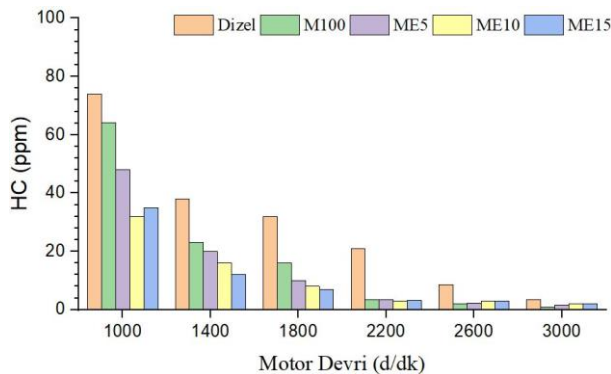
Motor testlerinde kullanılan deney yakıtlarının CO<sub>2</sub> emisyon değişimleri Şekil 10'daki grafikte gösterilmiştir. Her test devrinde M100 ve etanol katkılı karışımlar için karbondioksit emisyonları dizel yakıtı kıyasla düşük çıkmıştır. Mikroalg biyodizeli kullanımında CO<sub>2</sub> emisyonları önemli derecede düşüş olsa da etanol ilavesi ile CO<sub>2</sub> emisyonları artmıştır (Farooq vd, 2022). Ancak bu artışa rağmen etanol katkılı biyodizelin karbondioksit emisyonları dizel yakıtın emisyon değerlerinden kıyasla daha düşük sonuçlar vermiştir.

Mikroalg biyodizeli %98.9 metil esterinde yaklaşık ağırlıkça %71 karbon, %12 hidrojen ve %17 oksijen bulunmaktadır. Dizel ise yaklaşık %85 ve üssü karbon içeriğine sahiptir. Deney yakıtların kullanılmasıyla dizel yakıtı kıyasla mikroalg biyodizelinde daha az CO ve CO<sub>2</sub> emisyonları oluşmuştur.



Şekil 10. CO<sub>2</sub> emisyon değişimleri

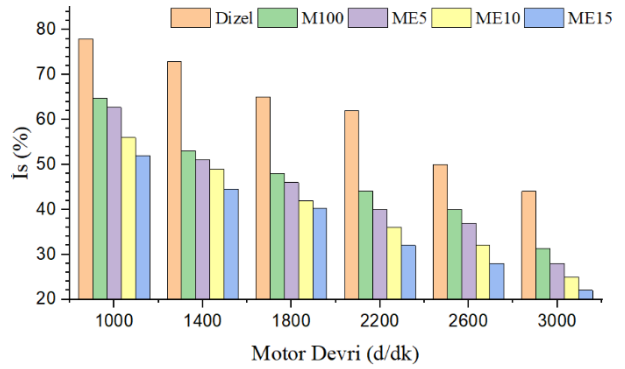
Silindirde hava-yakıt oranının bölgesel olarak yer yer fakir ve zengin olmasından dolayı oksidasyon reaksiyonu yavaşlamakta dolayısıyla yanma tamamlanmamaktadır (Jacob vd, 2022; Ge vd, 2022). Silindir ve piston arasında oluşan alevin aniden sönmesi ve ısı kayıpları hidrokarbon emisyonlarının oluşmasına sebep olmaktadır (Makareviciene vd, 2014; Wahlen vd, 2013). Hidrokarbonların egzoz gazı emisyon oranlarının grafiği Şekil 11'de gösterilmiştir.



Şekil 11. HC emisyon oranları grafiği

Daha düşük motor devirlerinde HC emisyonları fazla iken, artan motor devriyle beraber bu emisyonlar da azalmaktadır. HC emisyonlarının mikroalg ve mikroalg-etanol karışımlarında önemli derecede azaldığı görülmektedir (Jacob vd, 2022; Ge vd, 2022).

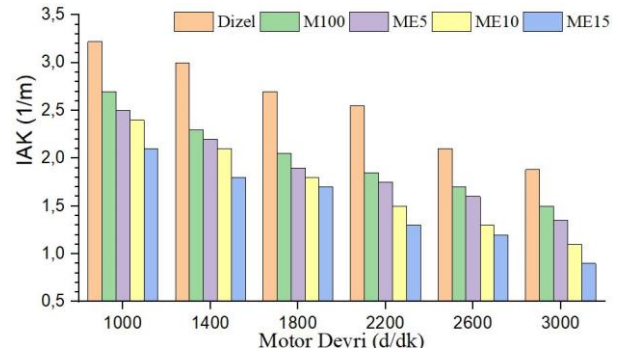
İs emisyonları; partiküller, yakıt karbon artıkları, sülfür, aromatik bileşikler ve hidrokarbonlardan oluşmaktadır (Satputaley vd, 2017). Şekil 12'de is değerleri görülmektedir. Mikroalg biyoyakıtı ve etanol yakıt karışımlarında O<sub>2</sub> miktarının artmasından dolayı is oluşumu büyük ölçüde azalmıştır. İs emisyonları motor devrinin artmasıyla azalmıştır.



Şekil 12. İs emisyonu

İs emisyonları, maksimum torkun elde edildiği devirde M100 için %23.6, Yakıt ME5'te %28.3, ME10 karışımında %34.6 ve ME15 yakıtında %37.5 oranında dizel'e göre azalmıştır. 2600 d/dk ise bu azalma M100, ME5, ME10 ve ME15 için sırasıyla %20.5, %26, %36.5 ve %44.2 olmuştur.

IAK (Işık absorpsiyon katsayısı) ise emisyonların aydınlatma şiddetini azaltan bir katsayıdır. Emisyonların mikroalg biyodizel yakıtlarda önemli derecede düşmesinden dolayı dizel yakıtı kıyasla düşüktür (Zhu vd, 2010; Wong vd, 2022). Devire bağlı ışık absorpsiyon katsayısı Şekil 13'te verilmiştir.



Şekil 13. Işık absorpsiyon katsayısı değerleri

## SONUÇLAR

Mikroalgler, ekim yapılan verimli tarım alanlarını işgal etmemesi, büyüme hızı ve hammaddeden yağ elde oranının çok yüksek olmasından dolayı biyodizel olarak kullanımına en uygun ürün olarak nitelendirilmektedir. Bu çalışmada tam yükte farklı motor devirlerinde mikroalg, mikroalg-etanol biyoyakıt kullanımı ile motor torku, gücü ve emisyon değerleri ölçülmüştür. Bu bağlamda önemli sonuçlar aşağıda verilmiştir.

Transesterifikasyon işleminde yüksek verimli bir esterleşme sonucunda sodyum metilatın kullanılmasıyla faz ayrılma süresi yaklaşık %80 oranında azaltılmıştır.

Geleneksel katalizör kullanımı yerine sodyum metilat kullanılması ve gözenekli kil toprak ilavesi ile filtre işlemi, bu çalışmada önemli ölçüde enerji sarfiyatı ve proses süresini azaltmasıyla endüstriye önemli bir çözüm sunmaktadır.

*Chlorella protothecoides* mikroalg yağından iyileştirilmiş ve geliştirilmiş transesterifikasyon sonucunda yağın %99'dan fazla biyodizel elde edilmiştir. "0 Atık" ürün olan mikroalg posası da kozmetik, temizlik, gıda, tarım toprak besini, ek gıda takviyesi sektöründe de kullanılmaktadır.

TSE Petrol Analiz Laboratuvarında EN 14214 standardına akredite uygunluğu onaylanmıştır. Yapılan benzer çalışmalara kıyasla, bu çalışmada geliştirilen reçetenin, biyoyakıtın %98.9 gibi yüksek verimli ester içeriğine sahip oluşu literatüre önemli bir katkı sağlamıştır. Mikroalg biyodizelinin dizel yakıtı göre setan sayısı ve yoğunluğu artarken, ısıl değer ve viskozitesi düşmüştür. Mikroalg biyodizelinde yoğunluk ve viskozitenin artmasıyla püskürtme kayıpları artmaktadır.

Mikroalg biyoyakıtına etanol katılmasıyla yakıtın oksijen içeriği artarken setan sayısı, yoğunluğu, ısıl değeri ve viskozitesi düşmüştür; fakat viskozite düşüşü ile yakıtın atomizasyonu sağlamış olup, püskürtme penetrasyonu ve dispersiyonu iyileşmiştir. Dizele kıyasla mikroalg biyoyakıtı ile CO, CO<sub>2</sub> ve HC emisyonlarında azalış olmaktadır. Mikroalg biyodizeline etanol ilavesi bu emisyonların azalmasında olumlu katkı sağlamıştır.

Mikroalg biyodizelinin yanması sonucu ortaya çıkan is emisyonu dolayısıyla IAK değeri dizele göre azalmıştır. Bu azalış oranı M100'e etanol ilavesiyle artmaktadır.

Motor testlerinde en yüksek güç; dizel ve ME15 yakıtında olurken, M100 kullanımında dizele göre %2,81 daha düşük güç elde edilmiştir. Bu duruma rağmen fosil yakıtı önemli bir alternatif olmuştur. ME15 kullanımında maksimum motor gücünün elde edildiği

devirde dizel yakıt kullanımına göre motor gücü %0,67 daha düşük çıkarken, ME15 için elde edilen maksimum tork dizele göre çok benzerdir.

Mikroalg biyoyakıtına, etanol ilavesi ile motor gücü ve torkunda artış olmuştur. Bu durum aynı zamanda atık yağlardan elde edilen biyodizellere ek; mikroalg biyodizelinin, biyoetanol ve dizel yakıt karışımları ile de kullanılmasına teşvik etmiştir.

Mikroalg biyoyakıtı ve farklı oranlarda etanol karışımıyla elde edilen yakıtların farklı devirlerde yanması sonucu ortaya çıkan emisyon değerleri dizel yakıtı göre önemli oranda azalmıştır. Küresel ısınmaya sebep olan CO<sub>2</sub> emisyonlarında, maksimum motor torku ve gücün elde edildiği devirlerde M100 yakıtının dizel yakıtı göre sırasıyla %6 ve %15,5 oranında düşmüştür. Bu düşüş ME15 için %0,8 ve %2,7 olmuştur.

Sonuç olarak dizel yakıtı kıyasla ME15 yakıtı kullanımında ortalama tork değerleri benzer ve motor gücünde minimal kayıplar meydana gelmesine rağmen egzoz emisyon gazları ciddi oranlarda azalmıştır. Mikroalg biyoyakıtı ve biyoetanol karışımı kullanımının uygunluğu bu çalışma ile ülkemiz için önerilmiştir.

## TEŞEKKÜR

Gönenç DURAN, BİDEB 2210-C ve 2211 Bilim insanı destekleme programı kapsamındaki ilgi ve özenlerinden dolayı TÜBİTAK'a ve YÖK'e teşekkürlerini sunar.

## KAYNAKLAR

Alkidas A. C., 2007, Combustion advancements in gasoline engines, *Energy Conversion and Management*, 48, 2751-2761.

Al-lwayzy H. S. and Yusaf T., 2017, Diesel engine performance and exhaust gas emissions using microalgae *Chlorella protothecoides* biodiesel, *Renewable Energy*, 101, 690-701.

Sanni S., Ezurike B., Okoro E., 2022, Effect of corrosion rates of preheated *Schinzochytrium* sp. microalgae biodiesel on metallic components of a diesel engine, *Alexandria Engineering Journal*, 61, 7509-7528.

Behçet R., Oktay H., Çakmak A. and Aydın H., 2015, Comparison of exhaust emissions of biodiesel-diesel fuel blends produced from animal fats, *Renewable and Sustainable Energy Reviews*, 46,157–165.

Chhandama M., Satyan K., Changmai B., Vanlalveni C., Rokhum S., 2021, Microalgae as a feedstock for the

- production of biodiesel: A review, *Bioresource Technology Reports*, 15, 100771.
- Chisti Y., 2007, Biodiesel from microalgae, *Biotechnology Advances*, 25, 294-306.
- Çakmak A., Özcan H., 2021, Gliserin eterlerinin ikinci nesil biyoyakıt olarak dizel motorda kullanımının araştırılması, *J. of Thermal Science and Technology*, 41,2, 191–204.
- Çelik M., Solmaz H., Yücesu S. H., Yılmaz E., 2016, Kanola metil esterine n-heptan katkısının motor performansı ve yanma karakteristiklerine etkilerinin incelenmesi, *J. of Thermal Science and Technology*, 36,1, 9-16.
- Farooq W., Naqvi S., Sajid M., Shrivastav A., Kumar K., 2022, Monitoring lipids profile, CO<sub>2</sub> fixation, and water recyclability for the economic viability of microalgae *Chlorella vulgaris* cultivation at different initial nitrogen, *Journal of Biotechnology*, 345, 30–39.
- Ganesan A., Nawkarkar P., Kumar S., 2022, Chapter 17- Algal biodiesel: technology, hurdles, and future directions, Handbook of Biofuels, *Academic Press*, 331-351.
- Ge S., Brindhadevi K., Xia C., Khalifa A., Elfakhany A., Unpaprom Y., Doan H., 2022, Enhancement of the combustion, performance and emission characteristics of spirulina microalgae biodiesel blends using nanoparticles, *Fuel*, 308, 121822.
- Gongora B., Souza S. N., Bassegio D., Santos R. F., Siqueira J. A., Bariccatti R. A., Gurgacz F., Secco D., Tokura L. K., Sequinel R., 2022, Comparison of emissions and engine performance of safflower and commercial biodiesels, *Industrial Crops & Products*, 179, 114680.
- Harun R., Davidson M., Doyle M., Gopiraj R., Danquah M., and Forde G., 2011, Technoeconomic analysis of an integrated microalgae photobioreactor, biodiesel and biogas production facility, *Biomass and Bioenergy*, 35, 741-747.
- Hussan M. J., Hassan M. H., Kalam M. A., Memon L. A., 2013, Tailoring key fuel properties of diesel, biodiesel, ethanol blends for diesel engine, *Journal of Cleaner Production*, 51, 118-125.
- Holman P., 2012, Experimental methods for engineers, 8th Edition, *McGraw-Hill*, New York, USA.
- Ianda T., Kalid R., Rocha L., Padula A., Zimmerman W., 2022, Techno-economic modeling to produce biodiesel from marine microalgae in sub-Saharan countries: An exploratory study in Guinea-Bissau, *Biomass and Bioenergy*, 158, 106369.
- İlkilic C., Aydın S., Behcet R., Aydın H., 2011, Biodiesel from safflower oil and its application in a diesel engine, *Fuel Processing Technology*, 92:356-362.
- İnternet 1, 2022, Anadolu Motor, et:24.02.2022, <https://www.anadolumotor.com/tr/urunler/antor-4-ld-640>
- İnternet 2, 2022, Mobydic Egzoz Emisyon Cihazı, et:24.02.2022, <https://www.ozenektronik.com/egzoz-gaz-analiz-dizel-duman-test-cihazı-kombi-p.html>
- Jacob A., Ashok B., Usmand K., 2022, Production of *Chlorella pyrenoidosa* biodiesel by heterotrophic pathway to improve CI engine output characteristics using statistical approaches, *Process Safety and Environmental Protection*, 160, 478-490.
- Jacobs T. J., and Assanis D. N., 2007, The attainment of premixed compression ignition low-temperature combustion in a compression ignition direct injection engine, *Proceedings of the Combustion Institute*, 31, 2913-2920.
- Jafari A., Esmaeilzadeh F., Mowla D., Sadatshojaei E., Heidari S., Wood D. A., 2021, New insights to direct conversion of wet microalgae impregnated with ethanol to biodiesel exploiting extraction with supercritical carbon dioxide, *Fuel*, 285, 119199.
- Karthikeyan S., Prathima A., 2016, Emission analysis of the effect of doped nano additives on biofuel in a diesel engine, *Energy Sources, Part A: Recovery, Utilization, and Environmental Effects*, 1556-7230.
- Kass M., Kaul B., Armstrong B., Szybist J., Lobodin V., 2022, Stability, rheological and combustion properties of biodiesel blends with a very-low sulfur fuel oil (VLSFO), *Fuel*, 316, 123365.
- Kontsesa A., Dimaratos A., Keramidias C., Williams R., Hamjed H., Ntziachristosa L., Samarasa Z., 2019, Effects of fuel properties on particulate emissions of diesel cars equipped with diesel particulate filters, *Fuel*, 255, 115879.
- Kwanchareon P., Luengnaruemitchai A., Jai-In S., 2007, Solubility of a diesel-biodiesel-ethanol blend, its fuel

- properties, and its emission characteristics from diesel engine, *Fuel*, 86, 2007, 1053-1061.
- Ladanai S., Vinterback J., 2009, Global Potential of Sustainable Biomass for Energy, SLU Institutionen för energi och teknik report, *Swedish University of Agricultural Sciences Department of Energy and Technology*, 13, 1654-9406.
- Lebedevas S., Lazareva N., Rapalis P., Dauksys V., Cepaitis T., 2021, Influence of marine fuel properties on ignition injection delay and energy efficiency, *Vilnius Tech*, 36, 4: 339-353.
- Li S., Li X., Ho S., 2022, Microalgae as a solution of third world energy crisis for biofuels production from wastewater toward carbon neutrality: An updated review, *Chemosphere*, 291, 132863.
- Liu H., Hu B., Jin C., 2016, Effects of different alcohols additives on solubility of hydrous ethanol/diesel fuel blends, *Fuel*, 184, 440-448.
- Makareviciene V., Lebedevas S., Rapalis P., Gumbyte M., Skorupskaite V., Zaglinskis J., 2014, Performance and emission characteristics of diesel fuel containing microalgae oil methyl esters, *Fuel*, 120, 233-239.
- Mota G., Sousa I., Oliveira A., Cavalcante L., Moreira K., Cavalcante F., Souza J., Falcao I., Rocha T., Valerio R., Carvalho S., Neto C., Serpa J., Lima R., Souza M., Santos J., 2022, Biodiesel production from microalgae using lipase-based catalysts: Current challenges and prospects, *Algal Research*, 62, 20102616.
- Nagarajan R., Jain A., and Vora K., 2017, Biodiesel from Microalgae, *SAE Technical Paper*, 2017-26-0077.
- Neel C., Johnson D., Wardlow G., 2008, Performance, efficiency, and NO<sub>x</sub> emissions of a compact diesel tractor fueled with D2, B20, and B100 under steady-state loads, *Appl. Eng. Agric.*, 24, 717-721.
- Noorollahi Y., Azadbakht M., Ghobadian B., 2018, The effect of different diesterol (diesel -biodiesel-ethanol) blends on small air-cooled diesel engine performance and its exhaust gases, *Energy*, 142, 196-200.
- Oni B., Sanni S., Daramola M., Olawepo A., 2021, Effects of oxy-acetylation on performance, combustion and emission characteristics of *Botryococcus braunii* microalgae biodiesel-fuelled CI engines, *Fuel*, 296, 120675.
- Pandey A., Lee D. J., Chisti Y., Soccol C. R., 2014, Biofuels from Algae, *Elsevier*, 978-0-444-59558-4.
- Rajak U., Nashine P., Dasore A., Balijepalli R., Chaurasiya P., Verma T., 2022, Numerical analysis of performance and emission behavior of CI engine fueled with microalgae biodiesel blend, *Materials Today: Proceedings*, 49, 301-306.
- Rajak U., Nashine P., Dasore A., Verma T., 2022, Utilization of renewable and sustainable microalgae biodiesel for reducing the engine emissions in a diesel engine, *Fuel*, 311, 122498.
- Satputaley S. S., Zodpe D. B. and Deshpande N. V., 2017, Performance, combustion and emission study on CI engine using microalgae oil and microalgae oil methyl esters, *Journal of the Energy Institute*, 90, 513-521.
- Subbaiah G. V., Gopal K. R., Hussain S. A., Prasad B., and Reddy K. T., 2010, Rice bran oil biodiesel as an additive in diesel-ethanol blends for diesel engines, *Int. J. Res. Rev. Appl. Sci.*, 3, 334-342.
- Şahin Z., and Durgun O. J., 2016, Improving of diesel combustion-pollution-fuel economy and performance by ethanol fumigation, *J. of Thermal Science and Technology*, 36,2, 69-82.
- TSE, TS EN 116, 2015, Dizel yakıtlar ve konut ısıtmada kullanılan yakıtlar, soğuk filtre tıkanma noktasının tayini, *Türk Standartları Enstitüsü*, Ankara.
- TSE, TS EN 12662, 2009, Sıvı petrol ürünleri, orta destile yakıtlar, kirlilik tayini, *Türk Standartları Enstitüsü*, Ankara.
- TSE, TS EN 14103, 2011, Hayvansal ve bitkisel yağ türevleri, yağ asidi metil esterleri (yame), ester ve linolenik asit metil ester içeriğinin tayini, *Türk Standartları Enstitüsü*, Ankara.
- TSE, TS EN 14214, 2014, Otomotiv yakıtları, yağ asidi metil esterleri (yame/biyodizel), dizel motorlar için özellikler ve deney yöntemleri, *Türk Standartları Enstitüsü*, Ankara.
- TSE, TS ISO 3930, 2009, Karayolu taşıtları için egzoz emisyon ölçüm cihazları, *Türk Standartları Enstitüsü*, Ankara.
- TSE, TS-1231, 2010, İçten yanmalı motorlar, muayene ve deney esasları, *Türk Standartları Enstitüsü*, Ankara.



- Ushakov S., Lefebvre N., 2019, Assessment of Hydrotreated Vegetable Oil (HVO) Applicability as an Alternative Marine Fuel Based on Its Performance and Emissions Characteristics, *SAE International J. Fuels Lubr.*, 04-12-02-0007.
- Viguera M., Marti A., Masca F., Prieto C., Calvo L., The process parameters and solid conditions that affect the supercritical CO<sub>2</sub> extraction of the lipids produced by microalgae, *J. of Supercritical Fluids*, 113, 16–22.
- Wahlen B. D., Morgan M. R., Curdy A. T., Willis R. M., Morgan M. D., Dye D. J., Bugbee B., Wood B. D., and Seefeldt L. C., 2013, Biodiesel from microalgae, yeast, and bacteria: engine performance and exhaust emissions, *Energy Fuels*, 27, 220–228.
- Wong P. K., Ghadikolaei M. A., Chen S. H., Fadairo A. A., Ng K. W., Lee S. M., Xu C. J., Lian Z. D., Li S., Wong H., Zhao J., Ning Z., Gali, N., 2022, Physicochemical and cell toxicity properties of particulate matter (PM) from a diesel vehicle fueled with diesel, spent coffee ground biodiesel, and ethanol, *Science of the Total Environment*, 824, 153873.
- Wu Y., Wang P., Farhan S. M., Yi J., Lei L., 2019, Effect of post-injection on combustion and exhaust emissions in DI diesel engine, *Fuel*, 258, 116131.
- Yeşilyurt M. K., Arslan M. Ve Eryılmaz T., 2018, Biyodizel-Dizel Yakıt Karışımlarına Etanol Katılmasının Performans, Yanma ve Emisyon Karakteristiklerine Etkisinin Deneysel İncelenmesi, *J. of Thermal Science and Technology*, 38, 129–150.
- Yeşilyurt M. K., Cesur C., Aslan V., Yılbaş Z., 2020, The production of biodiesel from safflower (*Carthamus tinctorius* L.) oil as a potential feedstock and its usage in compression ignition engine: A comprehensive review, *Renewable and Sustainable Energy Reviews*, 119, 109574.
- Yilmaz N., and Sanchez T. M., 2012, Analysis of operating a diesel engine on biodiesel-ethanol and biodiesel-methanol blends, *Energy*, 46, 126-129.
- Yilmaz N., Vigil F. M., Donaldson A. B., Darabseh T., 2014, Investigation of CI engine emissions in biodiesel–ethanol–diesel blends as a function of ethanol concentration, *Fuel*, 115, 790-793.
- Zaharin M. S., Abdullah N. R., Najafi G., Sharudin H., Yusaf T., 2017, Effects of physicochemical properties of biodiesel fuel blends with alcohol on diesel engine performance and exhaust emissions: A review, *Renewable and Sustainable Energy Reviews*, 79, 475–493.
- Zhu L., Cheung C. S., Zhang W. G., and Huang Z., 2010, Emissions characteristics of a diesel engine operating on biodiesel and biodiesel blended with ethanol and methanol, *Science of the Total Environment*, 408, 914–921.
- Zhu L., Cheung C. S., Zhang W. G., and Huang Z., 2011, Combustion, performance and emission characteristics of a DI diesel engine fueled with ethanol–biodiesel blends, *Fuel*, 90, 1743-1750.



## THE PERFORMANCE OF WATER JET PUMPS AND THEIR APPLICATION IN SLURRY TRANSPORTATION

Mehmet Ali KÖKPINAR \* and Mustafa GÖĞÜŞ\*\*

\*TED University, Civil Engineering Department, Kolej, Ankara

mehmet.kokpinar@tedu.edu.tr, ORCID ID: 0000-0001-9550-8330

\*\* Çankaya University, Civil Engineering Department Eskişehir yolu, Ankara

mgogus@cankaya.edu.tr, ORCID ID: 0000-0002-7723-5954

(Geliş Tarihi: 14.06.2022, Kabul Tarihi: 26.04.2023)

**Abstract:** This present work is focused firstly on an experimental investigation for the optimum design of water jet pumps to be used in the hydrotransport of solid particles through pipeline systems. Experiments were conducted in a closed test loop using five types of jet pumps with various dimensions of the driving nozzle, suction nozzle, mixing chamber, and diffuser employing water as driving and suction fluid. The efficiency of each water jet pump element was analyzed and interpretations of results related to each water jet pump were made about the parts to be considered in the optimum design of a water jet pump. From the experimental results, the water jet pump having the optimum mixing chamber, suction nozzle, driving nozzle location, and cross-sectional dimensions produced a maximum efficiency of about 33%. In the second part of the study, the solid particle carrying capacity of water jet pumps in a pipeline system was studied under saltation, moving bed, and heterogeneous flow regimes by introducing seven different types of solid particles having various concentrations into the closed test loop. The effect of jet pumps on separating solid particles from flow in a region was investigated. A curved form of a by-pass system called the 'flow division unit' was added to the main pipeline system and through the flow division unit, then most of the solid particles in the flow were forced to flow towards the suction pipe of the jet pump. As a result of this, only water with very small particle concentrations passed through the centrifugal pumps, and in this way, the wear risk of the centrifugal pump was reduced considerably. **Keywords:** water jet pump, pipeline system, slurry transportation, centrifugal pump wear.

### SU JET POMPALARININ PERFORMANSI VE KATI-SIVI KARIŞIM TAŞIMACILIĞINDA UYGULANMASI

**Özet:** Bu çalışma öncelikle, katı parçacıkların boru hattı sistemleri aracılığıyla suyla taşınımında kullanılacak su jeti pompalarının optimum tasarımı için deneysel bir araştırmaya odaklanmıştır. Deneyler, hem tahrik hem de emme sıvısı olarak su kullanan tahrik nozulu, emme nozulu, karıştırma haznesi ve difüzörün çeşitli boyutlarına sahip beş tip jet pompası kullanılarak kapalı bir test döngüsünde gerçekleştirildi. Her bir su jeti pompası elemanının verimliliği analiz edilmiş ve her bir su jeti pompasına ilişkin sonuçların, bir su jeti pompasının optimum tasarımında dikkate alınması gereken parçalar hakkında yorumları yapılmıştır. Deneysel sonuçlardan, optimum karıştırma haznesi, emme nozulu, tahrik nozulu konumu ve kesit boyutlarına sahip su jet pompası, yaklaşık %33'lük maksimum verimle üretilmiştir. Çalışmanın ikinci bölümünde, bir boru hattı sistemindeki su jeti pompalarının katı madde taşıma kapasitesi, çeşitli konsantrasyonlara sahip yedi farklı katı maddenin kapalı test döngüsüne sokularak sıçramalı, hareketli yatak ve heterojen akış rejimleri altında incelenmiştir. Jet pompasının bir bölgedeki katı partikülleri akıştan ayırmadaki etkisi araştırıldı. Ana boru hattı sistemine 'akış bölme ünitesi' adı verilen kavisli bir by-pass sistemi eklendi ve akış bölme ünitesi aracılığıyla, akıştaki katı parçacıkların çoğu jet pompasının emme borusuna doğru akmaya zorlandı. Böylece santrifüj pompalardan sadece çok küçük partikül konsantrasyonlarına sahip su geçmiş ve bu şekilde santrifüj pompanın aşınma riski önemli ölçüde azaltılmıştır.

**Anahtar Kelimeler:** su jeti pompası, boru hattı sistemi, bulamaç nakliyesi, santrifüj pompa aşınması.

#### NOMENCLATURE

##### Abbreviations

<i>A</i>	Area
<i>C</i>	Concentration
<i>D</i>	Diameter (or size)
<i>E</i>	Total head
<i>g</i>	Gravitational constant

<i>L</i>	Length
<i>M</i>	Non-dimensional flow ratio
<i>m</i>	Mass flux
<i>N</i>	Non-dimensional head ratio
<i>Q</i>	Discharge
<i>V</i>	Velocity
<i>t</i>	Time
<i>x</i>	Distance

$\eta$	Efficiency
$\theta$	Angle
$\rho$	Density of the fluid
$\gamma$	Specific weight of the fluid

*Subscripts*

<i>d</i>	driving line
<i>ds</i>	diffuser
<i>in</i>	into the system
<i>mix</i>	mixture
<i>mc</i>	mixing chamber
<i>n</i>	nozzle, nominal diameter
<i>o, out</i>	out from the system
<i>p</i>	pump
<i>s</i>	suction line
<i>sn</i>	suction nozzle
<i>sp</i>	solid particle
<i>w</i>	water, weight

**INTRODUCTION**

The flow of slurries in pipes takes place in a variety of industrial applications due to its economic importance. Mixtures of liquids, mainly water and solids such as sand, gravel, clay, coal, various ores, plastics, etc., are transported over short and long distances. While transporting solid-liquid mixtures, a number of flow regimes can be encountered as the flow velocity increases. Detailed information on those of the flow regimes of solid-liquid mixtures in closed-conduits was extensively given by Graf (1971) and ASCE (1975). The transport of relatively coarse particles has been limited to short distances because of high necessary operating velocities resulting in extensive wear in the pipeline system and excess energy consumption. When designing a solid-transporting pipeline system using centrifugal pumps, it is necessary to know the effect of solids on the performance of the pumps. For example, even a small deviation in pump speed from a predetermined mean value over a long period of time can be very expensive due to increased wear in the system. Frequent pump disassembly and installation not only consumes much time, but the frequent replacement of the flow passage components is very expensive also (Peng et al. 2020). In addition, the flow of solids through the pump causes additional hydraulic losses due to the relative movement of coarse particles or the viscous effects of high concentration of solid particles due to the different densities of solids and liquids. As the concentration of solid particle increases, the damage because of abrasion becomes more serious. In order to avoid these problems, somehow the amount of solid particles which will pass directly through pumps should be reduced. This situation can be achieved if the combination of a centrifugal pump and a jet pump is used in the system as shown in Figure 1.

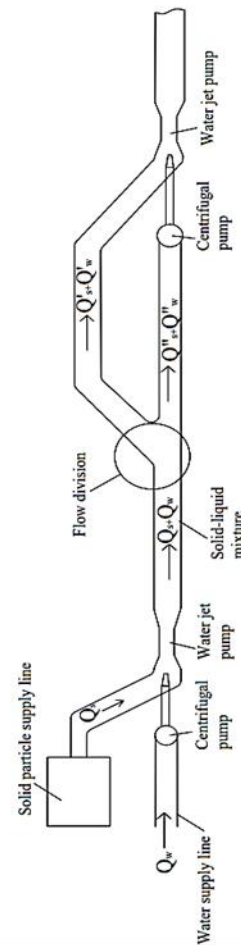


**Figure 1.** A general layout of a solid-liquid carrying pipeline system with the combination of bypass and water jet pump

The jet pump operates without moving parts and consists of four main elements; i.e. driving nozzle, suction nozzle, mixing chamber, and diffuser. Because the jet pumps do not contain any moving parts, they are less affected by the abrasion. Beside this obvious advantage, its simple design, easy maintenance, simple operation, and applicability to high-density fluids are some of the other significant benefits of jet pumps. Jet pumps can be made of great variety of materials and they can be used in various fields like fluid jet mixers, jet heaters, or steam jet compressor depending on the flow mediums used. If the driving and suction fluids are water, the jet pump is named as “water jet pump (WJP)” which is the main concern of this paper. Water jet pumps are used in many civil engineering practices like deep-well pumping and dredging.

Water jet pump was first used by Thomson after the development of the two streams mixing theory by Rankine (Reddy and Kar, 1968). In the later works, the researchers tried to obtain the geometry of a water jet pump for which the maximum performance would be achieved. The past research showed that the efficiencies of jet pumps tested were varied in the range of 20.8-42 % at flow ratios M, which is the ratio of suction flowrate to

driving flowrate, of 0.2-1.2 (e.g. Muller (1964), Reddy and Kar (1968), Cairns and Na (1969), Cunningham (1995), Wang and Wypych (1995), El-Sawaf (1999), Winoto et al. (2000), Neto (2011), Xiao and Long (2015), Yapıcı and Aldaş (2013), Sheha et al. (2018), Zhao and Sakuragi (2018)).

In a water jet pump, the pumping action is performed by the transfer of energy from a high velocity jet to one of low velocity suction fluid. In case of solid-liquid flow in a pipeline, a typical jet pump as shown in Fig. 2 is operated by a pump producing a driving jet of clean liquid through a nozzle which will entrain to the solid-liquid mixture. The momentum exchange between the driving jet and entrained mixture occurs within a mixing chamber and the high kinetic energy is then converted into pressure energy through a diffuser.

The main contribution of this study in slurry transporting systems is to reduce the ratio of solid particles passing through the centrifugal pump by using water jet pumps with a flow separation unit and to prevent the centrifugal pump wear problem. To the knowledge of the authors, there is no study using these two elements (water jet pump and flow separation unit) together. In the present experimental work, a water jet pump and a flow division unit have been used in conjunction with a centrifugal pump in order to avoid solid particles passing through the centrifugal pump in a pipeline system transporting solid-liquid mixture. The efficiencies of the water jet pumps tested were determined and the amounts of solid particles passing through the centrifugal pump were measured for different solid particles having various concentrations and for different flow regimes; namely in saltation, moving bed, and heterogeneous regimes. Seven different types of solid particles, five types of suction nozzles, driving nozzles, and mixing chambers were examined in the course of this study.

## THEORETICAL BACKGROUND

### Water Jet Pump

The performance of a water jet pump is commonly expressed in terms of its efficiency  $\eta$ , which is simply defined as the ratio of power output to power input of the system (Fig. 2),

$$\eta = \frac{(Power)_{out}}{(Power)_{in}} = \frac{Q_s(E_d - E_s)}{Q_p(E_p - E_d)} = MN \quad (1)$$

in which,  $(Power)_{in} = \gamma_w Q_p (E_p - E_d)$ ,  $(Power)_{out} = \gamma_w Q_s (E_d - E_s)$ ,  $\gamma_w$  is the specific weight of water,  $Q_s$  is the suction fluid flow rate;  $Q_p$  is the driving fluid flow rate;  $E_d$  is the total head at the exit of the diffuser (Section (d)-(d));  $E_s$  is the total head of the suction liquid (Section (s-s));  $E_p$  is the total head of driving liquid (Section (p-p)); and the non-dimensional volume flow rate, and the non-dimensional head ratio, are defined as  $M = Q_s/Q_p$ ,

and  $N = (E_d - E_s)/(E_p - E_d)$ , respectively. It should be noted that (1) is non-dimensional and includes the overall losses encountered in the water jet pump.

In the experimental analysis of a water jet pump, in order to obtain the highest possible efficiency one should consider geometrical parameters of each element of the jet pump, that is, different values for lengths, diameters and angles made with respect to each other have to be investigated. It is obvious that making all these changes and tests will be time consuming and also very costly. The experiments were conducted with varying dimensions of driving nozzle, mixing chamber, suction nozzle, and diffuser. The minimum energy just before the jet pump prevails at Section (s)-(s). The maximum total head to which the suction fluid will be raised, which can also be named as the pump lifting height, is equal to  $(E_d - E_s)$ . The power output from the pump is determined by  $\gamma_w Q_s (E_d - E_s)$  whose division by  $\gamma_w Q_p (E_p - E_d)$  produces the pump efficiency given in (1).

### Slurry Flow with Water Jet Pumps

Solid-liquid mixtures having high solid concentrations have strong influences on pump head, efficiency, and pump power consumption. These influences vary with material types and different particle sizes. Ni et al. (1999) reported that when volumetric concentration  $C_v$  was equal to 42%, the centrifugal pump efficiency could drop almost 60% in the coarse sand slurry as compared to the efficiency that of only water. They also pointed out that power requirement increases with relative density of the slurry.

The function of a water jet pump in the solid transporting pipeline system is mainly to avoid the particles from passing through the centrifugal pump. As it has been stated before, the abrasive action of the solid particles gives damages to rotating parts of the centrifugal pumps as well as to pipes. Since centrifugal pumps are the most important elements of a solid transporting pipeline system, a special attention should be given and ways of preventing them from wear should be searched. Noon and Kim (2016) numerically investigated erosion prevention caused by the lime slurry and its effects on head and efficiency losses in centrifugal pumps. They found that erosion loss increased with impact velocity, concentration by weight, and diameter of solid particles. Tarodiya and Gandhi (2019) focused on investigating the relationship between the abrasive wear profile of the pump body and the simulated flow field experimentally and numerically to determine the influence of the dominant factors affecting the wear of the pump bodies under different operating conditions. Li et al. (2020) numerically simulated solid-liquid flow in a centrifugal pump using CFD-discrete element method coupling. They stated that with the increase in the particle concentration, the head and efficiency of the centrifugal

pump dropped significantly, and the wear rate of the centrifugal pump wall was closely related to the particle concentration.

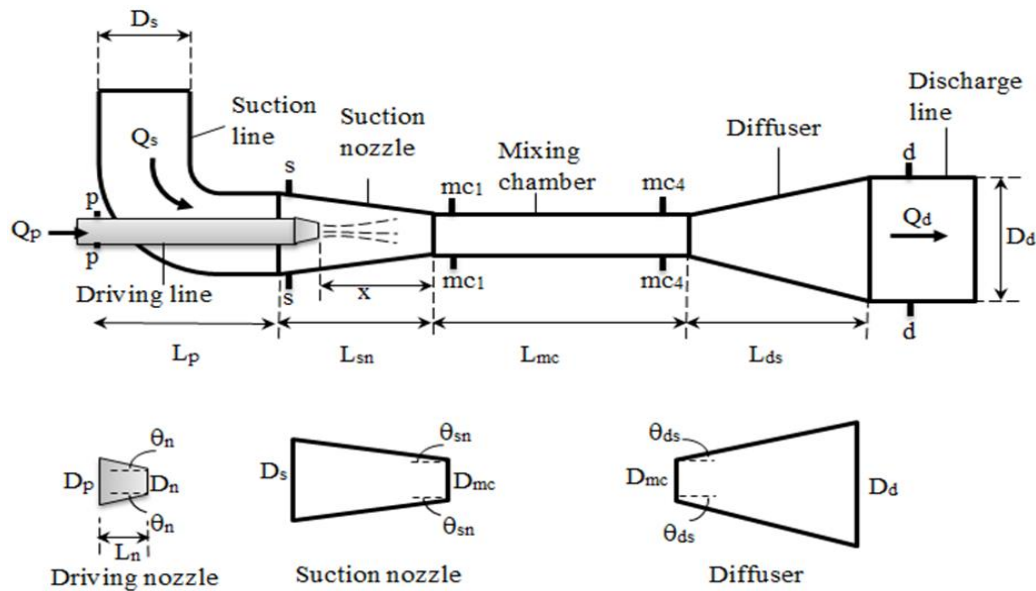


**Figure 2.** A typical water jet pump with its elements

In this study, a jet pump, a centrifugal pump, and a flow division unit were used in a laboratory closed test loop to minimize the amount of solids, which could pass through the centrifugal pump as seen in Figs. 3 and 4. The pipeline system at the by-pass was divided into two branches (named as “Flow Division Unit”) before the centrifugal pump. While one of the branches (outer) was directly connected to the centrifugal pump, the second one (inner) was making a curvature and forming a by-pass. It is known that when a solid-liquid mixture flow approaches a bend of either a pipe or an open channel, the fluid particles and solid particles at the bottom levels of the flow have a tendency to move towards the inner side of the bend due to the effect of centrifugal forces that cause secondary currents at the cross section (Graf, 1971; ASCE, 1975, Julien, 2002). Referring to this principle it was shown that more solid particle discharge of the system was passing through the inner branch and then combining with the rest of the solid particle discharge after the jet pump unit.

In addition to the emphasized advantage of the by-pass system, there is another important point that should not be forgotten is the additional energy losses. When a pipeline system with by-passes and jet pumps (as seen Fig. 1) are to be preferred to the one which is free of by-passes and having only centrifugal pumps at certain locations, some additional energy losses occur in the whole system due to the by-passes and jet pumps. These undesired losses can be minimized by using optimum

design criteria to be obtained from theoretical and experimental studies for by-passes and jet pumps.

The theoretical work to be done here is valid for the control volume applied to the system where all experiments were performed. The equations used in the determination of solid particle concentrations passing through the suction line and pump were derived from the basic law of conservation of mass applied to the pipeline system shown in Fig. 3. In the case of having water as the fluid being transported, the mass flux entering the system through the driving line  $m_p$ , is equal to the mass flux leaving the system  $m_o$ , because the rate of change of mass of water inside the system is zero. The mass flux in the discharge line,  $m_d$ , is equal to the summation of the mass fluxes in the suction line  $m_s$ , and that leaving the system  $m_o$ , or entering the system  $m_p$ .

Introducing solid particles of known weight into the system changes the calculation procedure to a degree. Since the driving fluid in this study is always water, then the mass fluxes of the fluid entering and leaving the system are not same. Some fraction of the solid particles introduced escaped out as a function of time; therefore, the rate of change of mass of solid-water mixture inside the system is not zero.

Applying the law of conservation of mass for the pipeline system, one can write,

$$\frac{\Delta m_d}{\Delta t} + m_o - m_p = 0 \quad (2)$$

where  $\frac{\Delta m_d}{\Delta t}$  is the rate of change of mass of solid-water mixture inside the control volume,  $m_o$  is the mass flux flowing out of control volume and  $m_p$  is the mass flux flowing inside the control volume. From experiments conducted, values of  $m_o$  and  $m_p$  were determined and by

means of (2) the magnitude of  $\frac{\Delta m_d}{\Delta t}$  was calculated. However, it was seen that this amount was negligible compared to other terms. Then (2) takes the form of,

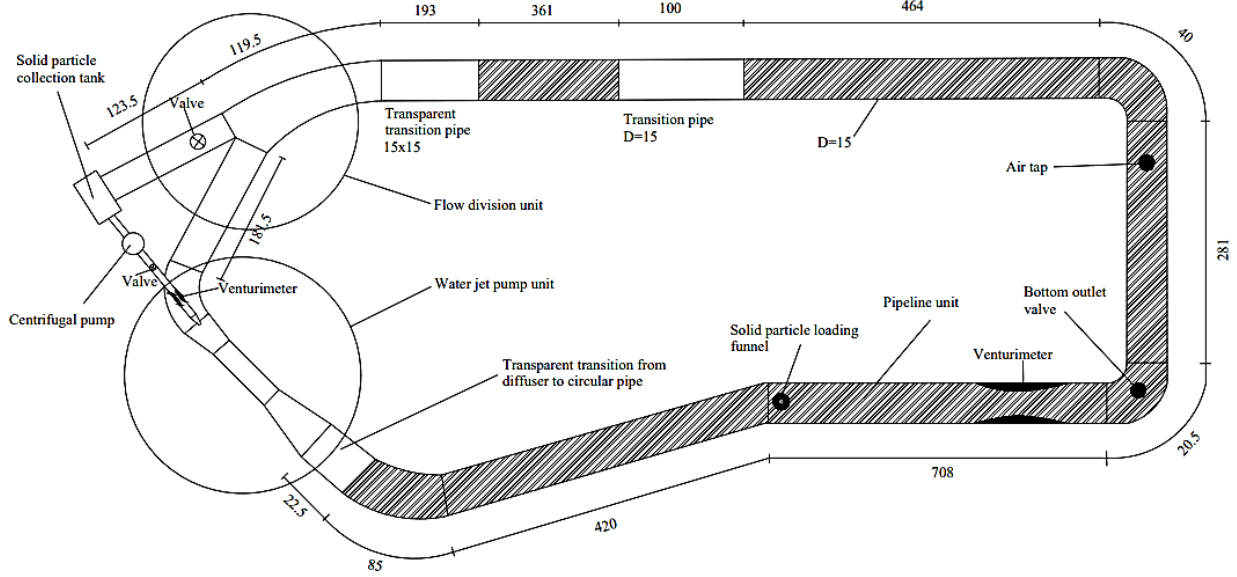


Figure 3. Experimental set-up used in the study

$$m_o \cong m_p \quad (3)$$

Expressing  $m_o$  and  $m_p$  as,

$$m_o = (\rho_{mix} Q_{mix})_o \quad (4)$$

and,

$$m_p = (\rho_w Q_w)_p \quad (5)$$

where  $\rho$  is the density,  $Q$  is the discharge and the subscripts “mix” and “w” refer to mixture and water, respectively. Substituting (4) and (5) into (3),

$$(\rho_{mix} Q_{mix})_o = (\rho_w Q_w)_p \quad (6)$$

The results of experiments carried out with different solid particles revealed that  $(\rho_{mix})_o \cong (\rho_w)_p$  from which the following relation can be written,

$$(Q_{mix})_o \cong (Q_w)_p \quad (7)$$

The total dry weight of the solid-water mixture  $W_{mix}$  escaped out from the system during the time period of  $\Delta t$  can be determined as,

$$(W_{mix})_o = (\gamma_{mix} Q_{mix} \Delta t) = \gamma_w Q_p \Delta t \quad (8)$$

where  $\gamma$  is the unit weight. The weight concentration of the solid particles,  $C$ , flowing out of system, which is actually the concentration of the solid particle which will pass through the centrifugal pump, is computed from the equation below,

$$C_o = C_p = \frac{(W_{sp})_o}{(W_{mix})_o} = \frac{(W_{sp})_o}{\gamma_w Q_p \Delta t} \quad (9)$$

where  $(W_{sp})_o$  is the total weight of the solid particle flows out of the system during the time period of  $\Delta t$  and subscript “sp” refers to solid particle dry weight.

In a similar way, the concentration of the solid particles passing through the suction line can be determined as

$$C_s = \frac{\gamma_{sp} Q_s}{(\gamma_{mix} W_{mix})_s} \quad (10)$$

## EXPERIMENTAL ARRANGEMENT AND PROCEDURE

Test facility used in this study was designed and assembled at the Hydraulics Laboratory of Middle East Technical University. Following the construction of the test set-up, several research activities were conducted on hydraulic transport of solids in pipes (i.e. İnci (1987), Kökpinar (1990), and Kökpinar and Göğüş (2001)).

Figure 3 shows the general layout and dimensions of experiment set-up. The whole system horizontally mounted on steel supports of height 0.60 m above the laboratory bottom level can be analyzed into three parts; pipeline unit, flow division unit, and water jet pump unit. The pipeline unit consisted of a steel pipe 0.15 m in diameter and 26 m long.

As it is seen in Fig. 3, the pipeline unit started following the water jet pump unit and continued up to the transparent transition pipe of square cross-section, with dimensions of 0.15 cm x 0.15 cm. The transparent pipe which was 1.0 m long and 0.15 m in diameter located close to the downstream end of the pipeline unit was used as an observation pipe during the experiments. Solid particles were introduced into the system by means of a funnel. The total flow discharge passing through the pipeline unit was measured by a venturimeter of 0.1 m in throat diameter. The bottom outlet valve was used to unload the system after finishing each experiment.

The sketch showing geometrical details of flow division unit and its photographs before and after installation are seen in Fig. 4. This unit, which was at the downstream of the transparent transition pipe of square cross-section with dimensions of 0.15x0.15 m, was divided into two branches. The first branch (outer branch), which works as outlet conduit, has a rectangular cross-section of width and height 0.10 m and 0.1125 m, respectively. At the end of this pipe, a valve was located for the adjustment of the flowrate leaving the system. The second branch (inner branch) of the flow division unit with a different radius of curvature than the first one but has a rectangular cross-section with the same dimensions of the first branch works as a suction conduit for the jet pump unit. Just at the downstream of the pipe, a sliding gate was constructed to divert the flow when cleaning up the system from settled solid particles. A 90°-bend of constant cross-section area connects the suction pipe to the water jet pump. In all experiments the dimensions of the elements forming the flow division unit were kept constant.

The water jet pump unit was composed of a suction nozzle, a mixing chamber, a diffuser, and a driving line with a driving nozzle. The length and diameter of the driving line and the suction line, which connected the suction chamber to the flow division unit, were kept constant in all experiments. The flow rate of the driving fluid was measured by a venturimeter of throat diameter 0.028m. Five types of jet pumps with different dimensions were manufactured and tested with varying driving nozzle diameters as seen from Table 1.

Seven types of solid particles of different properties (fine and coarse tuffs, blue and black granular plastics, coal, fine sand, and coarse aggregate) were used in the solid-liquid transportation experiments. Table 2 shows the

characteristics of solid particles used in the experiments. The specific gravities of the solid particles were varying in the range of 1.05-2.60. The granular plastic particles had uniform dimensions with 1.5x2.0x2.0 mm. Particle size distribution of the non-uniform particles are given in Fig. 5.

For several values of driving line water discharge  $Q_p$ , starting from the minimum up to the maximum obtainable ones, the experiments were carried out and static pressure head in the piezometer tubes on manometers were recorded. The presence of turbulence caused fluctuations in water levels of piezometer tubes and required special attention to obtain the water levels in each piezometer tube under the same hydraulic condition. The maximum height of the variation observed in the measurements of water levels in piezometer tubes was about 0.015 m causing  $\pm 3\%$  error in the measured pressure head. In addition, the measurement of the mixture discharge involved using a Venturi meter positioned in the pipeline unit. However, it was found that during high flow rates, variations in the water manometers linked to the Venturi meter could lead to a potential 2% discrepancy in the discharge measurement, thereby generating an equivalent mistake in the flow velocity. In order to achieve accurate experimental values for each parameter (such as pressure, discharge, solid weight, etc.), the tests were conducted multiple times using the same amount of particles, with a minimum of two or three repetitions.

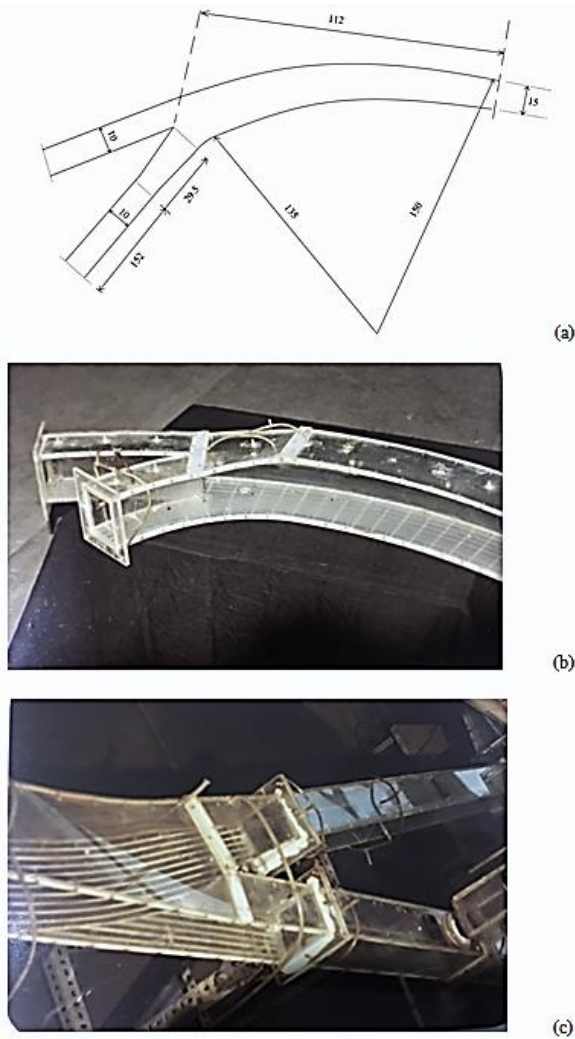


**Figure 4.** Flow Division Unit a) geometrical details, b) photo before installation (view from inner branch), and c) after installation (view from outer branch)

After completing the experiments on water jet pumps to obtain highest efficiency geometry, following experiments were conducted to investigate the effect of a jet pump on solid particle transport capacity of the system and to observe the performance of the flow division unit on the separation of solid particles. Seven different types of solid particles with various specific gravity values were used as test materials. For the jet pump and driving nozzle, a flowrate was set in the system by adjusting valves on driving line and outlet valve. Then, the experiments for a given type and weight of the solid particle was carried out by slowly introducing the solid particles through the loading funnel. The solid particles were carried away through the pipe under the influence of flow in the pipe. The movement of the solid particles was observed through the transparent pipes on the system to define the regime of solid transport. Since the discharge of the driving line was kept initially at a low value most of the time solid particles settled in the pipe forming discrete steps in rectangular shape with a gentle

upstream but steep downstream slopes. Only the grains on the top of these steps moved along the flow direction and settled in front of the downstream slopes, after travelling relatively short distances. Accumulations of the solid particles especially along the inner branch of the flow division unit and at the suction line were always observed. While the flow occurring in the system, a small fraction of the solid particles was withdrawn through the flow outlet pipe, but collected in a collection tank. After the solid particles were observed at almost any section of the whole system, not necessarily in moving form, the solid particles collected in the collection tank were added to the flow of the system. Then, for a period of about 3 minutes, the flow of solid-water mixture was observed and the particles flowing out of the system were collected. When the period was completed, the solid particles collected in the collection tank were weighed and recorded. This measurement procedure was repeated for the other system discharges obtained from increasing driving line discharge  $Q_p$  and necessary observations and data were recorded or collected accordingly. Figure 6 presents the process chart of the experimental program.

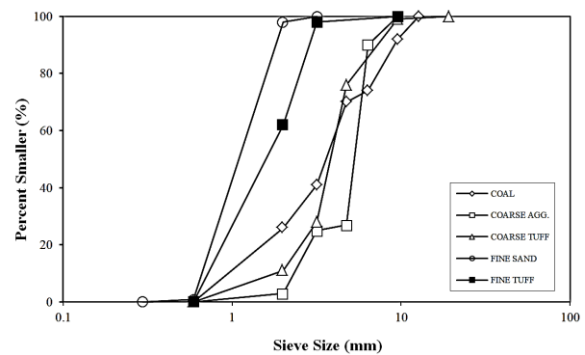


**Figure 5.** Grain size distribution of non-uniform solid materials used in the experiments

## INTERPRETATION OF RESULTS

### Water Jet Pump Efficiency

#### Effect of driving nozzle diameter

Figures 7a-7c have been created to compare and analyze the performance of each type of water jet pump (WJP) used in the experiments. The comparison is based on the relationship between the input power  $(Power)_{in}$  and the output power  $(Power)_{out}$ , with the driving nozzle diameter,  $D_n$ , used as a parameter for a given mixing chamber dimension. The first three WJPs (WJP-1 to WJP-3), which have different mixing chamber and suction nozzle geometries as outlined in Table 1, were tested to determine the effect of the driving nozzle diameter  $D_n$  on the overall efficiency of the WJPs. It is worth noting that in all three WJP tests, as shown in Figure 2, the driving nozzle was located at the entrance section of the suction nozzle, with a value of  $x = L_{sn}$ .



**Table 1.** Geometric characteristics of water jet pump elements used in the experiments (lengths in cm and angles in degree)

Water Jet Pump	Driving line		Driving nozzle		Suction line	Suction nozzle			Mixing chamber		Diffuser		Discharge line
	$D_p$	$L_p$	$D_n$	$L_n$	$A_s$	$\theta_{sn}$	$L_{sn}$	$x$	$A_{mc}$	$L_{mc}$	$\theta_{ds}$	$L_{ds}$	$D_d$
WJP 1.1	5	50	2.0	2.5	10x11.25	7.12	20	20	5x5	33	5.95	48	15
WJP 1.2			3.0	2.5									
WJP 1.3			4.0	2.0									
WJP 2.1	5	50	2.0	2.5	10x11.25	4.29	20	20	7x7	33	4.75	48	15
WJP 2.2			3.0	2.5									
WJP 2.3			4.0	2.0									
WJP 2.4			4.5	2.0									
WJP 2.5			5.0	2.0									
WJP 3.1	5	50	3.0	2.5	10x11.25	1.14	25	25	9x9	26	3.43	50	15
WJP 3.2			4.0	2.0									
WJP 3.3			4.5	2.0									
WJP 3.4			5.0	2.0									
WJP 4.1	5	50	4.5	2.0	10x11.25	1.14	25	25	9x9	65.5	3.43	50	15
WJP 4.2								4.5					
WJP 4.3								13					
WJP 5.1	5	50	4.5	2.0	10x11.25	2.29	12.5	5.5	9x9	78	3.43	50	15
WJP 5.2								6.1					
WJP 5.3								10.5					

**Table 2.** Characteristics of solid particles used in the experiments

Solid Particle	Specific weight	Median diameter	Nominal diameter
	$\gamma$ (gr/cm <sup>3</sup> )	$d_{50}$ (mm)	$d_n$ (mm)
Coarse tuff	1.05	3.89	
Blue plastics	1.20		2.25
Fine Tuff	1.31	1.65	
Black plastics	1.35		2.25
Coal	1.74	3.70	
Coarse gravel	2.55	5.34	
Fine sand	2.60	1.09	

During the experiments on WJP-1, which had a mixing chamber diameter of 5 cm, three different driving nozzle diameters were tested:  $D_n = 2$  cm,  $D_n = 3$  cm, and  $D_n = 4.5$  cm, labeled as WJP 1.1, WJP 1.2, and WJP 1.3, respectively. However, despite the input power  $(Power)_{in}$  ranging up to 1400 watts, the maximum  $(Power)_{out}$  achieved was only about 15.6 watts. This resulted in a low efficiency for the jet pump, determined by dividing  $(Power)_{out}$  by  $(Power)_{in}$ . Out of the driving nozzle diameters tested,  $D_n = 4.5$  cm was the worst performer in terms of system efficiency. For a given  $(Power)_{in}$  value, the other driving nozzle diameters yielded nearly the same amount of power.

In the WJP-2 experiments with a mixing chamber diameter of 7 cm, the slopes of the lines connecting the same series of data points were found to be steeper than those in Figure 7a. Within the range of experiments

conducted,  $D_n = 4.5$  cm (WJP 2.4), followed by  $D_n = 3.0$  cm (WJP 2.2) and  $D_n = 4.0$  cm (WJP 2.3), produced the maximum  $(Power)_{out}$  for a given  $(Power)_{in}$ .

In the WJP-3 experiments with a mixing chamber diameter of 9 cm, the data points for  $D_n = 4.0$  cm (WJP 3.2) and  $D_n = 4.5$  cm (WJP 3.3) were almost coinciding and produced the highest values of  $(Power)_{out}$  for the given  $(Power)_{in}$  values. Comparing Figures 7a, 7b, and 7c, it can be concluded that WJP-3 with a driving nozzle diameter of  $D_n = 4.0$  cm or 4.5 cm yielded the maximum pump efficiency of about  $\eta = 0.27$ .

For the next two water jet pumps, i.e. WJP-4 and WJP-5, the driving nozzle diameter and mixing chamber cross-section dimensions were fixed at  $D_n = 4.5$  cm and  $D_{mc} = 9$  cm, respectively, in order to analyze the effects of driving nozzle location, suction nozzle length, and mixing chamber length on the overall water jet pump efficiency. The corresponding driving nozzle to mixing chamber cross-section area ratio was  $A_n/A_{mc} = 0.198$  for the case of  $D_n = 4.5$  cm and  $D_{mc} = 9$  cm.

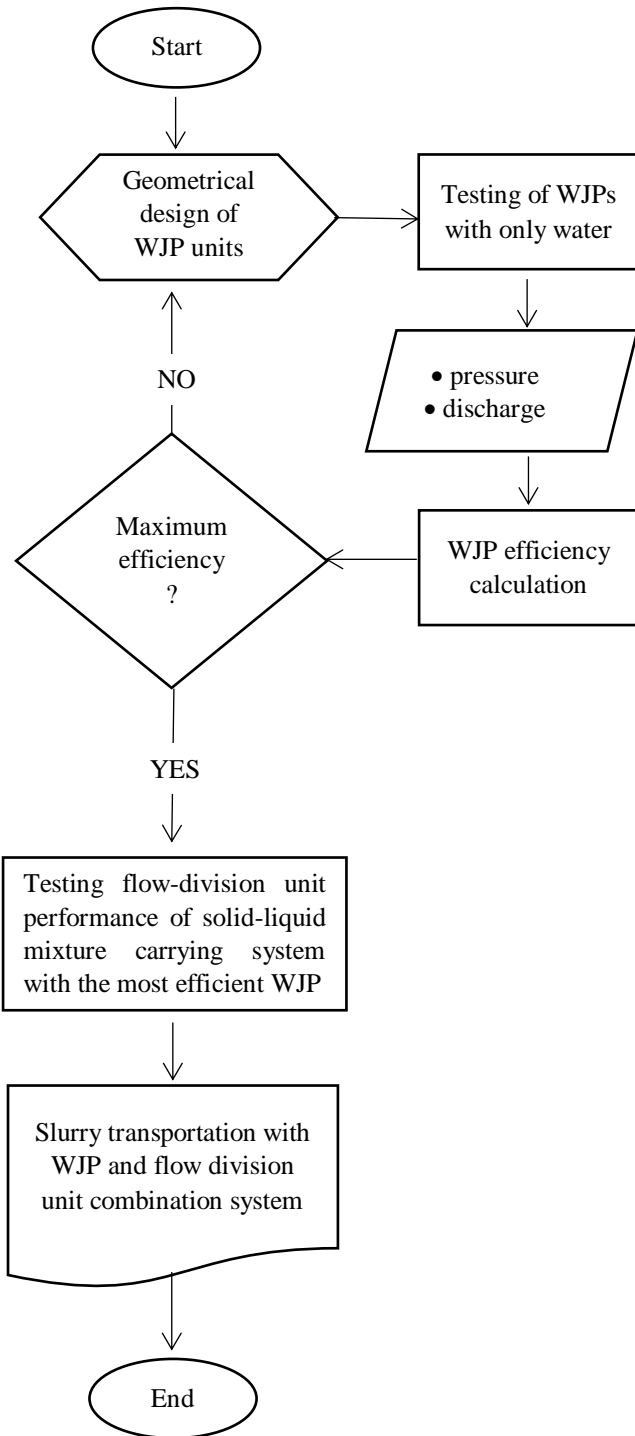


Figure 6. Process chart of the experimental program

### Effect of driving nozzle location

In Figure 2, the distance between the entrance of the mixing chamber and the tip of the driving nozzle location (referred to as "x") was varied along the suction nozzle to test its effect on the water jet pump's efficiency for each pump in the series of WJP-4 and WJP-5. The efficiency of each case of "x" was calculated and normalized with suction nozzle length  $L_{sn}$ , i.e.,  $x/L_{sn}$ . Figure 8 shows  $(Power)_{out}$  versus  $(Power)_{in}$  to compare the performance or efficiency of each water jet pump as a function of the

driving nozzle location. WJP 4.1 has the highest pump efficiency for a given  $(Power)_{in}$  with driving nozzle location at  $x=25$  cm ( $x/L_{sn}=1.0$ ). However, the efficiencies of WJP 4.2 and WJP 4.3 are not significantly different from that of WJP 4.1. Similarly, WJP 5.3 at  $x=10.5$  cm ( $x/L_{sn}=0.84$ ) gives the highest  $(Power)_{out}$  values for high values of  $(Power)_{in}$ , which corresponds to an efficiency of  $\eta=0.329$ .

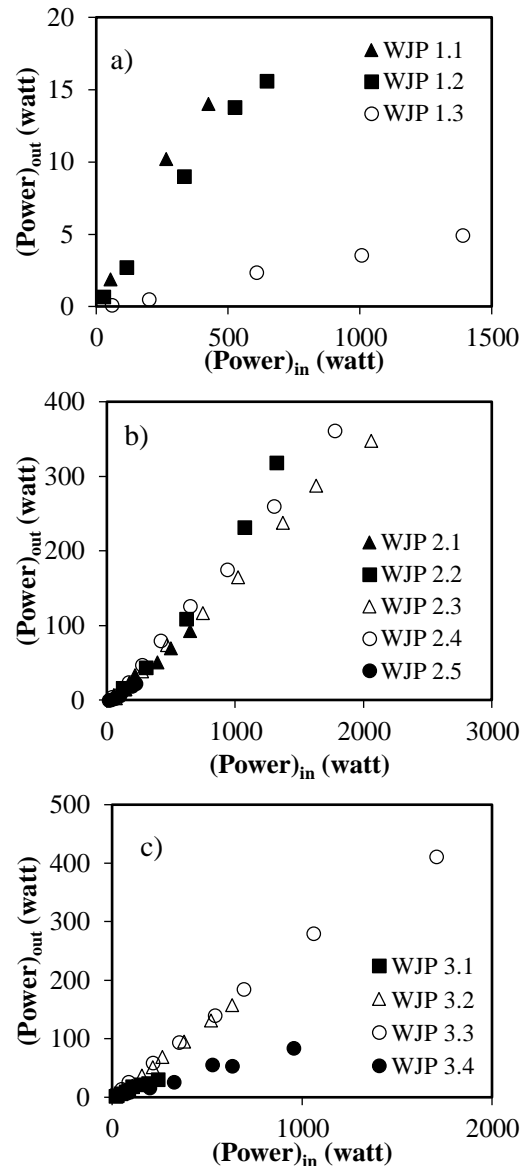
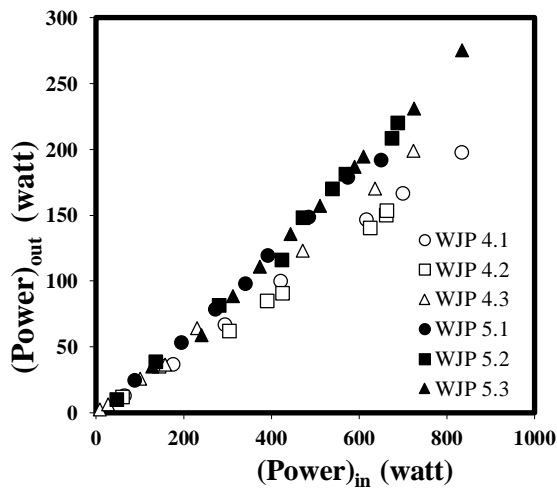


Figure 7. Variation of  $(Power)_{in}$  versus  $(Power)_{out}$  for various water jet pumps tested as a function of mixing chamber and driving nozzles dimensions for all series of; a)  $D_{mc}=5$  cm for WJP-1, b)  $D_{mc}=7$  cm for WJP-2, c)  $D_{mc}=9$  cm for WJP-3

### Relationship between flow ratio (M) and water jet pump efficiency ( $\eta$ )

To investigate the impact of suction nozzle length, mixing chamber length, and diffuser angle on the efficiency of water jet pump, Equation (1) was used to calculate the efficiency of each water jet pump. Figure 9 presents the relationship between the flow ratio

( $M=Q_s/Q_p$ ) and efficiency ( $\eta$ ) of all the water jet pumps tested in the study, along with the geometrical details of each pump provided in Table 1. The  $M$  versus  $\eta$  data for all the tested WJPs are shown under the envelope curve in the figure. It can be observed that WJP 5.3 consistently exhibited higher  $\eta$  values than the other tested WJPs. Based on the experimental data presented in Figure 9, the maximum WJP efficiency value of  $\eta=0.329$  was achieved at a flow ratio of  $M=1.62$ . Based on the general trend observed in all experimental data, it can be inferred that the efficiency of the pump first increases and then decreases as  $M$  increases, with a maximum value in between. This trend is consistent with previous studies, such as Helios and Asvapoositkul (2021), who achieved a maximum WJP efficiency of  $\eta=0.233$  at  $M=0.87$ , and Schulz and Fasol (Yapıcı and Aldas, 2013), who obtained the maximum jet pump efficiency value of  $\eta=0.36$  at  $M=1.4$ . Yapıcı and Aldas (2013) attributed this trend to the internal structure of flow through the driving and suction lines, which plays a crucial role in the initial increase and subsequent decrease in efficiency with increasing  $M$ . The findings of the current study suggest that using a  $90^\circ$  suction line connection to the suction nozzle leads to higher energy losses in the system, ultimately causing a decrease in efficiency. This trend persists even at relatively high efficiency levels, as evidenced by the recorded efficiency of  $\eta=0.329$  at  $M=1.62$ .



**Figure 8.** Variation of  $(Power)_{in}$  versus  $(Power)_{out}$  for various water jet pumps tested as a function of driving nozzle location

### Effect of Flow Division Unit on Separation of Solid Particles

The studies conducted in this section are based on the analogy of free-surface flows in curved channels. Predicting momentum and sediment transport in curved channels is crucial in river engineering practice. In bends, pressure gradients and centrifugal forces combine to create transverse circulations, also known as secondary flows, spiral flows, or helical flows. These three-dimensional helical flow patterns significantly impact

flow behavior and sediment transport in curved channels (Khosronejad et al., 2007), as observed in the scour mechanism in natural curved channels.

In a curved channel, scouring occurs along the outer bank while accumulation takes place along the inner bank due to secondary flows. Secondary flows are closed-circuit flows in a plane perpendicular to the main flow direction. They occur because a fluid element in meandering flow is influenced by two lateral forces. The first one is the pressure gradient in the lateral direction, which has the same value at every point on a vertical section since the pressure distribution is hydrostatic. The second force is the centrifugal force, which decreases as it approaches the bottom because flow velocity is high near the surface and low near the base. Therefore, a fluid element near the surface tends to move to the outside of the curvature, while an element near the bottom moves to the inside. The combination of the secondary flow with the main flow results in a helical flow at the bend. As a result, the secondary flow directed from the outer bank at the base to the inside carries material from the outer bank to the inner bank.

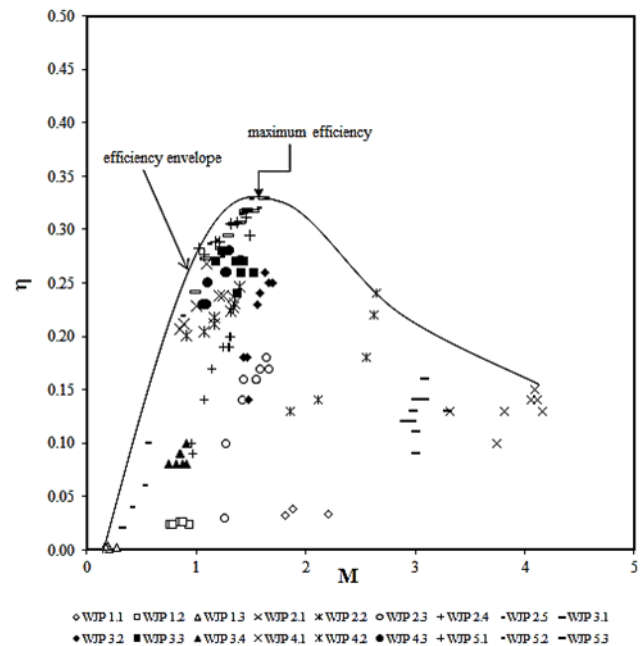


**Figure 9.** Variation of water jet pump efficiency  $\eta$  with flow ratio  $M$  for all water jet pumps tested

Based on the theoretical explanations given above, the experiments conducted in the previous section identified the most efficient type of water jet pump, which was then used to convey seven different types of solid materials through a pipeline system. The aim of this series of experiments was to investigate how the performance of the flow division unit is affected by the particle size and density of the solid materials, as well as the slurry flow regime.

Using the equations developed in the *Slurry flow with water jet pumps* section, the weight concentrations of the solid particles passing through the centrifugal pump ( $C_w)_p$  and suction line ( $C_w)_s$  were calculated and compared to the concentration of solid material introduced into the system by weight in the discharge line ( $C_w)_d$ . These concentrations were then plotted and presented in Figures 10a-u. Upon analyzing these figures, it was observed that the concentrations of solid materials passing through the suction line varied between 3.45% and 20.82% for ( $C_w)_d$  values ranging from 1.83% to 12.62%, while those passing through the centrifugal pump varied between 0% and 1.49%.

The efficient operation of a flow division unit is greatly influenced by the size of solid particles. For example, when coarse aggregates (Figures 10j,k,l) and fine sand (Figures 10p,q,r) were used in the experiments, the measured concentrations of solids passing through the centrifugal pump, ( $C_w)_p$ , were found to be in the range of 0.038% - 1.49% and 0% - 0.185%, respectively, when the concentrations of solids in the discharge line, ( $C_w)_d$ , were between 1.83% - 9.00% for both solid materials. These results indicate that the concentration of coarse particles passing through the centrifugal pump is always higher than that of fine particles, when the solid concentrations in the main pipeline system are the same for the two types of solids with similar densities.

In addition, experiments showed that fine particles tend to move close to each other, especially in the flow division unit, where they follow a path towards the inner branch of the unit, resulting in most of the solid particles returning to the main system, while a small amount goes into the outer branch. The photograph of the movement of fine sand materials along the inner branch in the flow separation unit is shown in Figure 11. These experimental findings are consistent with previous predictions on river bends, such as Allen (1970), Parker and Andrews (1985), Ikeda et al. (1987), Bridge (1976, 1992), and Sun et al. (2001), where coarser grains feel a larger ratio of transverse gravitational force to fluid force than finer grains, leading to lateral sediment size sorting.

In their laboratory tests, Ikeda et al. (1987) concluded that coarser bed materials experience a greater ratio of transverse gravitational force to fluid force than finer grains, making it the primary mechanism for dynamic sorting. They also found that sediment size tends to increase towards the outer bank, resulting in a reduction in lateral bed slope in the outer area of bends. Accordingly, similar to the present study, some of the coarse particles move directly towards the outer branch connected to the centrifugal pump at the beginning of the flow division unit.

Furthermore, the effectiveness of the flow division unit was investigated under different flow regimes of solid-liquid mixtures, which can be classified into four flow regimes (Abulnaga, 2002): a) stationary bed, b) saltation and moving bed, c) heterogeneous mixture with all solids in suspension, and d) homogeneous mixtures with all solids in suspension. In this experimental study, all tests were conducted under the flow regimes of b) and c). While a linear relationship was observed in the moving bed flow regime, the most data scattering was seen in both saltation and heterogeneous flow regimes. Regardless of the material used, data scattering is particularly noticeable at low ( $C_w)_d$  values. Thus, it can be concluded that the most stable flow regime is the moving bed flow regime, which is near the critical flow regime.

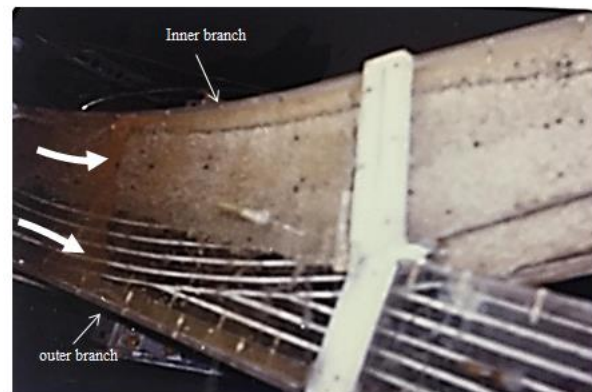


**Figure 11.** Accumulation of fine sand particles along inner bend of the flow division unit

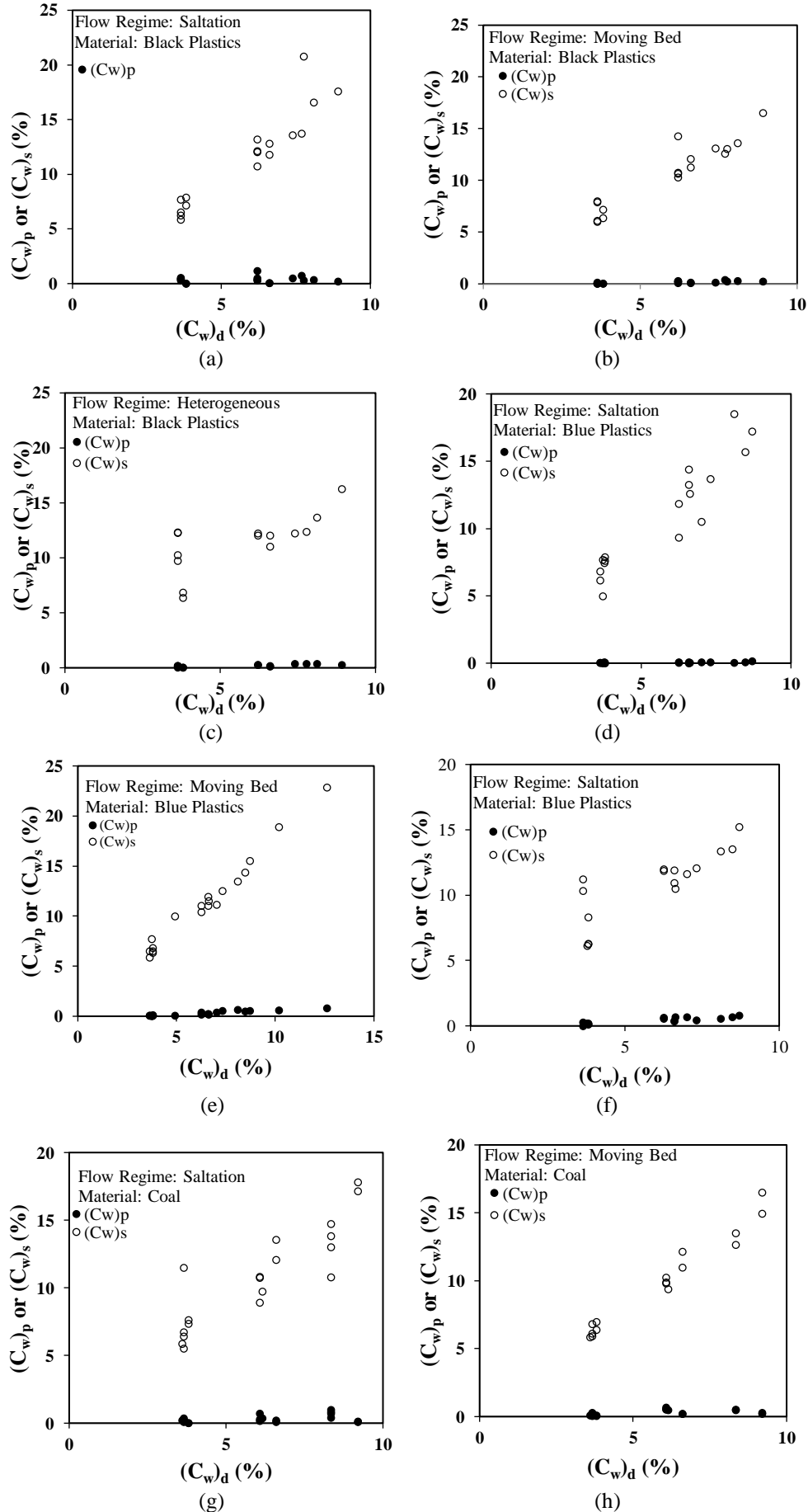


**Figure 10.** Variation of  $(C_w)_p$  or  $(C_w)_s$  with  $(C_w)_d$  as a function of flow regime and material used

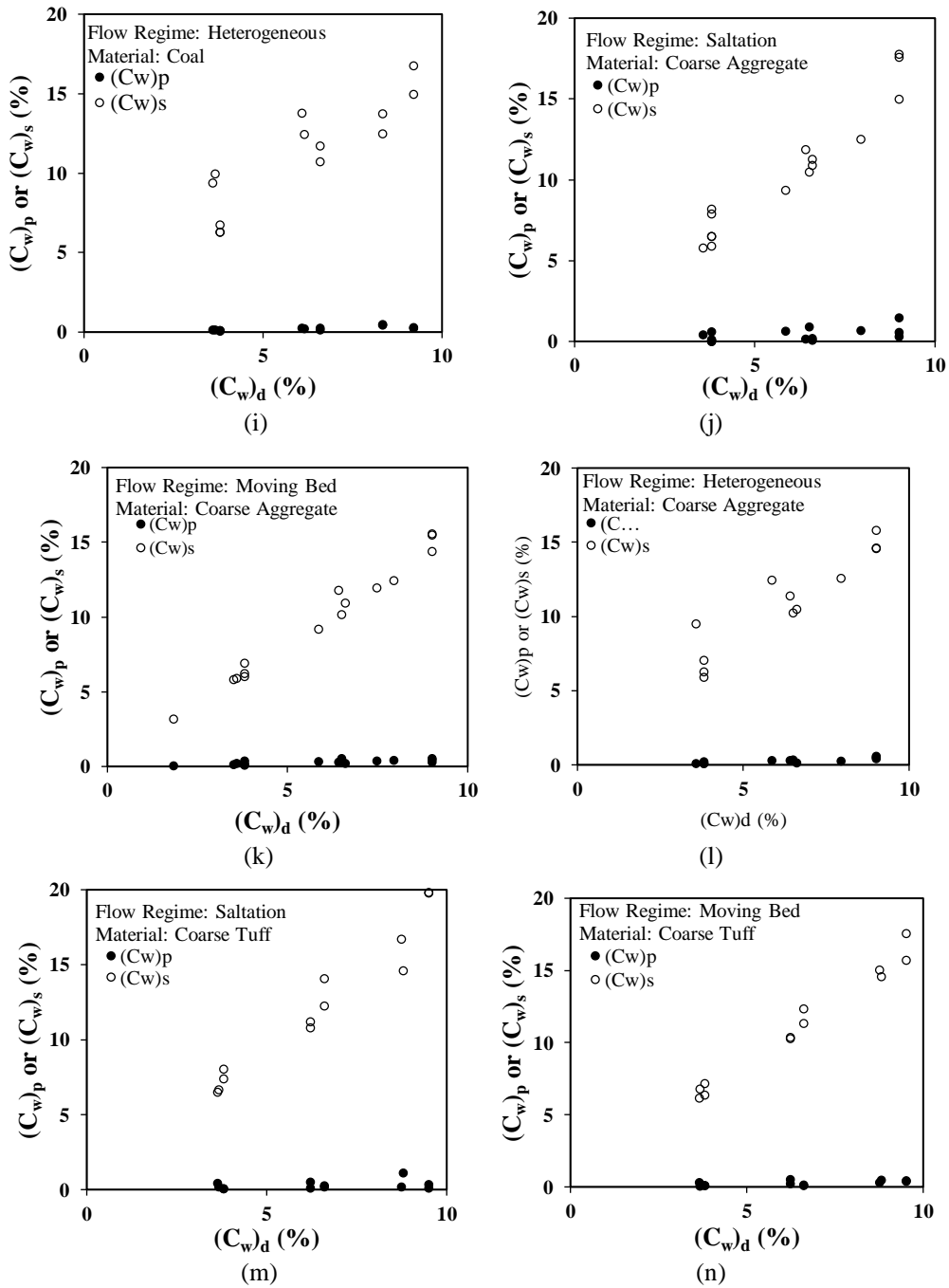


Figure 10. Variation of  $(C_w)_p$  or  $(C_w)_s$  with  $(C_w)_d$  as a function of flow regime and material used (cont.)

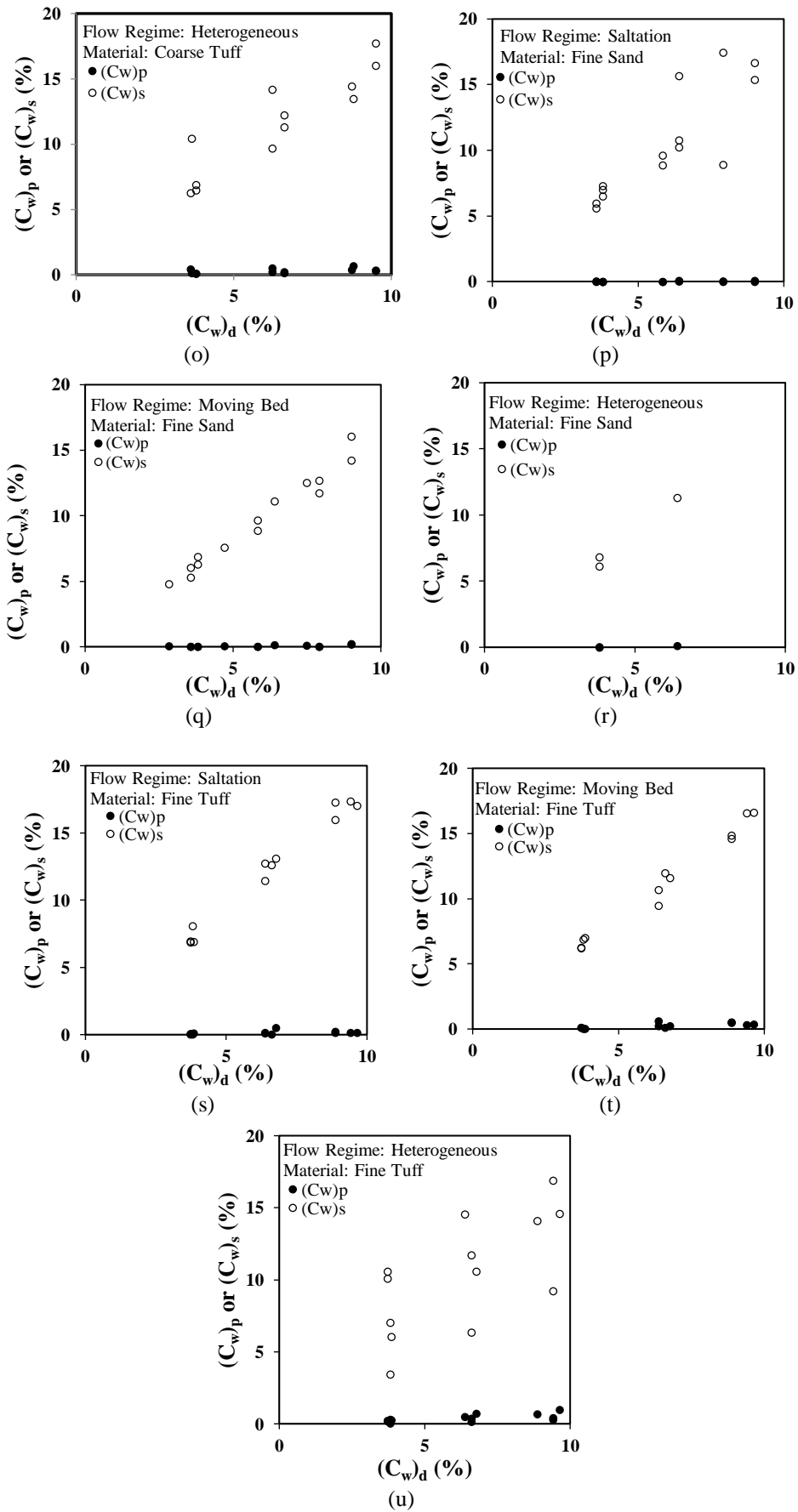


Figure 10. Variation of  $(C_w)_p$  or  $(C_w)_s$  with  $(C_w)_d$  as a function of flow regime and material used

## CONCLUSIONS

Apart from hydraulic conditions causing high friction losses in pipeline systems, the conveyance of solid particles through pipelines can also result in the undesirable abrasive action on pipes and the moving parts of centrifugal pumps. To mitigate this wear effect, one alternative solution is to use a water jet pump alongside a centrifugal pump in the pipeline system. The experimental study led to the following conclusions:

(1) Of all the water jet pumps tested and listed in Table 1, WJP 5.3 demonstrated the highest efficiency of  $\eta=0.329$ . This was achieved through an area ratio of driving nozzle to mixing chamber of  $A_n/A_{mc}=0.198$ , a non-dimensional driving nozzle location ratio of  $x/L_{sn}=0.84$ , a mixing chamber length to mixing chamber cross-section dimension of  $L_{mc}/D_{mc}=8.66$ , and a diffuser angle of  $\theta_{ds}=3.53^\circ$ .

(2) From the plot of pump efficiency  $\eta$  versus flow ratio  $M$  (Figure 9), it was concluded that for the water jet pump of WJP 5.3, the highest efficiency of  $\eta=0.329$  was obtained at  $M=1.62$ .

(3) A Flow Division Unit was added to the test setup in order to reduce the number of solid particles passing

through the centrifugal pump. Seven types of materials were used to create a slurry mixture with varying concentrations, and regardless of the type of solid material tested, the concentration of solid particles passing through the centrifugal pump did not exceed 10% of the initial concentration.

(4) It was observed that coarser solid particles move towards the outer branch of the flow division unit while fine particles tend to move towards the inner branch. This phenomenon was confirmed by comparing the measured data of coarse aggregate versus fine sand and coarse tuff versus fine tuff materials. In other words, fine particles are more effectively distributed between the two branches of the flow division unit than coarse particles.

(5) The slurry flow regime during operation also has an effect on the performance of the Flow Division Unit. The moving bed regime near the critical flow velocity was found to be more stable than the other flow regimes for all types of materials tested. A high scattering of concentration data was obtained from saltation and heterogeneous flow regimes, especially for low concentrations of materials introduced to the test loop.

## REFERENCES

- Abulnaga, B.E., 2002, Slurry Systems Handbook. The McGraw-Hill Book Co., New York. N.Y. USA.
- Allen, J.R.L., 1970, A quantitative model of grain size and sedimentary structures in lateral deposits. *Geol. J.* 7:129-146, <https://doi.org/10.1002/gj.3350070108>.
- ASCE, 1975, Sedimentation engineering. Manuals and reports on engineering practice, No.54, V.A. USA. Vanoni, ed.
- Bridge, J. S., 1976, Bed topography and grain size in open channel bends. *Sedimentology* 23: 407-414, DOI:10.1111/j.1365-3091.1976.tb00058.x.
- Bridge, J.S., 1992, A revised model for water flow, sediment transport, bed topography and grain size sorting in natural river bends. *Water Resources Research*, 28(4), 999-1013, DOI:10.1029/91WR03088.
- Cairns, J. R. and Na T.Y., 1969, Optimum design of water jet pumps. *J. Eng. Power* 91(1):62-68. DOI: 10.1115/1.3574677.
- Cunningham, R.G., 1995, Liquid jet pumps for two-phase flows. *ASME J. Fluids Engrg.* 117:309-316, DOI:10.1115/1.2817147
- El-Sawaf, I.A., 1999, Comparison between annular-type and two-peripheral-nozzles-type jet pumps for floating weed removal. 14th International Conference on Slurry Handling and Pipeline Transport, HYDROTRANSPORT 14, British Hydraulic Research (BHR) Group Publication No:36, pp.131-140, Maastricht, The Netherlands.
- Graf, H.W., 1971, *Hydraulics of sediment transport*. McGraw-Hill Book Co. New York. N.Y.USA.
- Helios, M.P. and Asvapoositkul, W., 2021. An experimental study of the effect of the projection ratio and throat-aspect ratio on the efficiency and loss coefficient of a water jet pump. *Journal of Mechanical Engineering and Sciences (JMES)*. 15(3): 8277 – 8288.
- Ikeda, S., Yamasaka, M., and Chiyoda, M., 1987, Bed topography and sorting in bends. *J. Hydraul. Eng.*113(2):190-204.
- Inci, G., 1987, Optimum design of water jet pumps with application to solid transportation through pipeline systems. MSc Thesis, Middle East Technical University, Ankara, Turkey.
- Julien, P.Y., 2002, *River Mechanics*. Cambridge University Press. 1st Edition. Cambridge. UK.
- Khosronejad, A., Rennie, C.D., Salehi Neyshabouri, S.A.A., and Townsend, R.D., 2007, 3D Numerical Modeling of Flow and Sediment Transport in Laboratory Channel Bends. *ASCE J. Hydraul. Eng.* 133(10):1123-1134.
- Kökçinar, M.A., 1990, Design criterions for water jet pumps and determination of critical flow velocity in



- sediment carrying pipeline systems. MSc Thesis, Middle East Technical University, Ankara, Turkey.
- Kökpinar, M.A. and Göğüş, M., 2001, Critical flow velocity in slurry transporting horizontal pipelines. *ASCE J. Hydr. Engrg.*, 127(9):763-771.
- Li, Y., Zeng, X., Lv, W. and He, Z., 2020, Centrifugal pump wear for solid–liquid two-phase flows based on computational fluid dynamics–discrete element method coupling. *Advances in Mechanical Engineering*, 12(7):1–17, DOI:10.1177/1687814020937951.
- Mueller, N.H.G., 1964, Water jet pumps. *ASCE Journal of Hydraulic Division* 90(3):83-110, DOI:10.1061/JYCEAJ.0001059.
- Neto, I.E.L., 2011., Maximum suction lift of water jet pumps. *Journal of Mechanical Science and Technology* 25(2):391-394, DOI:10.1007/s12206-010-1221-7.
- Ni, F., Vlasblom, W.J., and Zwartbol, A., 1999, Effect of high solid concentration on characteristics of a slurry pump. 14th International Conference on Slurry Handling and Pipeline Transport, Hydrotransport 14, British Hydraulic Research (BHR) Group Publication No: 36, pp.141-149, Maastricht, The Netherlands.
- Noon, A.A. and Kim, M-H., 2016, Erosion wear on centrifugal pump casing due to slurry flow, *Wear* 364-365:103–111, DOI:10.1016/j.wear.2016.07.005.
- Peng, G., Huang, X., Zhou, L., Zhou, G., and Zhou, H., 2020, Solid-liquid two-phase flow and wear analysis in a large-scale centrifugal slurry pump. *Engineering Failure Analysis*, 114 104602, DOI: 10.1016/j.engfailanal.2020.104602.
- Reddy, Y. R. and Kar, S., 1968, Theory and performance of water jet pump. *ASCE Journal of Hydraulic Division* 94(5):1261-1278, DOI:10.1061/JYCEAJ.0001873.
- Sheha, A.A.A., Nasr, M., Hosien, M.A., and Wahba, E.M., 2018, Computational and Experimental Study on the Water-Jet Pump Performance. *Journal of Applied Fluid Mechanics* 11(4):1013-1020, DOI: 10.29252/jafm.11.04.28407.
- Sun, T., Meakin, P., and Jossang, T., 2001, A computer model for meandering rivers with multiple bed load sediment sizes: 1. Theory. *Water Resources Research* 37(8): 2227-2241, DOI:10.1029/2000WR900396.
- Tarodiya, R. and Gandhi, B.K., 2019, Experimental investigation of centrifugal slurry pump casing wear handling solid-liquid mixtures. *Wear* 434–435 (2019) 202972. DOI:10.1016/j.wear.2019.202972.
- Wang, D. and Wypych, P.W., 1995, Water-only performance of proportioning jet pumps for transportation of solids. *Powder Technology* 84(1):57–64, DOI:10.1016/0032-5910(94)02965-Q.
- Winoto, SH, Li, H and Shah, DA (2000) Efficiency of jet pumps. *ASCE J. Hydr. Engrg.*, 126(2):150-156, DOI: 10.1061/(ASCE)0733-9429(2000)126:2(150)
- Xiao, L. and Long X., 2015, Cavitating flow in annular jet pumps. *International Journal of Multiphase Flow* 71 (2015):116–132.
- Yapıcı, R. and Aldas, K., 2013, Optimization of water jet pumps using numerical simulation. *Proc IMechE Part A: J Power and Energy* 227(4):438–449, DOI: 10.1177/0957650913487529.

# ISI BİLİMİ VE TEKNİĞİ DERGİSİ İÇİN MAKALE HAZIRLAMA ESASLARI

Isı Bilimi ve Tekniği Dergisi'nde, ısı bilimi alanındaki özgün teorik ve deneysel çalışmaların sonuçlarının sunulduğu makaleler ve yeterli sayıda makaleyi tarayarak hazırlanmış olan literatür özeti makaleler yayınlanmaktadır. Makaleler, Türkçe veya İngilizce olarak kabul edilmektedir. Makaleler ilk sunumda serbest formatta hazırlanabilir. Ancak yayın için kabul edilmiş olan makaleler dergimizin basım formatına tam uygun olarak yazarlar tarafından hazırlanmalıdır. Aşağıda, ilk sunuş ve basıma hazır formatta makale hazırlamak için uyulması gereken esaslar detaylı olarak açıklanmıştır.

## İLK SUNUŞ FORMATI

İlk sunuşta, makale A4 boyutundaki kağıda tek sütun düzeninde, 1.5 satır aralıklı ve sayfa kenarlarından 25'er mm boşluk bırakılarak yazılmalıdır. Yazı boyutu 11 punto olmalı ve **Times New Roman** karakter kullanılmalıdır. Şekiller, tablolar ve fotoğraflar makale içinde **olmaları gereken yerlere** yerleştirilmelidir. Makale, elektronik olarak editörün e-posta adresine gönderilmelidir.

## BASIMA HAZIR MAKALE FORMATI

Hakem değerlendirmelerinden sonra, yayın için kabul edilmiş olan makaleler, dergimizin basım formatına tam uygun olarak yazarlar tarafından hazırlanmalıdır. Makaleler yazarların hazırladığı haliyle basıldığı için, yazarların makalelerini basım için hazır formatta hazırlarken burada belirtilen esasları titizlikle takip etmeleri çok önemlidir. Aşağıda, basıma hazır formatta makale hazırlamak için uyulması gereken esaslar detaylı olarak açıklanmıştır.

### Genel Esaslar

Makaleler genel olarak şu başlıklar altında düzenlenmelidir: Makale başlığı (title), yazar(lar)ın ad(lar)ı, yazar(lar)ın adres(ler)i, özet (abstract), anahtar kelimeler (keywords), semboller, giriş, materyal ve metod, araştırma sonuçları, tartışma ve sonuçlar, teşekkür, kaynaklar, yazarların fotoğrafları ve kısa özgeçmişleri ve ekler. Yazılar bilgisayarda tek satır aralıklı olarak, 10 punto Times New Roman karakteri kullanılarak Microsoft Office Word ile iki sütun düzeninde yazılmalıdır. Sayfalar, üst kenardan 25 mm, sol kenardan 23 mm, sağ ve alt kenarlardan 20 mm boşluk bırakılarak düzenlenmelidir. İki sütun arasındaki boşluk 7 mm olmalıdır. Paragraf başları, sütunun sol kenarına yaslanmalı ve paragraflar arasında bir satır boşluk olmalıdır.

Birinci seviye başlıklar büyük harflerle kalın olarak, ikinci seviye başlıklar bold ve kelimelerin ilk harfleri büyük harf olarak ve üçüncü seviye başlıklar sadece ilk harfi büyük olarak yazılır. Bütün başlıklar sütunun sol kenarı ile aynı hizadan başlamalıdır ve takip eden paragrafla başlık arasında bir satır boşluk olmalıdır. Şekiller, tablolar, fotoğraflar v.b. metin içinde ilk atıf

yapılan yerden hemen sonra uygun şekilde yerleştirilmelidir. İlk ana bölüm başlığı, Özetten (Abstract'tan) sonra iki satır boşluk bırakılarak birinci sütuna yazılır.

### Başlık, Yazarların Adresi, Özet, Abstract ve Anahtar Kelimeler

Yazılar Türkçe veya İngilizce olarak hazırlanabilir. Her iki durumda da makale özeti, başlığı ve anahtar kelimeler her iki dilde de yazılmalıdır. Eğer makale Türkçe olarak kaleme alınmışsa, Türkçe başlık ve özet önce, İngilizce başlık ve Özet (Abstract) sonra yazılır. Eğer makale İngilizce olarak kaleme alınmışsa önce İngilizce başlık ve özet (abstract) sonra Türkçe başlık ve özet yazılır. Başlık, sayfanın üst kenarından 50 mm aşağıdan başlar ve kalın olarak 12 punto büyüklüğünde, büyük harflerle bütün sayfayı ortalayacak şekilde yazılır. Yazar(lar)ın adı, adresi ve elektronik posta adresi başlıktan sonra bir satır boşluk bırakılarak yazılmalıdır. Yazarların adı küçük, soyadı büyük harflerle yazılmalı ve bold olmalıdır. Yazarların adresinden sonra üç satır boşluk bırakılarak, Özet ve Abstract 10 punto büyüklüğünde bütün sayfa genişliğinde yazılır. Özet ve Abstracttan sonra anahtar kelimeler (Keywords) yazılır.

### Birimler

Yazılarda SI birim sistemi kullanılmalıdır.

### Denklemler

Denklemler, 10 punto karakter boyutu ile bir sütuna (8 cm) sığacak şekilde düzenlenmelidir. Veriliş sırasına göre yazı alanının sağ kenarına yaslanacak şekilde parantez içinde numaralanmalıdır. Metin içinde, denklemlere '**Eş. (numara)**' şeklinde atıfta bulunulmalıdır.

### Şekiller

Şekiller 8 cm (bir sütun) veya 16 cm (iki sütun) genişliğinde olmalıdır ve makale içerisinde olmaları gereken yerlere bilgisayar ortamında sütunu (veya bütün sayfa genişliğini) ortalayacak şekilde yerleştirilmelidir. Şekil numaraları (sıra ile) ve isimleri şekil **altına, 9 punto büyüklüğünde** yazılmalıdır.

## Tablolar

Tablolar 8 cm (bir sütun) veya 16 cm (iki sütun) genişliğinde olmalıdır. Makale içerisinde olmaları gereken yerlere bilgisayar ortamında sütunu (veya bütün sayfa genişliğini) ortalayacak şekilde yerleştirilmelidir. Tablo numaraları (sıra ile) ve isimleri tablo **üstüne, 9 punto büyüklüğünde** yazılmalıdır.

## Fotograflar

Fotograflar, siyah/beyaz ve 8 cm (bir sütun) veya 16 cm (iki sütun) genişliğinde olmalıdır. Fotograflar digitize edilerek, makale içinde bulunmaları gereken yerlere bilgisayar ortamında sütunu (veya bütün sayfa genişliğini) ortalayacak şekilde yerleştirilmelidir ve şekil gibi numaralandırılmalı ve adlandırılmalıdır.

## Yazar(lar)ın Fotoğraf ve Kısa Özgeçmişleri

Yazarların fotoğrafları digitize edilerek, makalenin en sonuna özgeçmişleri ile birlikte uygun bir şekilde yerleştirilmelidir.

## SEMBOLLER

Makale içinde kullanılan bütün semboller alfabetik sırada Özetten sonra liste halinde tek sütun düzeninde yazılmalıdır. Boyutlu büyüklükler birimleri ile birlikte ve boyutsuz sayılar (Re, Nu, vb.) tanımları ile birlikte verilmelidir.

## KAYNAKLAR

Kaynaklar metin sonunda, ilk yazarın soyadına göre alfabetik sırada listelenmelidir. Kaynaklara, yazı içinde, yazar(lar)ın soyad(lar)ı ve yayın yılı belirtilerek atıfta

bulunulmalıdır. Bir ve iki yazarlı kaynaklara, her iki yazarın soyadları ve yayın yılı belirtilerek (Bejan, 1988; Türkoğlu ve Farouk, 1993), ikiden çok yazarlı kaynaklara ise birinci yazarın soyadı ve "vd." eki ve yayın yılı ile atıfta bulunulmalıdır (Ataer vd, 1995). Aşağıda makale, kitap ve bildirilerin kaynaklar listesine yazım formatı için örnekler verilmiştir.

Ataer Ö. E., Ileri A. and Göğüş, Y. A., 1995, Transient Behaviour of Finned-Tube Cross-Flow Heat Exchangers, *Int. J. Refrigeration*, 18, 153-160.

Bejan A., 1998, *Advanced Engineering Thermodynamics* (First Ed.), Wiley, New York.

Türkoğlu H. and Farouk B., 1993, Modeling of Interfacial Transport Processes in a Direct-Contact Condenser for Metal Recovery, *Proc. of 73<sup>rd</sup> Steel Making Conference*, Detroit, 571-578.

Türkoğlu H., 1990, *Transport Processes in Gas-Injected Liquid Baths*, Ph.D. Thesis, Drexel University, Philadelphia, PA, USA.

İnternet, 2004, Türkiye İstatistik Kurumu, *Atıksu İstatistikleri*, <http://www.tuik.gov.tr/HaberBulteni>.

## DIĞER HUSUSLAR

Hakem değerlendirmesinden sonra kabul edilen makaleler, yukarıda açıklandığı şekilde dizilerek basıma hazırlandıktan sonra, bir elektronik kopyası editöre gönderilmelidir. Makalenin basıma hazır kopyası ile birlikte, "Telif Hakkı Devri Formu" da doldurularak gönderilmelidir. Telif Hakkı Devri Formu'na ve bu yazım klavuzuna [www.tibt.org.tr](http://www.tibt.org.tr) adresinden ulaşılabilir.



**TÜRK ISI BİLİMİ VE TEKNİĞİ DERNEĞİ**  
**ÜYELİK BAŞVURU FORMU**

FOTOĞRAFINIZ

A. Adınız Soyadınız :  
Ünvanınız :  
Doğum yeri : : Doğum tarihi: / / 19 T.C. Kimlik No:  
İş Adresiniz :  
Ev adresiniz :  
Telefonunuz : İş Ev Cep  
E-posta :

B. \*Derneğe Asil üye Fahri üye olmak istiyorum.

1. Sizi tanıyan dernek üyesi (Üyelik için) :

2. Mezun olduğunuz  
Yüksek Okullar Yıl Branşınız Ünvanınız

3. İlgilendiğiniz konular :

2015 yılı aidatı olarak toplam 25 YTL (Yirmibeş Milyon TL) derneğin

İş Bankası Maltepe Şubesi Hesap No: 42120867567  
IBAN: TR08 0006 4000 0014 2120 8675 67

hesabına yatırılmıştır.

Tarih :

İmza :

\* Asil üye olmak için beş yıllık deneyim gereklidir.  
Fahri üyelik için yüksekokul mezunu olma şartı yoktur.

Türk Isı Bilimi ve Tekniđi Derneđi  
Gazi Üniversitesi  
Mühendislik Fakültesi  
Makina Mühendisliđi Bölümü  
06570 Maltepe/ ANKARA

## İÇİNDEKİLER / CONTENTS

<b>Numerical investigation of plate cooling using multiple impinging jets in different alignments</b> <i>Farklı dizilimlerde çoklu çarpan jetler ile plaka soğutmasının sayısal olarak incelenmesi</i> Alperen YILDIZELI and Sertaç ÇADIRCI	<b>1</b>
<b>Investigation of heat transfer improvements of graphene oxide-water and diamond-water nanofluids in cross flow impinging jet flow channels having fin</b> <i>Kanatçıklı çapraz akış çarpan jet akışlı kanallarda grafen oksit-su ve elmas-su nanoakışkanlarının ısı transferi iyileştirmelerinin araştırılması</i> Koray KARABULUT	<b>11</b>
<b>Investigation of heat convection during vehicle braking</b> <i>Taşıt frenlemesi esnasında oluşan ısı taşınımının incelenmesi</i> Cansu AY GÖKÇE and Abdullah DEMİR	<b>31</b>
<b>Difüzyon absorpsiyonlu soğutma sisteminde CuO ve TiO<sub>2</sub> nano partiküllerinin enerji ve ekserji performansına etkisi</b> <i>The effect of CuO and TiO<sub>2</sub> nano particles on energy and exergy performance in diffusion absorption refrigeration system</i> Abdullah YILDIZ ve Sinan SUNAL	<b>41</b>
<b>Analysis of thermal crack formation in water-charged air-cooled heat exchangers for heavy-duty vehicles</b> <i>Ağır hizmet araçları için su şarjlı hava soğutmalı ısı değiştiricilerinde ısıl çatlak oluşumunun analizi</i> İsmail Hakkı SAVCI	<b>59</b>
<b>Damlacık sayısı ve damlacıklar arası yatay mesafenin maksimum yayılma alanı ve ısı transferi performansı üzerine etkilerinin sayısal incelenmesi</b> <i>Numerical investigation of the effects of droplet number and horizontal distance on maximum spreading area and heat transfer performance</i> Ahmet GÜLTEKİN, Nejdet ERKAN, Üner ÇOLAK ve Shunichi SUZUKI	<b>69</b>
<b>Effects of roughness elements on V-corrugated absorber plate solar air heaters</b> <i>Pürüzlülük elemanlarının V-kat levhali güneş hava ısıtıcılarına etkileri</i> Hussain SHAWISH and Murat ÖZDENEFE	<b>81</b>
<b>Geometric optimization of a nanostructured W-SiO<sub>2</sub>-W selective emitter with temperature dependent emissivity for thermophotovoltaic applications</b> <i>Sıcaklığa bağlı yayınım gösteren nano yapıları W-SiO<sub>2</sub>-W seçici yayıcının termofotovoltaik uygulamalar için geometrik optimizasyonu</i> Eslem Enis ATAK, Elif Begüm ELÇİOĞLU and Tuba OKUTUCU-ÖZYURT	<b>95</b>
<b>Mikroalg ve mikroalg-etanol karışımları kullanımının motor performans ve emisyonları üzerine bir inceleme</b> <i>An investigation on engine performance and emissions of using microalgae and microalgae-ethanol blends</i> Gönenç DURAN, Muhammed DÖNMEZ ve Cumali İLKILIÇ	<b>107</b>
<b>The performance of water jet pumps and their application in slurry transportation</b> <i>Su jet pompalarının performansı ve katı-sıvı karışım taşımacılığında uygulanması</i> Mehmet Ali KÖKPİNAR and Mustafa GÖĞÜŞ	<b>119</b>